WIFFEN

DOE/ET-0065/5

Damage Analysis and Fundamental Studies

Quarterly Progress Report
January-March, *1979*

May *1979*

U.S. Department of Energy
Assistant Secretary for Energy Technology
Office of Fusion Energy

Available from:

National Technical Information Service (NTIS)
U.S. Department of Commerce
5285 Port Royal Road
Springfield, Virginia 22161

Price: Printed copy: $10.75
Microfiche: $3.00

DOE/ET-0065/5
UC-20, 20c

Damage Analysis and Fundamental Studies

Quarterly Progress Report
January-March, 1979

May *1979*

U.S. Department of Energy
Assistant Secretary for Energy Technology
Office of Fusion Energy
Washington, D.C. 20545

FOREWORD

This report is the fifth in a series of Quarterly Technical Progress Reports on ***"Damage Analysis and Fundamental Studies"*** (DAFS) which is one element of the Fusion Reactor Materials Program, conducted in support of the Magnetic Fusion Energy Program of the U. S. Department of Energy. Other elements of the Materials Program are:

- ***Alloy Development for Irradiation Performance (ADIP)***
- ***Plasma-Materials Interaction (PMI)***
- ***Special Purpose Materials (SPM).***

The DAFS program element is a national effort composed of contributions from a number of National Laboratories and other government laboratories, universities, and industrial laboratories. It was organized by the Materials and Radiation Effects Branch, Office of Fusion Energy, DOE, and a Task Group on ***Damage Analysis and Fundamental Studies*** which operates under the auspices of that Branch. The purpose of this series of reports is to provide a working technical record of that effort for the use of the program participants, for the fusion energy program in general, and for the Department of Energy.

This report is organized along topical lines in parallel to a Program Plan of the same title (to be published) so that activities and accomplishments may be followed readily relative to that Program Plan. Thus, the work of a given laboratory may appear throughout the report. Chapters 1 and 2 report topics which are generic *to* all of the DAFS Program: DAFS Task Group Activities and Irradiation Test Facilities, respectively. Chapters 3, 4, and 5 report the work that is specific to each of the subtasks around which the program is structured: A. Environmental Characterization, B. Damage Production, and C. Damage Microstructure Evolution and Mechanical Behavior. The Table of Contents is annotated for the convenience *of* the reader.

This report has been compiled and edited under the guidance of the Chairman of the Task Group on ***Damage Analysis and Fundamental Studies,*** D. G. Doran, Hanford Engineering Development Laboratory, and his efforts, those of the supporting staff of HEDL and the many persons who made technical contributions are gratefully acknowledged. T. C. Reuther, Materials and Radiation Effects Branch, is the Department of Energy counterpart to the Task Group Chairman and has responsibility for the DAFS Program within DOE.

Klaus M. Zwilsky, Chief
Materials and Radiation
Effects Branch
Office of Fusion Energy

CONTENTS

CONTENTS (Cont'd)

CONTENTS (Cont'd)

CONTENTS (Cont'd)

CONTENTS (Cont'd)

CONTENTS (Cont'd)

CONTENTS (Cont'd)

FIGURES

FIGURES (Cont'd)

FIGURES (Cont'd)

FIGURES (Cont'd)

Page

CHAPTER 4 (Cont'd)

CHAPTER 5

Installation of High Resolution Mass Spectrometer for Studies of Vacuum Ambient Effects on Microstructural Evolution in Dual-Ion Bombarded Refractory Alloys

FIGURES (Cont'd)

Page

CHAPTER 5 (Cont'd)

FIGURES (Cont'd)

FIGURES (Cont'd)

FIGURES (Cont'd)

Page

CHAPTER 5 (Cont'd)

TABLES

Page

CHAPTER 3

Helium Analyses of Be(d,n)- and T(d,n)- Irradiated Pure Elements

High Energy Neutron Cross Sections for Transport and Damage Calculations

FMIT Damage Parameter Sensitivity Study

TABLES (Cont'd)

CHAPTER 1

DAFS TASK GROUP ACTIVITIES

DAFS TASK GROUP ACTIVITIES

I. DAFS Task Group (D. G. Doran, Chairman)

A. Workshop

A Workshop on Techniques for Radiation Damage Analysis, sponsored by the Materials and Radiation Effects Branch of the Office of Fusion Energy, was held at the Oak Brook Hyatt House, Oak Brook, Illinois, on March 8-9, 1979. Speakers and their subjects were:

M. Hayns (Harwell) - Current Understanding of the Primary Defect Microstructure

H. Wiedersich (Argonne) - Current Understanding of the Secondary Damage Microstructure

R. W. Siegel (Argonne) - Positron Annihilation

D. Joy (Bell Labs) - Energy Dispersive X-ray Analysis, and Energy Loss Spectroscopy

R. Sinclair (Stanford) - Ultra High Resolution TEM and Microdiffraction

T. Picraux (Sandia) - Channelling Techniques

R. W. Hendricks (Oak Ridge) - Diffuse Scattering of Neutrons and X-rays

D. N. Seidman (Cornell) - Field Ion Microscopy

J. A. Sprague (Naval Research Lab) - Data Handling for Transmission Electron Microscopy

F. Fradin (Argonne) - Hyperfine Interactions

M. G. Lagally (U. Wisc.) - Surface Techniques

Documentation of the Workshop is currently in preparation by the Workshop committee: P. Wilkes (U. of Wisc.), J. A. Spitznagel (Westinghouse R & 3 Center), and F. V. Nolfi (Argonne National Lab).

B. Chairmen's Meeting

A meeting of DAFS Subtask Group Chairinen was held at Oak Brook, Illinois, on March 8, 1979.

II. Subtask Group A - Environmental Characterization (L. R. Greenwood, ANL, Chairinan)

A. Nuclear Data Needs

A meeting chaired by F. G. Perey (Oak Ridge), was held at Duke University on March 5-6, 1979, to review the Office of Basic Energy Sciences (OBES) Fusion Data Measurement Program. C. Head (DOE), L. Greenwood (Argonne), and H. Farrar IV (Rockwell) presented the nuclear data needs and prograins of the Magnetic Fusion Program. It appears that very little work is now in progress by OBES of immediate interest to the Fusion Materials Program. Specifically, some total cross sections are being measured up to 50 MeV by D. Larson (Oak Ridge), some H and He production measurements are being done below 15 MeV, and a few cross section calculations are planned. However, several OBES participants at the meeting were not aware of some of our requests. Hence, an official request by C. Head is now being revised for presentation at a DOE-Nuclear Data Conimittee meeting in April 1979.

B. RTNS-II Characterization

A formal dosimetry plan for the initial characterization of RTNS-II has now been completed by Rockwell, LLL, and Argonne. It is expected that the irradiation will take place in about 4-6 months, depending on the status of the large targets at RTNS-II.

III. Subtask Group B - Damage Production (M. W. Guinan, Chairman)

A meeting of this subtask group will be held at Livermore on June 7-8, 1979, to discuss the current status of displacement production calculations and to recommend directions for future studies.

IV. Subtask Group C - Damage Microstructure Evolution and Mechanical Behavior (G. R. Odette, Chairman)

A. OAFS Experiment in the ORR MFE-2 Test - G. R. Odette (UCSS), R. W. Powell (HEDL), and F. V. Nolfi (ANL)

1. Introduction

Experiments are being conducted at Oak Ridge National Laboratory (ORNL) in the Oak Ridge Research Reactor (ORR) to assess the effects of mixed spectrum neutron irradiations on the properties of metals. The OAFS Task Group is participating in these irradiations to determine the combined effects of helium generation and displacement damage on mechanisms of microstructure evolution and mechanical behavior.

The basic approach of the experiment was to vary the concentration, initial distribution and schedule of introduction of helium, while maintaining an approximately constant dpa level. This was accomplished by variations in nickel content (i.e., "pure 316 SS" versus E-19), or different pre-irradiation levels of helium implantation using a cyclotron. The initial distribution of helium was varied by post-irradiation heat

treatments and cold-working (CW)

It is now recognized that the schedule (e.g., pre-implantation versus simultaneous production) and conditions of introduction of helium (e.g., hot versus cold implantation) can have a strong effect on microstructural evolution. Hence, it would have been desirable to include some hot implantation specimens in this experiment; however, no facilities for hot implantation existed at the time the test was developed. Therefore, a major recommendation of the subtask group was that hot implantation capabilities be developed as part of the DAFS program. Argonne National Laboratory (ANL) agreed to assume this responsibility in conjunction with their cyclotron facility. It is anticipated that such capabilities will exist by September 1, 1979.

The experimental design was guided by model calculations and analysis of existing data. The experimental matrix is summarized in Tables 1a and 1b. The objective is to study some of the potentially important mechanisms governing the influence of helium on microstructural evolution, including: resolutioning helium from bubbles; helium diffusivity; void nucleation on bubbles and critical bubble size for void formation; and dislocation-bubble interactions. Clearly, to optimize the information derived from these experiments it will be necessary to analyze the resulting data using detailed computer models of microstructural development; such models are now under development.

2. Status

The second of a series of fusion materials experiments in ORR, designated MFE-2, began irradiation in September 1978. The DAFS test matrix for this experiment was reviewed by the Microstructural Evolution and Mechanical Behavior Subtask Group. Materials in the form of heat treated TEM disks were provided by ORNL. Implantations and heat treatments were carried out at ANL and specimens engraved and encapsulated at Hanford Engineering Development Laboratory (HEDL).

TABLE la

BASIC HELIUM MATRIX

He(appm)/ Heat Treatment	316 Pure*		E-19**	V-20Ti	V-15Cr-5Ti	Nb-1Zr
	SA	20CW	SA	SA	SA	SA
0	X	X	X	X	X	X
10	X	X	X	X	X	X
10a	X		X	X		
10b	X					
10c	X					
30	X	X	X	X	X	X
30a	X		X	X		
30b	X					
30c	X					

T_{irr} = 450, 550 and 650°C — 4 TEM disks each

Exposure ≈ 10 dpa

* Fe17Cr16.7Ni2.5Mo

** Fe15Cr20Ni, supplied by the Breeder Reactor Program

TABLE lb

HEAT TREATMENT MATRIX

He	316 SA			E-19			V-20Ti		
T_{irr}=	450	550	650	450	550	650	450	550	650
10a	600	700	700	700	700	700	800	800	800
10b	700	750	800						
10c	800	800	900						
30a	600	700	700	700	700	700	800	800	800
30b	700	750	800						
30c	800	800	900						

3. Future Work

The MFE-2 experiment is expected to be discharged froin the reactor in December 1979. Postirradiation examination of selected specimens will be initiated shortly after the test disassembly. Other complementary experiments in ORR and EBR-II are currently being planned.

CHAPTER 2

IRRADIATION TEST FACILITIES

STATUS OF IRRADIATION TEST FACILITIES

I. Rotating Target Neutron Source-I1 (RTNS-II)

Irradiations were begun this quarter on an interim basis using a reduced beam current and small (23 cm diameter) target. Maximum flux is 2-3 x 10^{12} n/cm^2-s.

CHAPTER 3

SUBTASK A: ENVIRONMENTAL CHARACTERIZATION

I. PROGRAM

Title: Dosimetry and Damage Analysis
Principal Investigator: L. R. Greenwood
Affiliation: Argonne National Laboratory

II. OBJECTIVE

To establish the best practicable dosimetry for mixed-spectrum reactors and to provide dosimetry and damage analysis for MFE experimenters.

III. RELEVANT DAFS PROGRAM TASK/SUBTASK

SUBTASK II. A. 1.1 Flux-spectral definition in a tailored fission reactor.

IV. SUMMARY

A low-power spectral measurement was conducted in the Oak Ridge Research Reactor in (ORR) during January. Dosimetry capsules from ORR-MFE-1 were also disassembled at this time. Analysis is currently in progress for both irradiations.

V. ACCOMPLISHMENTS AND STATUS

A. Experiments at the Oak Ridge Research Reactor - - L. R. Greenwood and R. R. Heinrich (ANL)

After considerable delays, the low power (1 MW) spectral measurement was conducted in ORR on January 12-14, 1979. The dosimetry capsule was irradiated in position E7, the same as ORR-WE-2 which was

removed from the reactor due to a helium leak. A dummy graphite cylinder was placed in position OC2 to simulate a graphite experiment during most of the lifetime of the MFE-2 experiment.

The dosimetry capsules for the low power run and for MFE-1 were disassembled at ORNL during the week of January 15. Dosimetry samples were returned to Argonne and helium samples to H. Farrar (Rockwell International). Most of the dosimetry samples have now been gamma counted for both runs and the data is now being analyzed prior to a flux-spectral unfolding.

VI REFERENCES

None

VII. FUTURE WORK

A complete flux-spectral unfolding and fluence mapping should be completed for both experiments (spectral and MFE-1) during the next quarter. The helium analysis may take much longer; however, we plan to integrate all of the results in order to improve our flux-spectral analysis and to test helium generation cross sections.

I. PROGRAM

Title: Dosimetry and Damage Analysis
Principal Investigator: L. R. Greenwood
Affiliation: Argonne National Laboratory

II. OBJECTIVE

To establish the best practicable dosimetry for Be(d,n) facilities and to provide dosimetry and damage analysis for OFE experimenters.

III. RELEVANT DAFS PROGRAM PLAN TASK/SUBTASK

SUBTASK 11. A.2.1 Flux-spectral definition in a Be(d,n) field.

SUBTASK II. A.3.1 Evaluate damage parameter sensitivity to flux/spectra uncertainties.

IV. SUMMARY

Flux and spectral mapping has been completed for the irradiation of tensile specimens by PNL at U.C. Davis (Be(d,n), E_d = 40 MeV) during September 1973. The dosimetry foils were cut into 12 subsections *to* determine flux-spectral contours on the smallest scale yet attempted. Radial flux and damage energy maps indicate steep gradients near the source.

V. ACCOMPLISHMENTS AND STATUS

A. Flux-Spectral Mapping at U.C. Davis - - L. R. Greenwood and R. R. Heinrich (ANL)

Dosimetry and damage analysis has been completed for PNL at U.C. Davis (Be(d,n), E_d = 40 MeV). Tensile specimens were irradiated at two locations, about 6 and 26 mm from the center of the neutron source volume. The dosimetry foils included Co, Nb, Fe, Zr, Au, Al, and Ni; the last two were gamma counted at LLL. Identical nickel foils were placed at the front and rear of each dosimeter packet to measure qeometric, scattering, and absorption effects; these effects were typically less than 10%. Selected nickel tensile wires were also counted to check the foil-to-wire correction.

All of the dosimetry foils were cut into 12 subsections, each measuring about 2 mm square. A complete spectral unfolding was then performed at each position to generate the most detailed spectral map ever attempted at a Be(d,n) source. The total fluence contours are shown in Figure 1. The scatter seen in close peonietry (6 mm) indicates that the flux field deviated slightly from cylindrical symmetry. The beam spot was probably elliptical with the long axis in the horizontal plane.

Complete damage calculations were then performed at each of the 24 locations where spectral analysis was performed. Figure 2 shows damage energy maps for nickel at the 6 and 26 mm positions. As can be seen, at close geometry (6 mm) the damage energy gradients are quite steep. In fact, the damage gradients are steeper than the flux gradients since the spectrum changes markedly with radial displacement from the beam axis. This is in contrast to calculations done for FMIT which show the damage gradients to be not so steep near the source. The difference can be easily explained by the difference in the beam profiles. Whereas the FMIT beam profile is roughly a square 1 CM by 4 - 10 cm, at U.C. Davis the beam spot is only 3 - 5 mm in diameter! Hence, spectral effects are greatly surpresscd at FMIT relative to U.C. Davis. Since the PNL tensile wires were about 1 cm in length, each wire saw an

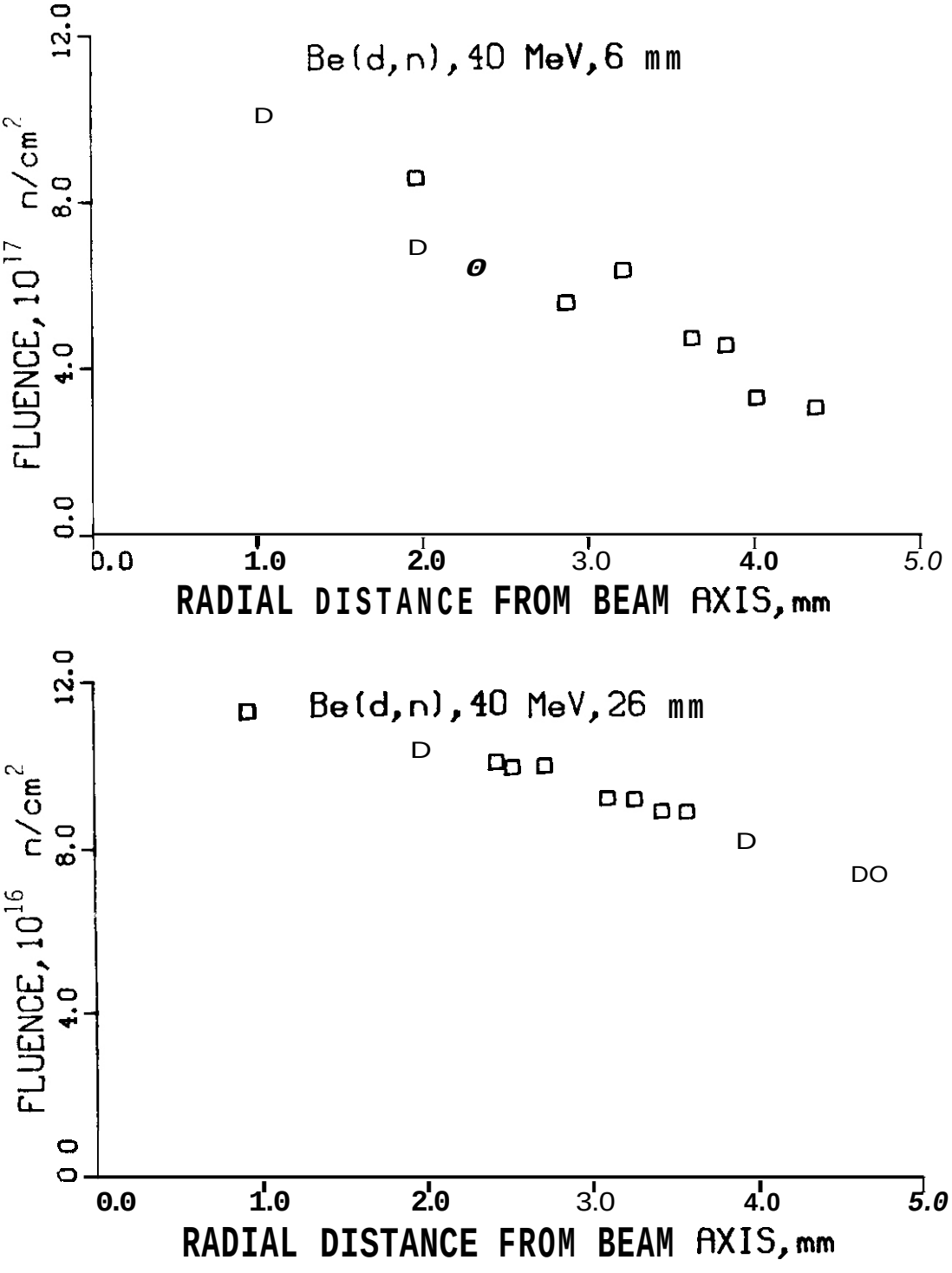

Figure 1. Fluence gradients as determined from unfolded spectra at 6 mm (top) and 26 mm (bottom) from the center of the neutron source. The scatter indicates some assymetry in the beam.

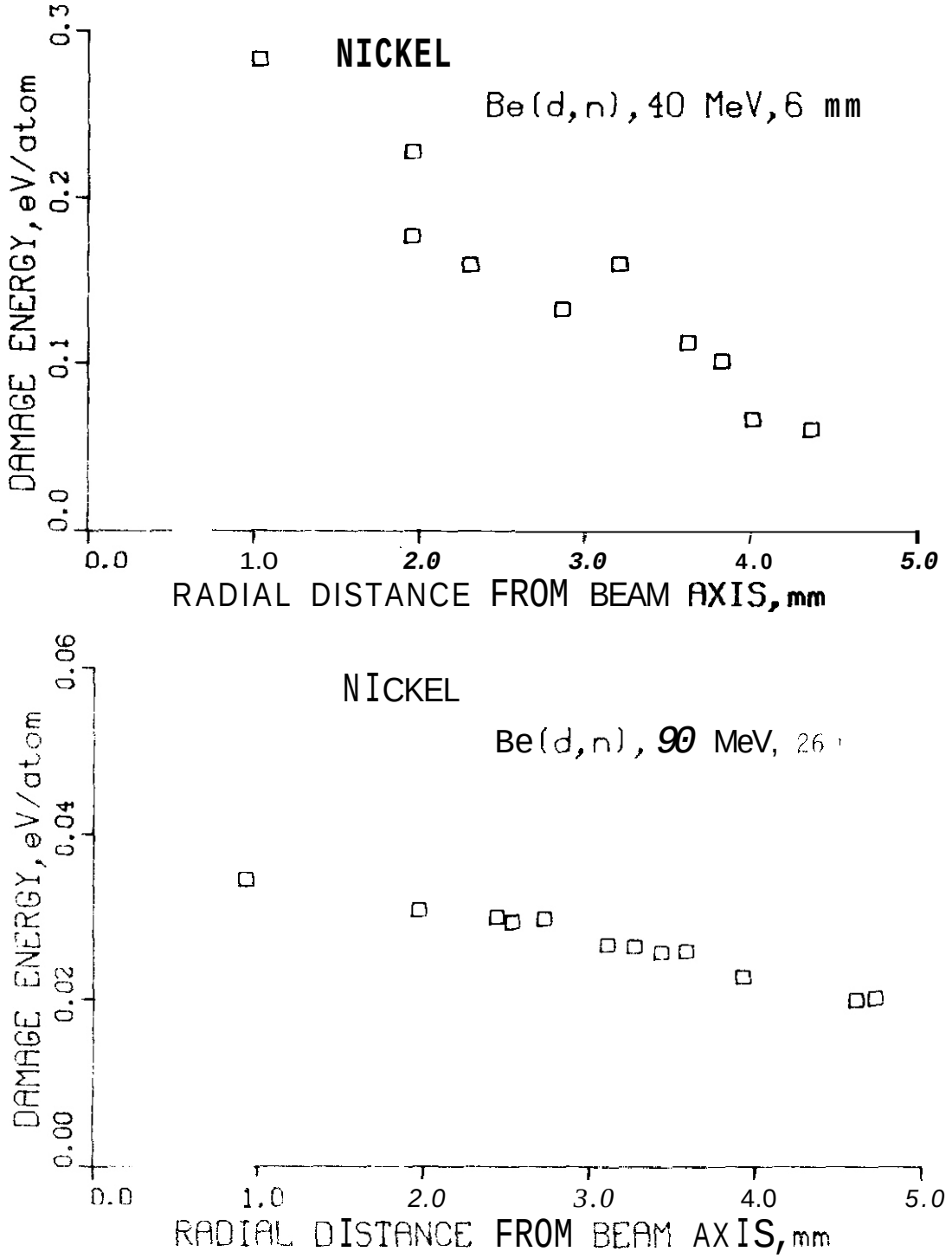

Figure 2. Damage energy gradients calculated for nickel from the unfolded spectra at 6 mm (top) and 26 mm (bottom) from the source. The steep gradient (top) reflects the large angular range subtended in close geometry.

average damage rate which can be computed from the damage map and variations between wires are much smaller than the gradient maps would suggest.

VI. REFERENCES

None

VII. FUTURE WORK

The E_d = 30 MeV characterization work at U.C. Davis with RI and LLL is nearly ready for spectral unfolding. Flux/spectral mapping will then be completed.

VIII. PUBLICATIONS

Previous results with PNL were presented at the First Topical Meeting on Fusion Reactor Materials, January 29-31, 1979, in Miami Beach, Florida.

High energy neutron activation cross sections have been published as an ANL report:

L. R. Greenwood, Extrapolated Neutron Activation Cross Sections for Dosimetry to 44 MeV, ANL/FPP/TM-115 (1978)

I. PROGRAM

Title: Helium Generation in Fusion Reactor Materials

Principal Investigators: D. W. Kneff, Harry Farrar IV

Affiliation: Rockwell International, Energy Systems Group

II. OBJECTIVE

The objectives of this work are to measure helium generation rates of materials for Magnetic Fusion Reactor applications in the Be(d,n) and T(d,n) neutron environments, to characterize the Be(d,n) neutron fluence and neutron energy distributions as a function of position relative to the neutron source, particularly in the high-flux region, and to develop helium accumulation fluence monitors *for* neutron fluence and energy spectrum dosimetry for the various fusion-program neutron test environments.

III. RELEVANT DAFS PROGRAM PLAN TASK/SUBTASK

SUBTASK II.A.2.1	Flux-Spectral Definition in the Be(d,n) Field
SUBTASK II.A.4.2	T(d,n) Helium Gas Production Data
SUBTASK II.A.4.3	Be(d,n) Helium Gas Production Data
SUBTASK II.A.5.1	Helium Accumulation Monitor Development

IV. SUMMARY

Helium analyses have been completed for 26 pure element specimens of C, Ti, V, Cr, Nb, and Mo irradiated in Be(d,n) and T(d,n) neutron fields. Approximate values of their relative helium generation rates have been obtained for FMIT design application. The total helium generation cross section for chromium in a T(d,n) neutron environment has been estimated to be ~36 mb. Final data reduction is in progress for an additional 44 Al, Fe, and Ni pure element helium accumulation dosimetry segments from the Be(d,n) irradiation.

V. ACCOMPLISHMENTS AND STATUS

Helium Analyses of Be(d,n)- and T(d,n)-Irradiated Pure Elements -- D. W. Kneff, Harry Farrar IV, and M. M. Nakata (Rockwell International, Energy Systems Group)

Helium analyses are continuing of the materials irradiated in two joint Rockwell International-Argonne National Laboratory (ANL)-Lawrence Livermore Laboratory (LLL) Be(d,n) and T(d,n) irradiation experiments. The objectives of these experiments were to measure the spectrum-integrated helium generation cross sections of a large number of pure elements and other materials of potential fusion reactor design interest, characterize these neutron environments, and develop the use of helium accumulation materials as neutron dosimeters. The Be(d,n) irradiation[1] was conducted with 30-MeV deuterons using the isochronous cyclotron at the University of California, Davis. The T(d,n) irradiation[2] was conducted with the Rotating Target Neutron Source-I (RTNS-I) at LLL. Previous analyses for these experiments have been reported in earlier Quarterly Progress Reports.[2,3]

The emphasis during the present reporting period was on obtaining estimates for the relative helium generation rates in pure elements important to the design of the Fusion Materials Irradiation Test Facility (FMIT). The helium analysis results for 26 pure element specimens of C, Ti, V, Cr, Nb, and Mo irradiated in the Be(d,n) and T(d,n) neutron fields are presented in Table 1. These results were obtained by first etching the specimens (with the exception of carbon) to remove the effects of helium recoil into or out of their surface layers, weighing them against standards traceable to the National Bureau of Standards, and analyzing them for helium by high-sensitivity gas mass spectrometry. The amount of etching was based on calculations of helium recoil ranges, and on estimated neutron spectrum shapes. The variation in the helium concentration

TABLE 1

MEASURED HELIUM CONCENTRATIONS IN Be(d,n)- AND T(d,n)-IRRADIATED PURE ELEMENTS

Spectrum	Element	Specimen	Mass (mg)	Measured Number of 4He Atoms	Helium Concentration (appb)*
Be(d,n)	C (diamond)	GC-7	1.502	1.20×10^{13}	159
		GC-8	1.301	4.04×10^{12}	61.6
	Ti	GTI-3A	0.623	4.611×10^{10}	5.89
		GTI-3B	1.621	1.180×10^{11}	5.79
		GTI-3C	1.058	7.696×10^{10}	5.7%
	V	GV-2A	5.233	8.02×10^{10}	1.20
		GV-2B	3,938	6.96×10^{10}	1.50
	Cr	GCR-2	2.023	7.19×10^{10}	3.0:
		GCR-6	2.860	2.42×10^{11}	7.3;
	Nb	GWR-2A	3.106	5.28×10^{10}	1.54
	Mo	GMO-3A	1.592	1.41×10^{10}	1.41
		GMO-3B	1.351	9.49×10^{9}	1.12
T(d,n)	C (diamond)	FC-4	1.907	1.22×10^{13}	128
		FC-5	2.022	6.78×10^{12}	66.8
	V	FV-2A	5.872	1.62×10^{11}	2.33
		FV-2B	2.355	5.95×10^{10}	2.14
	Cr	FCR-1A	3.787	2.55×10^{11}	5.82
		FCR-1B	1.682	1.06×10^{11}	5.46
		FCR-2A	5.232	2.29×10^{11}	3.78
		FCR-2B	4.721	2.26×10^{11}	4.14
		FCR-4	2.125	1.55×10^{11}	5.24
		FCR-6	4.353	1.42×10^{11}	2.81
	Nb	FNB-A	15.111	9.80×10^{10}	0.59
		FNB-B	13.067	9.39×10^{10}	0.65
	Mo	FMO-1A	4.228	1.69×10^{10}	1.77
		FMO-1B	2.327	1.78×10^{10}	1.22

*Helium concentrations in atomic parts per billion (10^{-9} atom fraction). The variation in the results for each element reflects the neutron fluence variation with neutron source angle and distance.

results for each element is due primarily to the large neutron fluence gradients over the sample volumes of the two irradiation assemblies.

Although cross sections will not be derived from these final helium generation results until the neutron dosimetry mapping for these experiments is complete (a joint effort with ANL and LLL), the results were nevertheless used to estimate the relative helium generation rates for these materials. The objective is to provide timely input on helium generation for the final design of FMIT. The relative helium generation rates are given in Table 2, where they are normalized to the helium generation for copper. The Be(d,n) results are given in Column 2, where they have been corrected approximately for the steep fluence gradient. The corrections were based on the measurement by Meulders, et al.[4] of the Be(d,n) neutron flux gradient as a function of source angle, and on an estimate of the fluence change with distance from the Be(d,n) source using ANL's radiometric counting results for the $^{54}Fe(n,p)^{54}Mn$ and $^{93}Nb(n,2n)^{92m}Nb$ dosimetry reactions.[5] The Be(d,n) results reported earlier[3] for Al, Fe, and Ni are also included here, where they have been renormalized to copper and include some additional geometric corrections. The copper normalization was chosen to permit direct correlation with copper damage calculations previously made for FMIT.[6]

Column 3 of Table 2 gives the T(d,n) cross section ratios determined from a previous RTNS-I irradiation experiment,[7] and includes an estimate for chromium based on the present results. The measured chromium helium generation rate was normalized to the helium generation rates reported previously[2] for the pure element helium accumulation dosimetry wires included in this experiment, and includes estimated fluence gradient corrections. This normalization gives an estimated T(d,n) total helium generation cross section for chromium of ~ 36 mb.

Column 4 of Table 2 summarizes the cross section ratios measured by this laboratory some years ago for an EBR-II core neutron spectrum,[8] for comparison with the present results.

TABLE 2

APPROXIMATE RELATIVE HELIUM-GENERATION RATES OF PURE ELEMENTS

Element	Helium Generation Fate Relative to Copper		
	Be(d,n) Geometry-Corrected	T(d,n) RTNS-I (Incl. Ref. 7)	EBR-II Core (Peference 8)
cu	1	1	1
C	13	17.6	---
Al	2.9	2.80	1.87
Ti	0.8	0.75	0.73
V	0.3	0.35	50.97
Cr	0.6	0.7	−0.40
Fe	1.0	0.94	0.99
Ni	2.4	1.92	13.2
Nb	0.1	0.33	0.35
Mo	0.1	0.29	0.29

It must be emphasized that the Be(d,n) results and the chromium T(d,n) results are presented only as initial estimates, intended for FMIT design guidance. The results are based on very few helium analyses for C, Ti, V, Cr, Nb, and Mo, and treat several iinportant factors in a very approximate manner. The factors include effects of distance from the neutron source, capsule axis offset, helium generation cross section variations with neutron source angle, finite dimensions of the neutron source spot, and sample geometries. These factors are particularly important for the Be(d,n) irradiation, because of the steep neutron fluence and energy spectrum changes with neutron source angle. The results will be reevaluated, arid total helium production cross sections will be determined, when additional helium analyses *of* these materials are completed, and the neutron fluence/energy spectra are mapped out in detail for these irradiations.

Other progress on the Be(d,n) experiment during the report period included the mass spectrometric analysis of 44 additional pure element helium accumulation wire segments. These analyses included segments of iron and nickel wire aligned along radial lines from the capsule axis in the plane of the helium generation materials. The results will provide information on the variation in the helium generation rate as a function of the changing Be(d,n) neutron energy spectrum, associated with changes in the neutron source angle. The weighing of the radiometric dosimetry foil segments from the Be(d,n) irradiation experiment was completed during this report period.

VI. REFERENCES

1. D. W. Kneff and H. Farrar IV, "Helium Generation in Fusion Reactor Materials," Technical Progress Report for Period Apri 1-September 1977, AI-DOE-13219, Atomics International, Canoga Park, CA, January 1978.

2. D. W. Kneff, H. Farrar IV, and M. M. Nakata, "Helium Generation in Fusion Reactor Materials," in Damage Analysis and Fundamental Studies Quarterly Progress Reports, DOE/ET-0065/2 and DOE/ET-0065/3, U.S. Department of Energy.

3. D. W. Kneff, H. Farrar IV, and M. M. Nakata, "Helium Analyses of Be(d,n)-Irradiated Pure Elements," in Damage Analysis and Fundamental Studies, Quarterly Proqress Report October-December 1978, DOE/ET-0065/4, U.S. Department of Energy.

4. J. P. Meulders, P. Leleux, P. C. Macq, and C. Pirart, "Fast Neutron Yields and Spectra from Targets of Varying Atomic Number Bombarded with Deuterons from 16 to 50 MeV." Phys. Med. Biol. 20, 235 (1975).

5. L. R. Greenwood and R. R. Heinrich, "Experiments at the U.C. Davis Cyclotron, Be(d,n), E_d = 30-40 MeV," in Damage Analysis and Fundamental Studies Quarterly Progress Report October-December 1973, DOE/ET-0065/4, U.S. Department of Enerqy.

6. J. O. Schiffgens, R. L. Simons, F. M. Mann, and L. L. Carter, "Spatial Variations of Damage Parameters in FMIT and Their Implications," in Damage Analysis and Fundamental Studies, Quarterly Progress Report October-December 1978, DOE/ET-0065/4, U.S. Department of Energy.

7. H. Farrar IV and D. W. Kneff, "Helium Generation in Twelve Pure Elements by 14.8-MeV Neutrons," Trans. Am. Nucl. Soc. 28, 197 (1978).

8. E. P. Lippincott, W. N. McElroy, and H. Farrar IV, "Helium Production in Reactor Materials," in Nuclear Cross Sections and Technology, Vol I, R. A. Schrack and C. D. Bowman, eds., pp. 375-377, National Bureau of Standards Special Publication 425, U.S. Department of Commerce (1975).

VII. FUTURE WORK

The helium analyses of the Be(d,n)-irradiated pure elements will continue, with initial emphasis on expanding *the* data base of the elements reported above. The measurements will be extended to Zr and Sn, and the gold dosimetry wires will be analyzed more fully to examine their energy sensitivity with neutron source angle. The Be(d,n) neutron fluence and energy profiles will be mapped as a function of position in the irradiation capsule using the ANL and LLL counting results, and the nearly.. complete helium accumulation dosiiiietry measurements. The results will be used to determine *the* helium-generation cross sections for the irradiated pure elements.

VIII. PUBLICATIONS

1. A paper entitled "Helium Accumulation Fluence Dosimetry for Fusion Reactor Materials Irradiation," by D. W. Kneff and Harry Farrar IV, was presented at the First Topical Meeting on Fusion Reactor Materials at Miami Beach, Florida, on January 30, 1979, and the final manuscript was submitted for publication in J. Nucl. Materials.

2. A paper entitled "The Production Rate of Helium During Irradiation of Nickel in Thermal Spectrum Fission Reactors," by F. W. Wiffen, E. J. Allen (ORNL), Harry Farrar IV (Rockwell), E. E. Bloom, T. A. Gabriel, H. T. Kerr, and F. G. Perey (ORNL), was presented at the First Topical Meeting on Fusion Reactor Materials, Miami Beach, Florida, on January 30, 1979.

3. A paper entitled "Experimental and Theoretical Determination of Helium Production in Copper and Aluminum by 14.8-MeV Neutrons," by D. W. Kneff, Harry Farrar IV (Rockwell), F. M. Mann, and R. E. Schenter (HEDL) is in preparation.

I. PROGRAM

Title: Nuclear Data for FMIT (WH025/EDK)
Principal Investigator: R. E. Schenter
Affiliation: Hanforcl Engineering Development Laboratory (HEDL)

II. OBJECTIVE

The objective of this work is to supply immediate nuclear data needs for the design and operation of the Fusion Materials Irradiation Test (FMIT) facility.

III. RELEVANT DAFS PROGRAM PLAN TASK/SUBTASK

All tasks that are relevant to FMIT use, with emphasis upon:
SUBTASK II.A.2.3 Flux-spectra definition in FMIT
SUBTASK II.B.1.2 Acnuisition of Nuclear Data

IV. SUMMARY

Measurements and calculations have been made of neutron spectra from 35 MeV deuterons on thick lithium. These results are not described here but may be found in the section on damage production.

Measurements of the total and nonelastic cross sections have been made for neutrons on iron, calcium, oxygen, and carbon for energies of 35, 40, and 50 MeV. The data were obtained at the University of California at Davis cyclotron laboratory for the purpose of improving the accuracy of nuclear data for FMIT neutron transport calculations (e.g. shielding and calculational dosimetry) and for damage analysis.

Calculations of deuteron and neutron induced activation of FMIT structural iiiaterials have been initiated in order to determine the best designs from the standpoint of maintenance.

V. ACCOMPLISHMENTS AND STATUS

A. High Energy Neutron Cross Sections for Transport and Damage Calculations -- F. P. Brady, C. Zanelli, J. L. Romero, J. L. Ullmann, P. O. Urone (U.C. Davis) D. L. Johnson (HEDL)

Neutron transport calculations require extensive nuclear data for neutrons as a function of energy including differential elastic scattering cross sections, differential neutron emission spectra, and nonelastic cross sections for all important materials. Damage calculations also require elastic scattering and neutron emission data.

For FMIT, these data are required for neutron energies up to about 50 MeV. For transport calculations in the FMIT test cell (calculational dosimetry) and for damage calculations in similar spectra, data will be required to about 35 MeV for important structural materials such as iron, nickel, and chromium. For transport calculations of FMIT shielding through thick concrete, the dose is dominated by neutrons near the highest energies in the spectrum (up to ~50 MeV). Important elements for shielding are oxygen, iron, silicon, calcium, and carbon.

Measurements of the nonelastic and removal cross-sections were made for neutrons of 40.4 and 50.4 MeV incident on targets of carbon, oxygen, calcium and iron. The removal cross-section is defined as the sum of the nonelastic plus that part of the elastic scattering which scatters neutrons to angles of 25° or more in the laboratory. These data were obtained using the technique used by Voss and Wilson[1].

Preliminary results of these measurements are shown in Table I.

Table I

EXPERIMENTAL NONELASTIC AND REMOVAL CROSS-SECTIONS (barns)

	40.4 MeV		50.4 MeV	
	σ_{non}	σ_{rem}	non	rem
Carbon	.360±.050	.560±.036	.352±.036	.468±.029
Oxygen	.419±.042	.630±.033	.382±.047	.514±.040
Calcium	1.013±.072	1.264±.058	.867±.109	1.077±.092
Iron	.966±.068	1.284±.053	.915±.051	1.158±.042

In the analysis using the method of Voss and Wilson, an accurate value for the neutron total cross-section at the same energy is required. Such values were not available for calcium and iron, hence measurements were made at 35.3, 40.3 and 50.4 MeV. In addition, one measurement of the total cross-section of neutrons on carbon at 50.4 MeV was made to coinpare with previous measurements[2]. The results of these measurements are shown in Table II.

Table II

EXPERIMENTAL TOTAL CROSS-SECTIONS (barns)

	35.3 MeV	40.3 MeV	50.4 MeV
Carbon	-	-	.934±.010
Calcium	2.107±.032	2.448±.044	2.220±.050
Iron	-	2.371±.027	2.362±.026

The value for carbon is in excellent agreement with expectations from previous results[2].

B. Deuteron and Neutron-Induced Activation of FMIT Accelerator and Beam Transport Structural Materials -- F. M. Mann, K. E. Mead, R. E. Schenter (HEDL)

Intense activation of structural materials in and around the FMIT accelerator and beam transport system are expected as a result of stall

losses of the deuteron beam along its path. Activation can occur directly from deuteron induced nuclear reactions and also from the secondary neutrons that are produced by the deuterons.

An important goal in the design of the FMIT facility will be to achieve "hands on" maintenance as much as possible in order to minimize costs. This goal will be challenging. Important ingredients in determining the levels of activation that can occur are the cross-sections for deuteron and neutron induced activation reactions. At the high energies associated with FMIT, these data are often poorly known or totally unavailable, especially for deuteron induced activation.

Initial calculations of deuteron induced activation have been made for Cu, Au, ^{56}Fe, and Al. Results indicate very large activities with Al being least troublesome.

VI. REFERENCES

1. R. G. P. Voss and R. Wilson, Proc. Royal Soc. of London A236 (1956) 41.

2. M. Auman, F. P. Brady, J. A. Jungerman, W. J. Knox, M. R. McGie, and T. C. Montgomery, Phys. Rev. C5 (1972) 1.

VII FUTURE WORK

Evaluation of high energy neutron total, elastic, and nonelastic cross-sections for O, Fe, Ca, Si, and C will be performed using available data for energies above ENDF/B-V data (20 - 50 MeV).

Evaluation of deuteron and neutron induced activation cross sections for FMIT structural materials will be continued. Measurements are being considered to fill in gaps and check calculation.

I. PROGRAM

Title: Nuclear Data for Damage Studies and FMIT (WHO25/EDX)
Principal Investigator: R. E. Schenter
Affiliation: Hanford Engineering Development Laboratory (HEDL)

II. OBJECTIVE

The objective of this work is to supply nuclear data needed for damage studies and in the design and operation of the Fusion Material Irradiation Testing (FMIT) facility.

III. RELEVANT OAFS PROGRAM PLAN TASK/SUBTASK

SUBTASK	II.A.2.3	Flux Spectra Definition in FMIT
TASK	II.A.4	Gas Generation Rates
SUBTASK	II.A.5.1	Helium Accumulation Monitor Development
SUBTASK	II.B.1.2	Acquisition of Nuclear Data

IV. SUMMARY

The computer code HAUSER*5, which predicts nuclear cross sections, has been used to calculate helium production for Al and Cu, achieving excellent agreement with Rockwell International results.

Results of measurements of the yield of neutrons with energies greater than 1 MeV produced by 35 MeV deuterons on thick lithium are presented.

A least-squares analysis of the available experimental thick target neutron yield from d + Li for E_d > 14.5 MeV yields a non-constant deuteron energy dependence.

V. ACCOMPLISHMENTS AND STATUS

A. Cross Section Prediction — F. M. Mann (HEDL) and C. Yalbach (Triangle Universities Nuclear Laboratory)

The helium production from neutron bombardment of Al and Cu has been calculated for E_n = 5 to 40 MeV using the cross section prediction code HAUSER*5. (n,αx), (n,nα) and (n,2n) reactions were explicitly calculated, while other reactions such as (n,2nα), (n,pα) and (n,2α) were estimated from explicitly calculated cross sections. The agreement between the calculations and the 14.8 MeV data of Farrar and Kneff[1] is excellent.

Angular distributions of outgoing particles are needed for damage energy calculations, yet there exists very limited data. A simple two parameter function of the outgoing particle energy has been found for each coefficient b_i where b_i is defined by

$$\frac{d\sigma}{d\Omega} = \sigma \left[1 + \sum_{L=1}^{5} \frac{b_L P_L}{2*L+1} \right]$$

These coefficients are nearly independent of target mass, incoming projectile energy and type, dnd outgoing projectile type.

B. Neutron Yield Experiments -- D. L. Johnson and F. M. Mann (HEDL) J. W. Watson, J. Ullman, and W. G. Wyckoff (University of California at Davis)

Time-of-flight measurements of the neutron yields and spectra from 35 MeV deuterons on thick (2 cm) lithium for the FMIT facility were described in the last DAFS quarterly report. The yield of neutrons having energies greater than 1 MeV has been obtained for each of the measurement angles (θ) between 0° and 150°. The results dre shown in Figure 1. Also shown for each angle θ is the product of the yield and 2π sin θ. The dashed curve through these data indicates the relative importance

of neutrons emitted at any angle e to the total yield of neutrons emitted with energies greater than 1 MeV.

The total neutron yield obtained by integrating the data in Figure 1 over all angles from 0" to 180° is found to be 2.66 (10^{11}) neutrons/μc or 4.26 neutrons/100 deuterons. Only neutrons emitted forward of e ~90° can contribute significantly to the useful flux in the FMIT test cell. About 75% of the neutrons above 1 MeV are emitted in the forward direction. The forward yield is 1.99 (10^{11}) neutrons/μc or 3.19 neutrons/100 deuterons.

Additional preliminary measurements aimed specifically at the very low energy portion (<2 MeV) of the spectra were performed in Dec. 1978. Spectra were obtained at 12°, 45°, and 70". A comparison of the new results to previous data at 45° is shown in Figure 2. In the new (Dec. 78) data we were able to observe neutrons as low as ~0.4 MeV, with fairly good accuracy down to ~0.75 MeV. In the previous data (Mar 78) we were only able to observe neutrons down to ~0.9 MeV, with fairly good accuracy only to ~1.5 MeV. The March 1978 data is shown without uncertainties, to minimize confusion. Although we see a slight rise as the energy decreases, we do not see a dramatic rise or fall at very low energies in the neutron spectra.

C. Microscopic Neutron Yield Model -- F. M. Mann and F. Schmittroth (HEDL)

All experimental data for thick-target neutron yield from deuterons on lithium (E_d > 14.5 MeV) have been used to infer total neutron yield (E_n > 0 MeV) for any angle from 0 to 90° and any deuteron energy from 15 to 40 MeV. The experimental data were corrected for non-zero energy neutron detectron thresholds using the previously developed microscopic yield model and the latest HEDL-UDC low neutron energy results. The analysis which is based on generalized least squares[2] techniques shows that the data of Goland, et al.[3] are inconsistent with all other data

which are consistent with each other (<30% discrepant). The deuteron energy dependence is not constant with energy but varies in different ways depending on which of the six angular functions used in the fit is examined. This dependence has important consequences near the lithium target.

VI. REFERENCES

1. H. Farrar and D. W. Kneff, Symposium of Neutron Cross Sections from 10 to 40 MeV, BPIL (1977).

2. F. Schmittroth, "Generalized 1-east-Square For Data Analysis," HEDL-TME 77-51 (1978).

3. A. N. Goland, C. L. Snead, D. M. Parkin, and R. B. Theus, IEEE Transactions on Nuclear Science, NS-22, (1975) 1776.

VII. FUTURE WORK

The computer code HAUSER*5 will be used to calculate helium production and reactions needed for damage cross sections for selected materials. These materials will be selected after consultation with H. Farrar of Rockwell International and D. Doran of HEDL.

Final measurements of the very low energy portion (<2 MeV) of the d-Li neutron spectra are planned for May. Measurements of the yield from 35 MeV deuterons on thick ^{6}Li will also be performed for comparison to the yield from natural lithium.

The microscopic yield model will be updated using the deuteron energy dependence found using the least squares technique as well as the new HEDL-UCD experimental data.

VIII. PUBLICATIONS

A paper entitled, "Measurements and Calculations of Neutron Spectra from 35 MeV Deuterons on Thick Lithium for the FMIT Facility" by

D. L. Johnson, F. M. Mann, J. Watson, J. Ullmann, and W. G. Wyckoff was presented at the First Topical Meeting on Fusion Reactor Materials, Miami Beach, Florida (January 1979). The paper will be published in the Journal of Nuclear Materials, (HEDL-FP-1608).

A report entitled, "HAUSER*5, A Computer Code to Calculate Nuclear Cross Sections," is being prepared.

A paper entitled, "Experimental and Theoretical Determination of Helium Production in Copper and Aluminium by 14.8 MeV Neutrons," by D. W. Kneff, H. Farrar, F. M. Mann, and R. E. Schenter is being prepared.

VIII. PUBLICATIONS

P. P. Urone, C. I. Zanelli, F. P. Brady, C. L. Casteneda, M. Johnson, G. A. Needham, J. L. Romero, J. Ullmann, and D. L. Johnson, Neutron Nonelastic Cross-Section Measurements for ^{12}C, ^{16}O, ^{40}Ca, ^{56}Fe at E_n = 40 and 50 MeV, Bulletin A.P.S. 24, 657 (1979).

C. I. Zanelli, F. P. Brady, J. L. Romero, C. Id. Casteneda, ?no D. L. Johnson, Neutron Total Cross-Sections in Fe and Ca ai 33.3, 40.3, and 50.4 MeV, Bulletin A.P.S. 24, 658 (1979).

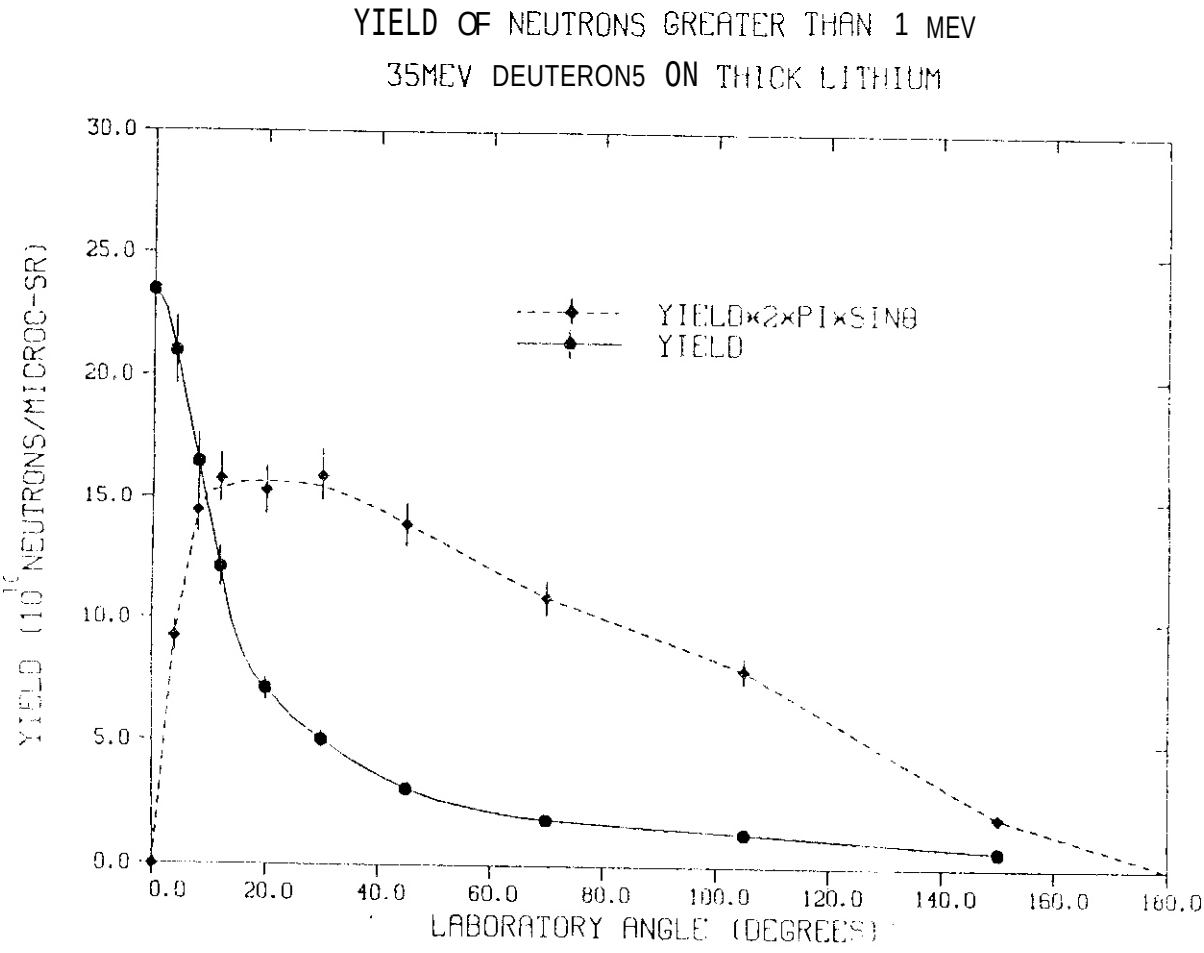

FIGURE 7. Yield of **Neutrons** greater than 1 MeV **from 35** MEV Deuterons **on** Thick Lithiun.

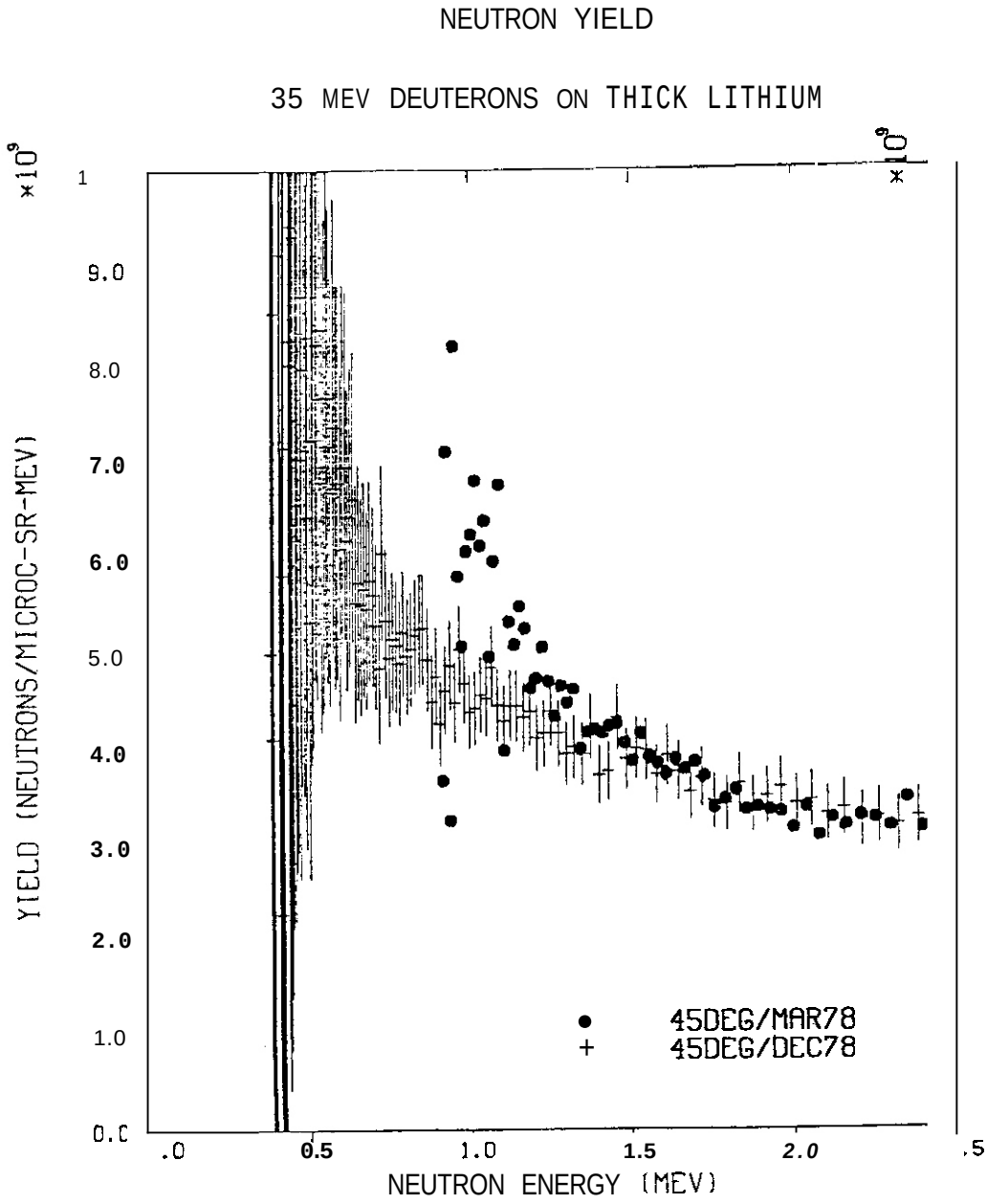

FIGURE 2. Very Low Energy Portion of the Spectrum at 45° from 35 MeV Deuterons on Thick Lithium. Comparison of March 1978 Data to Dec. 1978 Data.

I. PROGRAM

Title: Damage Analysis and Dosimetry Radiation Damage Analysis
Principal Investigator: A. N. Goland
Affiliation: Brookhaven National Laboratory

II. OBJECTIVE

Radiation damage analysis studies associated with the use of electrical insulators in fusion reactors.

111. RELEVANT DAFS PROGRAMS PLAN TASK/SUBTASK

SUBTASK **II.A.2.4 Flux Spectral Definition in FMIT**

SUBTASK II.B.1 Calculation of Displacement Cross Sections

IV. SUMMARY

An effort is being made to perform a substantial portion of our calculations on tlie computer at the National Magnetic Fusion Energy Computer Center. The MORSE-L version of *the* MORSE transport code will he used for this work. Several [problems have been set up and meaningful runs are anticipated when the cross section file is converted to the format required for use at the MFECC.

The neutron flux has been characterized for four different *test* assembly geometries when 35 MeV deuterons are incident upon A 2 × 10 × 1 cm^3 lithium target. A beam profile has been used that is linear along the 10 cm width of the target and which has a Gaussian profile across the 1 cm height of the target. The He/dpa ratio for Si and Cu are computed for neutron fluxes from tlie various geometries as well as for a Benchmark spectrum.

Gas generation in eleven materials of interest for use as insulators in fusion reactors has been calculated for the neutron flux spectrum from the lithium source as well as for a Benchmark spectrum.

V. ACCOMPLISHMENTS AND STATUS

Neutron Flux Characterizations and Damage Analysis Studies--
A. N. Goland, H. C. Berry, G. F. Dell and O. W. Lazareth (BNL).

Use of the MFE Computer

An effort has been made to use the computer at the National Magnetic Fusion Energy Computer Center for damage analysis calculations. The MORSE-L version of MORSE, available at the MFECC, has been used to transport neutrons for a problem having the FMIT geometry. The cross section file available at the MFECC extends only to 20 MeV. As only the absolute binary form of MORSE-L has been available for general use, it has not been possible to include a routine for generating source neutrons. Instead, an experimental spectrum at $\theta = 0°$ has been used, and a cos9 distribution has been used to approximate the angular dependence of the neutron flux. Thus, due to these limitations, the results obtained so far are not really meaningful.

A request has been made to have the source version of MORSE-L be made available to outside users. This request is being processed. In the meantime, the cross section file containing the high energy cross sections of Alsmiller and Barish' is being converted to a file that has the format required for use on the MFE computer. Once the source version of MORSE-L becomes available and conversion of the cross section file is completed, meaningful runs at the MFECC will be possible.

Flux Characterization

In order to facilitate comparison of simulation results obtained at

HEDL and at BNL, the MORSE ti-ansport code, as it exists at BNL, has been used tu recharacterize the neutron flux in an FMIT facility when 35 MeV deuterons, instead of 30 MeV deuterons, are incident upon a 2 cm thick lithium target. The fluxes obtained from MORSE have been converted to conventional units by multiplying them by the neutron yield per Coulomb of incident deuterons. As in the past the yield at energy E(MeV) was obtained by fitting the yields at lower energies' with the yield of Saltmarsh et al. at 40 MeV.[3]

$$\text{YIELD} = (-2.84 + 0.557E + 0.00831E^2) \times 10^{16} \text{ neutrons/Coulomb}$$

Neutrons are generated by a Monte Carlo source routine that includes both stripping and evaporation processes. The spectrum thus generated is arbitrarily truncated for neutrons having energy less than 0.9 MeV. This truncation results in a harder spectrum than that used at HEDL. (The HEDL spectrum is based on recent U.C.-Davis measurements.[4]) The differences in the source spectra do not affect the conclusions of this report.

The role that material in the test assembly has in varying the nature of the neutron flux spectrum has been determined by characterizing the flux for the following geometries:

1) a test assembly consisting of a 30 × 20 × 20 cm^3 block of iron having *a* density of 7.7 g/cm^3,

2) a test assembly consisting of a 30 × 20 × 20 cm^3 block of iron having a density of 1.925 g/cm^3,

3) a test assembly consisting of sub-assemblies having densities of 0.5, 0.25 and 0.1 times the density of iron,

4) an empty test assembly (vacuum).

Geometry #1 is the geometry used for past flux characterizations at BNL. Geometry #2 has a uniform density of 0.25 times the density of iron, geometry #3 is the traditional HEDL geometry[5] with iron instead of stainless steel, and geometry #4 gives the "pristine" flux from the lithium source.

The dependence upon depth within the test assembly of the uncollided, collided, and total fluxes for geometries #1 to #3 are shown, along with the pristine flux, in Figs. 1 to 3, respectively. The relative importance of the uncollided and collided fluxes changes as the average density of the test assembly increases. Since the collided flux results from scattering (which is frequently downscattering), the average neutron energy decreases as the number of scatterings increases. The dependence of the average neutron energy upon depth within the test assembly is shown in Fig. 4 for the four geometries listed above. For the dense test assembly of geometry #1, the average neutron energy decreases by a factor of three from the front to the rear of the test assembly. For the "pristine" spectrum the average neutron energy increases from the front to the rear of the test assembly. These results are consistent with the previous results of both BNL and HEDL.[6,7]

As yet the final structure of the test assembly is undetermined. The necessity for cooling as well as the desirability for remote manipulation of sample subassemblies will result in an overall density that is less than that used in geometry #1. However, efficient use of the FMIT facility will probably dictate a high packing efficiency of samples in the highest flux volume near the lithium target. Within this reduced volume the density could approach that used in geometry #1, and should be expected to alter appreciably the nature of the neutron flux spectrum.

The He/dpa ratios for silicon and copper samples exposed to fluxes determined for the four geometries mentioned above as well as for a Benchmark spectrum have been determined using the damage program DON with a displacement energy of 30 eV. The dependence of the He/dpa ratio upon

depth within the test assembly is shown in Fig. 5 for silicon and in Fig. 6 for copper. For copper the He/dpa ratios for geometries #2 to #4 are within 10 to 15% of the He/dpa ratio obtained for a Benchmark spectrum. For silicon samples the He/dpa ratio fur geometries #2 to #4 art over 50% greater than that obtained when using a Benchmark spectrum. This difference results from the $(n,n')\alpha$ reaction in silicon being important for the FMIT spectrum but not for the Benchmark spectrum. In evaluating materials, consideration should be given to tne different natures of the MIT and the Benchmark spectra; some reactions that are important with FMIT neutrons will not be important in a fusion reactor.

Application to Insulators

Computation of gas production in several insulator materials of interest for applications in fusion reactors[8] has been performed for both the pristine flux determined at a point 0.5 cm from the lithium target in an FMIT facility and lor a Benchmark spectrum. The value used for the pristine flux was $2.51 \cdot 10^{16}$ $n/(cm^2 \cdot A \cdot s)$, and a value of $3.81 \cdot 10^{14}$ $n/(cm^2 \cdot s)$ (1 MW/m^2 wall loading) was used for the Benchmark flux. Hydrogen and helium production were summed to yield the total gas production. The gas production for these materials is shown in Fig. 7 for the FMIT spectrum and in Fig. 8 for the Benchmark spectrum. The apparent gradual increase in gas production from Li_2O to Si_3N_4 in Figs. 7 and 8 may not be as pronounced as it appears; the ENDF/B cross section files are incomplete lor some elements. For lithium only the (n,d) reaction is included, and for carbon only the (n,α) reaction is included. Hence, gas production for Li_2O and for graphite are to be considered as lower limits.

The recoil energy not expended in producing recoil atom damage is dissipated in electronic processes. These processes are unimportant in producing displacements in metals but are expected to be important in producing displacements in insulators. Due to the higher efficiency for energy transfer between neutrons and light atoms and to the lower efficiency for light atoms in producing recoil atom damage, displacements

resulting from electronic processes should be particularly important for insulators composed of light elements.

VI. REFERENCES

1. R. G. Alsmiller, Jr. and J. Barish, Neutron-Photon Multigroup Cross Sections for Neutron Energies ≤ 60 MeV, ORNL/TM-6486, August 1978.

2. P. J. Persiani, W. Becker and J. Conahue, Symposium on Neutron Cross-Sections from 10 to 40 MeV, Brookhaven National Laboratory, May 3-5, 1977, BNL-NCS-50681, p. 151.

3. M. J. Saltmarsh, C. A. Ludemann, C. B. Fulmer and R. C. Styles, Nuclear Instruments and Methods 145, p. 81 (1977).

4. D. L. Johnson, F. M. Mann, S. Watson, J. Ullman and W. C. Wyckoff, Damage Analysis and Fundamental Studies Quarterly Technical Progress Report, October-December 1978, p. 39, DOE/ET-0065/4.

5. J. O. Schiffgens, R. L. Simons, F. M. Mann and L. L. Carter, Damage Analysis and Fundamental Studies Quarterly Technical Progress Report, April-June 1978, p. 39, DOE/ET-0065/2.

6. A. N. Goland, H. C. Berry, G. F. Dell and O. W. Lazareth, Damage Analysis and Fundamental Studies Quarterly Technical Progress Report, October-December 1978, p. 26, DOE/ET-0065/4.

7. J. O. Schiffgens, R. L. Simons, F. M. Mann and L. L. Carter, Damage Analysis and Fundamental Studies Quarterly Technical Progress Report, October-December 1978, p. 48, DOE/ET-0065/4.

8. **Proceedings of the Meeting on** CTR Electrical **Insulators, May** 17-19, 1976, at Los Alamos Scientific Laboratory, CONF-760558, p. 5.

VII. FUTURE WORK

Future work will include: 1) using the computer at the MFECC *to* perform more definitive determination of neutron and gamma ray flux spectra, and 2) use of the present flux spectra as well as the more definitive flux spectra to evaluate gas generation in insulators and *to* evaluate displacements arising from recoil atom damage, displacements induced by gamma rays, and displacements produced by ionization processes.

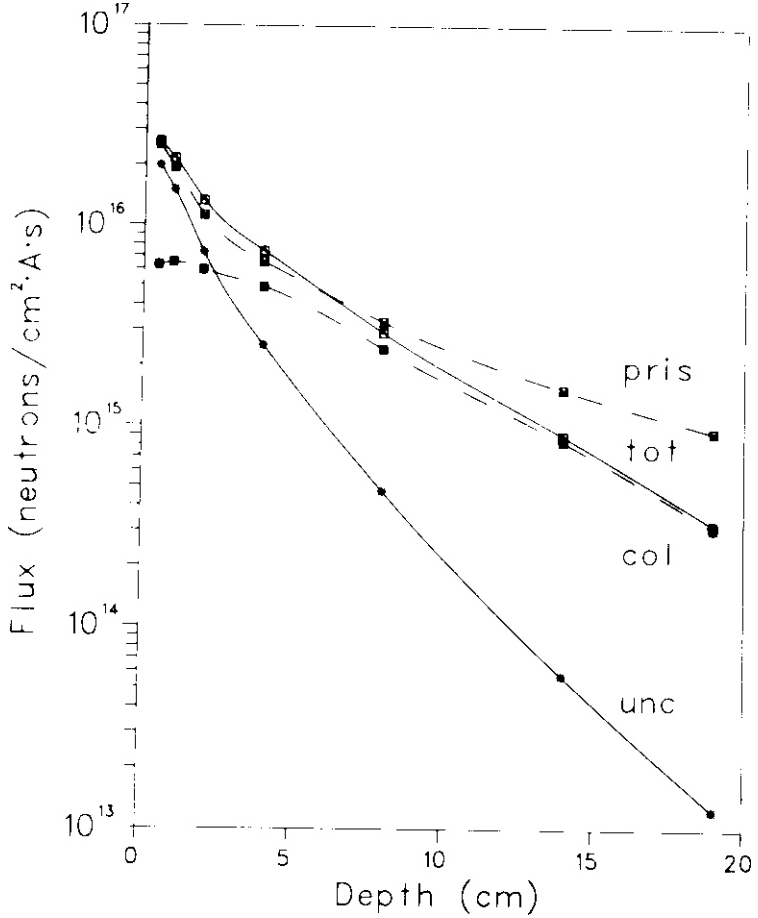

Figure 1. Dependence of the uncollided (unc), collided (col), total (tot), and pristine (pris) fluxes upon depth within a $30 \times 20 \times 20$ cm^3 iron block having density of 7.7 g/cm^3.

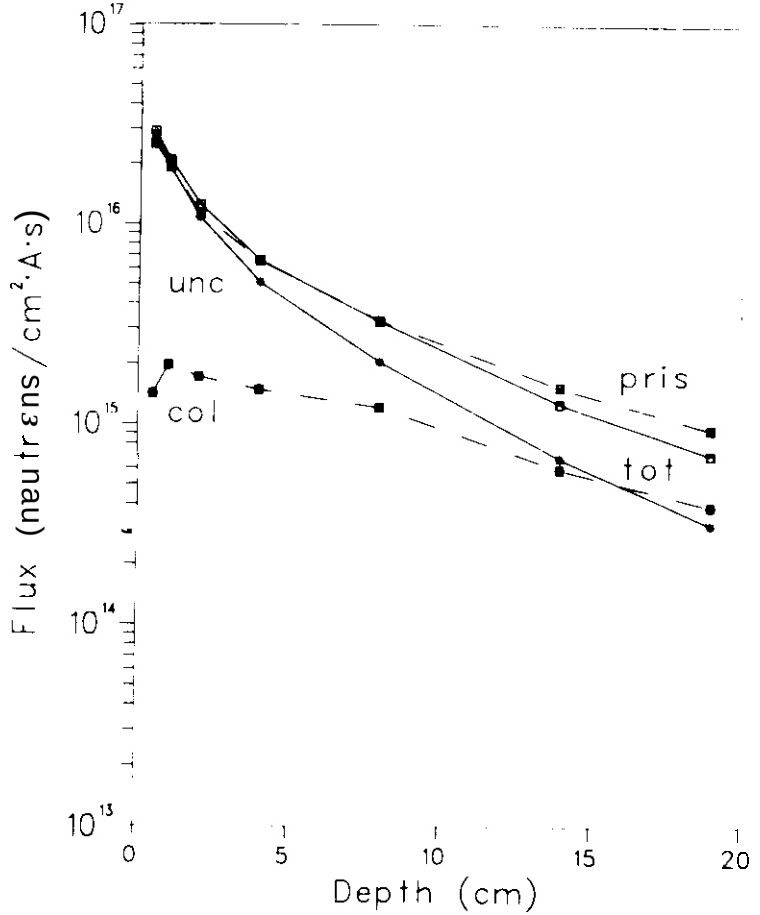

Figure 2. Dependence of the uncollided (unc) collided (col), total (tot), and pristine (pris) fluxes upon depth within a $30 \times 20 \times 20$ cm^3 iron block having density of 1.925 g/cm^3.

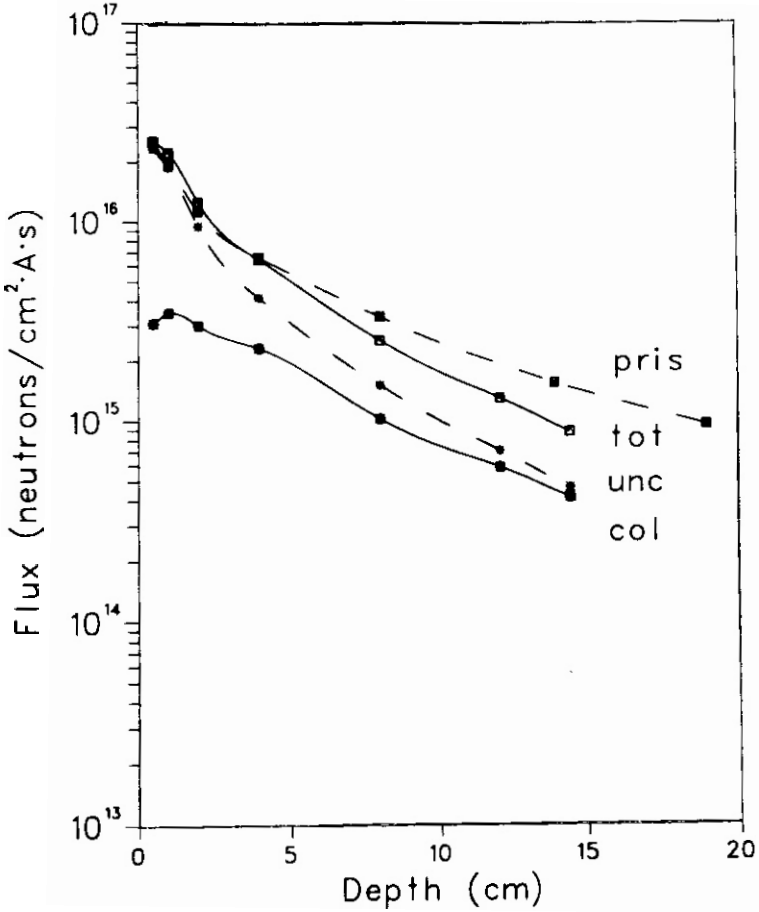

Figure 3. Dependence of the uncollided (unc), collided (col), total (tot), and pristine (pris) fluxes upon depth within a $20 \times 12 \times 15$ cm^3 assembly having iron subassemblies with densities of 0.77, 1.925 and 3.85 g/cm^3.

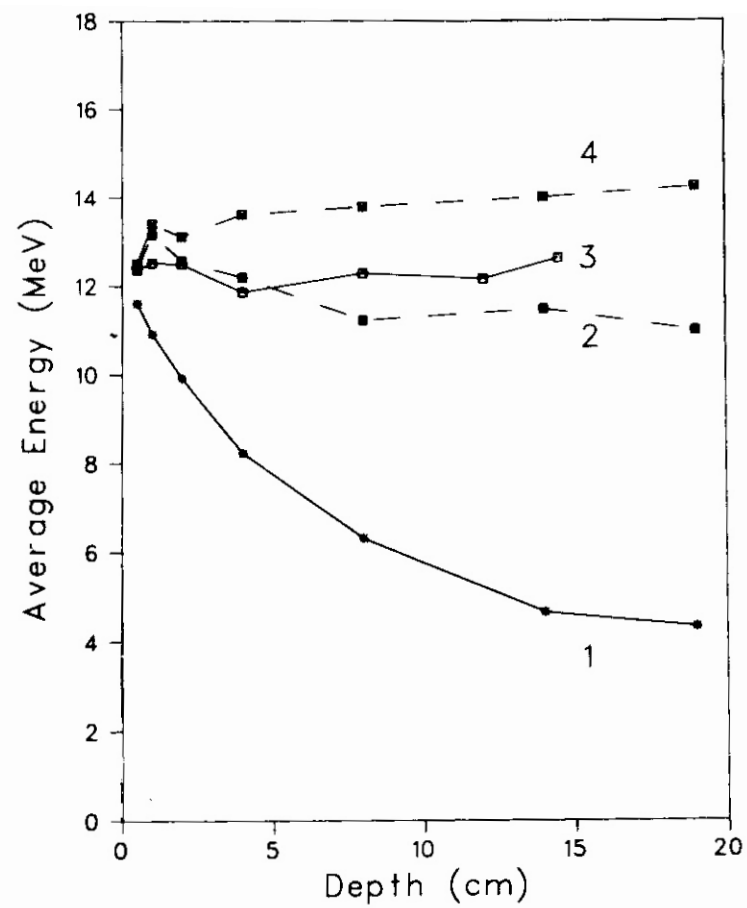

Figure 4. Dependence of the average neutron energy upon depth within test assemblies having geometries 1 to 4.

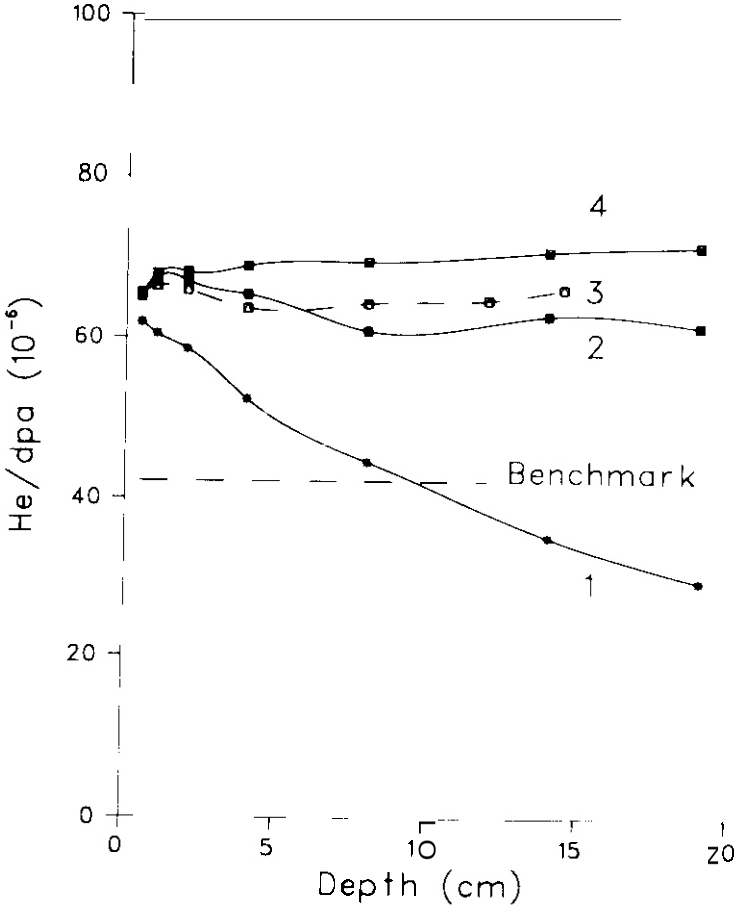

Figure 5. Silicon. Comparison of the He/dpa ratios within test assemblies having geometries 1 to 4 with the He/dpa ratio for a Benchmark spectrum.

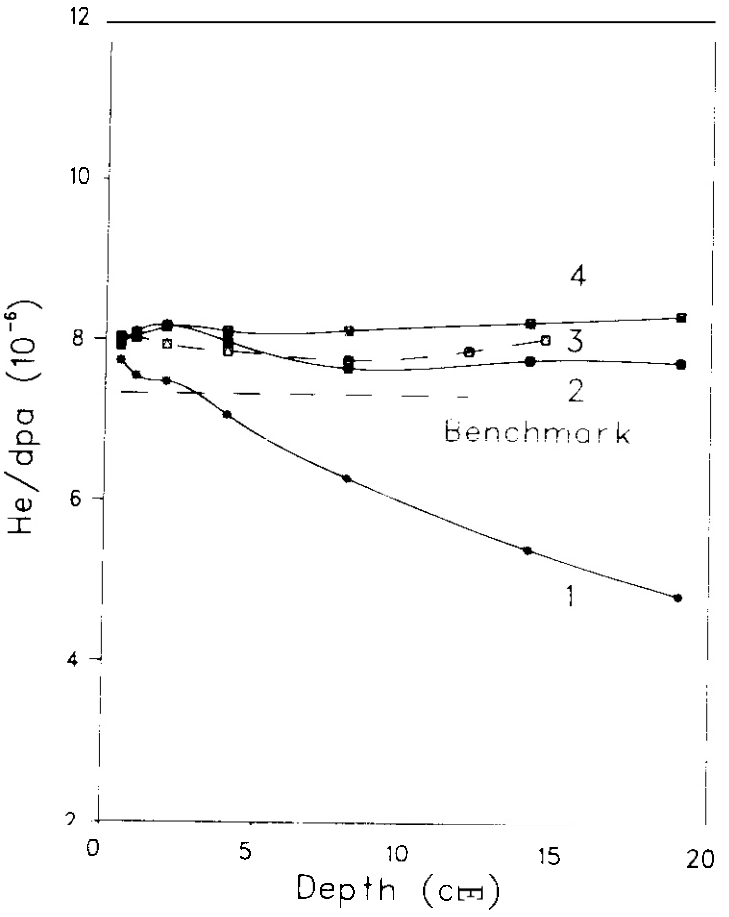

Figure 6. Copper. Comparison of the He/dpa ratios within test assemblies having geometries 1 to 4 with the He/dpa ratio for a Benchmark spectrum.

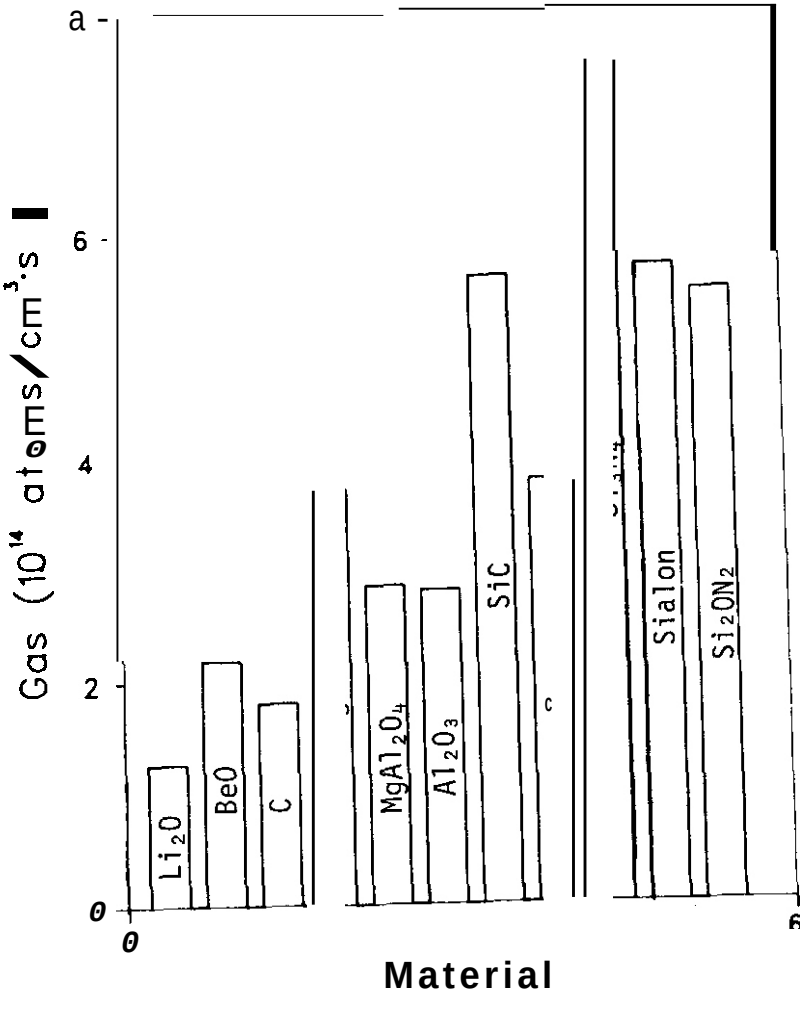

Figure 7. Gas production in insulator materials exposed to the pristine flux in an FMIT facility.

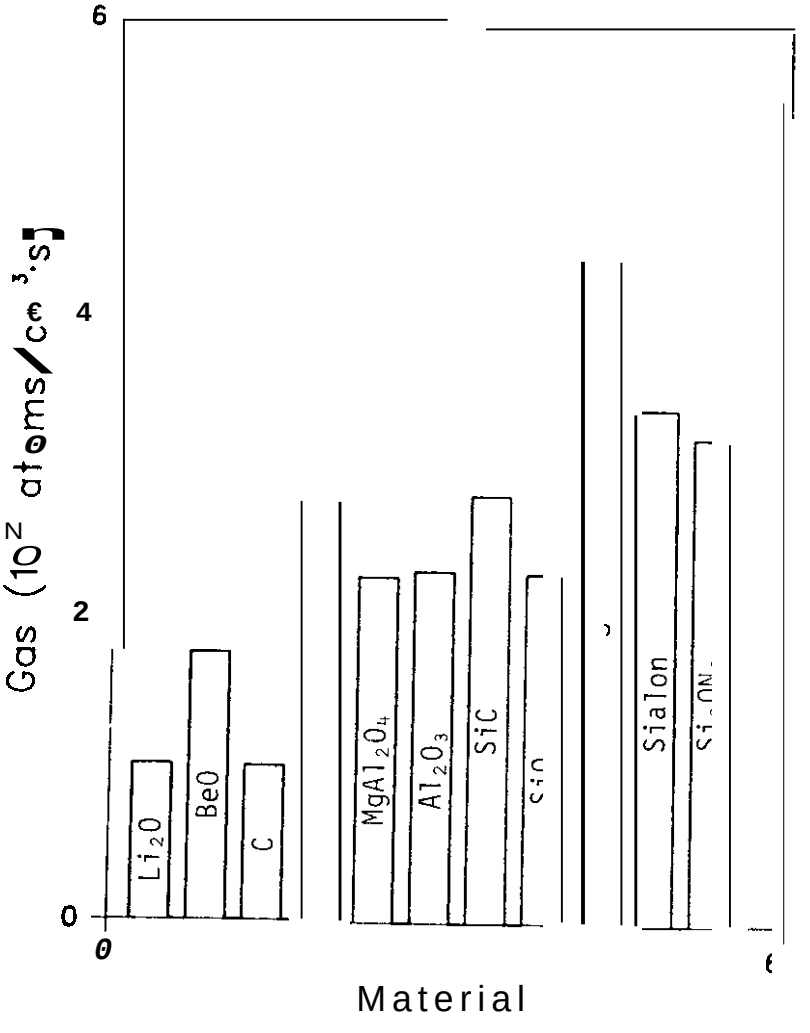

Figure 8. Cas **production in insulator materials exposed to a Benchmark spectrum with 1 MW/m^2 wall loading.**

I. PROGRAM

Title: Irradiation Effects Analysis (WHO11/EDA)
Principal Investigator: D. G. Doran
Affiliation: Hanford Engineering Development Laboratory

11. OBJECTIVE

The objective of this work is to predict the spatial variations of radiation damage parameters within the test volume of the Fusion Materials Irradiation Test (FMLT) facility, and the sensitivity of these parameters to cross section and spectrum uncertainties.

II. RELEVANT DAFS PROGRAM PLAN TASK/SUBTASK

SUBTASK II.A.2.4 Flux Spectrum Definition in FMIT
SUBTASK II.B.1.5 Calculation of Displacement Cross Sections

IV. SUMMARY

Concern about accounting accurately for the effects of the highest energy neutrons in FMIT spectra produced by 35 MeV deuterons led to the design requirement of a second operating energy near 20 MeV. It is recognized that the softer neutron spectra are purchased at a cost of a significant decrease in neutron source strength. Calculations show that, for the same beam current (0.1 amp) but a thinner lithium target, the displacement rate is decreased by 30 to 80% throughout the irradiation volume of interest. consequently, the volume in which the displacement rate exceeds that in a D-T fusion reactor first wall at a loading of 1 MW/m^2 is only 20 cm^3, compared with 140 cm^3 at a deuteron energy of 35 MeV. The spectral-averaged displacement and helium cross sections both decrease such that the helium-to-displacement ratio is lowered by about a factor of two.

V. ACCOMPLISHMENTS AND STATUS

A. FMIT Damage Parameter Sensitivity Study - J. O. Schiffgens, R. L. Simons, F. M. Mann, and L. L. Carter.

1. Introduction

A damage parameter sensitivity study for FMIT has been in progress for the past year.(') The highest priority objective of the study was the development of codes for modeling the neutron source and calculating the flux-spectrum in the test cell with and without a test module present. Such codes were developed and used to explore the effect of neutron source model parameter variations on the neutron field within the test cell.(2-4) The calculated neutron fields were characterized in terms of damage parameters. We have concentrated on calculations of displacement and helium production rates, with emphasis on the assessment of the variations anticipated under likely operating conditions at locations of most interest for irradiation testing, i.e., where the displacement rate in stainless steel is greater than about 6 dpa/yr (half *of* a first wall value at 1 MW/m^2).

Neutron fluxes provided by FMIT increase with increasing deuteron beam energy or current. For an accelerator limited beam current of 0.1 amp, a beam energy of 35 MeV was chosen to yield acceptably high fluxes and irradiation test volumes.(4) Such high energy deuterons produce neutron spectra with large components of high energy neutrons. For example, at the center of the source face, 23 percent of the neutrons have energies greater than 15 MeV. Due to concern over accounting accurately for the effects of these high energy neutrons, a secondary set of beam-target specifications is a requirement for FMIT. At present, the secondary specifications call for a 0.1 amp beam of 20 MeV deuterons to strike a lithium target 1.5 cm thick. As for the 35 MeV deuterons, which require a lithium target thickness of 2 cm, the beam density is assumed to peak at the center of the target area and be Gaussian in the vertical and horizontal directions with full-widths-at-half-maximum (FWHM) of 1 cm and 3 cm, respectively.

This report deals with the comparison of damage parameters in neutron fields generated by 20 and 35 MeV deuterons.

2. Results

Figures 1-3 show neutron fluxes and spectra from *20* and *35* MeV deuterons at three positions within the test cell. These curves show a large decrease in flux and mean neutron energy (i.e., considerable softening *of* spectra) in going from 35 to *20* MeV deuterons. Note that at the center of the source face (the position: 0, 0, 0), for 20 MeV deuterons, only 3.6 percent of the neutrons have energies greater than 15 MeV, compared with *23* percent for *35* MeV deuterons. Figures 4 and 5 reveal the effect that such a change in neutron field has on damage parameters. Displacement rates versus distance normal to the source, at two heights relative to the source mid-plane, are presented for *35* and *20* MeV deuterons in Figure 4. Similar plots for helium production rates are shown in Figure *5.* The fractional rates of change in the displacement rate and helium production rate with distance normal to the source for 20 and 35 MeV deuterons differ by less than 30 percent at any point. However, the displacement and helium production rates at 20 MeV are as low as *20%* and 12%, respectively, of those at 35 MeV.

Spectral-averaged displacement and helium production cross sections at eleven positions are presented in Table 1. Throughout the region of most interest in the test cell. the flux varies by a factor of about *20* for 35 MeV deuterons and by a factor of about 10 for *20* MeV deuterons, while the spectral-averaged displacement and helium production cross sections for copper vary by less than factors of two and four, respectively, for either deuteron energy. Note that the corresponding helium-to-displacement ratio for 35 MeV deuterons ranges from *5* to 11 appm He/dpa, bracketing a fusion reactor first wall value for copper of 7.7 appm He/dpa, while for 20 MeV deuterons the helium-to-displacement ratio ranges from *2.5* to 6 appm He/dpa. At this time, however, the effects of factors-of-two differences in the helium-to-displacement ratio are not known.

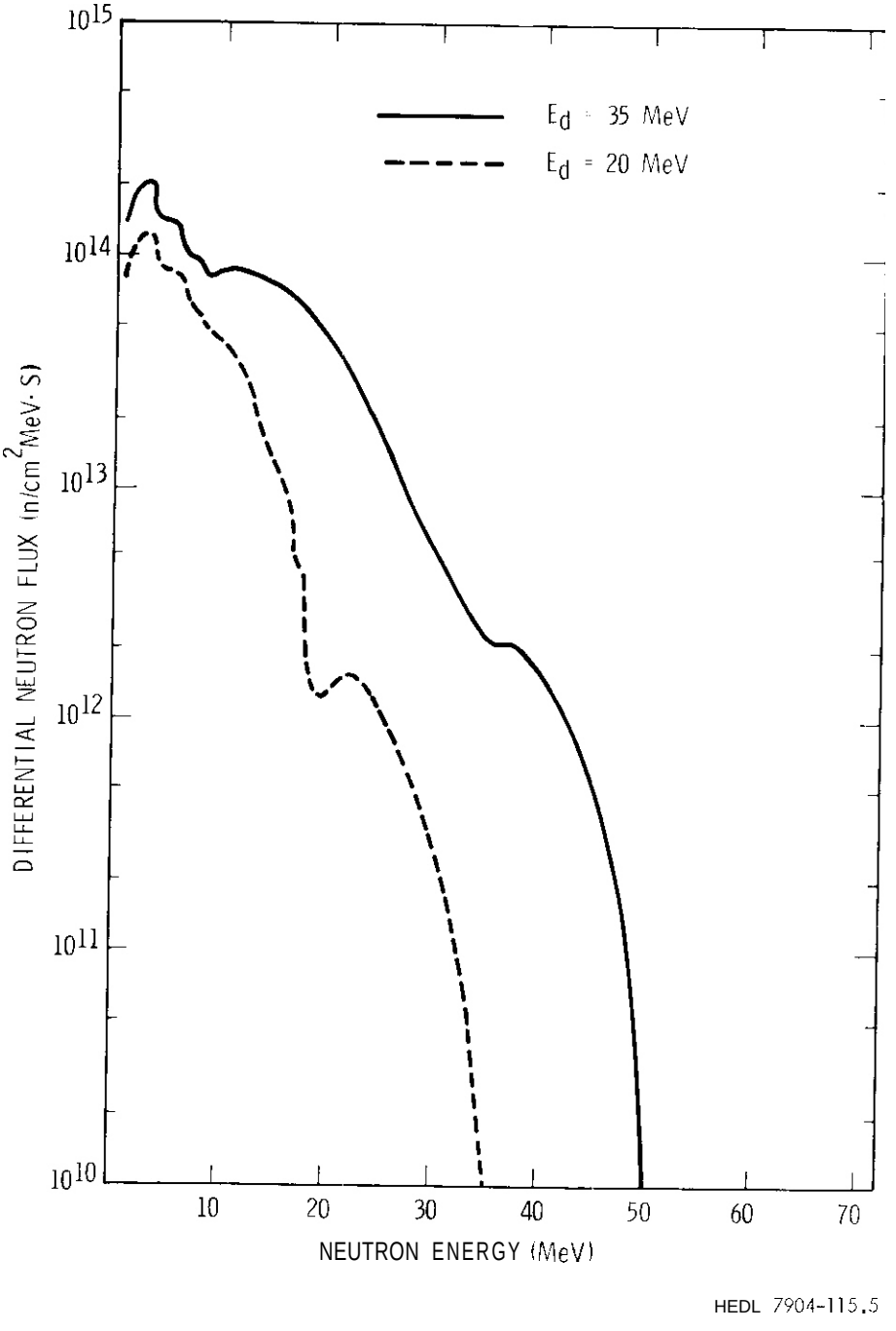

FIGURE 1. Calculated Neutron Spectra for Two Deuteron Beam Energies, 20 MeV and 35 MeV, at Position x = 0, y = 0, z = 0 cm (see Figure 4 for coordinate orientation).

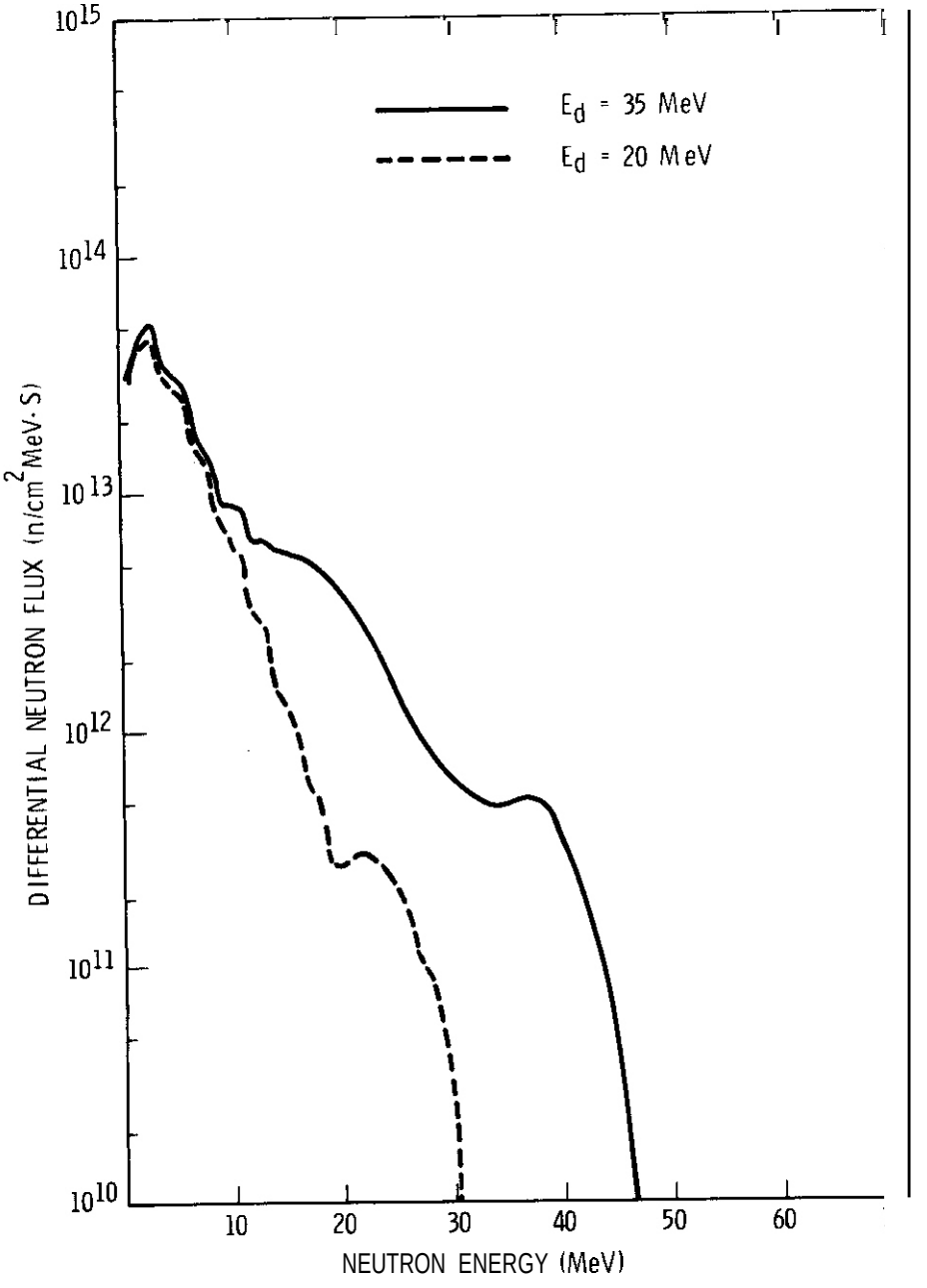

FIGURE *2.* Calculated Neutron Spectra for Two Deuteron Beam Energies, 20 MeV and 35 MeV at Position x = 0, y = 0, z = 2 cm (see Figure 4 for coordinate orientation).

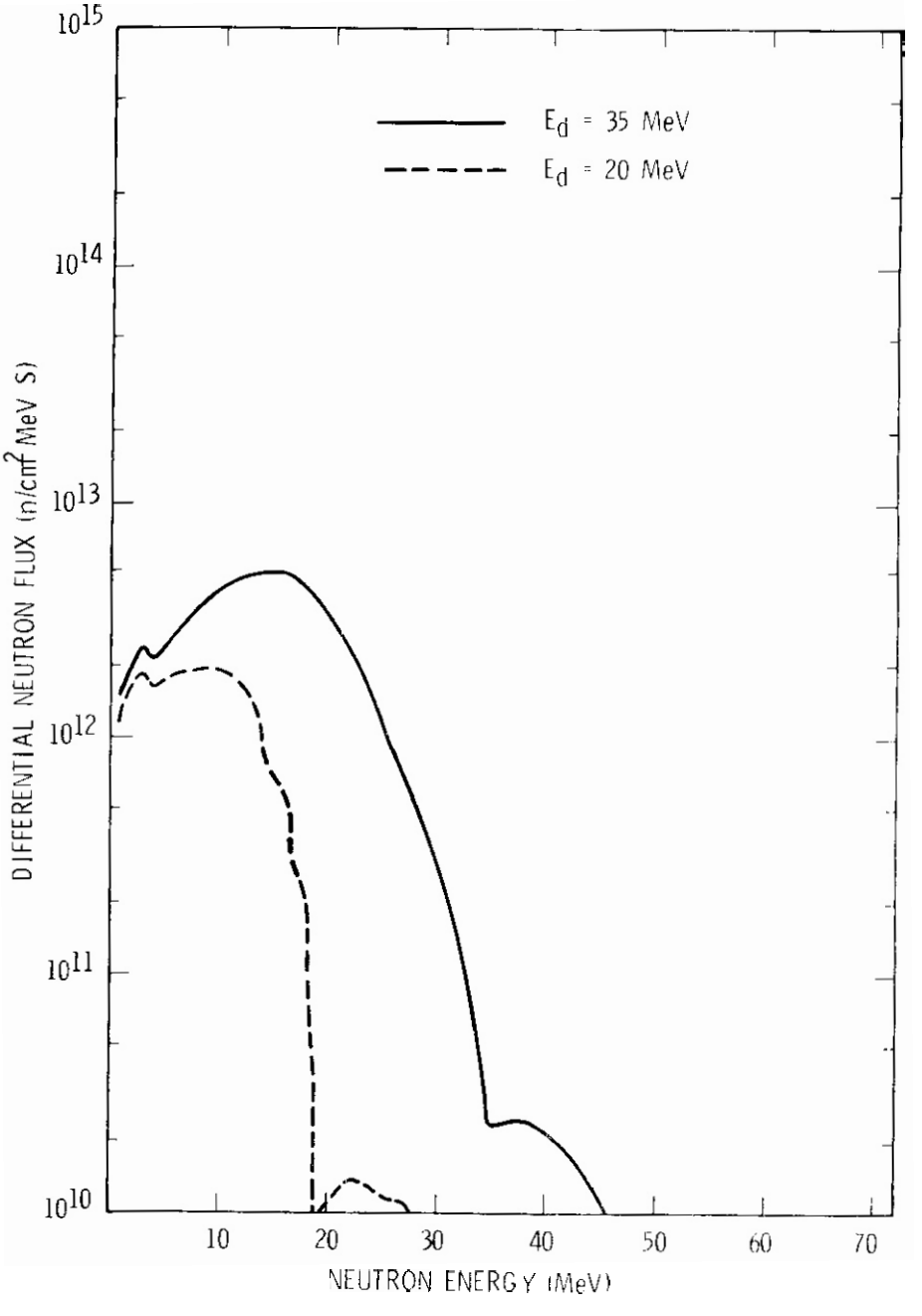

HEDL 7904-115.7

FIGURE 3 Calculated Neutron Spectra for Two Deuteron Beam Energies, 20 MeV and 35 MeV, at Position x = 15, y = 0, z = 0 cm (see Figure 4 for coordinate orientation).

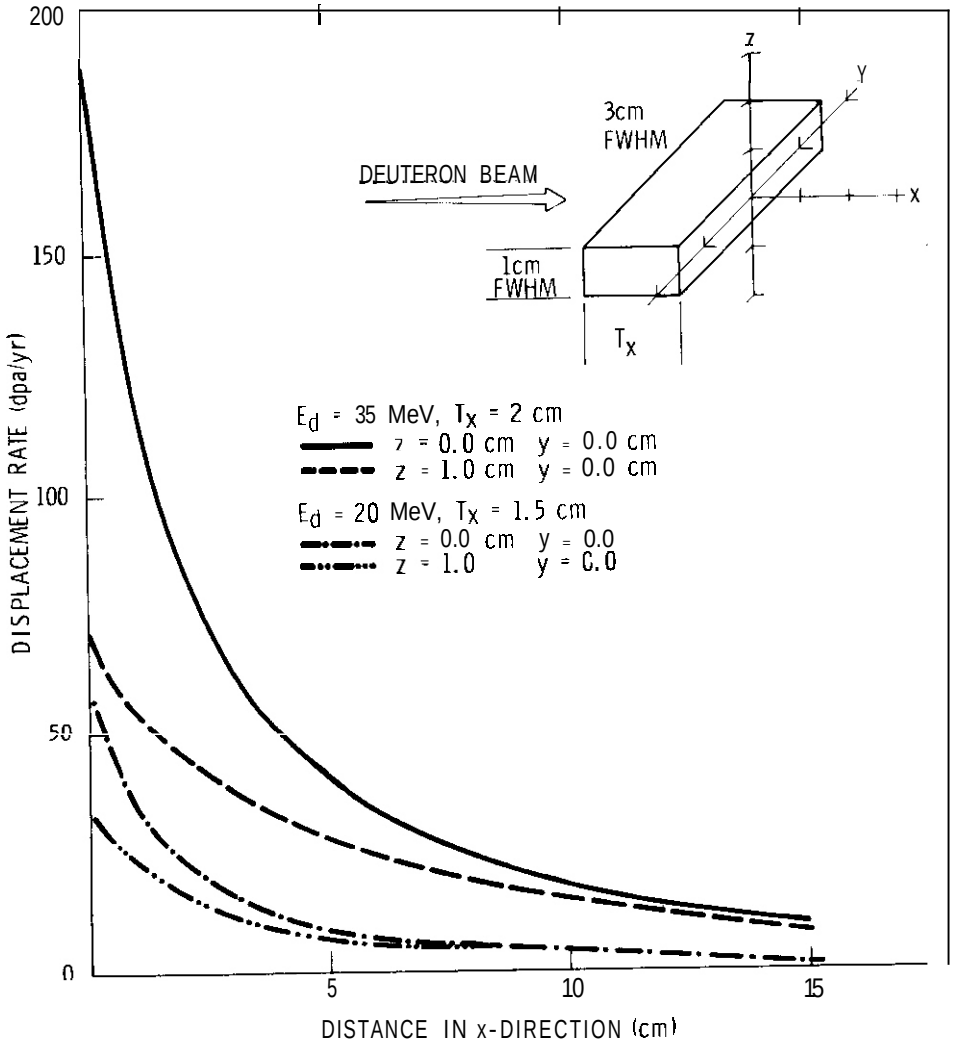

FIGURE 4. Displacement Rate Versus Distance Normal to the Source Surface for Deuteron Beam Energies of 20 and 35 MeV.

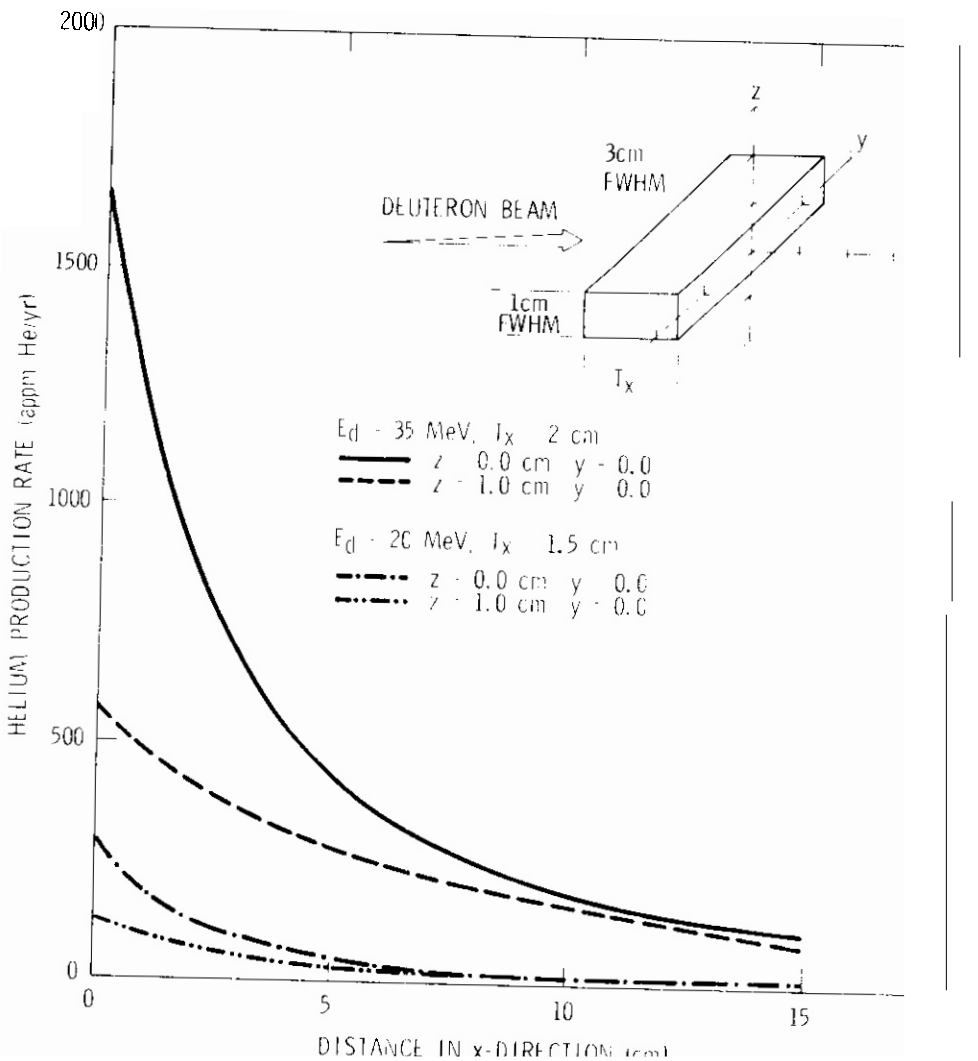

FIGURE 5. Helium Production Rate Versus Distance Normal to the Source Surface for Deuteron Beam Energies of 20 and 35 MeV.

TABLE 1

SPECTRAL-AVERAGED CROSS SECTIONS FOR COPPER WITHIN THE FMIT TEST CELL

(UNPERTURBED SPECTRA)

Position No.	x	y	z (cm)	E_d = 20 MeV, T_x = 1.5 cm*					E_d = 35 MeV, T_x = 2.0 cm*				
				(1				appm/He dpa				b)	appm/He dpa
1	0	0	0	9.5	5.7	2.1	9.≤	4.6	c∠.	ɔ.∠	2.8	24	ɔ.4
2	2	0	0	3.2	6.7	2.3	13.	5.6	8.2	11.	3.3	33	10.
3	5	0	0	1.2	7.2	2.4	15.	6.0	3.5	13.	3.5	36	11.
4	10	0	0	.48	7.5	2.5	15.	6.2	1.5	13.	3.6	39	11.
5	15	0	0	.25	7.6	2.5	16.	6.2	.84	13.	3.6	40	11.
6	0	2	0	4.≤	5.2	2.0	7.m	4.0	9.5	≤.5	2.6	21	7.win
7	z	2	0	2.o	6.1	2.z	11.	5.0	4.3	1o.	3.1	29	9.in
≤	0	0	z	2.6	4.3	⊣.≤	4.7	2.≤	3.3	≤.2	2.2	14	5.5
m	z	0	z	1.4	5.2	z.o	7.9	4.o	2.4	m.1	2.7	22	8.3
10	0	2	2	1.8	q.z	1.≤	4.4	2.5	2.2	5.9	2.⊣	1m	5.1
11	2	2	2	1.1	.o	1.m	7.0	3.6	1.7	8.4	2.≤	2o	7.8

* Lithium thickness

Figures 6 and 7 show, for copper, the percent response (i.e, the percentage of the reactions which occur within a given neutron energy range) versus energy for displacements and helium production, respectively. The figures show, for example, that for 35 MeV deuterons, 95 percent *of* the displacements are produced by neutrons with energies less than 31 MeV, while for 20 MeV deuterons, 95 percent are produced by neutrons with energies less than 17 MeV. Similarly, for 35 MeV deuterons, 95 percent of the helium atoins are produced by neutrons with energies less than 34 MeV, while for 20 MeV deuterons, 95 percent are produced by neutrons with energies less than 25 MeV. The fraction of displacements produced above 15 MeV is 50% at 35 MeV and only 8'1 at 20 MeV.

It *is* instructive to coinpare primary knock-on atom (PKA) spectra[5] produced by neutron spectra froni a variety of test facilities with that produced by a D-T fusion reactor first wall neutron spectrum. Table 2 shows the percentage of recoil atoms in each of several recoil energy groups due to irradiation in various neutron spectra. The table illustrates quite clearly that none of the test facilities produce PKA spectra which are exactly like a D-T fusion reactor first wall PKA spectrum. However, comparing only the dominant displacement producing regions of the PKA spectra")(i.e., those for which E_{PKA} >10 keV) shows that the Rotating Target Neutron Source-I1 (RTNS-II), FMIT, and D-T fusion reactor first wall spectra are similar (see Table 3); the 20 MeV deuteron FMIT spectruni being most like the first wall spectruiii.

Table 4 contains irradiation volumes for which the displacement rates in copper are greater than the stated values. Note the dramatic decrease in volume at each displacement rate when the deuteron energy is decreased from 35 to 20 MeV.

The reader should keep in mind that, while calculated PKA spectra and displacement and heliurii production rates are convenient for comparing the neutron fields produced in a variety of neutron irradiation

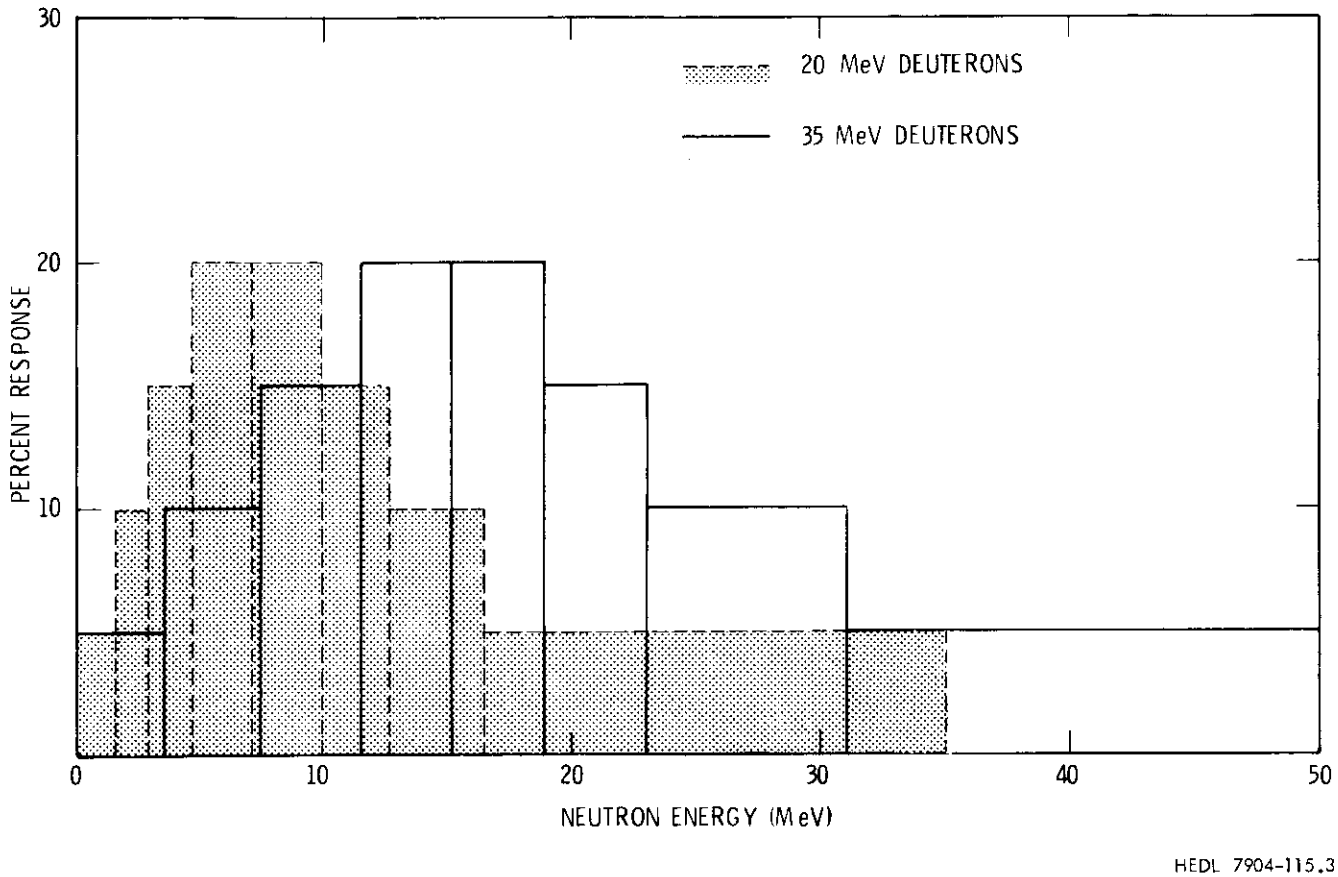

FIGURE 6. Percent Response for Displacements Versus Neutron Energy for Deuteron Beam Energies of 20 and 35 MeV.

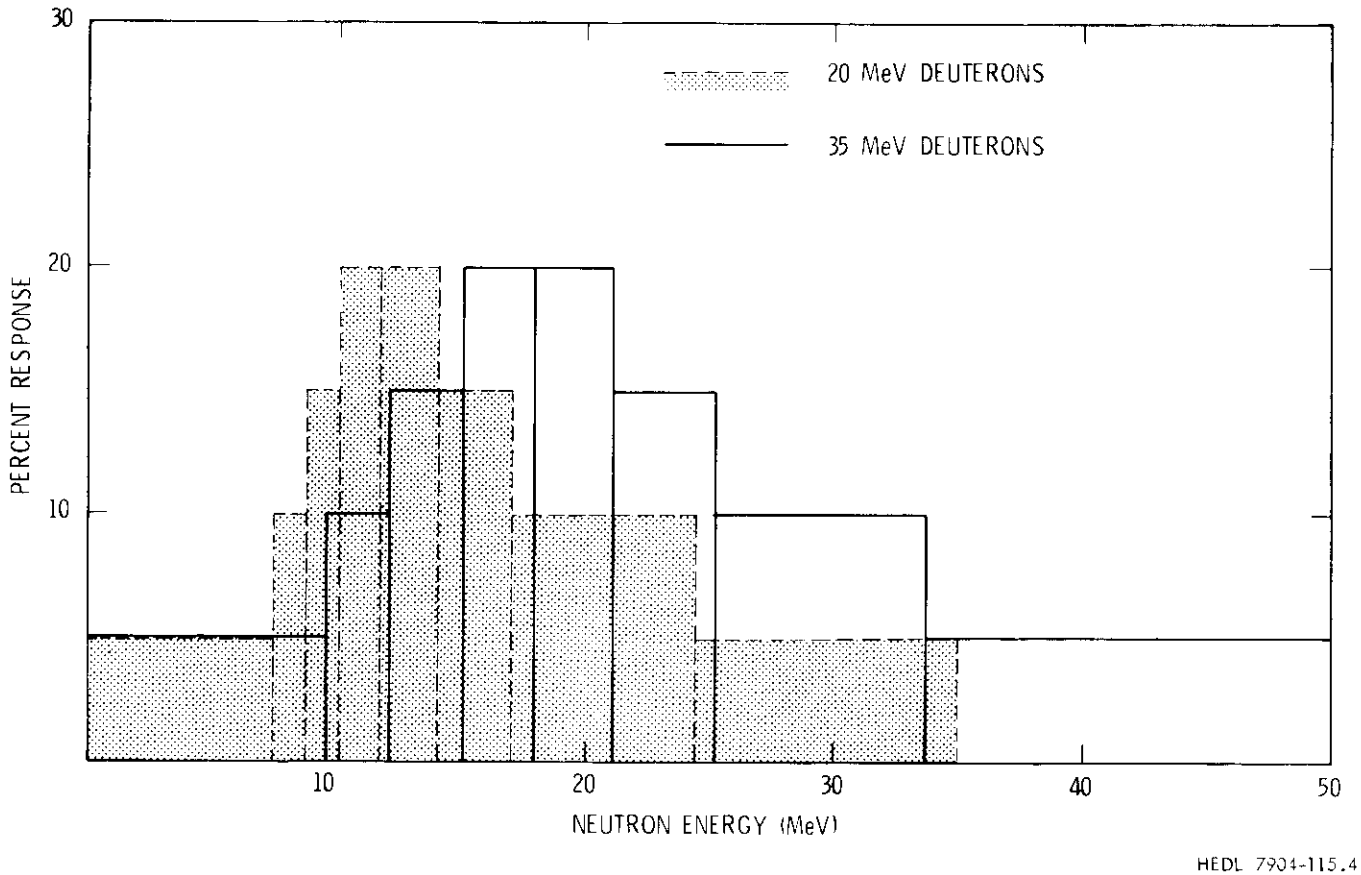

FIGURE 7. Percent Response for Helium Production Versus Neutron Energy for Deuteron Beam Energies of 20 and 35 MeV.

TABLE 2

PERCENTAGE OF RECOIL ATOMS IN IRON PRODUCED IN EACH ENERGY GROUP DURING EXPOSURE TO NEUTRONS FROM A VARIETY OF NEUTRON IRRADIATION FACILITIES*

PKA-Energy (keV)	HFIR/PTP	FTR (Row 4,z=2.5)	EBR-II (R=5.2, z=0.0)	RTNS-II	†FMIT-35	†FMIT-20	D-T Fusion First Wall
0 <.1	12%	6%	1%	0%	0%	0%	5%
.1 <1	27%	27%	11%	1%	2%	3%	24%
1 <5	23%	37%	29%	4%	7%	10%	28%
5 <10	9%	12%	17%	5%	7%	10%	10%
10 <50	19%	15%	33%	23%	29%	35%	17%
50 <100	6%	2%	6%	10%	13%	15%	5%
100 <500	4%	1%	3%	46%	36%	26%	10%
500 <T_{max}	0%	0%	0%	11%	5%	1%	1%

* The models described in Reference 5 were used to calculate these recoil atom percentages. All neutrons with energies greater than 12.2 MeV were counted as being in the 12.2 to 14.9 MeV energy group. Note that only 3.6 percent of the neutrons from the 20 MeV deuteron source and 23 percent of the neutrons from the 35 MeV deuteron source have energies greater than 15 MeV.

† Neutron spectra at the center of the source face, unperturbed by any material in the test cell, were used for these calculations.

TABLE 3

PERCENTAGE OF RECOIL ATOMS IN IRON PRODUCED IN EACH ENERGY GROUP ABOVE 10 keV IN A VARIETY OF NEUTRON IRRADIATION FACILITIES

PKA-Energy (keV)	HFIR/ PTP	FTR (Row 4, z=2.5)	EBR-II (R=5.2, Z=0.0)	RTNS-II	FMIT-35	FMIT-20	D-T Fusion First Wall
10 <50	66	83	79	27	35	45	52
50 <100	21	11	14	12	15	19	15
100 <500	14	6	7	54	43	34	30
500 $<T_{max}$	0	0	0	13	7	2	3

facilities, they contain too little information to permit accurate comparison of damage (i.e., property change) rates. Effects of changes in cascade configurations on defect production efficiencies and damage microstructure evolution are not included; nor are the effects of differences in the production rates of solid transmutants.

Ongoing work will enable predictions of damage rates in softer neutron spectra, esp. a D-T fusion reactor first wall spectrum, to be made from data obtained with the 35 MeV deuteron spectra. It is essential, however, that corroborative data be obtained. Operating FMIT at an energy near 20 MeV, while less desirable because of lower specimen throughput, (without a substantial increase in current), would provide neutron test spectra that a) produce PKA spectra which are significantly more like that produced in a first wall, b) are hard enough to produce significant helium, and c) provide displacement rates sufficiently high to make such tests practicable.

TABLE 4

DISPLACEMENT RATE - VOLUME DATA

Displacement Rate (dpa/yr)	Volume* (cm) E_d = 35 MeV (cm)	E_d = 20 MeV (cm)
17	139	20
30	54	4.7
50	20	0.3
83	6.0	0.0

* The design beam current (0.1 amp) was used for both deuteron energies.

VI. REFERENCES

1. J. O. Schiffgens, R. I Simons, F. M. Mann, and L. L. Carter, Damage Analysis and Fundamental Studies Quarterly Technical Progress Report, October - December 1978, p. 42, DOE/ET-0065/4.

2. J. O. Schiffgens, R. L. Simons, and F. M. Mann, Dainage Analysis and Fundamental Studies Quarterly Technical Progress Report, January - March 1978, p. 43, DOE/ET-0065/1.

3. J. O. Schiffgens, R. t.. Simons, F. M. Mann, and L. L. Carter, Damage Analysis and Fundamental Studies Quarterly Technical Progress Report, April - June 1978, p. 39, DOE/ET-0065/2.

4. J. O. Schiffgens, R. L. Simons, F. M. Mann, and L. L. Carter, Damage Analysis and Fundamental Studies Quarterly Technical Progress Report, July - September 1978, p. 42, DOE/ET-0065/3.

5. D. G. Doran and N. J. Graves, HEDL-TME 76-70, December 1976

6. D. M. Parkin and A. N. Goland, Rad. Eff. 28, 31 (1976).

VII. FUTURE WORK

Spatial variations in PKA spectra will be analyzed and calculations to better define the effects of possible cross section uncertainties will be made.

I. PROGRAM

Title: Synergistic Helium Production by Boron Doping of Splat Cooled Alloys

Principal Investigator: O. K. Harling

Affiliation: Nuclear Reactor Laboratory, Massachusetts Institute of Technology

II. OBJECTIVE

This work is directed toward the development of better simulation techniques for the synergistic production of helium and displacement damage in first wall structural materials.

III. RELEVANT DAFS PROGRAM PLAN TASK/SUBTASK

A number of tasks are relevant since adequate experimental simulation of fusion reactor irradiation effects is a major reason for the DAFS program. Some of the tasks/subtasks which are significantly affected are:

TASK	II.A.4	Gas Generation Rates
	II.C.2	Effects of Helium on Microstructure
	II.C.8	Effects of Helium and Displacement on Fracture
	II.C.13	Effects of Helium and Displacement on Crack Initiation and Propagation.

IV. SUMMARY

The amount of ^{10}B which should be added to stainless steel in order to simulate CTR helium production rates in fast reactors has been estimated for various fast test reactor irradiation positions. The amount of ^{10}B required depends largely on the irradiation position chosen. 5000 appm ^{10}B has been chosen as a representative goal and will be used for further alloy doping studies on this project.

This amount of boron can only be distributed homogeneously throughout stainless steel by rapid quenching techniques. In addition, initial calculations have indicated that to keep this amount of horon from segregating during reasonable test times and temperatures, it will he necessary to tic the boron up in a fine dispersion of a stable boride.

V. ACCOMPLISHMENTS AND STATUS —

A. Boron Doping of Stainless Steel by Rapid Quenching - S. Best, C. Dansfield, H. Frost, J. Megusar, O. Harling, and K. Russel! (M. I. T.)

1. Introduction

It is generally understood that existing irradiation facilities, i.e. accelerators and fission reactors, will **have** to be used for the initial irradiation testing of controlled thermonuclear reactor (CTR) structural materials. Damage rates and helium production rates should simulate the expected rates in CTR's. Only fission reactors offer the required large testing volumes with fast neutron fluxes which produce damage rates which equal or exceed those expected for near term CTR's. Helium production rates, with the exception of nickel alloys in nixed spectrum reactors, cannot be reproduced by direct nuclear reaction on the alloy constituents. The present studies are directed toward the development of techniques for the production of helium during fission reactor irradiations. Current efforts emphasize the doping of structural alloys with boron. To assure the uniform distribution of boron, the alloy is produced by rapid quenching from the melt. Cooling rates of 10^5 - 10^9°C/sec offer the possibility of uniform boron concentrations which are much higher than those which can be maintained without segregation during normal solidification rates. The usefulness of this approach to boron doping will also depend upon the maintenance of a uniform boron distribution during thermo-mechanical consolidation, and during the use of the consolidated material in the temperature, stress and radiation environnent

of the fission reactor. Furthermore, the effect of boron on the physical properties of the boron doped alloys, whether segregated to grain boundaries or uniformly distributed, must be understood.

2. Initial Calculations of the Concentration of ^{10}B Required for CTR Helium Embrittlement Simulations Conducted in Fast Test Reactors

The amount of helium which will be generated in a boron doping experiment to simulate CTR helium production will depend on the amount of boron added to the material, the total neutron flux in the irradiation position of interest, and the cross section for the $^{10}B(n,\alpha)^{7}Li$ reactionaveraged over the neutron spectrum. The amount of ^{10}B burned up will depend only on the spectrum averaged ^{10}B cross section, the total flux and the irradiation time. Thus for a given irradiation period, the amount of helium produced can most easily be adjusted by tailoring the initial amount of ^{10}B added to the alloy to be tested.

In fusion reactor simulation experiments, it is generally felt that helium should be produced at a rate such that the ratio of helium produced (in appm) to dpa produced is approximately 20:1 in stainless steel and 3-5:1 for some of the refractory alloys. To determine the amount of helium desired, it is thus necessary to know the magnitude of the displacement rate. Given all of the factors mentioned above, it is then straightforward to calculate the initial amount of ^{10}B required in any experiment. Table 1 shows total fluxes and spectrum averaged displacement and ^{10}B cross sections for three fast test reactor irradiation positions. (It should be noted that the fluxes and spectrum averaged cross sections quoted in Table 1 for a given irradiation position are those currently available in the literature and do not always correspond exactly to that position. When possible, the exact locations for which the cross sections and fluxes were initially cited are listed directly beneath the table. These calculations will be updated as more data become available.) Also shown in this table are the percentage of

^{10}B burned up in one full power year and the initial amount of ^{10}B required for an irradiation lasting one full power year. As expected, the initial concentration of ^{10}B required to simulate the CTR helium production rate varies greatly from one irradiation position to another. it is apparent, however, that: several thousand appm of ^{10}B dopant would provide useful helium generation rates for SS and considerably lower concentrations would be of interest for refractory alloys based on V, Nb and Mo. For this reason, 5000 appm has been picked as a goal for initial ^{10}B concentrations.

3. Initial Estimates of the Kinetics and Distribution of Boron in Stainless Steel

The helium nucleus produced by the $^{10}B(n,\alpha)^{7}Li$ reaction recoils through stainless steel about 2.6 ± 0.17 μm in a random direction.[4] Thus a small region of high boron concentration will produce a spherical halo of helium with a radius of about 2.6 μm and a thickness of about 0.17 μm. To have helium distributed homogeneously we need the boron distributed substantially more finely than 2 μm, so that the halos will overlap. Ideally we would like the boron distributed as finely as 0.17 μm so that the distinction between one halo and another halo will he entirely blurred. This would be accomplished by having the boron distributed in 10^{15} particles/cm^3 (a spacing of about 0.1 μm). If the boride made up 0.1 volume percent of the !structure, the particles would be about 100 A in diameter.

The maximum solubility of boron in stainless steel is about 400 to 500 appm at about 1100°C. This amount can be retained in solid solution by rapid quenching from 1100°C to room temperature.[5] To keep substantially more than 500 appm boron in solution, we must quench directly from the melt, not from a homogenization anneal. Ruhl and Cohen[6] were able to retain about half of the boron in solution during splat quenching (at about 10^6 to 10^8 K/sec) of Fe-Ni alloys with 8 atomic % boron. In addition, Wood and Honeycombe[7] have recently

TABLE 1 ESTIMATES OF AMOUNT OF ^{10}B TO BE ADDED TO STAINLESS STEEL IN FAST REACTOR BORON DOPING EXPERIMENTS

Reactor	$\bar{\sigma}_d$ (18/8 SS) (barns)	Total Flux (n/cm^2 S)	$\bar{\sigma}$ $^{10}B(n,\alpha)^7Li$ (barns)	Dpa per Full Power Year	% ^{10}B Burned Up In 1 Year	Appm Helium Desired (*) After 1 Yr.	Appm ^{10}B Required
EBR-II Core	417 [1]	Z 69×10^{15} [Z]		35.3	8.1	707	
EBR-II Blanket Row2, Z = +50	16Z	4 87×10^{14}	8.4	2.5	12.1	50	
FTR Core	Z73	5 88×10^{15}	Z 4b	51 Z	35 9	1030	Z 9×10^3

*Based on a He/dpa ratio of 20/1

Sources of Cross Sections and Fluxes

[1] Ref. 1, EBR-II core center midplane.
[2] Ref. 2, EBR-II core center, Z = 0, R = 5.2cm
[3] Ref. 1, EBR-II core center midplane.
[4] Ref. 1, EBR-II Row 2 Z = +50cm.
[5] Ref. 2, EBR-II, Z = +50cm, R = 9cm.
[6] Ref. 1, exact EBR-II position not known.
[7] Ref. 2, FTR Materials Test Assembly(MOTA), Z = 2.5cm, Row 4.
[8] Ref. 2, FTR MOTA, Z = 2.5cm, Row 4.
[9] Ref 3, FTR Core Cent

been able to retain all of 5000 appm E (and, in another experiment, all of 25,000 appm B plus 2.3 wt % of Ti) in solid solution in an Fe-20%Cr-25%Ni alloy by quenching from the melt at about 10^7 K/sec. We therefore expect that we can retain the majority of 5000 appm boron in solution by rapid quenching from the melt to room temperature.

Boron cannot be kept irom diffusing out of a solid solution to segregate at grain boundaries for small grain sizes and reasonable test times and temperatures (e.g. 10 microns or less, 10^6 seconds, and 400°C). A diffusion coefficient has been reported for boron in gamma Fe for temperatures between 950" - 1300°C by F. E. Busby et al:[8]

$$D = 2 \times 10^{-3} \exp \frac{21 \pm 7 \text{ kcal/mole}}{}$$

The experimental points for this are the open circles in Figure 1. We must assume that the actual data points are reasonably accurate, but the extrapolation to low temperatures (at 21 kcal/mole) may be wildly inaccurate. For comparison, Figure 1 also shows data for diffusion of carbon in Fe-17Cr-12Ni and 316 stainless steel. D_{carbon} and D_{boron} are comparable at 1000°C, but D_{carbon} is far lower than the 21 kcal/mole extrapolation at 500°C and below. Boron and carbon are expected to diffuse by the same interstitial mechanism, which should have similar activation energies. We therefore expect that 21 kcal/mole is much too low, and propose an estimate of 30 kcal/mole. This is still a lo!: estimate! because carbon diffuses with at least 37 kcal/mole. Figure 1 shows an estimated diffusion coefficient for boron, based on 30 kcal/mole and passing through the Busby et al. data (D_o = 0.08 cm^2/sec). We will use this estimate Cor further calculations.

The characteristic distance an atom will diffuse in time t is $\sqrt{Dt}$. A scale of $\sqrt{Dt}$ for t = 10^4 seconds (2.8 hours) is added to Figure 1. Based on the estimated boron diffusion coefficient, boron would reach the boundaries of 1 micron size grains in 3 hours at any temperature above 400°C. It would segregate to 10 micron size grain boundaries in 3

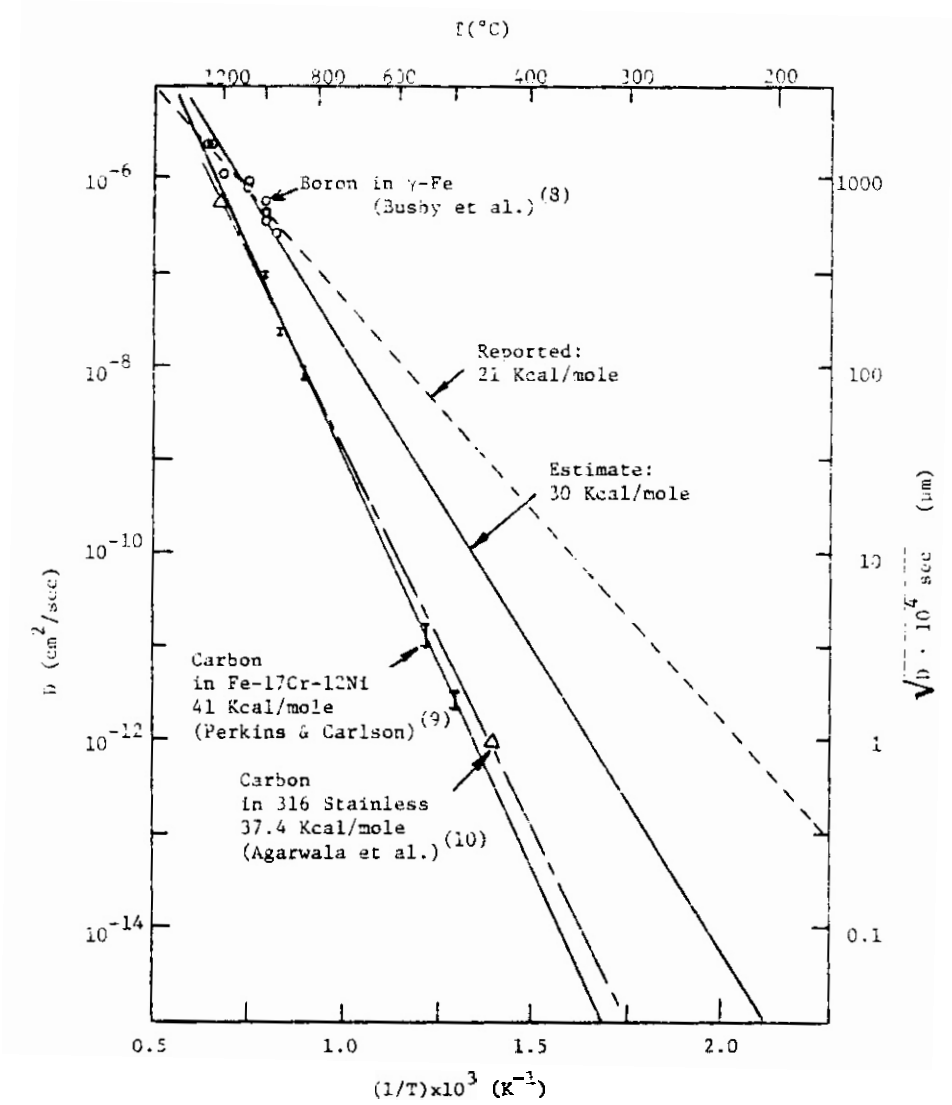

Figure 1. DIFFUSIVITY OF BORON AND CARBON IN AUSTENITE

hours at 500°C or above. A rough confirmation of this analysis is found in Kawasaki et al.[11] They found that boron segregated to the boundaries of 316 stainless steel (grain diameter ≈ 300 microns). At 700°C they observed segregation after 60 minutes, but not after 30 minutes. We would estimate, at 700°C and 60 minutes that $\sqrt{Dt}$ = 72 microns, or about half the grain radius.

It may be possible to hold boron in a finely dispersed state by tying it up in a fine dispersion of a stable compound. Prime candidates are TiB_2 and ZrB_2. Either of these is far more stable than the nickel, iron, or chromium borides. ZrB_2 has a slightly higher enthalpy of formation:[12]

TiB_2: $\Delta H_f^\circ(298) = 66.8 \pm 4$ kcal/mole

ZrB_2: $\Delta H_f^\circ(298) = 77.1 \pm 1.6$ kcal/mole.

ZrB_2 should therefore be more stable. If we assume that the activity coefficients of boron and titanium or zirconium in stainless steel are approximately unity, we have:

$$C_B^2 \, C_{Ti} = \exp\left[-\frac{\Delta G^\circ_{formation}\ (TiB_2)}{RT}\right]$$

$$\text{or} \quad C_B^2 \, C_{Zr} = \exp\left[-\frac{G_f^\circ\ (ZrB_2)}{RT}\right]$$

where C_B, C_{Ti}, and C_{Zr} are atomic fractions in the austenite matrix. This is a conservative estimate because the activity coefficients of boron, titanium, and zirconium in austenite will be substantially greater than unity, and the matrix concentrations in equilibrium with the boride will be correspondingly lower. At small boron concentrations, most of the boron can be tied up in TiB_2 or ZrB_2 precipitates with an excess over stoichiometry of 0.1 atomic % Ti or Zr. Since Shepard[13] was able to precipitate 2×10^{15} NbC particles per cm^3 in stainless steel, we expect that it is possible to precipitate a fine dispersion of these TiB_2 or ZrB_2

particles by appropriate heat treatment. We will find that C_{Zr} or C_{Ti} in the matrix will remain about 0.1%, and can calculate C_B with this assumption, as shown in Figure 2.

4. Coarsening of TiB_2 or ZrB_2 Precipitates.

a. Without Irradiation

Bhattacharyya and Russell[14] show that the coarsening of A_aB_b precipitates is controlled by whichever species (A or B) has the smallest product of matrix concentration (C_A or C_B) times matrix diffusion coefficient (D_A or D_B). If A is controlling, the average particle radius, $\bar{r}$, is given as a function of time, t, by:

$$\bar{r}^3 = \bar{r}_o^3 + \frac{8\, D_A C_A\, \sigma\, V_m^2\, t}{9\, RT\, a}$$

σ = matrix--particle interfacial energy (about 500 ergs/cm^2)

V_m = molar volume of A_aB_b; $V_m(TiB_2)$ = 15.5 cm^3; $V_m(ZrB_2)$ = 18.3 cm^3

To see whether boron or zirconium controls the coarsening, we have to compare D_BC_B to $D_{Zr}C_{Zr}$. C_{Zr} is assumed and D_BC_B we have calculated (Figure 3). We still need to estimate D_{Zr} in stainless steel because it has not been measured. Zirconium probably diffuses by the standard vacancy mechanism, with some preferential binding to the vacancy. We can then guess that it diffuses only slightly faster than the host metal. Figure 4 shows D(nickel) in stainless steel, and an estimate for D_{Zr}. Q = 60 kcal/mole, D_o = 1.0 cm^2/sec. The same estimate would work for titanium. We then find $D_{Zr}C_{Zr} < D_BC_B$ above 250°C. (The same would be true for Ti.)

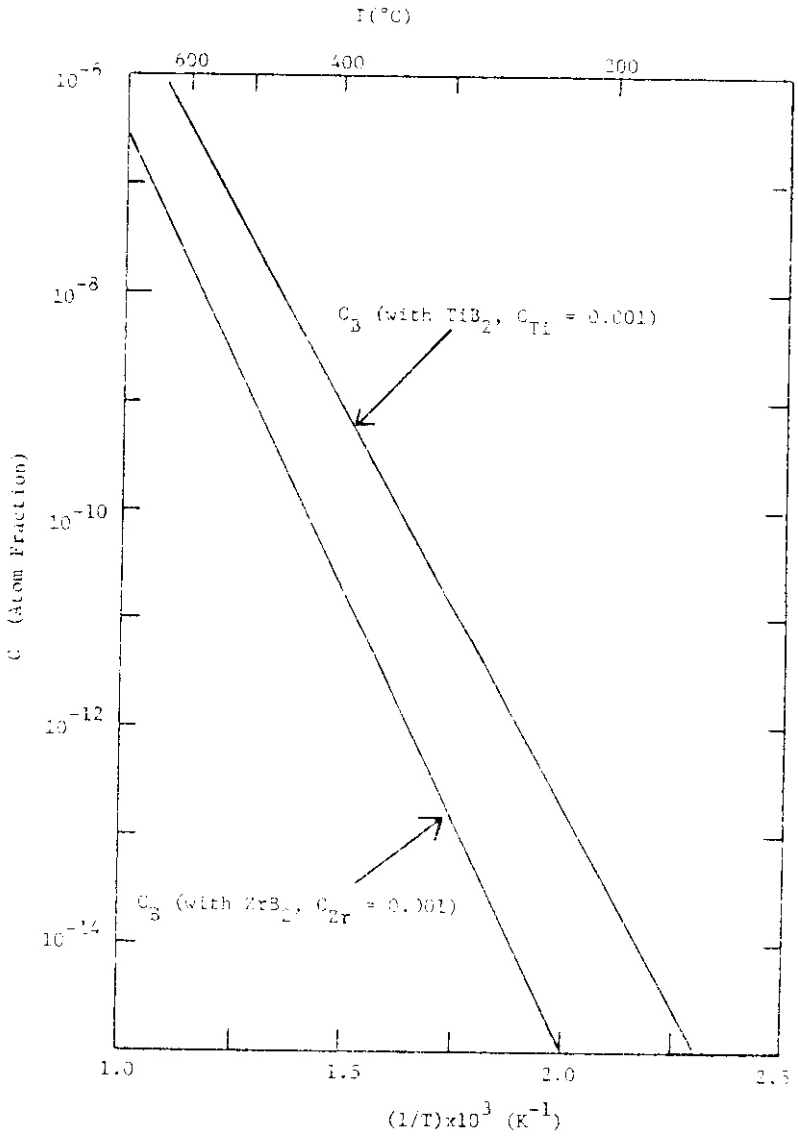

Figure 2. BORON CONCENTRATION IN AUSTENITE MATRIX (IN EQUILIBRIUM)

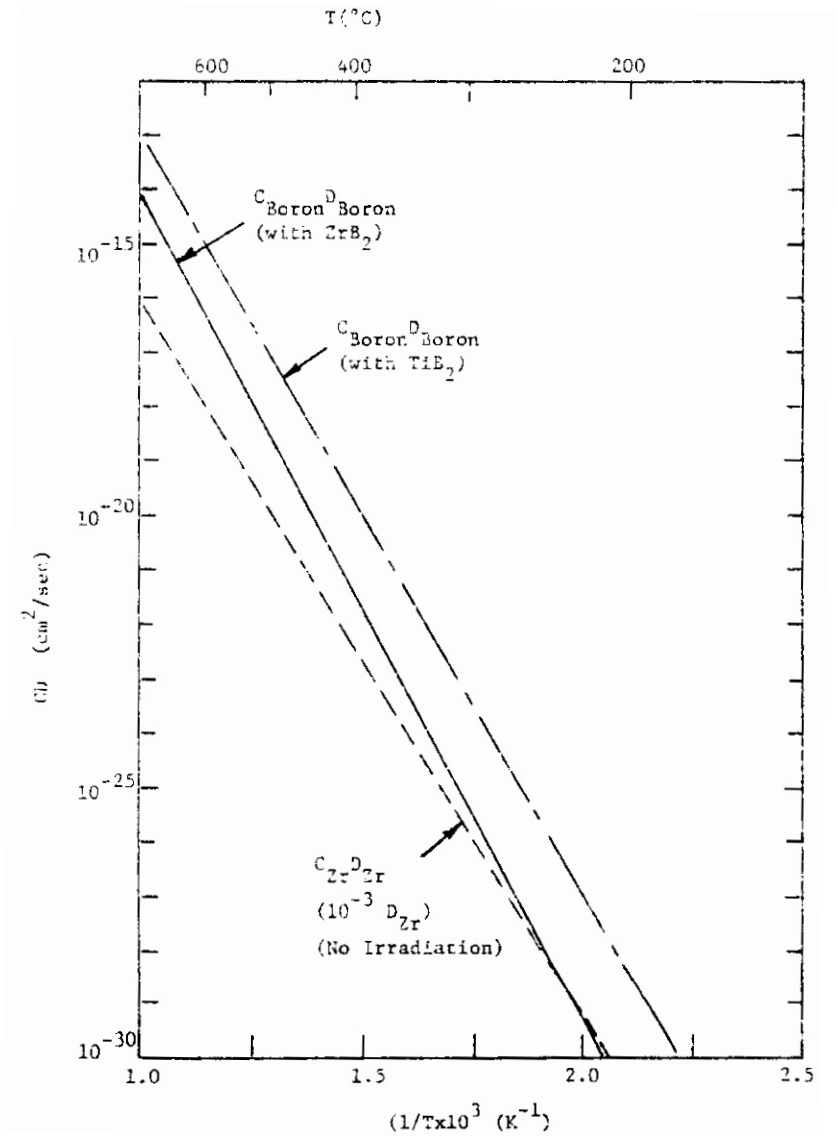

Figure 3. VALUE OF CD vs. **TEMPERATURE** FOR **BORON** AND ZIRCONIUM

The above estimate may be improved by considering the possibility of enhanced diffusion of Zr along dislocation cores, which we expect at these temperatures. Figure 4 shows the contribution that core diffusion would make in pure nickel with a dislocation density of 10^{10} cm^{-2}. Although core diffusion should he slower in the solid solution than in the pure metal, it still might contribute substantially at lower temperature. We need not estimate this accurately, however, because under irradiation the Zr diffusion will not be rate controlling, as will be shown in the next section.

b. With Irradiation

Diffusion of both species will be speeded up by irradiation by various mechanisms, hut the metal should be much more strongly affected. The diffusion coefficients of Ti and Zr should be increased by a factor of 10^4 to 10^6 or more. The interstitial diffusion of boron should he increased some because of interactions with vacancies and divacancies, but not by nearly as much as Ti or Zr. This means that tlie control of the coarsening will switch to boron transport. Using values of $C_B D_B$ from Figure 3, we have plotted $(\bar{r}^{-3} - \bar{r}_o^{-3})^{1/3}$ values lor the boron controlled case in Figure 5. This predicts that 100A radius particles would coarsen appreciably in 10^8 seconds at 550°C, but not at 450°C. Particles of radius 1000A would not coarsen appreciably :it 550°C, but would above 650°C. For TiB_2 particles we would expect somewhat faster coarsening because Ti binds tlie boron Less strongly than Zr and the matrix concentration of boron would be higher.

c. Summary

To produce helium uniformly, boron must be distributed homogeneously to a scale of 1 micron or less. Boron cannot be kept this finely distributed in solid solution because it diffuses fast enough to segregate to the grain boundaries during reasonable test times and test temperatures. The boron probably can be held in a fine dispersion of

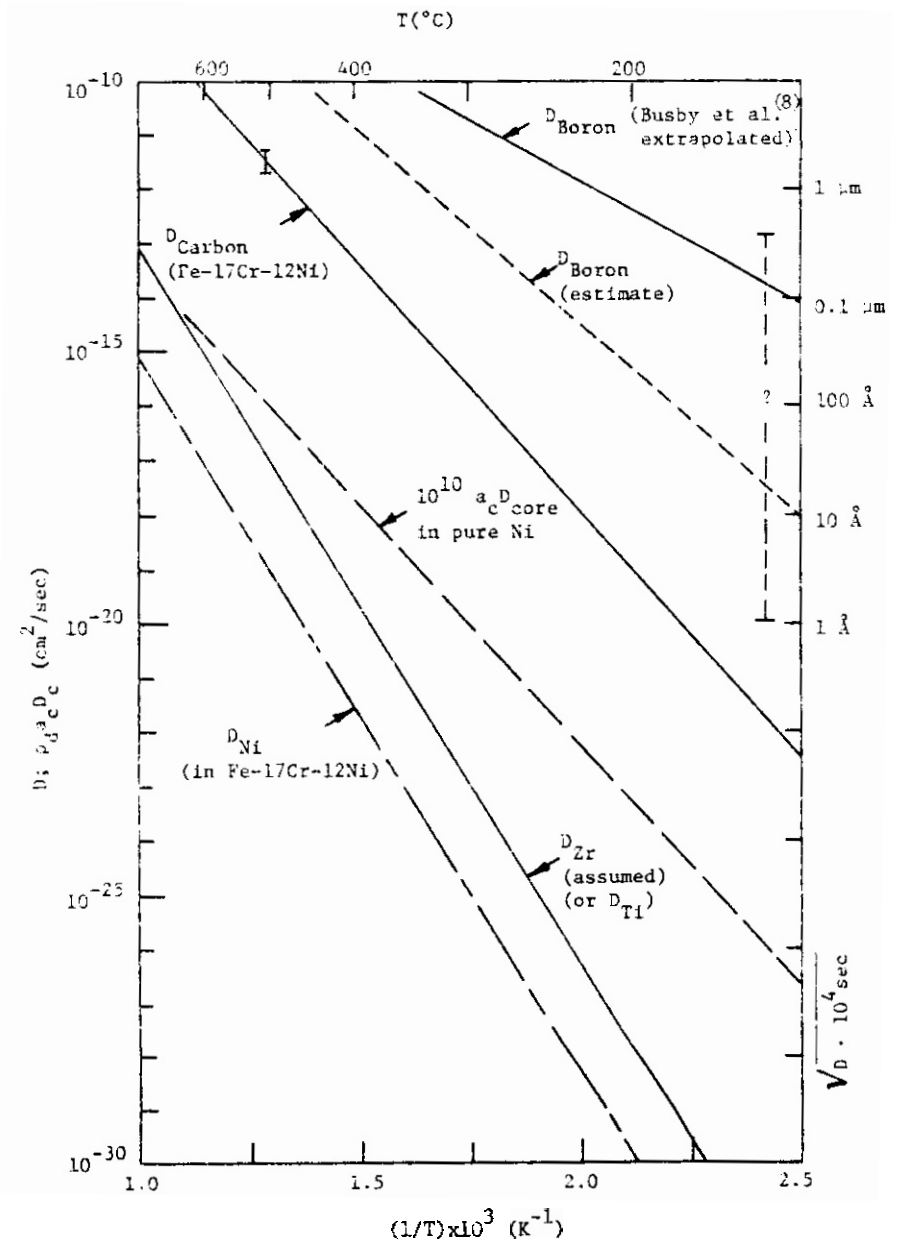

Figure 4. DIFFUSIVITY OF NICKEL, ZIRCONIUM AND TITANIUM

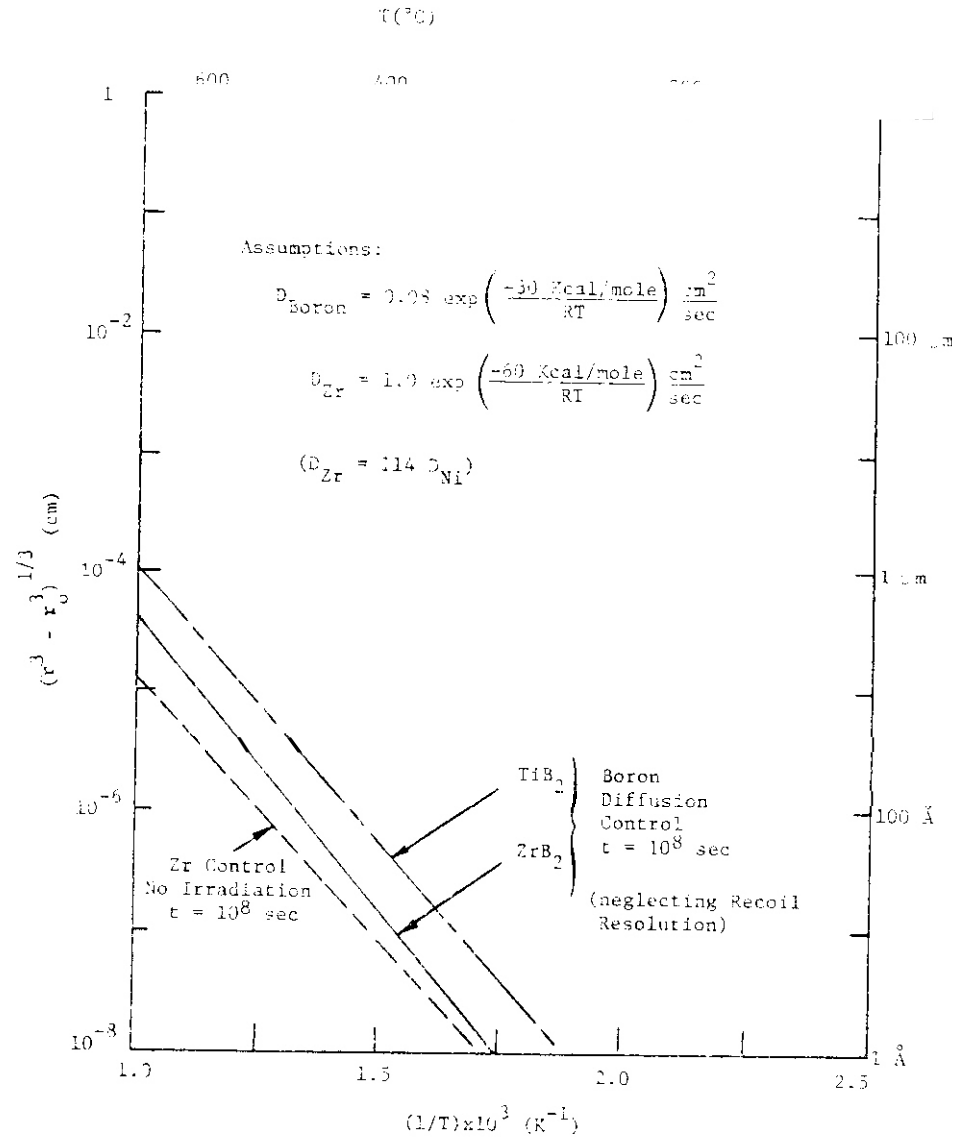

Figure 5. COARSENING OF THE TiB_2 AND ZrB_2 PRECIPITATES IN STAINLESS STEEL.

stable boride particles, such as ZrB_2. With a slight excess of Zr in solution, and under irradiation, the particle coarsening should be controlled by boron diffusion. Our estimates indicate that the coarsening will be slow enough to retain the dispersion at a scale finer than 1 micron for useful test times and temperatures.

5. Production of Boron Doped Stainless Steel Alloys

The production of boron doped materials using splat cooling consists of: producing master alloys; producing material for splatting; splat cooling; processing splat cooled foils; and consolidation of the foils. In the last quarter, our emphasis was on the first three areas.

Master alloy production at a pound lot scale was investigated to determine the optimum furnace design for producing our alloys. The production of master alloys and actual splatting compositions was attempted under various conditions. Based on this, an optimized furnace for master alloy production has been designed and is being constructed.

Splat cooling small lots of boron doped stainless steel was accomplished using a melt-spinning device. In this device, a sample lot of about 10gm is splatted on a spinning copper ring. Although this device is too small to produce enough material for consolidation, it does provide enough material for transmission electron microscopy. Previously we reported work with a roll quenching device: however, this machine requires a minimum of about one pound of material per run. The melt spun foils will be used to determine the boron precipitation and segregation kinetics referred to in section 3 of this report.

VI. REFERENCES

1. R. L. Simons, "Helium Production in FBR Out-of-Core Structural Components," *HEDL-SA-1439,* to be published in the Proceedings of the 9th International Symposium on Effects of Radiation on Structural

Materials, Richland, WA, July 1978, cited by D. S. Gelles and F. A Garner, "An Experimental Method to Determine the Role of Helium in Neutron-Induced Microstructural Evolution," to be published in the Proceedings of the First Topical Meeting on Fusion Reactor Materials, Miami Beach, January 1979.

2. D. G. Doran and N. J. Graves, "Displacement Cross Sections and PKA Spectra: Tables and Applications," HEDL-TME 76-70 (1976).

3. Calculated by R. L. Simons, Hanford Engineering Development Laboratory (1978).

4. D. S. Gelles and F. A. Garner, "An Experimental Method to Determine the Role of Helium in Xeutron-Induced Microstructural Evolution." to be published in the Proceedings of the First Topical Meeting on Fusion Reactor Materials, Miami Beach, .January 1979.

5. H. J. Goldschmidt, J. Iron and Steel Inst. 209 (1971) p. 910.

6. R. C. Ruhl and Pi. Cohen, Trans. AIME 245 (1969) p. 253.

7. J. V. Wood and R. W. K. Honeycomhe, "Splat Quenching of a Nickel-Chromium Steel Containing Boron and Titanium Additions," accepted for publication in Phil. Mag

8. P. E. Busby, M. E. Warga and C. Wells, Trans. AIME 197 (1953) p. 1463.

9. R. A. Perkins and P. T. Carlson, Met. Trans. 5 (1974) p. 1511.

10. R. P. Agarwala, M. C. Naik, M. S. Anand and A. R. Paul, J. Nucl. Mat. 36 (1970) p. 41.

11. S. Kawasaki, A. Hishinuma and R. Nagasaki, J. Nucl. Mat. 39 (1971) p. 166.

12. J.A.N.A.F. Thermochemical Tables, 2nd Edition (1970).

13. J. P. Shepard, Met. Sci. [illegible] p. [illegible]

14. S. K. Bhattacharyya and K. C. Russell, Met. Trans. 3 (1972) p. 2195.

VII. RECENT REPORTS FROM THIS PROJECT

1. H. Andresen and O. K. Harling, "A New Approach to Simulation of Helium and Simultaneous Damage Production in Fusion Reactors--In Reactor Tritium Trick," presented at the First Topical Meeting on Fusion Reactor Materials, Miami Beach, January 1979.

2. S. Best, A. Fadaai and O. K. Harling, "Initial Results Using Splat Cooling in the Development of Boron Doping for the Simulation of Fusion Reactor Helium Embrittlement," presented at the First Topical Meeting on Rusion Reactor Materials, Miami Beach, January 1979.

VIII. FUTURE WORK (Near Term)

As improved flux and cross section data become available, the calculation of the initial ^{10}B concentration to be added to stainless steel to simulate CTR helium production rates will be refined. The initial calculations on the kinetics and distribution of boron in stainless steel will be continued. In particular, the next phase of this work will center around the effect of various radiation damage phenomena on the microstructure of the boron doped stainless steel.

Experimental efforts during the next quarter will concentrate on precipitation studies in stainless steel doped with various quantities of boron and zirconium.

CHAPTER 4

SUBTASK B: DAMAGE PRODUCTION

I. PROGRAM

Title: Irradiation Effects Analysis (WH011/EDA)
Principal Investigator: D. G. Doran
Affiliation: Hanford Engineering Development Laboratory

II. OBJECTIVE

The objective of this work is to develop computer models for the simulation of high energy cascades which will be used to generate defect production functions for correlation analyses of radiation effects.

III. RELEVANT OAFS PROGRAM TASK/SUBTASK

SUBTASK II.B.2.3 Cascade Production Methodology

IV. SUMMARY

Defect yields and cascade densities for PKAs in copper are being studied as a function of effective recombination distances. An interactive computer graphics program is being developed, and examples illustrating the graphics capabilities and the cascade studies are presented here.

V. ACCOMPLISHMENTS ANU STATUS

A. Computer Simulation of High Energy Cascades - H. L. Heinisch, Jr. (HEDL)

Comparisons of MARLOWE with results from dynamic simulation codes(1.2) continue to verify its usefulness and validity for the study of high energy cascades. While the need to further establish the validity of our high energy cascade models clearly exists, it is nevertheless desirable to proceed toward our objective of generating defect production functions using the best models available.

The aspect of displacement cascade development which appears to be very important but is least understood at this time is the dissipation of energy from the so-called "thermal spike" region (sometimes referred to as "afterglow"). A proper study of thermal spikes will necessitate dynamical simulations. That approach is practical only for mechanism studies with a few cascades. Dealing with large numbers of thermal spikes will require some relatively simple model for the average behavior of the defects. Perhaps the simplest approach is to assume an effective recombination distance (RD) for the Frenkel pairs produced in the cascade.

A spontaneous recombination distance on the order of two lattice parameters has been found appropriate in simulation studies.[1,3] This value is consistent with experimental[4] and theoretical[5] determinations of low temperature spontaneous recombination. Thus, a value of RD which simulates annealing in the thermal spike should be somewhat greater than two lattice parameters.

The effects of large RDs on defect yields and cascade density are being investigated for cascades in copper. To date, PKAs with energies in the range froni 1 keV to 40 keV have been studied using MARLOWE, and RDs up to seven lattice parameters have been applied. At each energy, in multiples of 5 keV, the results of ten cascades with randoinly chosen directions were averaged; one hundred cascades were generated at each of 1, 2, 3, and 4 keV.

When RDs in the range of five to seven lattice parameters are imposed on the cascades, the resulting Frenkel pair yields display the same energy dependence as defect yield curves which we have nunierically extracted from resistivity measurements of ion irradiated copper (this work is in progress; a detailed report will be prepared).

The average cascade density, defined as the average number of pairs divided by the average nuinber of sites involved in the simulation, is independent of eneryy above a few keV at any value of RD. That is, the

density varies with RD, but not with energy. The fraction of initially produced pairs which recombine as a function of RD is therefore independent of energy. This supports the idea that the size, but not the nature, *of* the damaged region varies with PKA energy. Thus, a recombination criterion may be at least a good first approximation for describing defect yields from thermal spikes above a few keV. Of course, such a criterion provides no indication of the actual physical processes occurring as the thermal spike cools off.

At energies up to a few hundred electron volts, cascades can be handled by the dynamical simulations. Between a few hundred and several thousand electron volts, there is a transition to thermal spike production, which may not easily be described by a simple recombination criterion. Above 5-10 keV a single recombination criterion, independent of energy, appears to be adequate.

It could be argued that as the cascade volume increases with energy, the surface to volume ratio decreases, and more time is required for dissipation of the energy. Thus, there is more chance for recombination to occur in the higher energy cascades, and an effective RD which increases with energy may be necessary. However, in the present study, this has not been found to be true above 5-10 keV. Perhaps this is because the cascades with higher energy do not increase in size equally rapidly in all three dimensions. If the cascades maintain linear or disk shapes, they can increase in size without appreciable changes in surface-to-volume ratio.

An alternative argument for an energy independent RD is the formation of subcascades having the same distribution of sizes and densities regardless of energy. A systematic graphical analysis of high energy cascades is expected to answer these questions and others concerning the spatial distribution of defects in cascades.

B. Analysis of High Energy Cascades Using Interactive 3-D Computer Graphics - H. L. Heinisch, Jr. (HEDL)

In addition to the MARLOWE cascade studies, we have been developing an interactive 3-D computer graphics program, SPACEwarp, for the purpose of graphical analysis of cascades (and ultimately for annealing studies as well).

In the current version, markers are plotted at the positions of the vacancies and interstitials in a 3-D perspective view. The cascade may be viewed from any angle or distance, and the perspective may be exaggerated by a scaling factor. Some examples of the graphics produced by this program are included here.

The following five figures are three-dimensional views of the distributions of interstitials and vacancies produced in computer simulated displacement cascades. Figure 1 illustrates the Frenkel pairs remaining after recombining all pairs separated by less than two lattice parameters (RD = 2). The cascade exhibits a "depleted zone" configuration.

To simulate the recombination which occurs as the highly excited cascade region dissipates energy, the recombination distance is increased to RD = 4 in Figure 2. The vacancy distribution retains its basically two-lobed shape, and the depleted zone is well-defined. The shape of this cascade may indicate a trend toward subcascade formation.

Figure 3 is a cascade froin a 10 keV PKA in the same direction as in Figure 1, with RD = 4. At 10 keV the cascade is smaller, has one well-defined depleted zone, and is found to be disk-shaped by viewing froin other anqles.

Even at 10 keV there is some evidence that subcascades can begin forming. This is illustrated in Figure 4, in which a 10 keV PKA in tne <100> direction produces two distinctly separated depleted zones. shown

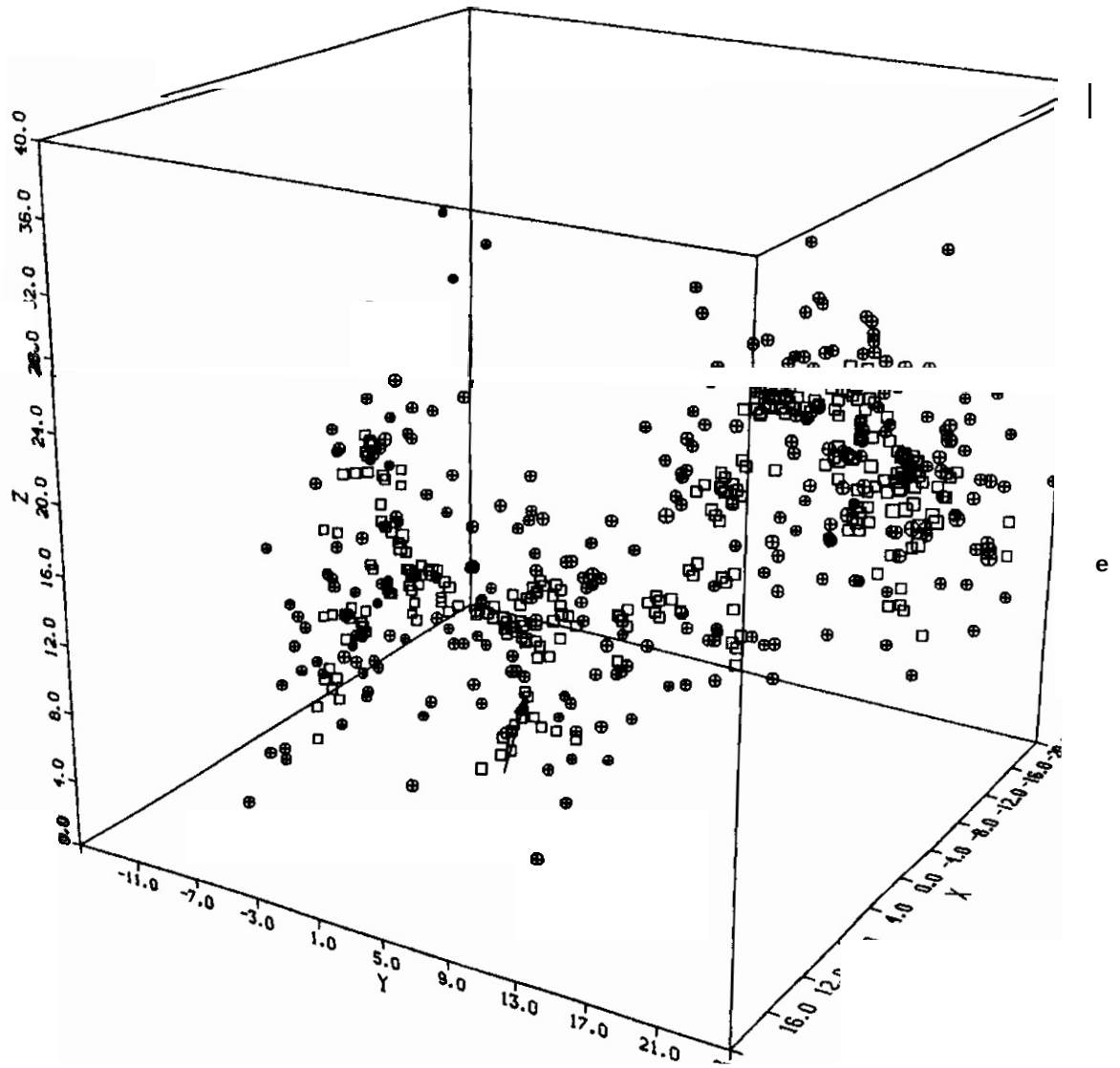

FIGURE 1. A Cascade in Copper Resulting From a 25 keV Primary Knock-On Atom (PKA) in a High Index Direction [A small arrow in the figure at (0, 0, 0) indicates the initial PKA direction.] In all the figures, the squares represent vacancies; the crossed circles represent interstitial atoms. The scale on the edges of the large cube is in units of lattice parameters (1 lattice parameter = .361 nm in copper). All symbols representing atoms or vacancies are nominally the same size, one half lattice parameter. Those which appear relatively larger (smaller) are at positions closer to (farther from) the viewer's eye.

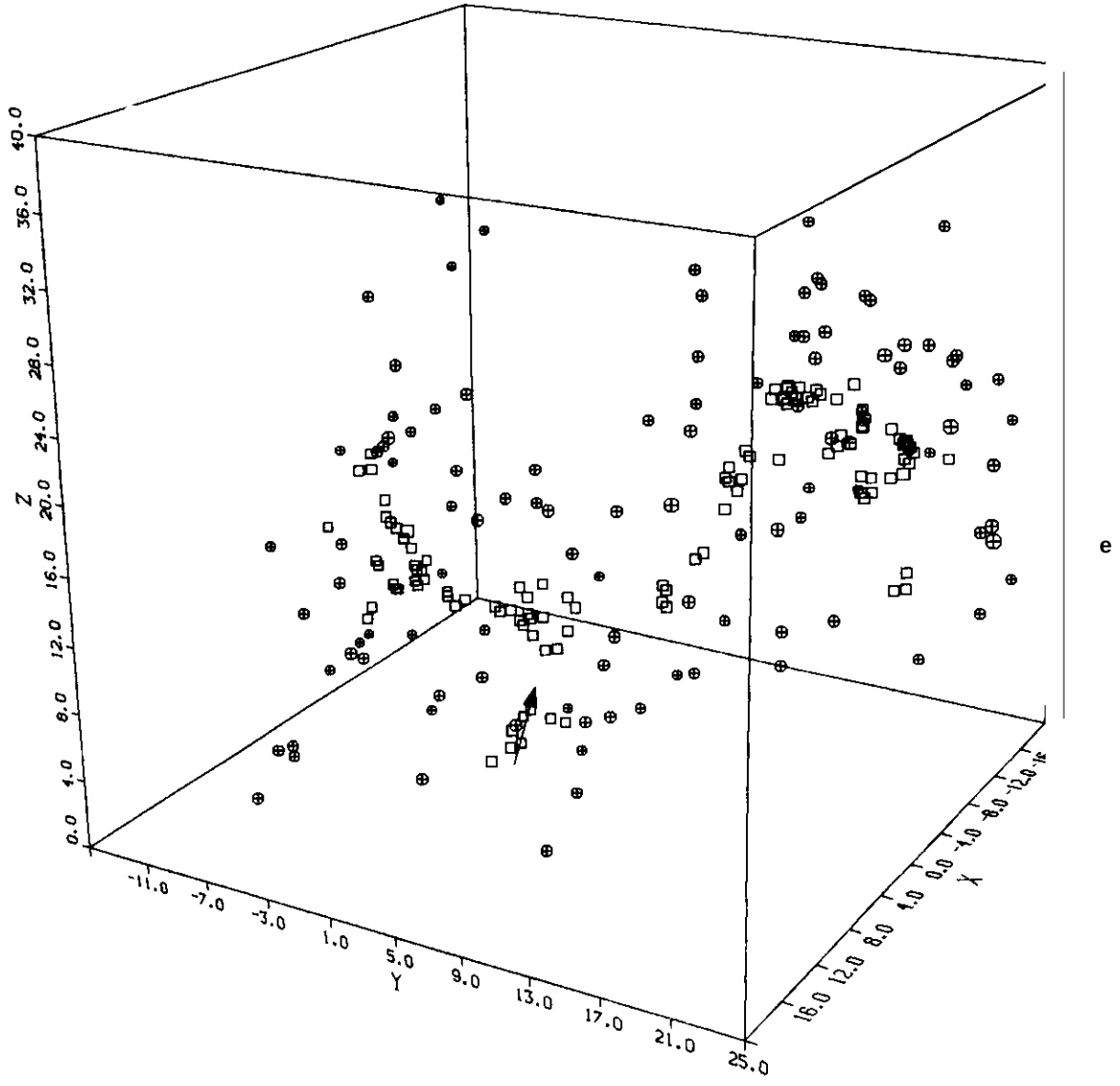

FIGURE 2. 25 keV Cascade in Cu. Reconibination Distance (RD) = 4

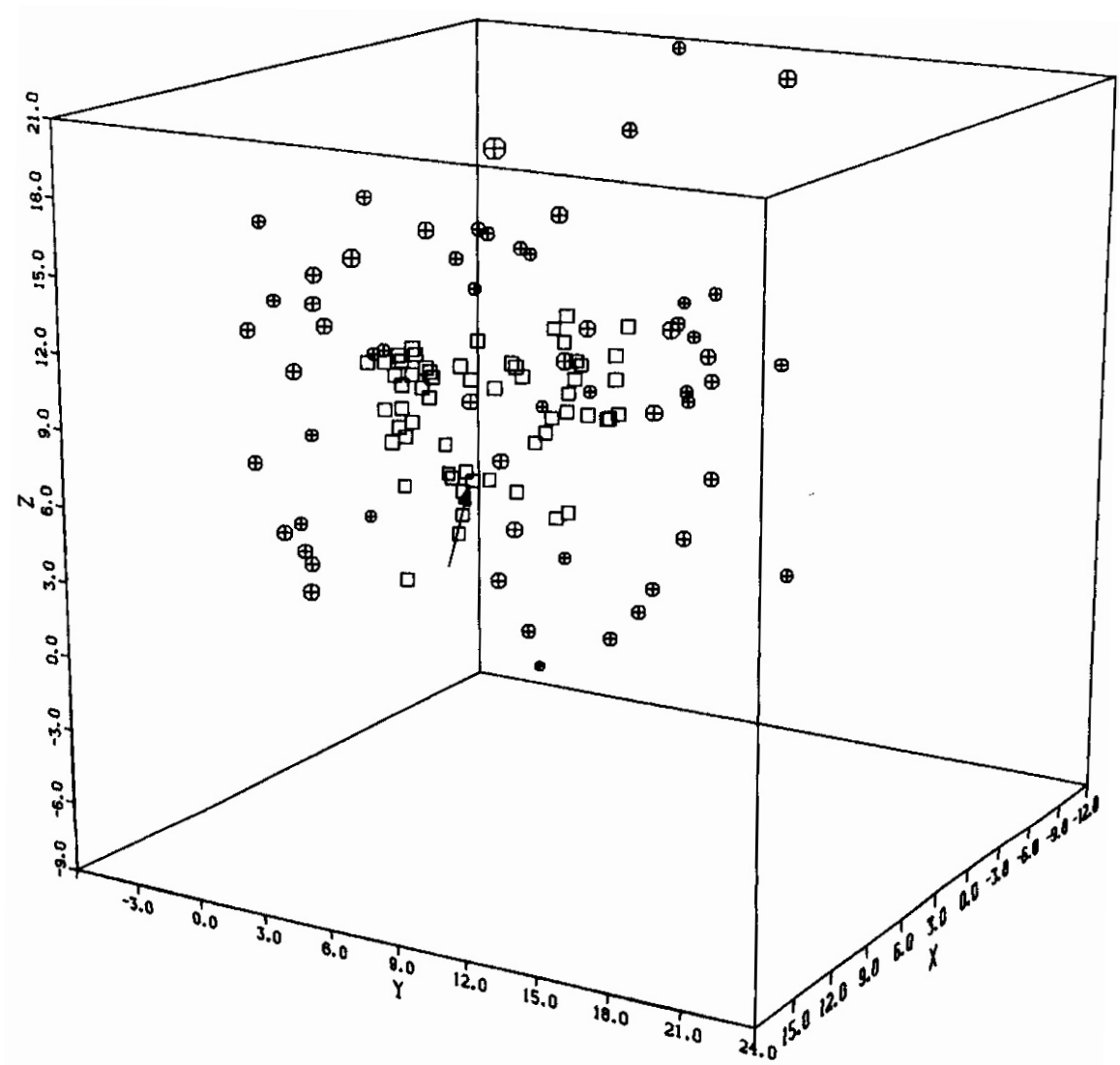

FIGURE 3. 10 keV Cascade in Cu. Recombination Distance (RD) = 4.

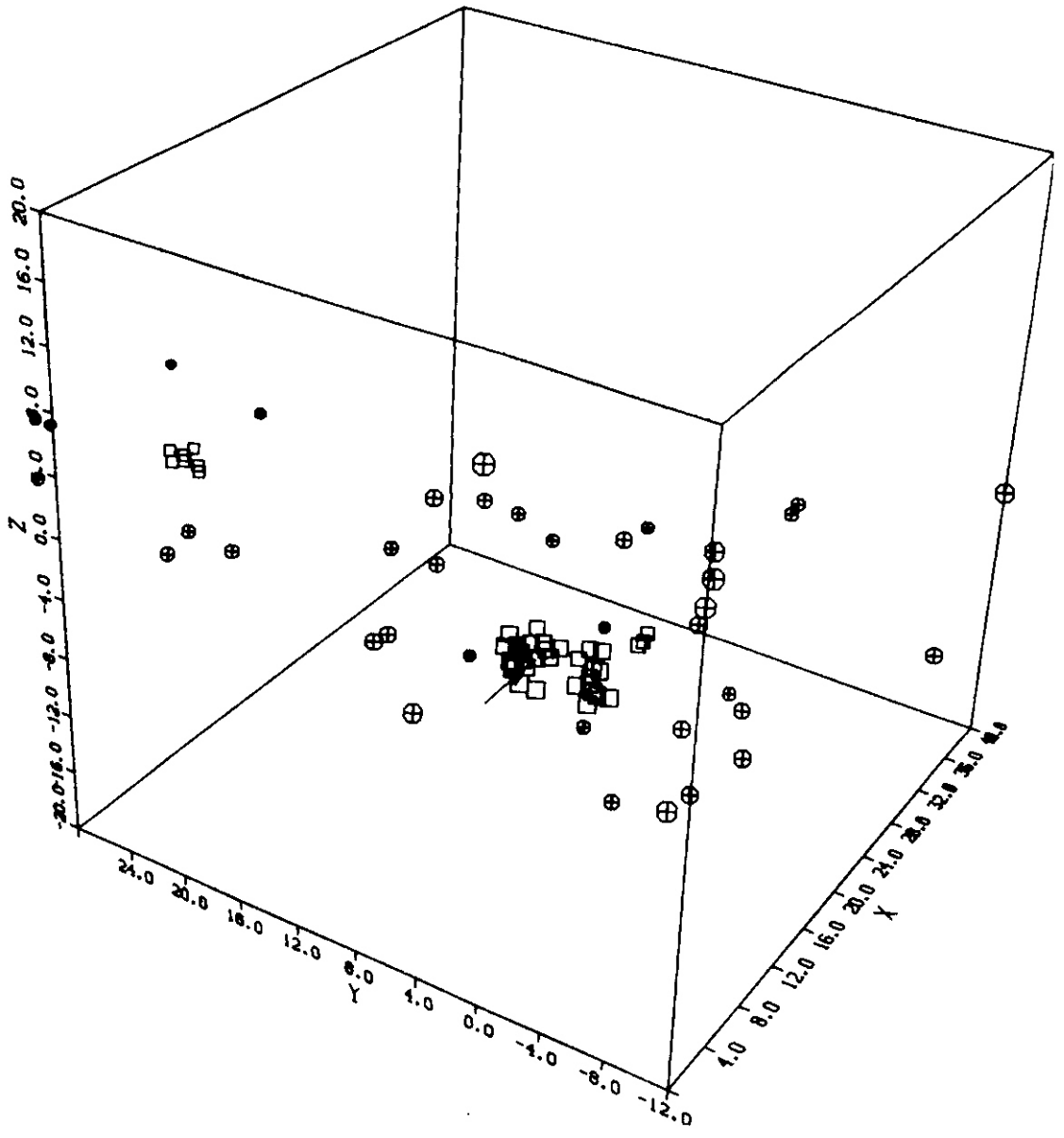

FIGURE 4. 10 keV Cascade in Cu. Recombination Distance (RD) = 5.

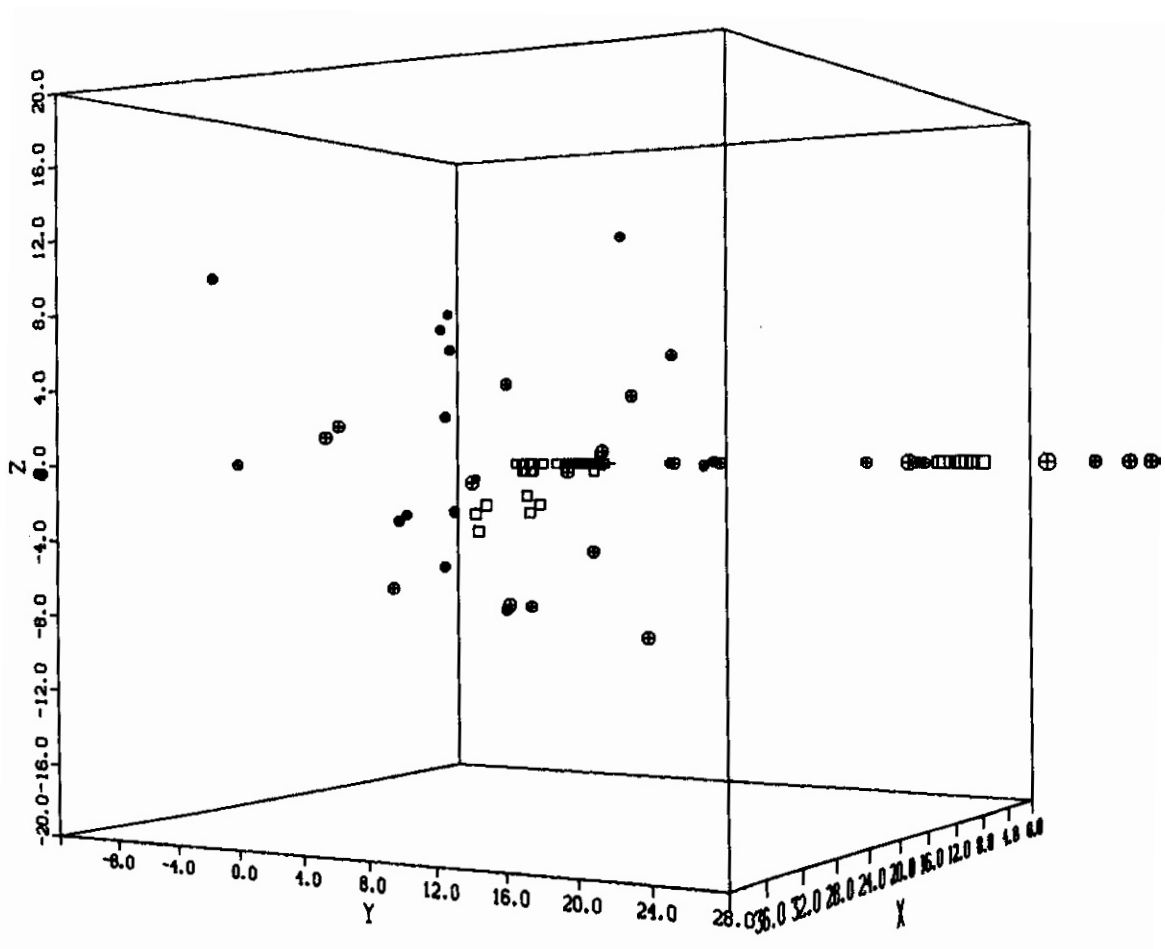

FIGURE 5. 10 keV Cascade in Cu. Recombination Distance (RD) = 5.

here at RD = 5, but distinct even at RD <2. An interesting feature of this cascade becomes more evident in Figure 5. Here the viewer's eye is in the equatorial plane (Z = 0) and the figure has been rotated 180". The defects are primarily confined to the Z = 0 plane. In fact, 85: of the vacancies lie within one lattice parameter of the Z = 0 plane.

VI. REFERENCES

1. H. L. Heinisch, J. O. Schiffgens, and D. M. Schwartz, J. Nucl. Mat., accepted for publication.

2. M. T. Robinson, DAFS Quarterly Progress Report, October - December 1978, in printing.

3. G. R. Odette and D. M. Schwartz, Trans. Am. Nucl. Soc. 27 (1977), 316.

4. G. Luck and R. Sizman, Phys. Stat. Sol. 5 (1964), 683

5. A. Scholz and C. Lehmann, Phys. Rev. B, 6 (1972), 813.

VII. FUTURE WORK

Both numerical and graphical analysis of cascades will be extended to higher energies (~100 keV).

I. PROGRAM

Title: Radiation Damage Analysis and Computer Simulation
Principal Investigator: Don M. Parkin
Affiliation: Los Alamos Scientific Laboratory of the University of California

II. OBJECTIVE

The objective of this work is to develop displacement functions for polyatomic materials.

III. RELEVANT DAFS PROGRAM PLAN TASK/SUBTASK

SUBTASK II.B.2.3 Cascade Production Methodology
II.B.4.1 Interface with other designs and other tasks
II.B.4.2 Develop theory of spectral and rate effects

IV. SUMMARY

The computer code DISPLC has been used to calculate net displacement functions in polyatomic materials. One of the important possibilities in ceramic materials is that atoms of one type cannot be captured on atom sites of another type during a displacement cascade. Calculations for CaO and Al_2O_3 show that this is an important effect for materials with mass ratio near one if the atom types have different displacement threshold energies.

V. ACCOMPLISHMENTS AND STATUS

A. Net Displacement Functions for Polyatomic Materials -- D. M. Parkin (LASL) and C. A. Coulter (The University of Alabama)

1. Results

One of the important properties of many ceramic and insulator materials that differs fro? metallic alloys is that the atoms in the crystal are bound by ionic forces and not by metallic forces. This situation leads to a characteristic change in the possible events that can occur in a displacement cascade. It is a good assumption that in an ionic material cations cannot be located at anion lattice sites and vice versa. The result of this fact is that, for example, in Al_2O_3, displaced Al atoms can displace other Al atoms and O atoms and be captured at Al atom sites but not at O atom sites and the corresponding case for O. In a metallic alloy this, of course, is not the case. Fur example, in Nb_3Sn, both Nb and Sn can be on any atom site.

To investigate the role of this effect on displacement cascades in polyatomic materials, calculations for CaO and Al_2O_3 were performed assuming first that atoms of type-i cannot be captured on type-j sites if $i \neq j$ and for the case where such captures are possible. CaO and Al_2O_3 are materials where the mass ratio is near one. For CaO we assumed that E_i^d = 50 eV and for Al_2O_3 we used 18 eV for Al and 72 for O.[1] For the no-capture-of-unlike-atoms case we assumed

$$E_{ii}^{cap} = E_i^d \tag{1}$$

and

$$E_{i\neq j}^{cap} = 0 \tag{2}$$

For the case where unlike atoms can be captured we assumed Eq. 1 and that

$$E_{i\neq j}^{cap} = \frac{\sum E_i^d}{2} \tag{3}$$

To analyze the results it is convenient to define the ratio of the net displacement functions $g_{ij}(E)$ for the two cases to be

$$\beta_{ij} = \frac{g_{1j}(E) \text{ for case one}}{g_{ij}(E) \text{ for case two}} \qquad (4)$$

where case one is the no-unlike-capture case using Eq. 2 and case two is the capture case using Eq. 3. The results for CaO are given in Table I and those for Al_2O_3 are given in Table 11.

The data in Table I for CaO show three principal effects. First, for the case i = j, the values of β_{ii} are greater than one below $2E_i^d$ and first increase then decrease as a function of energy. This behavior is a result of the importance of capture energy for low energy PKA's and low energy transfer events. Where unlike atom capture is allowed, for example, an initial PKA of Ca may convert into an 0 displacement. When no such capture is possible, the Ca PKA is "frozen" in the lattice below $2E_i^d$. As the PKA energy increases, displacement events in which this "freezing" is important become less in relative number. Second, for the case $i \neq j$, the values of β_{ij} increase with energy and although the "freezing" effect is present, it is not displayed in the same way. Third, for all β_{ij}, the values of β_{ij} reach a stable value by a few keV of 1.06.

The data for Al_2O_3 in Table II show the importance of knowing the probability of unlike atom capture when the displacement energies of the two atom types are different. In this case, for displacement of the atom with the smallest displacement energy, the results are similar to the results for CaO (i.e. β_{11}, β_{21}). For the atom with the largest displacement energy, 0 in this case, the "freezing" effect plays a major role in increasing the net number of 0 displacements. For an 0 PKA with energy near the 0 displacement energy, it cannot produce a second 0 displacement but will produce $\sim$.3 Al displacements. This fact gives a high probability of 0 capture on the Al site for capture energies of the order of the displacement energies. If this capture is not possible then the 0

displacement is "frozen" in. As the PKA energy increases, this low energy region, where the O atoms lose a large part of their energy in displacing Al atomsbut are "frozen" in as displacements, is an important part of tne total displacement process and, hence, the net number of O displacements significantly increases while the number of Al displacements is only slightly effected. As with CaO the β_{ij} reach stable values by a few keV.

VI. REFERENCES

1. G. P. Pells and D. C. Phillips, AERE Harwell Report AERE-R9138 (Harwell, UK, 1978).

VII. FUTURE WORK

Futurework will extend the analysis to include materials with mass ratio much different than one.

VIII. PUBLICATIONS

1. Don M. Parkin and C. Alton Coulter, "Displacement Functions for Diatomic Materials," to be published in J. Nucl. Mat.
2. C. Alton Coulter and Don M. Parkin, "Damage Energy Functions in Polyatomic Material," in preparation.

TABLE I

VALUE OF β_{ij} FOR CaO (Ca = 1, O = 2)

Energy (eV)	β_{11}	β_{22}	Energy (eV)	β_{12}	β_{21}
86	1.04	1.04	69	1.00	1.00
127	1.10	1.11	99	1.00	1.00
188	1.10	1.11	142	1.02	1.02
279	1.08	1.09	292	1.04	1.04
907	1.07	1.08	a59	1.06	1.06
2952	1.06	1.07	2531	1.06	1.06
9605	1.06	1.06	7455	1.06	1.06

TABLE II

VALUES OF β_{ij} FOR Al_2O_3 (Al = 1, O = 2)

Energy (eV)	β_{11}	Energy (eV)	β_{22}	Energy (eV)	β_{12}	Energy (eV)	β_{21}
72	1.00	72	1.38	a7	1.39	72	1.03
95	1.02	106	1.45	97	1.40	93	1.02
126	1.05	179	1.50	123	1.41	121	1.02
166	1.06	302	1.50	175	1.43	158	1.02
290	1.05	660	1.47	281	1.45	267	1.02
670	1.04	1110	1.40	721	1.46	767	1.02
1540	1.03	2420	1.48	1460	1.47	1680	1.03
9450	1.03	8900	1.47	9610	1.47	9350	1.03

I. PROGRAM

Title: Irradiation Effects Analysis (WHOll/EDA)
Principal Investigator: D. G. Doran
Affiliation: Hanford Engineering Development Laboratory

II. OBJECTIVE

The objective of this work is to determine the effects of high energy neutrons on damage production and evolution, and the relationships of these effects to effects produced by fission reactor neutrons. Specific objectives of current work are the planning and performance of an irradiation program at the Rotating Target Neutron Source (RTNS)-II and post-irradiation testing.

III. RELEVANT DAFS PROGRAM PLAN TASK/SUBTASK

SUBTASK II.B.3.2 Experimental Characterization of Primary Damage State; Studies of Metals
II.C.6.3 Effects of Damage Rate and Cascade Structure on Microstructure; Low-EnergylHigh-Energy Neutron Correlations
II.C.11.4 Effects of Cascades and Flux on Flow; High-Energy Neutron Irradiations
II.C.17.1 Microstructural Characterization; Monitor and Assess New Methodologies
II.C.18.1 Relating Low- and High- Exposure Microstructures; Nucleation Experiments

IV. SUMMARY

Materials selected for irradiation in RTNS-II include pure metals (Ni, Cu, Ti, V, Nb), binary alloys (Ni and Cu based), a simple Fe-Ni-Cr alloy with and without Mo, and three, more complex alloys from the Alloy

Development for Irradiation Performance (ADIP) program. The rationale for their selection is described and a test matrix presented. Specimens have been prepared and mounted in a capsule in preparation for the initial room temperature irradiations. It has been demonstrated that small changes in ultimate tensile strength can be monitored using microhardness measurements on TEM specimens.

V. ACCOMPLISHMENTS AND STATUS

A. RTNS-II Irradiation Program Plan - R. W. Powell and N. F. Panayotou (HEDL), G. R. Odette and G. E. Lucas (UCSS)

1. Introduction

The RTNS-II located at the Lawrence Livermore Laboratory will be used to study the effects of high energy neutron (14 MeV) damage on material properties. An understanding of the primary damage state, subsequent microstructure evolution, and the resultant mechanical behavior is important in developing the capability of projecting fission reactor data to fusion reactor environments. HEDL plans to address each of these areas in its experimentation at RTNS-II. In addition, selective Be(d,n) irradiations will be performed at UC-Davis and fission reactor irradiations will be done at the Livermore Pool-Type Reactor (LPTR) to assess the spectral sensitivity of radiation-induced effects.

2. Selection of Materials

The pure metals chosen for RTNS-II experiments are listed in Table 1. The effects of crystal structure, atomic weight, and stacking fault energy on the primary damage state, subsequent microstructure evolution, and resultant changes in mechanical behavior will be examined with these materials. All of the pure metals listed in Table 1 have a direct tie to the Alloy Development for Irradiation Performance (ADIP) program materials.

TABLE 1

PURE METALS FOR RTNS-II IRRADIATIONS

Metal	Characteristics*
Ni	FCC, Mid-A, High SFE
cu	FCC, Mid-A, Low SFE
Ti	HCP, Mid-A
V	BCC, Mid-A
Nb	BCC, High-A

* FCC = face centered cubic crystal structure
HCP = hexagonal close packed crystal structure
ECC = body centered cubic crystal structure
A = atomic weight
SFE = stacking fault energy

Nickel and copper are similar to the ADIP Fe-Ni-Cr Path A (austenitic) and B (high strength) alloys. Both have the face-centered cubic (FCC) crystal structure and both have atomic weights near those of the main constituents. The stacking fault energy (SFE) of nickel, however, is considerably higher than that of the alloys, while copper has a more representative value. The SFE should affect the driving force for cascade collapse into a vacancy dislocation loop.

Titanium, vanadium and niobium are similar to the Path C (reactive and refractory) materials. Comparison of the FCC metals with the hexagonal close packed (HCP) titanium and body centered cubic (BCC) vanadium should elucidate the effects of crystal structure since all have similar atomic weights. Vanadium (BCC) and niobium (BCC) comparisons will illustrate the effects of atomic weight. Each of these three metals serves as the base component of a set of ADIP Path C alloys.

The alloys chosen for RTNS-II experiments are listed in Table 2 and span the range from simple binaries to complex commercial purity alloys. The first set of binaries is intended to study the effects of solute characteristics on replacement sequence length. The solute characteristics chosen for study were derived from cascade evolution models which predict a decrease in replacement sequence length for local disturbances of the lattice. The effects of a difference in atomic weight between the solute and matrix atoms, as well as a difference in atomic size, hence lattice strain, will be studied. Solute additions for this series, except for carbon, are at the 5 atomic percent level whick is within the normal single phase region of each alloy and provides approximately two solute atoms within the first three nearest neighbor shells of each solvent atom. A carbon level of 0.05 wt.% was chosen to study the effect of interstitia1 inpurities.

As an example of the solute characteristics under study, consider the three nickel-base binaries with additions of Si, Al, or Zn. Comparison of the Si and Al additions will be used to study the relative effectiveness of positive and negative atomic misfits in replacement sequence lengths; both additions are lower in atomic weight than the base metal but Si contracts the lattice while Al expands the lattice. Atomic weight effects will be studied with Ni + 5% Al and Ni + 5% Zn. Al and Zn both expand the lattice approximately the same amount but have significantly different atomic weights.

Other phenomena being studied with simple alloys include phase stability and helium effects, and their projection to simple ternary and quaternary alloys. Ni_3Si precipitation in the Ni + 5% Si and Ni + 8% Si alloys will be used to study free defect production in different spectra. Free defect production, through enhanced diffusivity, should influence the observance of a low temperature miscibility gap in the Cu + 50% Ni alloy; this transformation will be monitored with a magnetometer since the phase separation will produce a ferromagnetic phase.

TABLE

ALLOYS FOR RTNS-II TIONS

	Alloy	Comments
Replacement Sequence Series	Cu + Al(5%)	Al: Low-A, expands lattice
	Cu + Zn(5%)	Zn: Mid A expands lattice
	Cu + Ni(5%)	Ni: Mid A contracts lattice
	Ni + Si(5%)	Si: Low-A, contracts lattice
	Ni + Al(5%)	Al: Low-A expands lattice
	Ni + Zn(5%)	Zn: Mid-A, expands lattice
	* Ni + C (.05%)	C: Interstitial impurity
Free Defect Production/Phase Stability	Ni + Si(5%)	Displacement rate effect on γ' formation
	Ni + Si(8%)	
	Cu + Ni(50%)	Low T miscibility gap
Helium Production	* Ni + C(1%)	Helium from C(n, 3α)
High Dose Correlation	*Fe-20Ni-15Cr	Mo: High A addition
	*Fe-20Ni-15Cr-2Mo	
	MFE 316	
	Path A	ADIP materials
	Path B	

* ition in wt

The Ni + 1% C alloy will be used to test the feasibility of studying the effects of spatially inhomogeneous helium generation at RTNS-II; carbon has a high helium generation cross section for 14 MeV neutrons.

The ternary and quaternary alloys will serve two main purposes. First, the comparison between the two alloys will serve to elucidate the effect of the heavy element molybdenum on replacement sequences in this system. Second, they will serve as low dose-high dose correlation materials to link the more complex alloys to EBR-II/ORR/FMIT experiments. The complex alloys included in the RTNS-II experiments were drawn directly from the ADIP materials stockpile for Paths A and B.

3. Evaluation of Techniques

The objective of a significant portion of the early experiments will be to evaluate the utility of various techniques and combinations of techniques for characterizing the primary damage state, microstructural evolution, and mechanical behavior in miniature specimens. The major techniques will be conventional transmission electron microscopy (TEM) and microhardness, but these will be combined with various postirradiation annealing schedules and other test techniques. Under examination are ultra-high resolution TEM, small wire tensile tests, x-ray diffuse scattering, and positron annihilation.

Conventional TEM will be used to characterize the majority of the high energy neutron induced microstructure. This technique has the capability of detecting defect clusters as small as 1.0-1.5 nm in diameter; it has the advantage of revealing spatial distributions. Selected post-irradiation anneals will supplement these measurements with indirect information on clusters smaller than the detectable limit as well as aiding the identification of cluster type. Scoping studies are currently underway to assess the application of ultra-high resolution TEM techniques such as lattice fringe imaging to the detection of clusters smaller than the conventional limit.

Microhardness measurements will serve two primary purposes. First, they will aid in characterizing the effect of high energy neutrons on mechanical properties (primarily the ultimate tensile strength) and, in conjunction with TEM, will be used to relate mechanical behavior to the high energy neutron induced microstructure. Second, the measurements will be used to guide the disposition of irradiated specimens. Since measurements are rapid and quasi-non-destructive, microhardness will be used as an indicator of when to perform TEM examination and when to re-irradiate.

Scoping experiments will be conducted which combine microhardness measurements with various postirradiation annealing schedules to assess their utility. Both isochronal and isothermal anneals will be performed to determine the activation energies of the recovery processes. Such data will be valuable in Characterizing the properties of tne defect clusters and the spectral sensitivity of these properties. Hot microhardness will be used to test at the irradiation temperature, and scoping studies will be performed to assess its application to recovery studies.

Small diameter wire tensile tests will be selectively performed to provide more information on mechanical behavior; it is anticipated that microhardness data will guide these tests.

Specimens will be included in RTNS-II irradiations to provide for x-ray diffuse scattering studies and positron annihilation measurements. The application of these techniques to radiation damage studies has not been fully deiiionstrated but the possibility of providing supplemental data to TEM examination should be pursued.

4. General Test Matrix

The overall HEDL RTNS-II test matrix is given in Table 3. A range of fluences will be obtained for each of three relative tenperatures. In addition to the fluences shown, fluences as low as 3 x 10^{16} n/cm^2 will be obtained by positioning specimens near the back of holders scheduled for

1 x 10^{18} n/cm^2. The maximum fluences shown in the table correspond to approximately three months of peak flux (1 x 10^{13} n/cm^2-sec) irradiation and approximately 0.1 dpa in AISI 316. This will provide comparisons with specimens irradiated to approximately 0.3 dpa in the ORR/MFE-I experiment. Higher RTNS-II fluences will be obtained if irradiation time is available.

TABLE 3

HEDL RTNS-II TEST MATRIX

	Fluence, n/cm^2			
Temperature	1 x 10^{18}	3 x 10^{18}	1 x 10^{18}	3-5 x 10^{19}
R.T.	X	X	X	
(0.3)T_m	X	X	X	X
(0.45)T_m	X	X	X	X

The temperatures shown in Table 3 are relative to the melting point (T_m) of each material and therefore represent more than three irradiation temperatures. Table 4 groups the materials into five irradiation temperatures. All materials will be irradiated at room temperature (this may be elevated to the 65°C ambient temperature of LPTR) and at approximately 0.3 T_m. The highest irradiation temperature for each material except Nb is at approximately 0.45 T_m; due to the high melting point of Nb, there are no current plans to irradiate this metal at an equivalent relative temperature (975°C).

TABLE 4

IRRADIATION TEMPERATURES FOR RTNS-II EXPERIMENTS

R.T.	150°C	250°C	350°C	550°C
All materials	Cu-Type	Ni-Type	V-Type Cu-Type Ti-Type	Ni-Type V-Type Ti-Type Nb-Type

5. Schedule

The test iiiatrix outlined in the previous section obviously represents more than one year's effort. Much of that iiiatrix is subject to modification as experience is gained with RTNS-II and as incremental data are obtained and analyzed.

Initial operation of the RTNS-II is with the small RTNS-II targets; the resulting neutron flux is between that of RTNS-I and the goal flux of RTNS-II. The initial HEDL experiments will emphasize the lower fluence primary damage objectives and will be limited to peak, fluences of 1×10^{13} n/cm^2. Major emphasis will be on room temperature irradiations and exploring the utility of 150°C irradiations. These near-term objectives are fully compatible with small target operation at. RTNS-II. It. is presently planned to reserve experiments at higher temperatures and higher fluences for large target ooeration.

B. RTNS-II Irradiation Program Status - N. F. Panayotou and R. W Powell (HEDL)

1. Specimen Preparation

A total of thirteen metals and alloy!; are currently available for irradiation at RTNS-II. Sheet stock (0.010 inch thick) of copper, nickel, titanium and niobium was obtained froin A. D. Mackay Inc. Wire and rod stock of these metals prepared froni identical lots was also obtained for use by Battelle-Pacific Northwest Laboratories (PNL) and Lawrence Livermore Laboratories, as well as HEDL. Except for copper, all pure metals were received in the as-cold-worked condition.

A quaternary alloy was arc melted at. PNL using a ternary alloy (Fe-Ni-Cr) as a base and with a nominal addition of 2.0 wt. percent Mo. A ctieiiiical overcheck indicated that the alloying procedure was indeed successful.

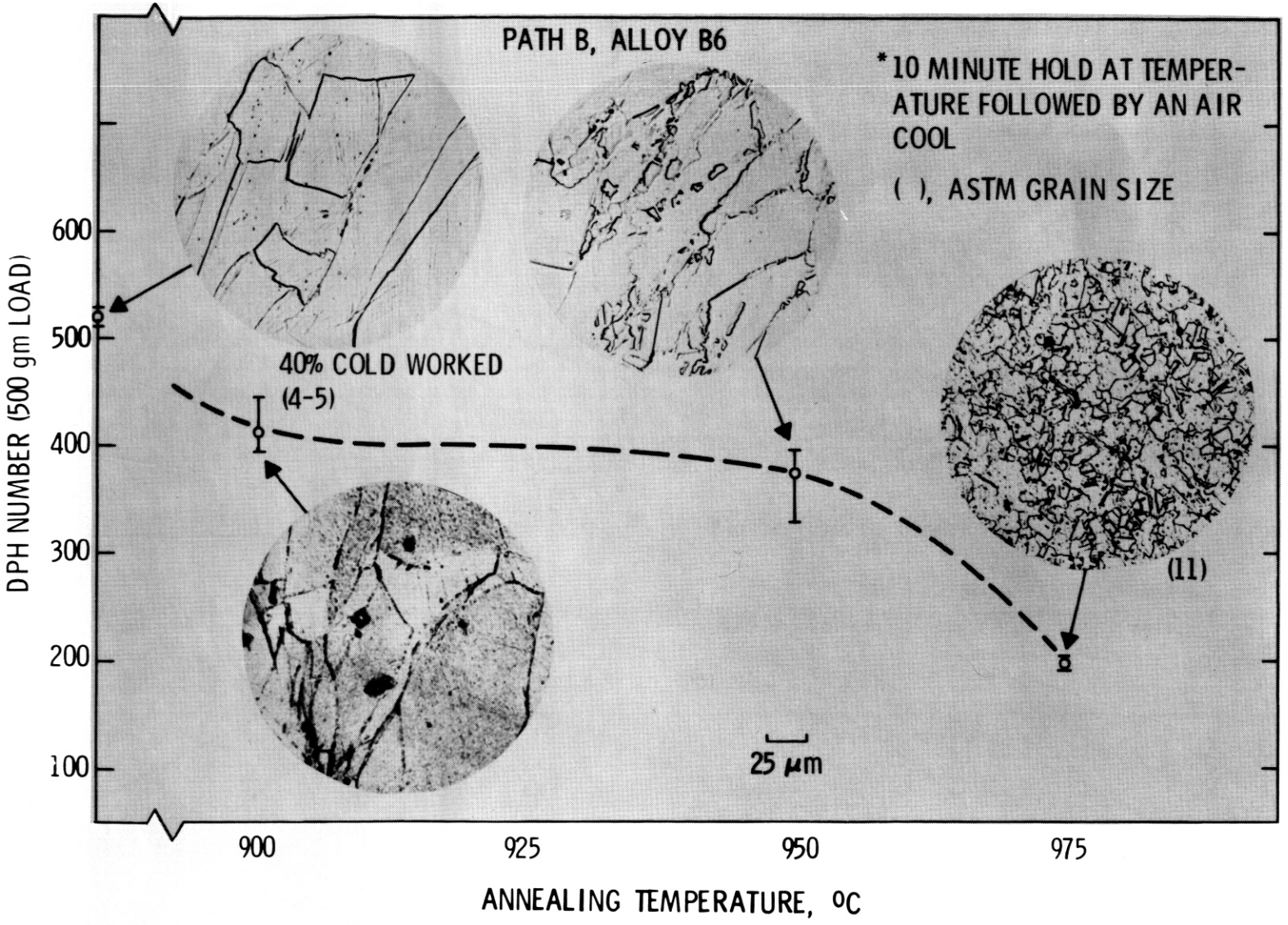

HEDL 7904-021.2

FIGURE 1. Determination of Initial Heat Treatment Specifications*

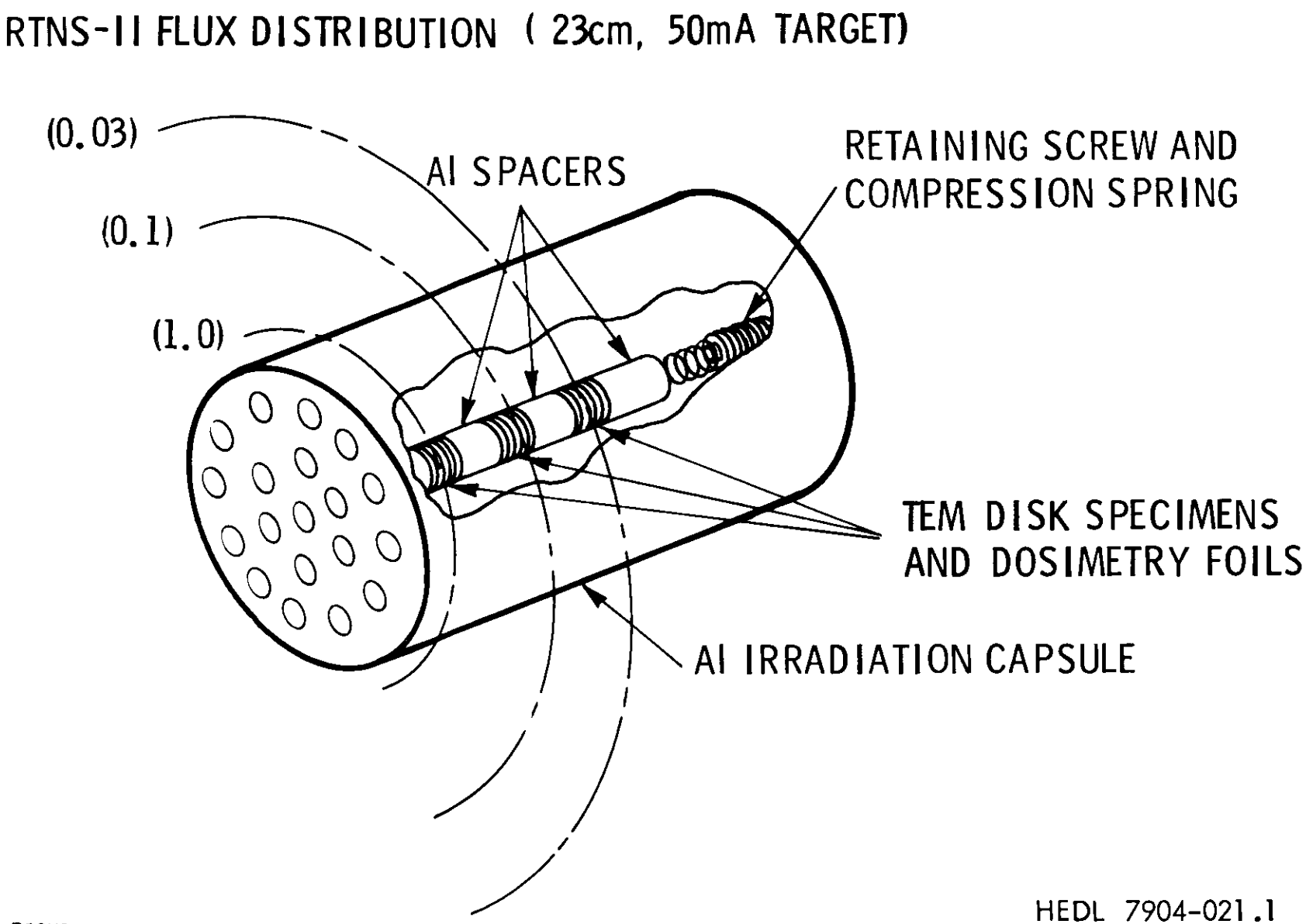

FIGURE 2. HEDL Room Temperature Irradiation Package

Two Path A and five Path B alloys were obtained from E. E. Bloom of ORNL. The quaternary and all Path A and Path B alloys were mechanically processed at PNL to a nominal, final, 40 percent cold worked level. Prior to mechanical processing Path B alloys were encapsulated in quartz (1/3 atm. argon) and heat treated for 30 minutes at 1149°C. The mechanical processing included forging as well as both hot and cold rolling. Forging and hot rolling were performed in air at 1010°C. Ouring cold rolling, intermediate anneals, 10 minutes at 1010°C with an air cool, were utilized. Below a thickness of 0.030 inches annealing was accomplished with the stock encapsulated' in quartz vials (1/3 atm. argon). After processing, the nominal thickness of the sheet stock was 0.014 inches.

TEM disks, 3 mm in diameter, were punched from the as-received pure metals and as-rolled alloys. The disks were deburred and permanently laser engraved using the standard HEDL engraving format.

An initial set of heat treatments was established for all metals and alloys using both microhardness results and metallographic examinations. The object was to produce a recrystallized, fine-grained structure. A fine grain size yields better microhardness statistics since more grains are sampled per indent. It is also important for miniature tensile specimens (0.010 in. gage section diameter). In each case the heat treatment was selected to be at least 0.45 T_m. It was determined that grain sizes in the range of ASTM 7-8 (25-35μm) or smaller could be obtained. An example *of* the data obtained by this method is shown in Figure 1.

2. Irradiation Hardware

Hardware for the irradiation of TEM disk specimens at RTNS-II has been fabricated. Aluminum and titanium specimen holders (low activation materials) are available for ambient and high temperature irradiations. The room temperature RTNS-II TEM disk holder is shown in Figure 2. Aluminum spacers are used to separate specimens into groups within which flux/fluence variations are about a factor of two. Specimens, spacers and Nb dosimetry

foils are held securely in place by compression springs and retaining screws. The flux distribution is also shown schematically in Figure 2 for the current RTNS-II source (23 cm, 50mA). Assuming a Gaussian beam profile with a 1 cm FWHM and a source strength of 1 x 10^{13} n/s, a range in flux/fluence of a factor of 30 can be obtained with this specimen holder. Initial experiments will accumulate a peak fluence of 1 x 10^{18} n/cm^2.

3. Hardness Testing

Preliminary microhardness tests at temperature (25-700°C) have been performed with a Nikon Hot Hardness instrument. The capabilities of this unique instrument include an inert testing environment, test temperatures of 25-1600°C, fast quench rates, and variable loads and time at maximum load.

Test procedures for hardness testing of TEM disk specimens have been specified including the use of a Vickers (Diamond Pyramid) type indentor. This type of indentor and the minimum machine load available (50 gm) were found to be the best compromise between the desire to obtain bulk hardness values and the need to limit the depth of the indentor penetration into the thin specimens. It has been found that changes in strength of only several ksi should be resolvable by this technique.

Microhardness can be used to monitor changes in mechanical properties due to neutron irradiation. Hardness values obtained for several different forms of AISI 316 stainless steel as a function of temperature are given in Figure 3. Using an empirical correlation, these results were used to predict the ultimate tensile strength of 316 as a function of temperature. A comparison of the predicted and actual strength values is shown in Figure 4. While the agreement is not perfect, it is clear that hot hardness can be used to monitor changes in mechanical properties. The effectsof variables such as surface finish maximum load, and time at maximum load on hardness values have also been examined.

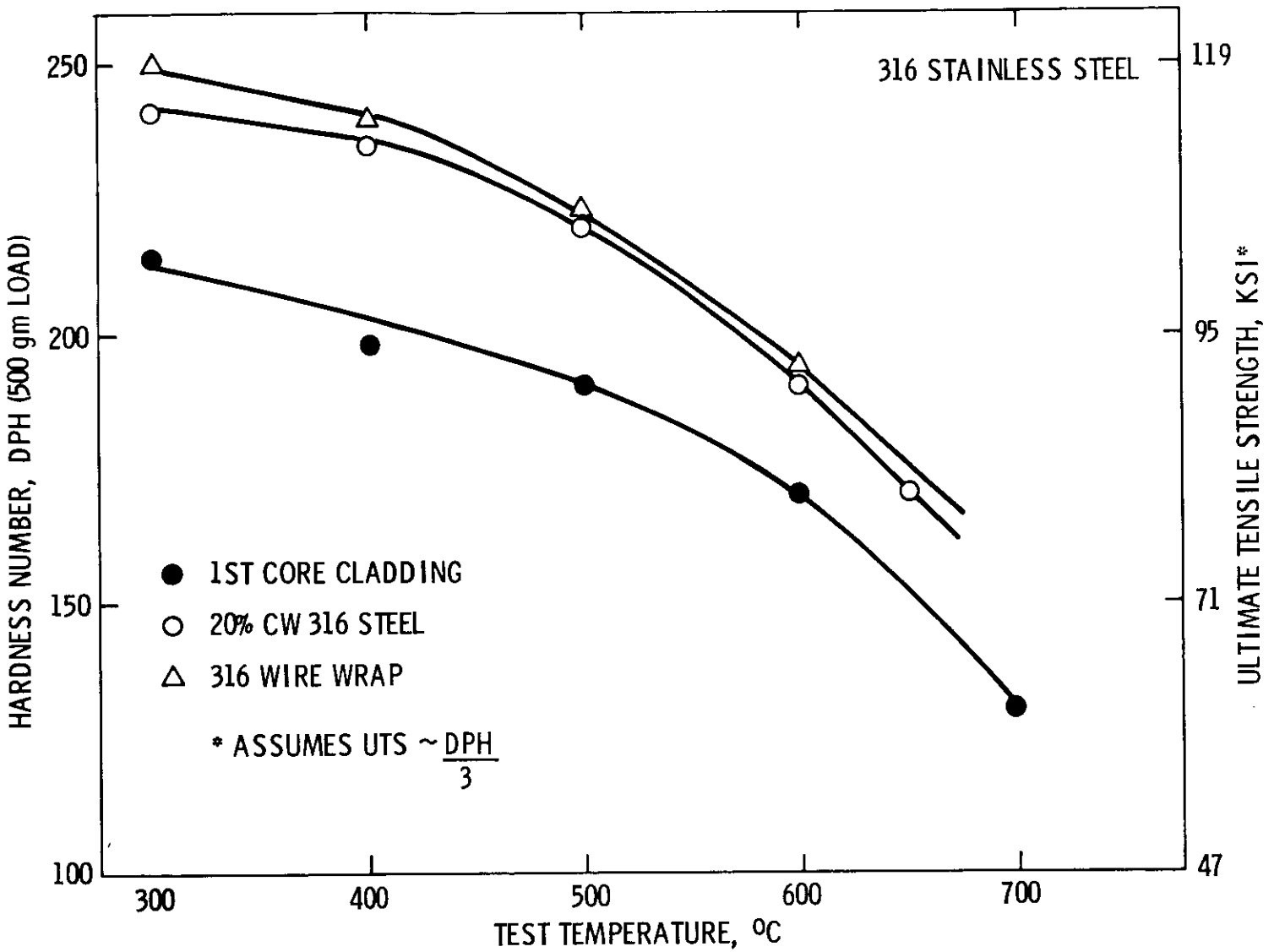

HEDL 7903-212.9

FIGURE 3. Hot Micro Hardness Results

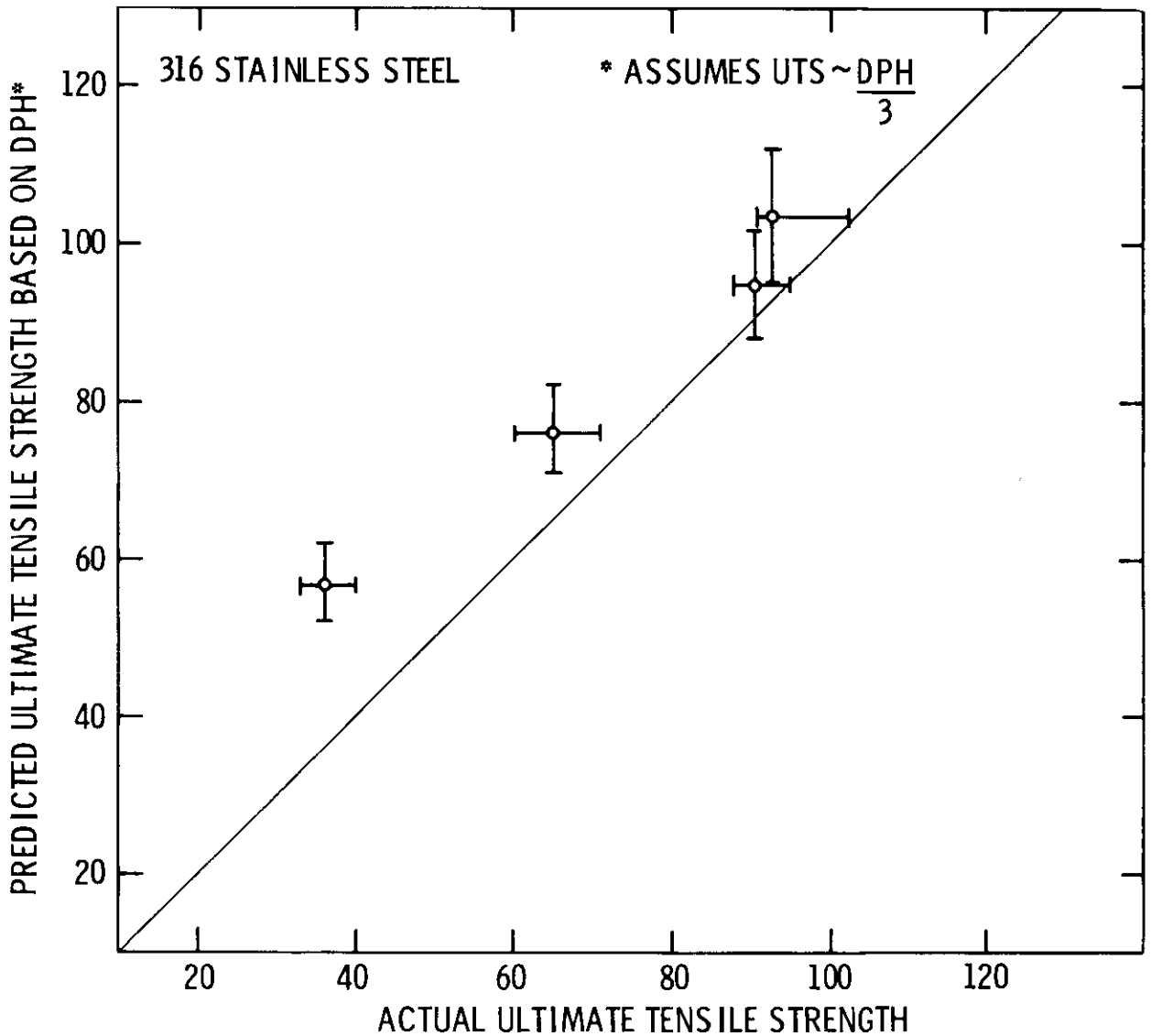

FIGURE 4. Comparison of Predicted and Actual Ultimate Tensile Strength.

VI. REFERENCES

None.

VII. FUTURE WORK

A holder for disk specimens for use in the Livermore Pool Type Reactor (LPTR) and a holder for miniature tensile specimens for use at RTNS-II have been designed and will be fabricated during the next quarter.

At least one room temperature irradiation at RTNS-II is planned for the next quarter and specimen examination will begin.

The determination of baseline microhardness data on archive specimens of pure metals and alloys will continue.

A collaborative effort with UCSB, directed at optimum utilization of RTNS-II, has been initiated.

CHAPTER 5

SUBTASK C: DAMAGE MICROSTRUCTURE EVOLUTION AND MECHANICAL BEHAVIOR

I. PROGRAM

Title: Irradiation Response of Materials
Principal Investigators: J. A. Spitznagel, W. J. Choyke, S. Wood
Affiliation: Westinghouse Research and Development Center

II. OBJECTIVE

The objective of this work is to assess the phenomenology and mechanisms of microstructural evolution in materials exposed to simultaneous helium injection and creation of atomic displacement damage by a second ion beam.

III. RELEVANT DAFS PROGRAM TASK/SUBTASK

SUBTASK II.C.1, II.C.2, II.C.3, II.C.5, II.C.9, II.C.18

IV. SUMMARY

A regime of rapid cavity growth was observed in solution annealed MFE 316 SS. Increasing the dislocation density by cold work prior to bombardment, and increasing the appm He/dpa ratio was observed to suppress the rapid growth. Dual-ion bombardments with periodic interruptions in the helium beam were conducted in an attempt to separate the effects of He on cavity nucleation and growth. MFE 316 SS specimens aged at 800°C to precipitate $M_{23}C_6$ carbides were bombarded under similar conditions at the Univ. of Pittsburgh and ANL Dual-Ion Facilities.

A high vacuum system and a high resolution mass spectrometer have been installed as part of the dual-ion beam sample assembly of the HEIBS (Univ. of Pittsburgh) facility. This new capability should make dual ion beam experiments of refractory metals possible within reasonable constraints. Examination of the effects of known quantities of H_2, CO, etc.

on the microstructure during dual ion bombardment will be undertaken in coming months.

V. ACCOMPLISHMENTS AND STATUS

A. Effect of Irradiation Temperature, and Time/Temperature History of Helium Doping and Atomic Displacement Damage on Microstructural Evolution in Solution Annealed, 20% Cold Worked and Aged MFE 316 SS.

It has been suggested[1] that the growth of cavities, under conditions where helium is introduced simultaneously with atomic displacement damage produced by fast neutrons or charged particles, may proceed very rapidly under certain "critical" conditions. Clearly it is important to determine whether such rapid swelling will occur in first wall and blanket structural components at helium generation and atomic displacement rates projected for current Tokamak designs.

Recent neutron irradiation data from a mixed-spectrum fission reactor (HFIR - High Flux Isotope Reactor at Oak Ridge National Laboratory) study has indicated that for appm helium/dpa ratios of $\sim$70[2], rapid growth of large cavities on grain boundaries and certain precipitate/matrix interfaces in 316 SS can occur at temperatures above 650°C.

We have previously reported dual-ion irradiation data which indicated a very rapid growth of selected cavities in solution-annealed type 316 SS from the MFE heat[3]. At a bombardment temperature of $\sim$650°C, simultaneous bombardment with 2 MeV He and 28 MeV Si^{+6} ions at a damage rate of $\sim 1 \times 10^{-4}$ dpa/s to damage levels $\sim$2 dpa resulted in cavities as large as 100 nm. In this quarter we have repeated several of these experiments to verify the results. Furthermore, the appm He/dpa ratio and the time/temperature history of the helium doping and atomic displacement damage have been varied to study the sensitivity of the rapid growth regime to the experimental parameters.

Because the individual ion beams can be varied independently, it is most helpful to describe the experiments pictorially by means of "vector" diagrams. In Fig. 1, for example, the diagram indicates that the helium and high energy ion beams coimpinged on the target for ~7.25 hours. Fig. 3 shows a case where helium was first implanted for 7.25 hours and then, with the He beam shut off, atomic displacement damage was produced for 7.25 hours with the 28 MeV Si^{+6} beam. Recent experiments have involved rather complex beam schedules, Fig. 9, in an attempt to separate nucleation and growth aspects of the observed microstructural evolution. In every case the ordinate represents some measure of accumulated exposure (helium concentration, deposited damage energy, dpa level etc.) and the abscissa the time which has elapsed since an ion beam first impinged upon the target. We will use a combination of the vector diagrams and selected micrographs to illustrate the rapid swelling regime.

For the solution annealed 316 SS targets (1050°C - 0.5 hours) rapid cavity growth and coalescence occur near ~600°C under dual-ion bombardment; as shown in Fig. 1, the voidage produced at fluences as low as 2 dpa is extremely large. Careful stereomicroscopy has revealed that the porosity is indeed contained within the foil and is not a surface artifact introduced during preparation of the target for TEM examination. The complex shapes resulting from cavity coalescence preclude accurate measurement of the void volume fraction using conventional particle-size analysis techniques. The voidage is interwoven with faulted dislocation loops and dislocation tangles. Decreasing the amount of helium from 88 appm to 18 appm (and the appm He/dpa ratio from ~44 to ~7.5) increased the tendency for this "explosive" cavity growth, Fig. 2. A very pronounced void alignment in <110> directions is observed which results in a 3-dimensional dendritic structure. The void volume is much too large to have resulted from coalescence of near-equilibrium helium bubbles and the complex shapes indicate that minimization of surface energy is far from complete. A background of very small cavities, which could be equilibrium bubbles, can be seen interspersed between the "arms" of the dendritic web.

Preimplanting the helium at 600°C over 7.25 hours followed by heavy ion bombardment for 7.25 hours resulted in less cavity growth and coalescence, Fig. 3. The swelling is still much larger than that observed at 550°C or 650°C for elevated temperature preimplantation as reported previously[3]. Thus rapid cavity growth and coalescence in the solution annealed 316 SS is apparently more sensitive to variations in bombardment temperature (and perhaps in damage rate) than to variations in appm He/dpa ratio or mode of helium implantation.

An interesting feature observed in specimens which show void alignment is radiation-induced precipitation, Fig. 3. Oark field imaging using satellite reflections reveals both precipitates and faulted dislocation loops. The precipitation which appears to be associated with the cavities occurs on a very fine scale and no positive phase identification has yet been possible.

The void alignment observed at 600°C for the solution annealed specimens is easily seen in the low magnification micrograph in Fig. 4. This void ordering has been observed at damage levels of 2-7.5 dpa (and up to 100 appm He) in solution annealed specimens bombarded simultaneously or sequentially at 600°C although no evidence of a void lattice is apparent. The voids are large and are aligned in the <110> directions which, for $z \sim [100]$ is the trace of the {111} planes.

To date, void arrays have not been reported in either neutron or ion-irradiated 316 SS, but they have been observed in other fcc metals, namely Al^+ bombarded aluminum[4] ($\leq$80 dpa, 50 and 75°C) and N_2^+ bombarded Ni-Al solid solutions[5] (10-70 dpa, 500°C) and in several bcc metals (e.g. Mo, Ta). In many instances, with the exception of aluminum, the void alignment appears to be contingent upon the presence of impurities. Ordering was not observed in pure Ni, for example, but was present in Ni-Al solid solutions, up to 8 wt.% Al[5]. Ion-irradiated Ta (3.2 Mev Ni ions, 55-78 dpa above 1120°k) doped with 2300 ppm oxygen developed

void arrays whereas a dopant level of 400 ppm oxygen produced no alignment[6] Thus, it has been suggested that the elastic interaction between voids is the mechanism for the stability of the void lattice and that this elastic interaction arises from solute segregation around voids. Furthermore, solute segregation enhances the tendency for cavities to nucleate non-randomly in the presence of existing cavities, since nucleation will occur preferentially in those regions of average solute concentration. As mentioned earlier, the behavior of aluminum does not seem to conform to the general pattern since less tendency for void array formation was observed in commercial purity than high purity material[4]. It should also be noted that ordering has been observed in pure Ni, but at much higher damage levels (360-480 dpa, 525°C, 5-6 MeV nickel ions and 6-11 MeV selenium ions).

To summarize, the literature suggests that the .formation of void arrays or the development of void alignment is contingent upon impurity content, damage level, temperature and material. For most of the 316 SS samples exhibiting void alignment, precipitation was also evident around the void peripheries (Fig. 3). Thus, it is possible that solute segregation has influenced cavity nucleation in this material. A second possibility is that, since the voids are large and aggregated, the alignment is due *to* coarsening, similar to the effect observed due to precipitate coarsening.

Rapid cavity growth and coalescence were greatly reduced by raising the helium injection rate to $\sim 1.1 \times 10^{-2}$ appm/s resulting in an appm He/dpa ratio of ~60, Fig. 5. The bimodal cavity size distribution with a high number density of barely resolvable cavities suggests that cavity growth is a very selective process and argues forcefully for the concept of a transition from slow bubble growth to rapid void growth once some "critical" bubble size is reached. The importance of the higher displacement rate on cavity growth for the experiment depicted in Fig. 5 is not known at present.

The conditions of damage rate and helium injection rate which resulted in rapid cavity growth and aggregation at 600°C produced only a low no. density of small cavities tied to acicular precipitates at 650°C, Fig. 6. We had previously indicated that the rapid growth regime might extend to 650°C[3], but additional experiments have shown that this is not true. In fact, the rapid growth regime seems to be bracketed by a fairly narrow range of bombardment temperatures for the conditions of these experiments. Additional ion bombardment experiments have been conducted at smaller temperature intervals, Fig. 10b, to better define the rapid growth regime. In addition, experiments have been run with lower target chamber pressures ($\leq 6.65 \times 10^{-6}$ N/m^2) to determine whether void alignment is related to impurity pickup during bombardment. Target chamber pressure was 4.7×10^{-5} N/m^2 for the experiments where rapid void growth has been observed. TEM analysis of these results is continuing.

Although no mechanical property measurements have as yet been performed on these ion-bombarded foils, it is likely that the development of microstructures such as those shown in Figs. 1-4 will have a deleterious effect on tensile ductility, fatigue life and fracture toughness. Thus it is important to study the phenomenology and determine the mechanisms responsible for the rapid cavity growth regime. In particular, the "scaling" of the phenomena in terms of damage rate, temperature appm He/dpa ratio, helium level and fluence must be established. The sensitivity of the phenomena to pre-irradiation microstructure must also be studied in detail.

Increasing the pre-irradiation dislocation density by cold-rolling the annealed strip to produce a 20% reduction in thickness prior to ion bombardment, apparently suppresses rapid cavity growth under the conditions of these experiments. Bimodal cavity size distributions with selective growth of a few cavities have been observed after dual-ion bombardment at 650°C, Fig. 7. However no cavities were visible after

bombardment at 600°C and only a few small cavities which were associated with acicular precipitates could be seen after bombardment at 700°C, Fig. 8.

One of the key questions to be addressed concerns the role of helium in promoting bubble nucleation and cavity growth. In an attempt to separate the effects of helium on nucleation and growth of cavities, dislocation loops and precipitates we have initiated a series of experiments in this quarter where the helium implantation is interrupted during dual-ion bombardment. A few of these experiments are illustrated by means of "vector" diagrams in Fig. 9. In addition, experiments involving continuous coimplantation but step-wise changes in target temperature during bombardment were begun during this quarter. Unfortunately no adequate theoretical framework or model exists for comprehensively analyzing such experiments. Similar experiments on 304 SS in a non-DoE funded effort, however, have provided useful information on the relative influence of helium on cavity nucleation and growth processes at high (65-300) appm helium/dpa ratios.

A series of dual-ion bombardments on MFE 316 SS aged at 800°C to precipitate $M_{23}C_6$ carbides prior to bombardment was also conducted in this quarter, Fig. 10a. The experimental parameters were selected to permit comparison with similar experiments conducted at Argonne National Laboratory on the same material. TEM examination is in progress.

B. Installation of High Resolution Mass Spectrometer for Studies of Vacuum Ambient Effects on Microstructural Evolution in Dual-Ion Bombarded Refractory Alloys

At the beginning of 1978 it was decided that the HEIBS dual ion beam facility should be prepared for the study of refractory metals such as vanadium and niobium - base alloys.

It is usually assumed that studies on these materials at elevated temperatures should be conducted in as excellent a vacuum environment as possible. Thus, two options were available:

(i) Install a totally bakeable true ultra-high vacuum system with capability of $<1.3 \times 10^{-7}$ N/m^2 near the sample. This would have required a total rebuilding of the facility since it would have required elaborate differential pumping on both the high energy heavy ion beam line and the He beam line. Such an undertaking would have been very costly in capital equipment and time.

(ii) A more pragmatic alternative was to rebuild the dual-ion-beam sample chamber complex in such a way that very good vacuums could be achieved near the sample ($<6.65 \times 10^{-6}$ N/m^2) and in addition a quadrupole mass spectrometer would be used to identify the remaining or intentionally added gas species during bombardments. This approach had the virtue of considerably lower cost in equipment and time and was the one selected. In any case, until experiment shows that radiation damage experiments with certain refractory metals truly require vacuums of 1.3×10^{-6} N/m^2 or better this intermediate solution has much to recommend it.

Figure 11 is an overview of the new dual-ion beam sample chamber complex. The main features of the new system are the installation of two turbo molecular pumps (Turbovac 450) on either side of the sample furnace assembly, a totally metal gasketed sample chamber, and a high resolution quadrupole mass spectrometer.

Figure 12 gives a detailed look at the new sample chamber assembly. The chamber now has visual access at 90° and 180". Ceramic insulators provide better than $10^{10}\Omega$ insulation from ground making reliable ion-beam measurements possible while at the same time providing "feed back" power to the "internal" and "external" sample furnace. Adjustments for thermocouple contact pressure on the sample mount is made possible by a small metal bellows. The sample is very simply removed from the assembly by breaking a single copper seal. Access to the high resolution mass spectrometer is attained through the 270" port.

Figure 13 shows the quadrupole mass spectrometer and its associated

electronics. As seen on the figure a shutter is inserted between the sample chamber and the axial ionizer. In fact, when the shutter is removed the axis of the ionizer bisects the front surface of the sample in the exact position used for dual ion bombardment. The Extranuclear Laboratories mass spectrometer is not too difficult to calibrate and convenient to operate. One can obtain a display on the screen shown in Figure 13 or record the results on a recorder which is not shown.

Finally, in Fig. 14 results are presented of the mass scans attainable with our new system. At low resolution it is convenient to scan from AMU 1 to AMU 60. Such a spectrum can be photographed from the oscilloscope screen and gives a rough measure of the sample ambient atmosphere. The measurement was taken at 2.7 x 10^{-5} N/m^2 Torr total pressure which gives some indication of the excellent sensitivity of this instrument. For more careful analysis the high resolution mode is appropriate. In this case, the output signal is recorded on chart paper. As can be seen in Figure 14, The CHO and C_2H_5 peaks are only separated by 0.026 mass units and yet are readily resolved.

VI. REFERENCES

1. M. R. Hayns, M. H. Wood and R. Bullough, J. Nucl. Mater. 75, 241 (1978).

2. P. J. Maziasz and E. E. Bloom, ADIP Quarterly Progress Report No. 1, p. 40, March (1978), DOE/ET-0058/1.

3. J. A. Spitznagel and W. J. Choyke, DAFS Quarterly Report No. 4, October-December (1978). DOE/ET-0065/4.

4. D. J. Mazey et. al., J. Nuc. Matls. 47 (1973) p. 137.

5. L. J. Chen and A. J. Ardell, J. Nuc. Matls. 75 (1978) p. 177.

6. B. A. Loomis and S. B. Gerber, J. Nuc. Matls. 71 (1978) p. 377.

VII. FUTURE WORK

TEM analysis of interrupted helium beam and temperature change experiments will be continued. Targets of MFE 316 SS in the solution annealed condition will be bombarded at lower damage rates (10^{-6} - 10^{-5} dpa/s) at various appm He/dpa ratios to determine whether the theoretically predicted rapid void growth regime occurs at the lower atomic displacement rates. TEM observations on aged and dual-ion bombarded MFE 316 SS will be compared with ANL results on the same material.

Vanadium alloy target materials will be obtained from the fusion reactor materials inventory at Oak Ridge National Laboratory. Targets will be fabricated and studies initiated to determine the effects of the vacuum ambient (different partial pressure of H, CO, etc.) on microstructural evolution under dual-ion irradiation.

VIII. PUBLICATIONS

None

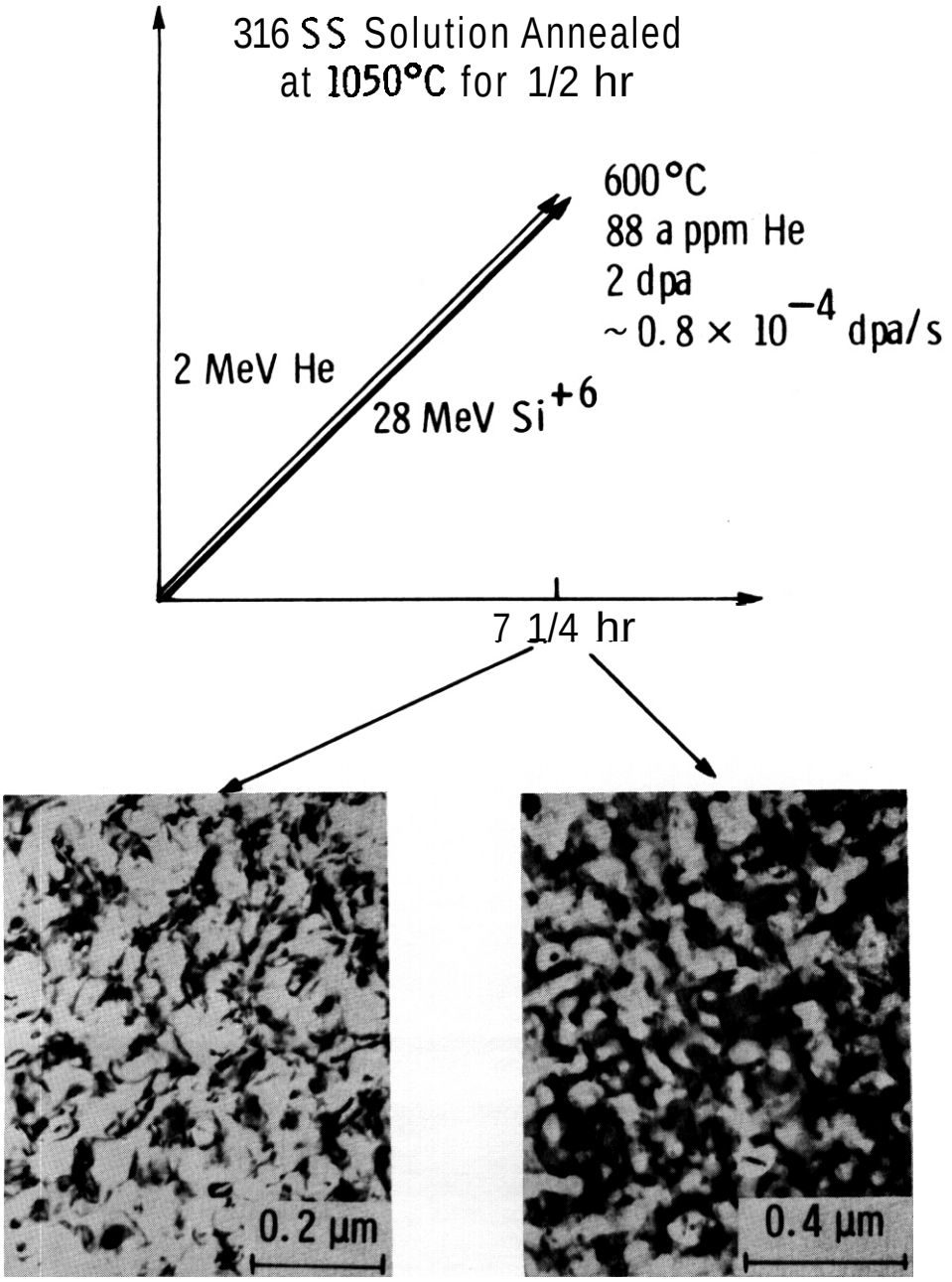

FIGURE 1. Effect of Simultaneous Bombardment on the Void and Dislocation Structures in Solution Annealed 316 SS.

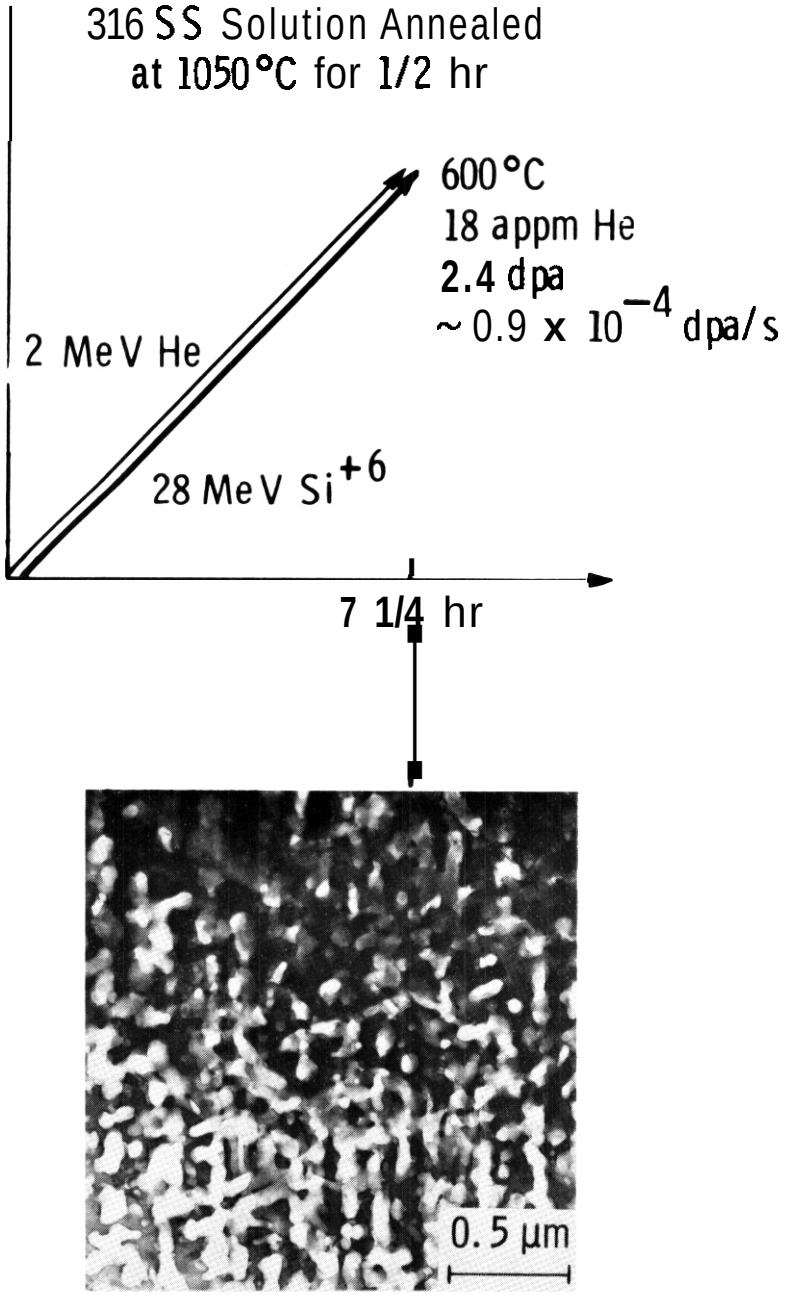

FIGURE 2. Void Alignment in Simultaneously Bombarded Solution Annealed 316 SS.

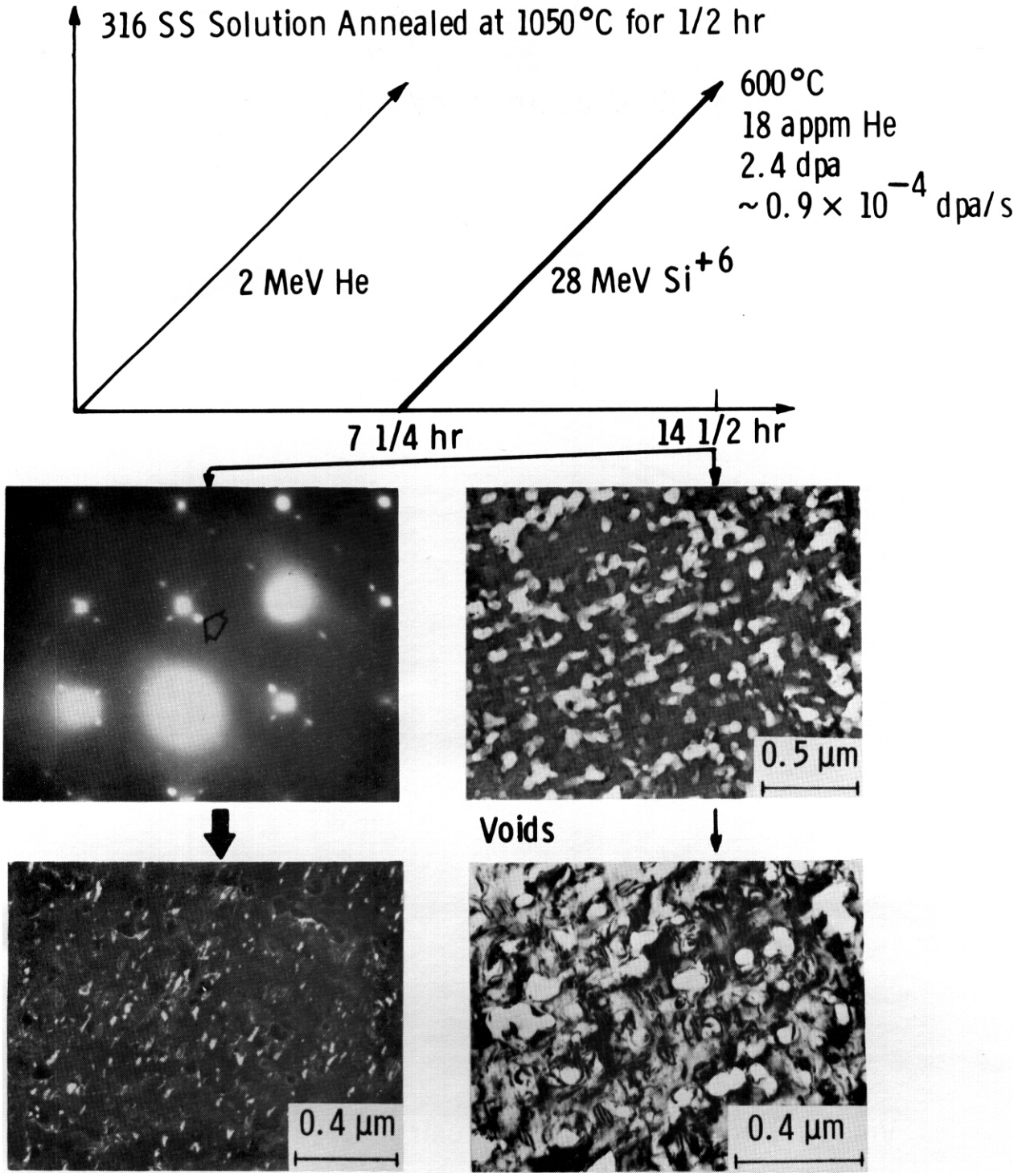

FIGURE 3. Microstructural Changes Induced by Sequential Bombardment of Solution Annealed 316 SS.

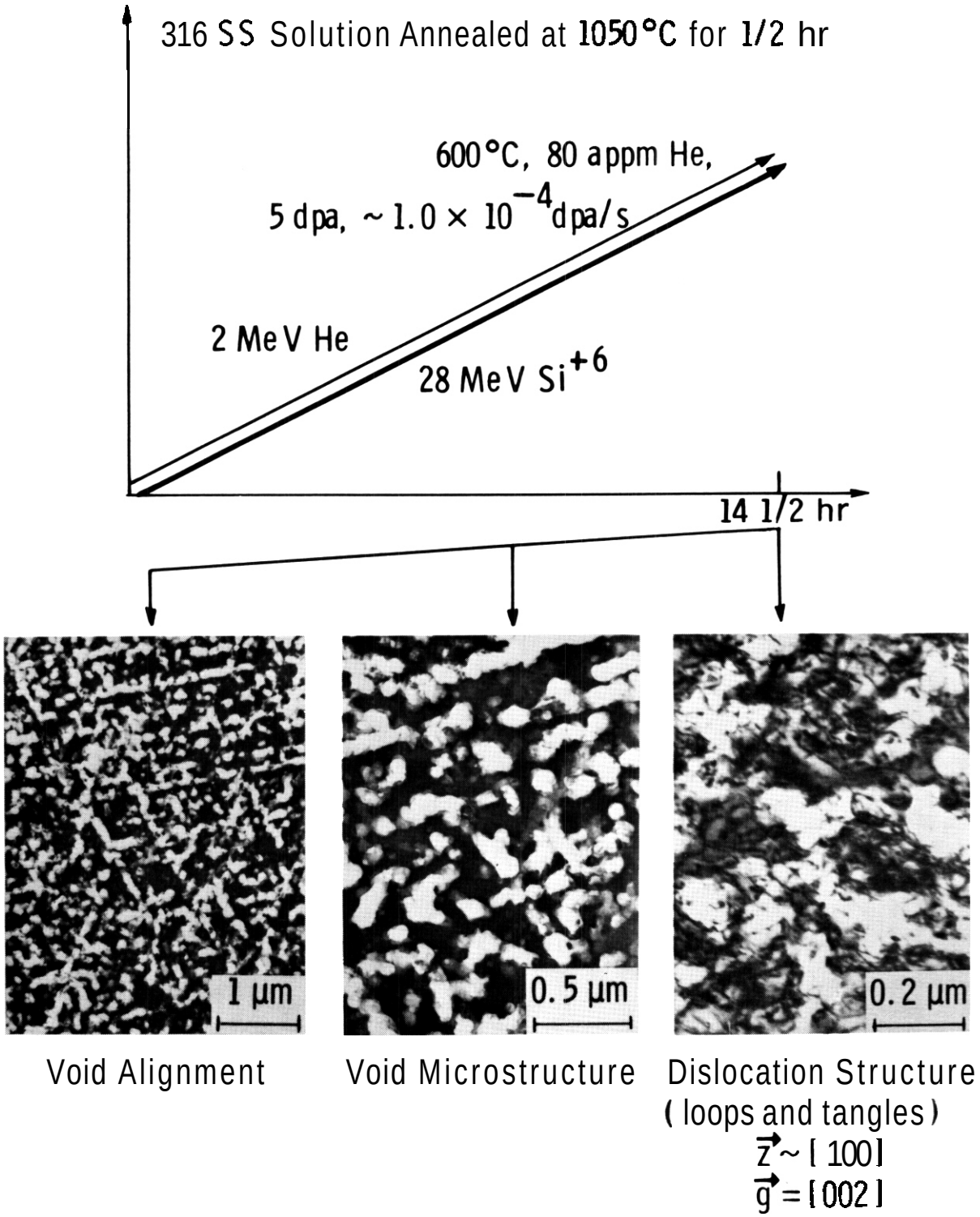

FIGURE 4. Void and Dislocation Structures Developed in Solution Annealed 316 SS After Simultaneous Bombardment for 14 1/2 hours.

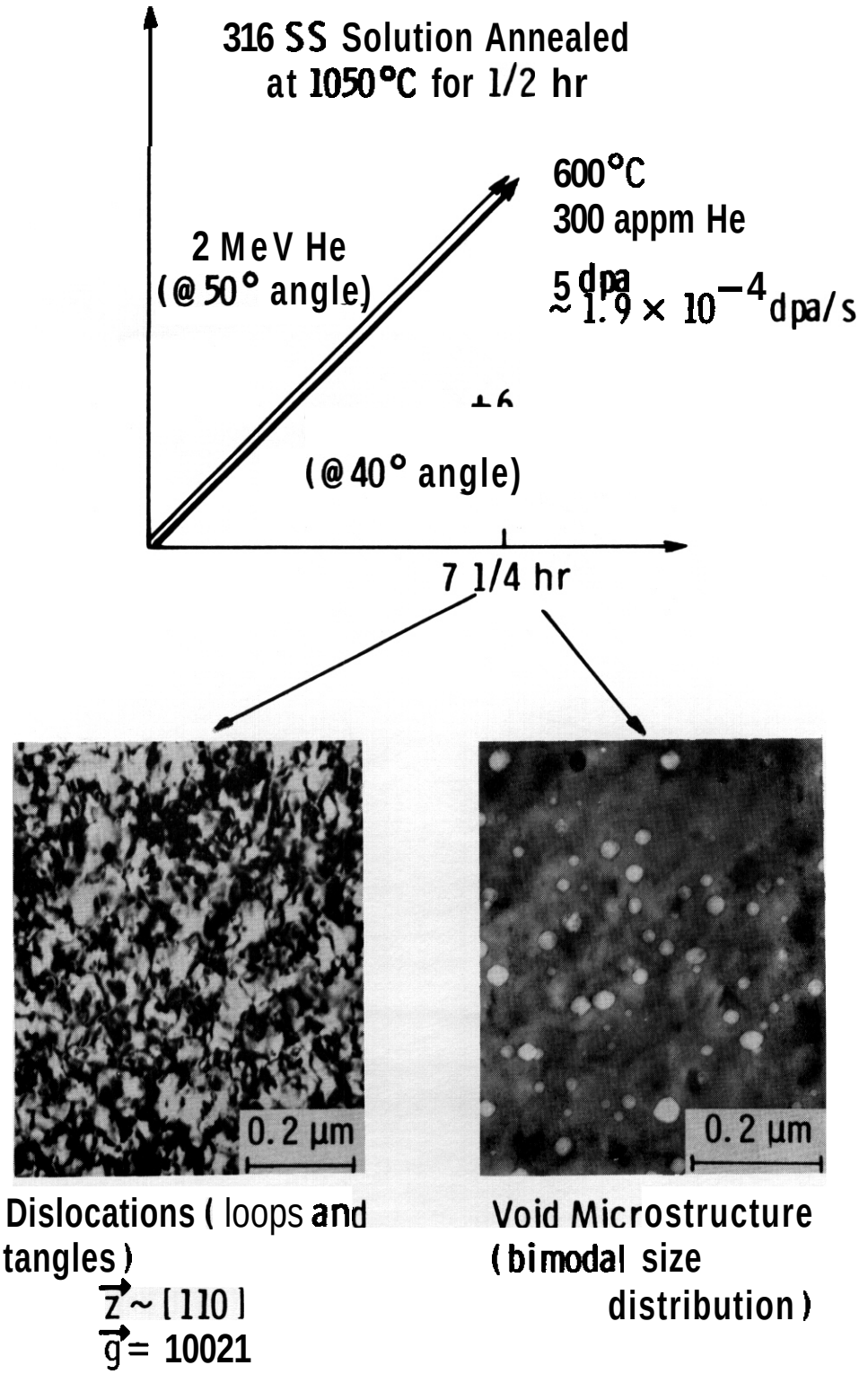

FIGURE 5. Microstructures Produced in Solution Annealed 316 SS After Simultaneous Bombardment With the $Si^{+}6$ Beam Inclined at 40° With Respect to the Specimen Surface.

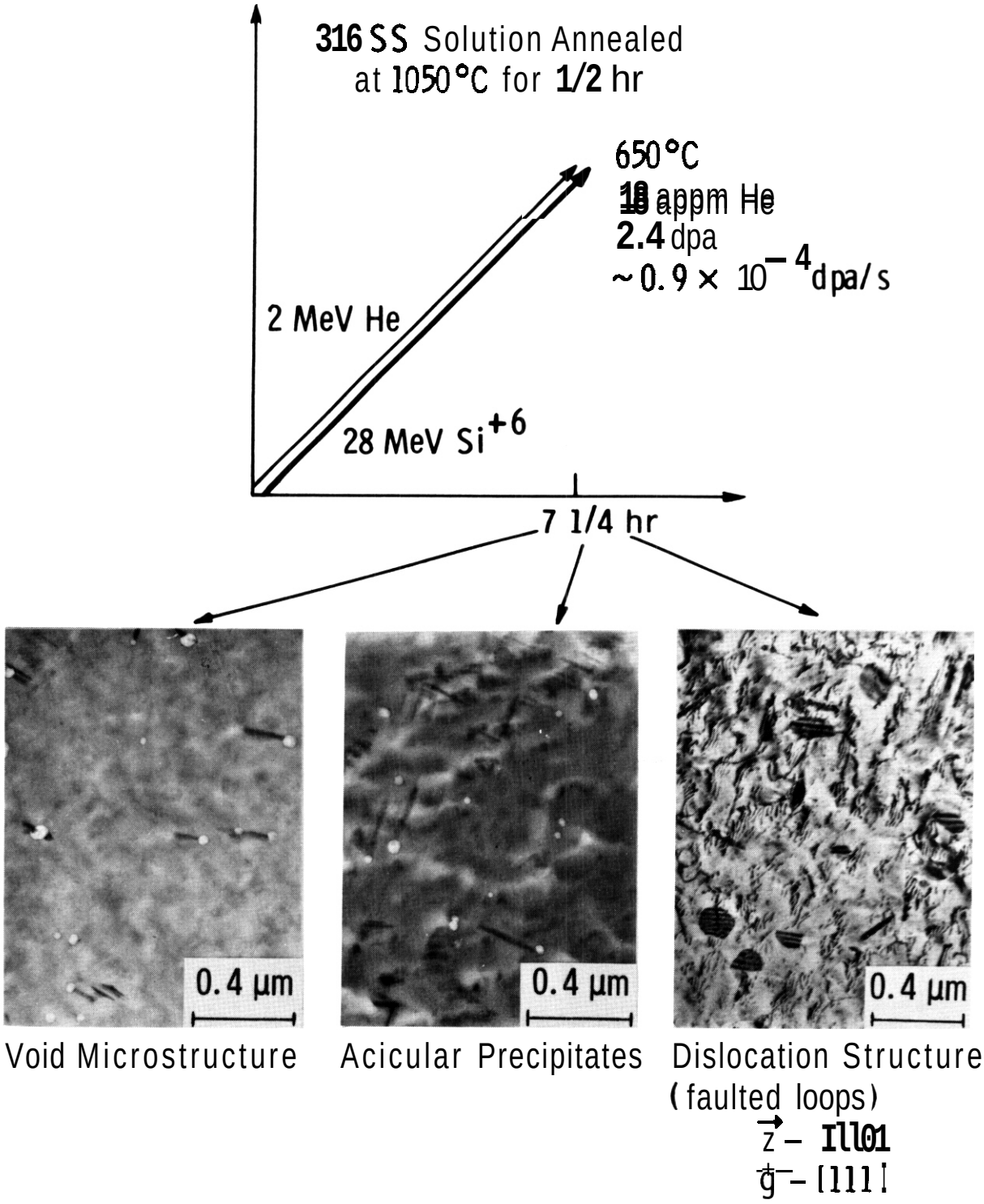

FIGURE 6. Nucleation of Voids on Acicular Precipitates and Development of Faulted Loops in Simultaneously Bombarded Solution Annealed 316 SS.

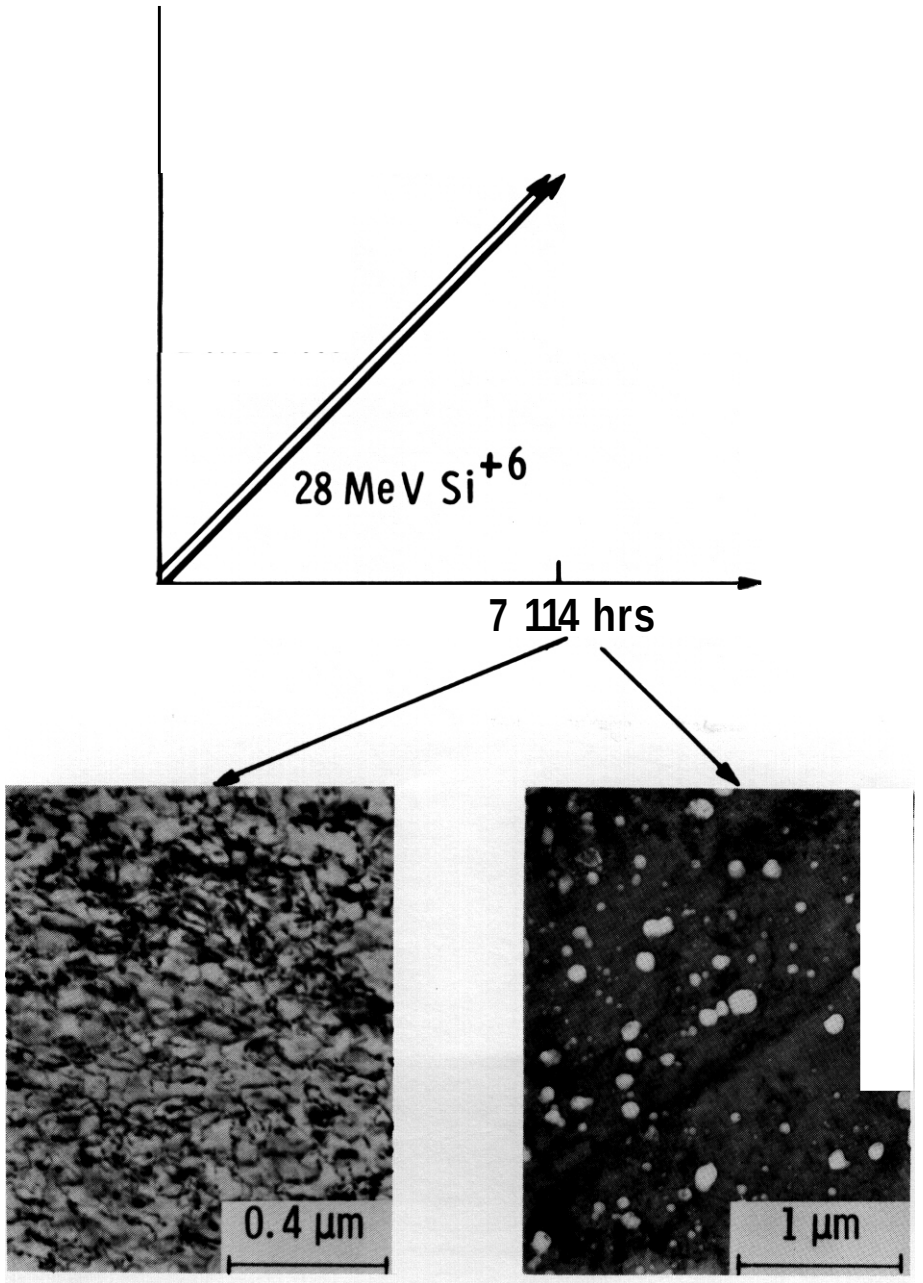

FIGURE 7. Effect of Simultaneous Bombardment on the Void and Dislocation Structures in Cold Rolled 316 SS.

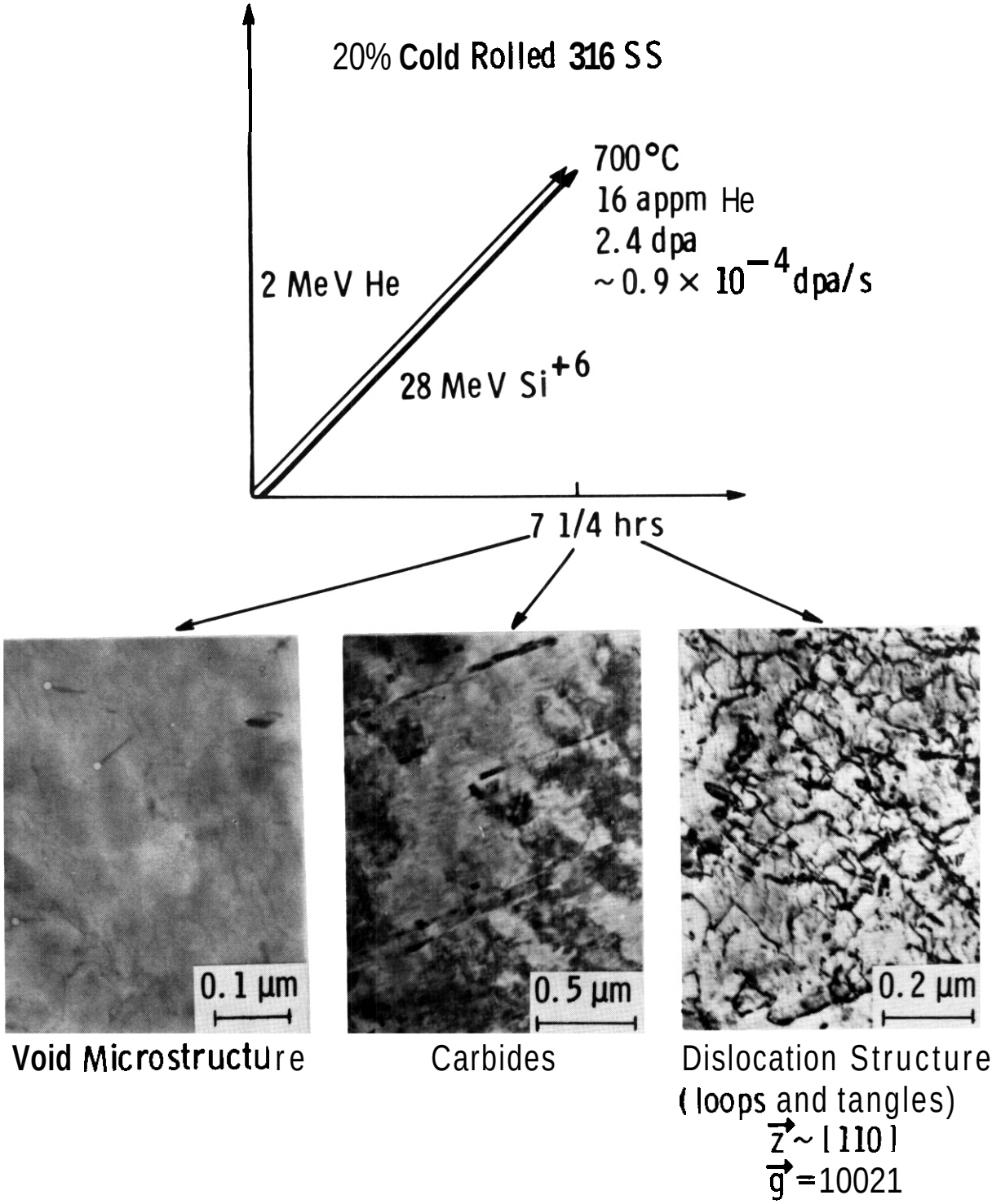

FIGURE 8. Heterogeneous Cavity Nucleation on Acicular Precipitates and Other Microstructural Features Induced by Simultaneously Bombarding Cold Rolled 316 SS.

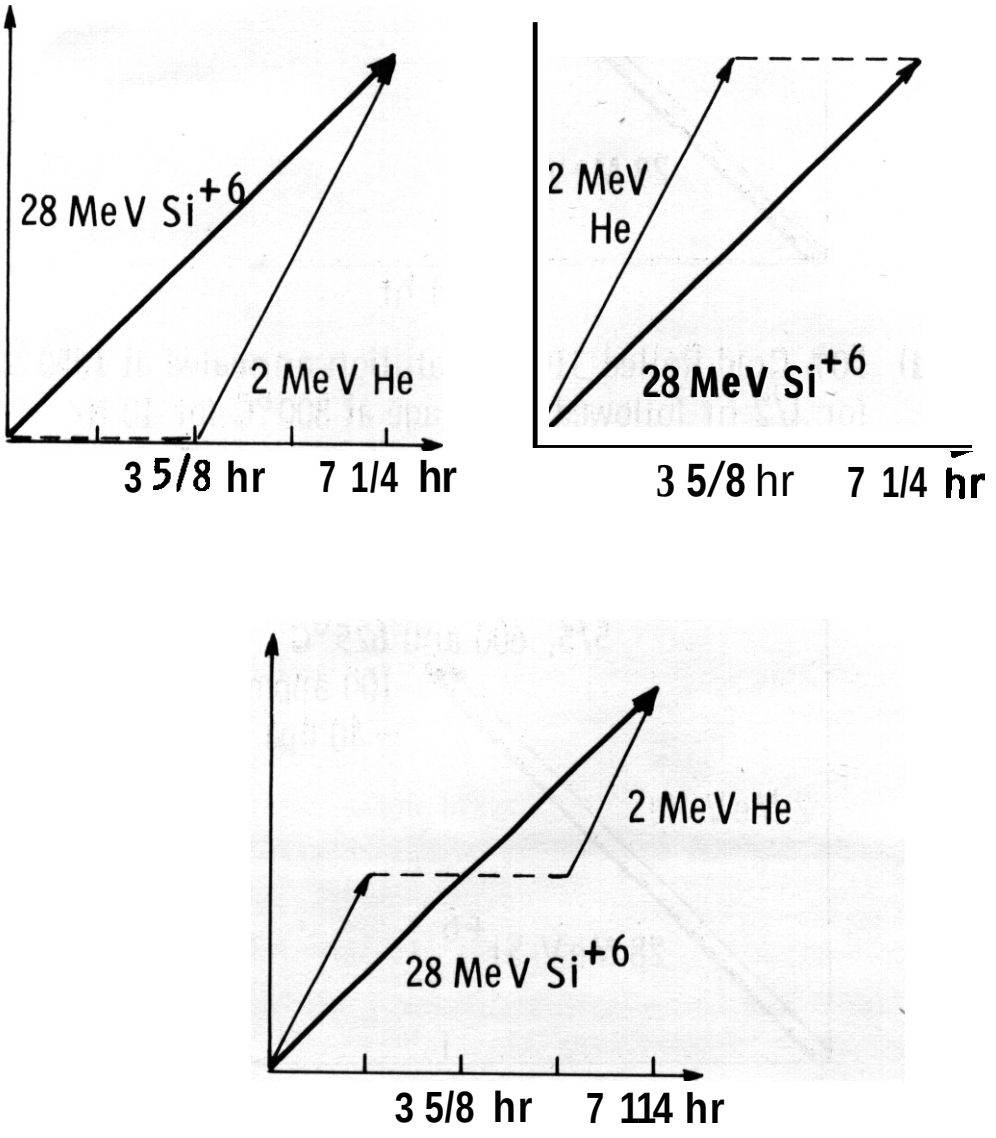

All samples 20% Cold Rolled 316 SS, bombarded at 600°C to peak values of 40 dpa and 100 appm He

FIGURE 9. Interrupted He Deposition Sequences During Simultaneous Bombardment of Cold Rolled 316 SS.

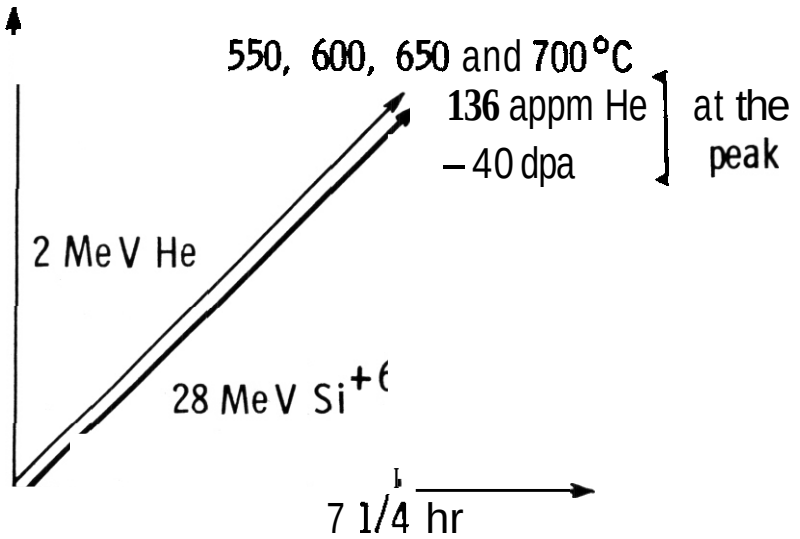

a) 50% Cold Rolled 316 SS solution annealed at 1050°C for 1/2 hr followed by an age at 800°C for 10 hr

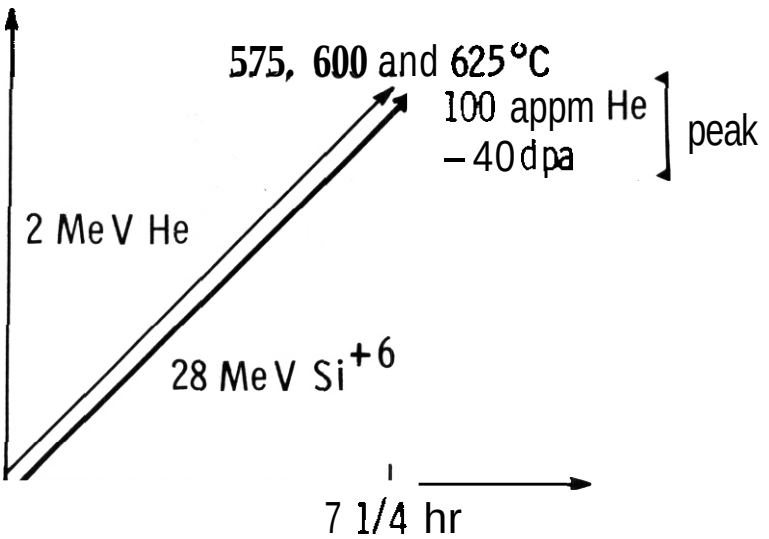

b) 316 SS Solution annealed at 1050°C for 1/2 hr

FIGURE 10. Simultaneous Bombardment Experiments on a) Aged 316 SS (With Carbide Precipitation); b) Solution Annealed 316 SS (to Investigate the Development of Void Alignment).

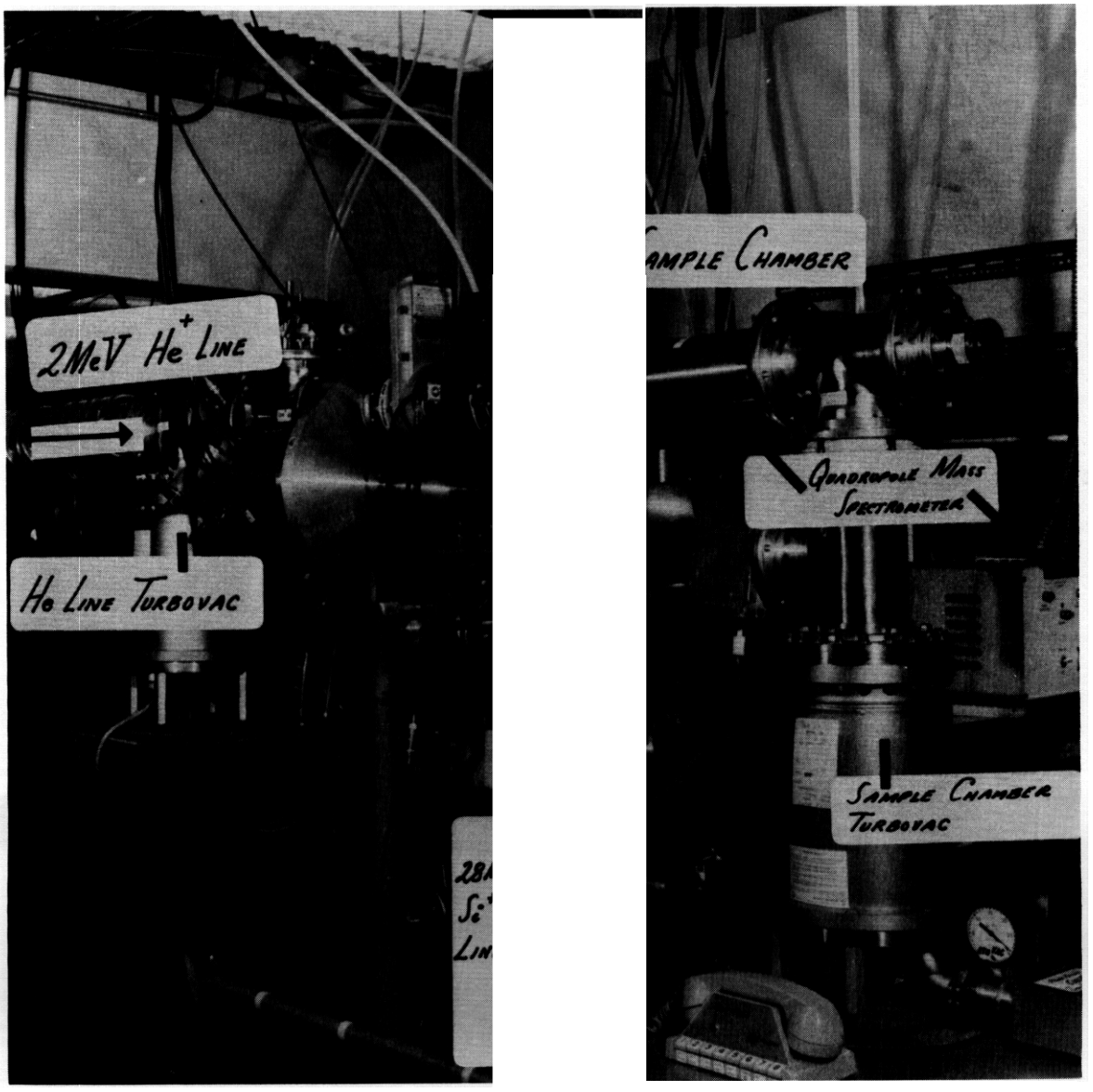

FIGURE 11. **Overview of New Sample Chamber, Turbo-Pumps, and Quadrupole Mass Spectrometer.**

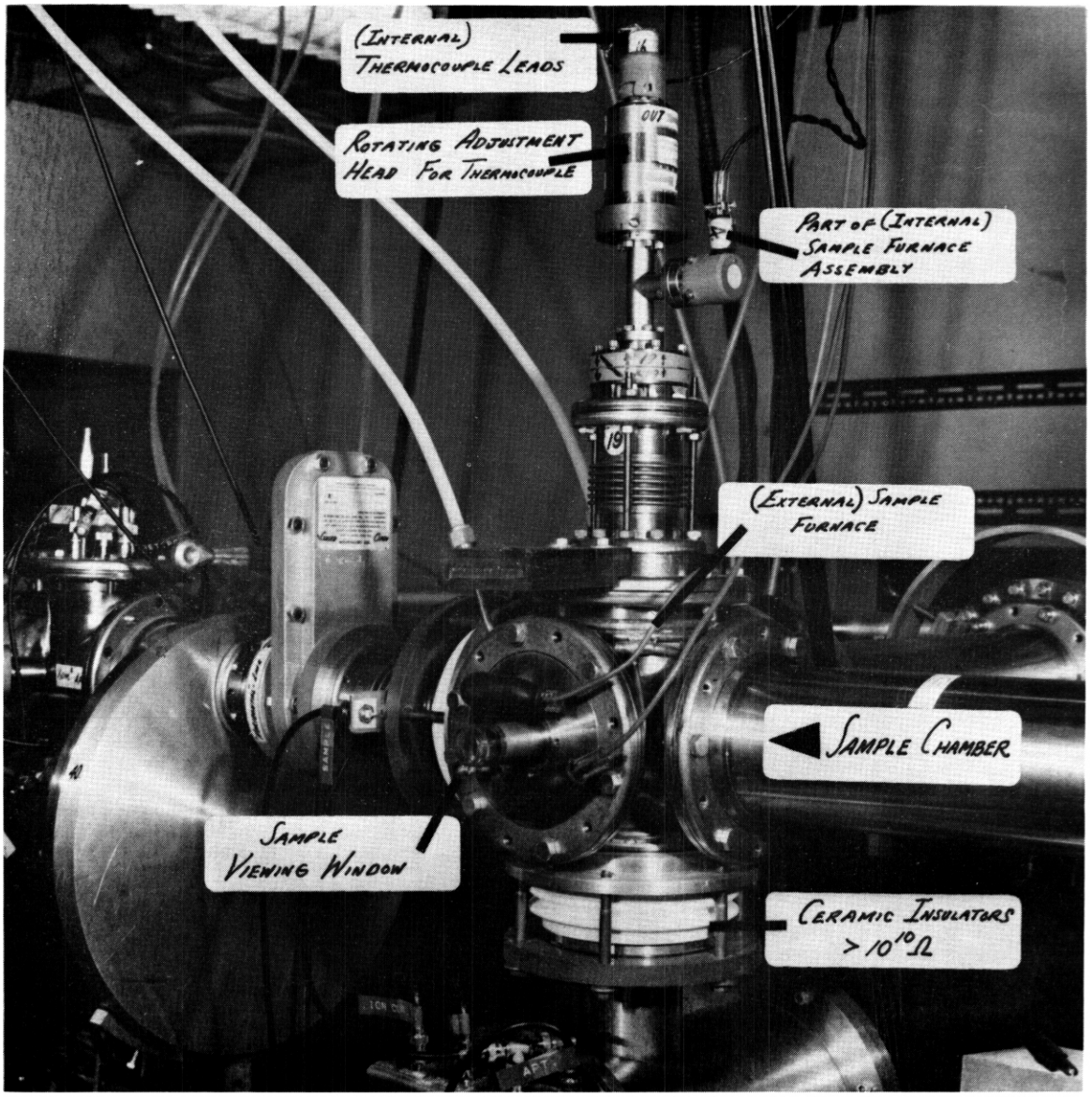

FIGURE 12. New Dual-Ion Beam Sample Chamber.

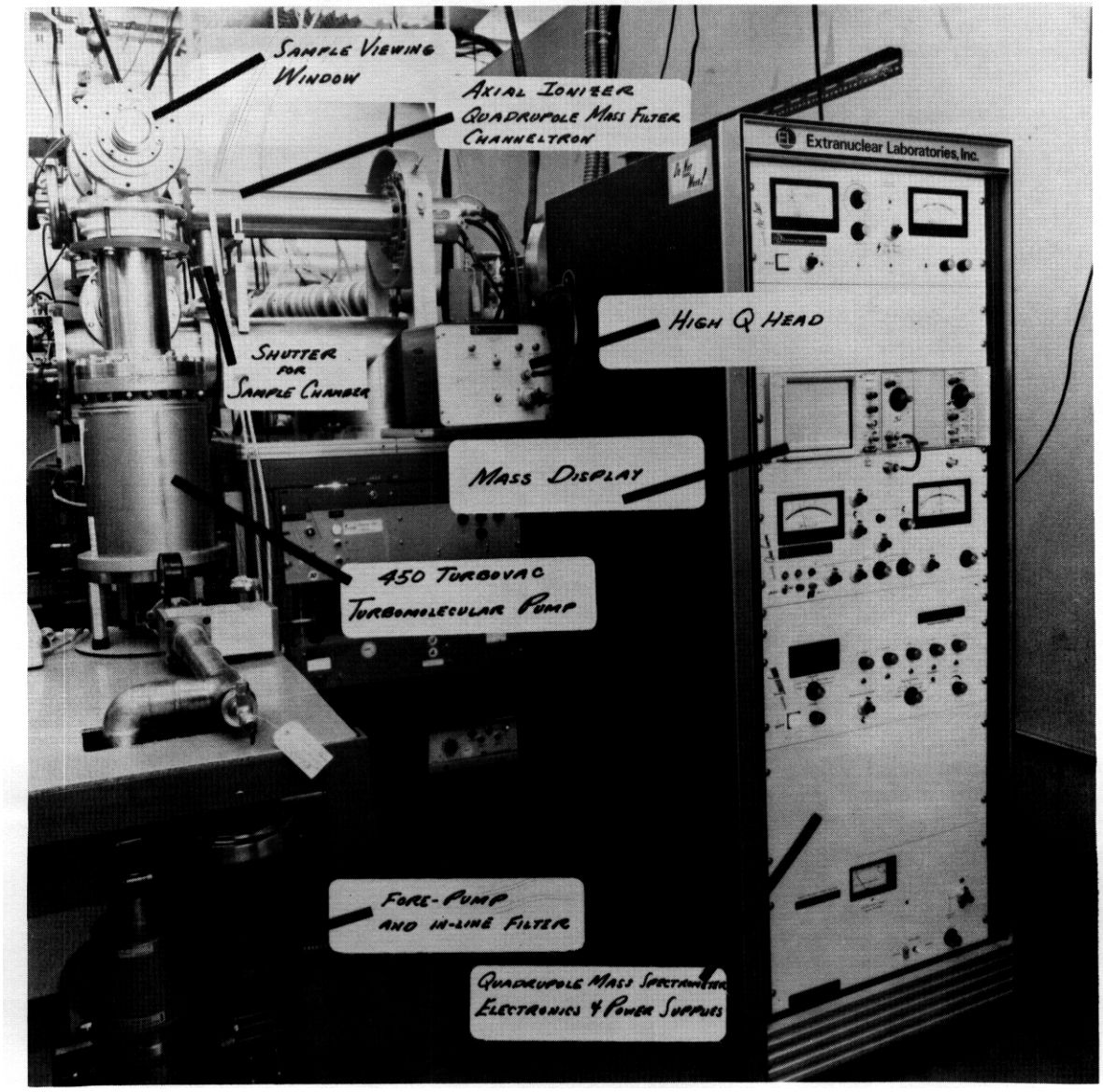

FIGURE 13. Quadrupole Mass Spectrometer for the Dual-Ion Beam Sample Chamber.

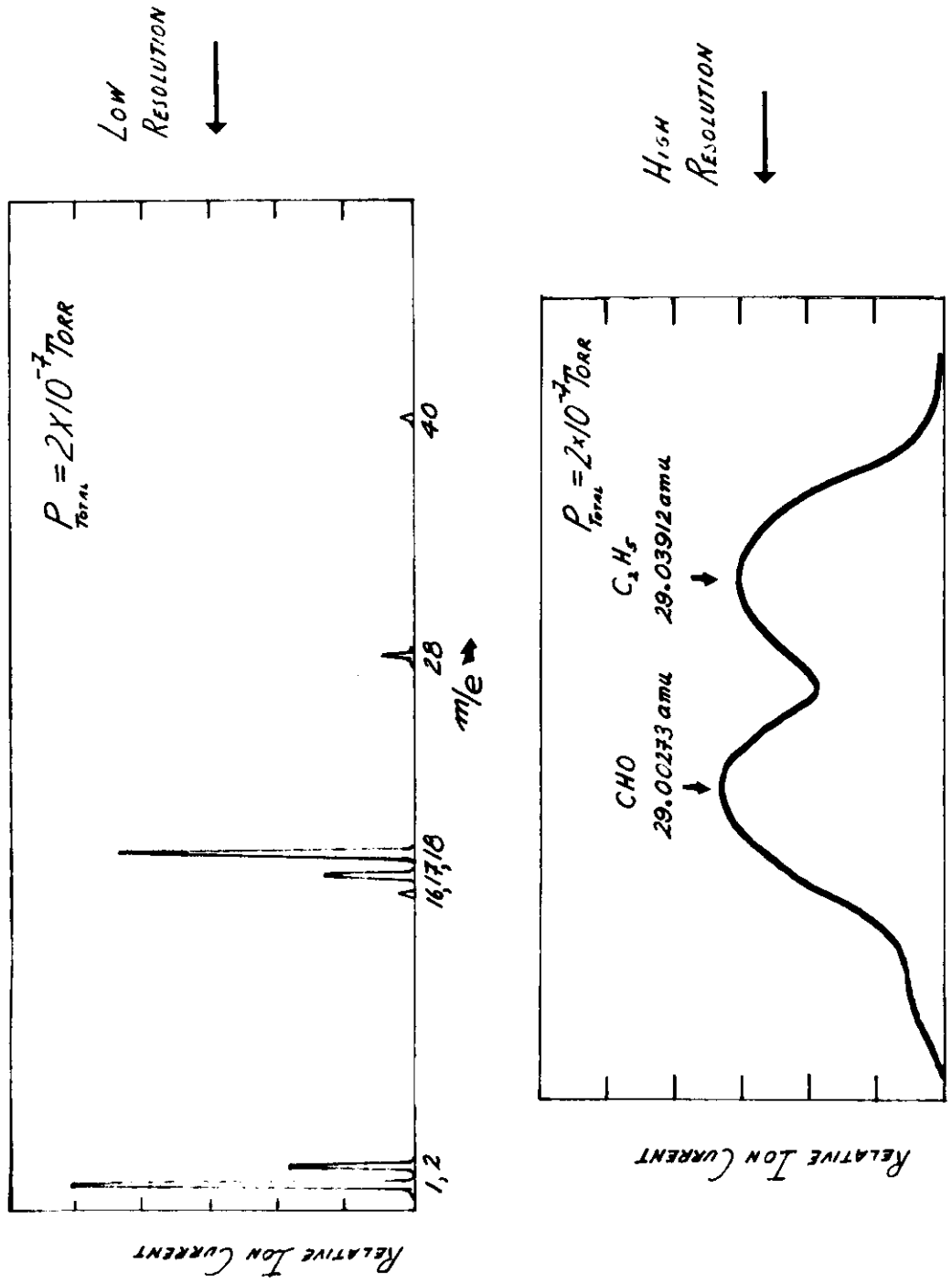

FIGURE 14. Dual-Ion Beam Chamber Mass Spectrometer Scans.

I. PROGRAM

Title: Mechanical Properties
Principal Investigator: R. H. Jones
Affiliation: Battelle, Pacific Northwest Laboratory

II. OBJECTIVE

1. Model the grain boundary segregation behavior of trace impurities which are particularly detrimental to the mechanical properties of nickel based alloys.

2. Compare the relative effects of thermally activated and irradiation induced segregation to grain boundaries.

III. RELEVANT DAFS AND ADIP TASK/SUBTASK

DAFS	Subtask IIC.1.1	Phase Stability Mechanism Experiments
	Subtask IIC.1.2	Modeling and Analysis
	Subtask IIC.8.2	Post-Irradiation Testing of ORR and EBR-II Specimens
ADIP	Subtask IC.1.3	Correlate Grain Boundary Segregation with Fracture Mode/Ductility Results

IV. SUMMARY

The predicted segregation behavior of sulfur in nickel has been examined in order to gain insight into trace element effects in path B alloys. Equilibrium segregation theory illustrates that it is energetically favorable for significant levels of sulfur to partition to grain boundaries in nickel even at bulk concentrations less than 1 atomic ppm. However, the kinetics of this segregation at temperatures below 500°C will probably limit the amount substantially below the equilibrium value and possibly less than the quantity reported to degrade elevated temperature mechanical properties.

V. ACCOMPLISHMENTS AND STATUS

1. Introduction

The segregation of solute elements to metal grain boundaries has a dramatic effect on a number of metallurgical processes; in particular, the tendency for intergranular fracture. Nickel and nickel-base alloys have been shown to exhibit intergranular fracture and a loss in high temperature tensile ductility due to the presence of elements such as S, Bi, Te, Pb and Se at bulk levels of a few ppm.[1-3] This embrittlement has been identified as resulting from the enrichment of several of these impurities at the grain boundaries.[4]

Irradiation has been discovered to significantly affect the segregation behavior of solute elements. Wiedersich, et al.[5] found a nearly continuous Ni-Be precipitate in the grain boundary of a Ni-1 at. % Be alloy after nickel ion irradiation. Such large solute segregations have been observed at free surfaces of stainless steel[6] and nickel alloys.[7] Unfortunately, the irradiation-induced segregation of elements which are potentially detrimental to mechanical properties have not been studied. It seems probable that both thermally activated and radiation induced segregation will have an effect on the mechanical properties of candidate fusion reactor materials. Selection of an alloy with optimum properties for application in a fusion reactor will require a knowledge of the relative kinetics of thermal and radiation induced segregation to grain boundaries.

2. Thermal Segregation

2.1 Equilibrium Segregation Theory

The enrichment of solute atoms in grain boundaries can result from two types of segregation, equilibrium or nonequilibrium. Irradiation-induced segregation is an example of nonequilibrium segregation; this

phenomenon will be discussed in a following quarterly. The equilibrium segregation of surface active solute elements has been documented in a number of different metals and alloys as Fe, Cu, W, etc.[8] Reasonable success has been obtained in modeling this behavior through the use of surface adsorption analogues.[9] The most versatile of these theories has been the grain boundary analogue to the Brunauer, Emmett and Teller (BET) isotherm.[10] Assuming the grain boundary has an array of identical adsorption sites, no interaction between adsorbate atoms and monolayer type adsorption; the truncated BET[11] may be written:

$$\frac{X_b}{X_{b_o} - X_b} = \frac{X_c}{X_{c_o}} \exp\left[\frac{E}{RT}\right]$$

where: X_b = grain boundary concentration
X_{b_o} = saturation value of X_b
X_c = bulk concentration
X_{c_o} = solubility limit
E = energy of segregation
T = temperature (°K)

The grain boundary concentration is a function of inverse solubility, so as temperature decreases, solubility decreases and the equilibrium amount of solute at the grain boundary increases. When the temperature reaches a value where the bulk concentration is greater than the solubility limit, the amount of solute in solution able to segregate becomes X_{c_o} and the equation simplifies to:

$$\frac{X_b}{X_{b_o} - X_b} = \exp\left[\frac{E}{RT}\right]$$

The segregation now rises more slowly with decreasing temperature toward a saturation value.

2.2 Segregation Kinetics

In practical situations, it is essential to know not only whether it is energetically favorable for a solute element to segregate but also the time dependence of the segregation. This dependence was evaluated by McLean[12] by considering the flow of solute atoms from two infinite half crystals separated by a grain boundary. Thus, the kinetics of grain boundary segregation is expressed by:

$$\frac{X_b(t) - X_b(o)}{X_{b(\infty)} - X_b(o)} = 1 - \exp\left(\frac{4Dt}{\alpha^2 d^2}\right) \operatorname{erfc}\left(\frac{4Dt}{\alpha^2 d^2}\right)^{1/2}$$

where: $X_b(o)$, $X_b(t)$, $X_b(\infty)$ = grain boundary concentration at times o, t, and at equilibrium.

D = diffusivity

α = grain boundary enrichment ratio = $\frac{X_b}{X_c}$

d = grain boundary width

2.3 Sulfur Segregation in Nickel

The equilibrium segregation of sulfur in nickel has been calculated for a series of sulfur bulk concentrations in Figure 1. The solubility data was taken from Kirkaldy,[13] and extrapolated for temperatures below 700°C. As a starting point, an energy of segregation of 1000 cal/mole was selected which has been found to describe sulfur segregation in iron.[14] The sulfur is assumed to be in elemental form at the boundary and to saturate at one monolayer. This may be an oversimplification; in binary Ni-S alloys, NiS precipitation (<50 Å thick) has been identified at grain boundaries. There is no conclusive evidence at this time to determine if such a second phase will form in nickel alloys.

The abrupt change in slope that can be noted for each bulk composition in Figure 1 reflects the temperature where the solubility limit is

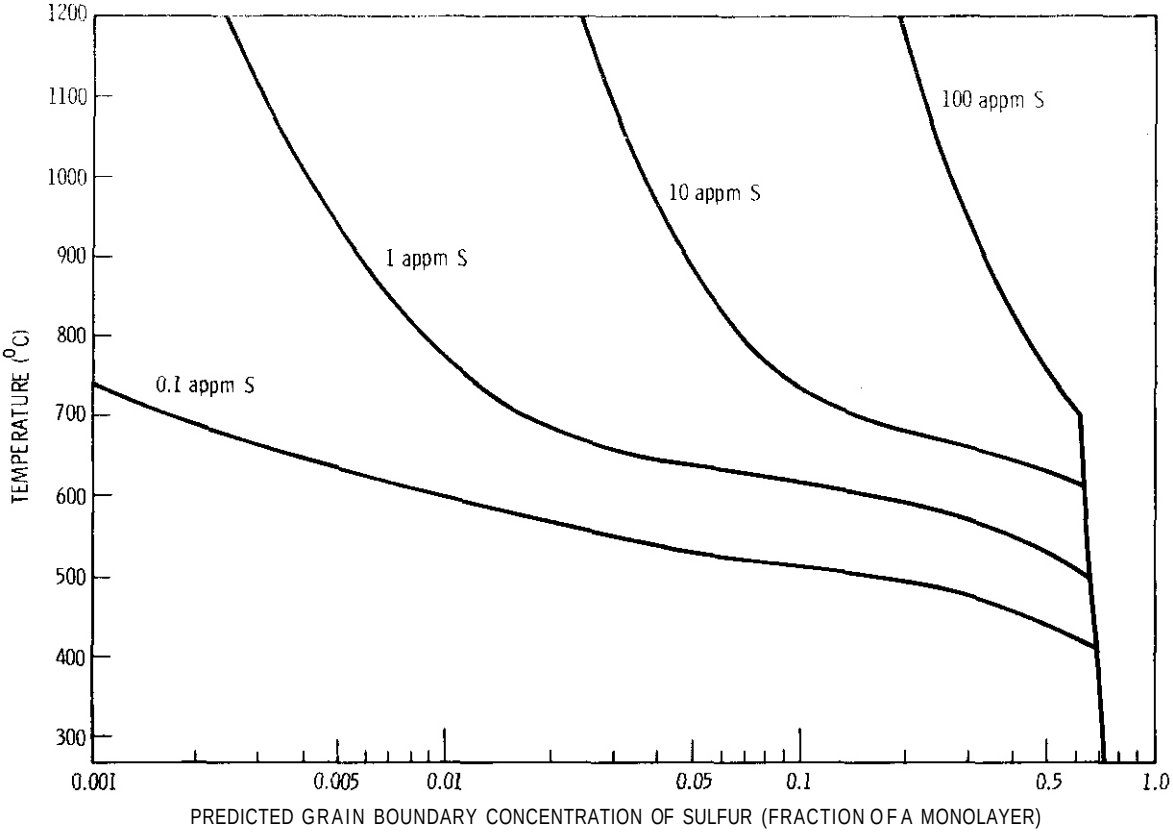

FIGURE 1. Predicted Equilibrium Grain Boundary Segregation of Sulfur in Nickel as a Function of Temperature for Four Bulk Sulfur Concentrations.

exceeded (i.e., for the 100 appm S alloy, $X_c > X_{c_o}$ at temperatures below 705°C). It is interesting to note that reducing the **bulk** sulfur composition from 100 to 1 appm does not change the predicted equilibrium segregation at 500°C since the amount of sulfur in solution at this temperature is less than 1 appm. This is also important in the kinetics aspect of the model, as seen in Figure 2 for the nickel-10 appm sulfur alloy. As the time at temperature is increased, the enrichment of the boundary increases until the equilibrium value is reached. For example, at 600°C the predicted grain boundary content rises from approximately 0.001 of a monolayer in 0.1 hour to 0.43 of a monolayer in 100,000 hours. The effect of solubility is illustrated by the extremely slow kinetics below 500°C. This

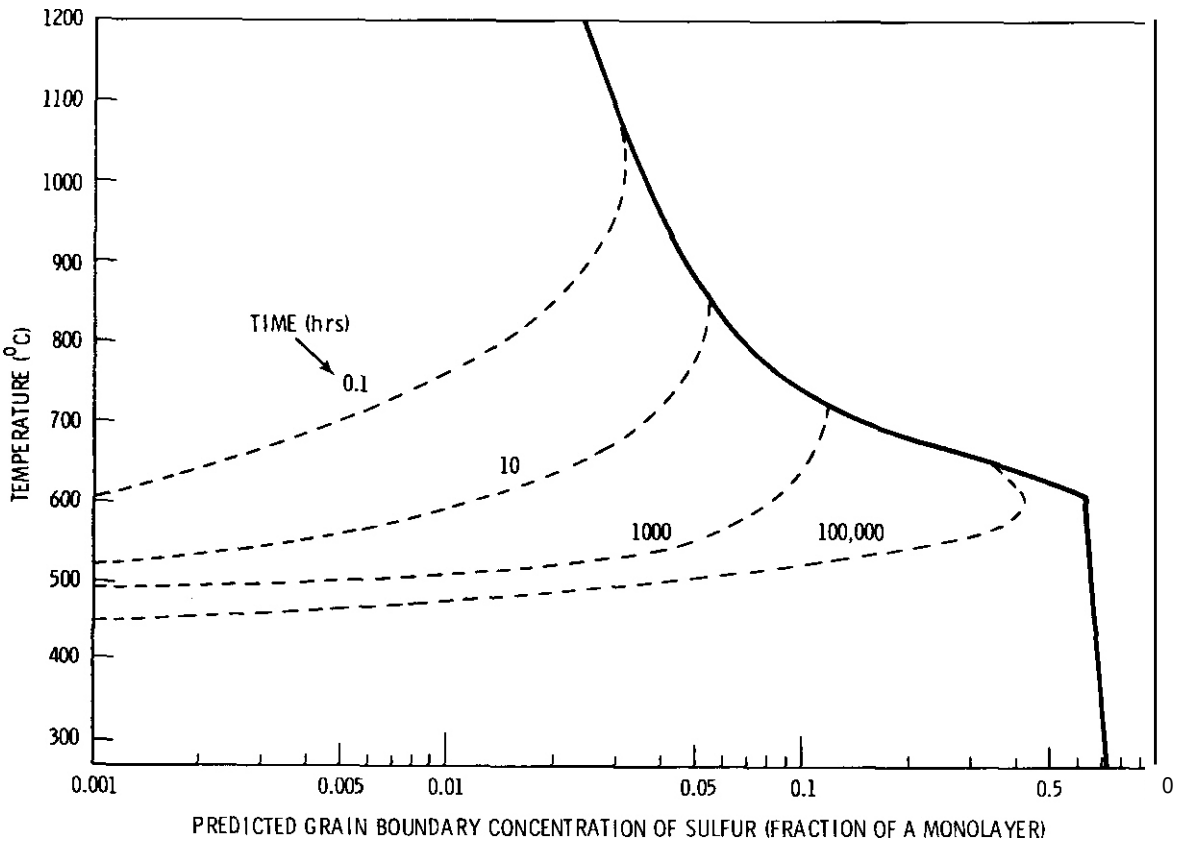

FIGURE 2. Predicted Grain Boundary Segregation of Sulfur in Nickel as a Function of Temperature and Time for a Nickel-10 Atomic ppm Sulfur Alloy.

reflects the very small amounts of sulfur in solution at these low temperatures.

As noted in the introduction, nickel and many nickel alloys exhibit a loss in elevated temperature tensile ductility when impurity elements as sulfur are present in bulk levels of several ppm. The fracture mode at these temperatures becomes intergranular and the reduction in area may drop from over 80% to less than 5% with increasing sulfur content.[3] The kinetics calculations suggest a possible reason for this ductility loss at temperatures between 600-1000°C. If the sulfur content is 10 appm or more, considerable grain boundary enrichment is possible in relatively short

times. From the limited grain boundary chemistry data that is available, the Auqer Electrori Spectroscopy results of Johnson, et al.[15] suggest that approximately 0.04 or more of a monolayer of sulfur is necessary at the boundary to induce the high temperature embrittlement phenomenon. The prediction for the Ni-10 appm S alloy shows the grain boundary sulfur content reaching this level after about 10 hours at 700°C. At higher bulk concentrations of sulfur, the kinetics would be considerably faster (i.e., in a Ni-100 appm alloy, 0.04 of a monolayer would be achieved in 5 minutes) More importantly for fusion reactor applications, at 500°C the model predicts that the sulfur segregation due to equilibrium processes in nickel (less than 50 appm S) may not be significant.

VI. REFERENCES

1. C. Bieber and R. F. Decker, Trans. TMS-AIME, 1961, vol. 221, p. 629.

2. O. R. Wood and R. M. Cook, Metallurgia, 1963, vol. 67, p. 109.

3. M. G. Lozinskiy, G. M. Volkogon, and N. Z. Pettsovskiy, Russ. Met., 1967, vol. 5, p. 65.

4. J. M. Walsh and N. P. Anderson, Surface Analysis Techniques for Metallurgical Applications, ASTM STP 596, 1976, p. 58.

5. H. Wiedersich, P. R. Okamoto and N. Q. Lam, Proc. Int. Conf. on Radiation Effects in Breeder Reactor Structural Materials, M. L. Bleiberg and J. W. Bennett, eds., p. 801.

6. P. R. Okamoto and H. Wiedersich, J. of Nucl. Matl., 53, 1974, 336.

7. L. E. Rehn, P. R. Okamoto, O. I. Potter and H Wiedersich, J. of Nucl. Matl., 74, 1978, 242.

8. E. O. Hondros and M. D. Seah, International Met. Reviews, Oec. 1977, p. 262.

9. E. D. Hondros and M. P. Seah, Met. Trans A, vol. 8A, 1977, p. 1363.

10. S. Brunauer, P. H. Emmett, and E. Teller, J. Am. Chem. Soc, 60, 1938, 309.

11. S. Brunauer, L. S. Deming, W. E. Deming, E. Teller, J. Am. Chem Soc., 62, 1940, p. 1723.

12. D. McLean, Grain Boundaries in Metals, 1957, Oxford, Clarendon Press.

13. J. S. Kirkaldy, Ser. Met., vol. 3, 1969, p. 947

14. M. P. Seah and E. D. Hondros, Proc. R. Soc., 335A, 1973, 191.

15. W. C. Johnson, J. E. Doherty, B. H. Kear, and A. F. Giamel, Ser. Met., vol. 8, 1974, p. 971.

VII. FUTURE WORK

The equilibrium segregation calculations will be extended to consider bismuth segregation in nickel. Bismuth has long been considered one of the most potent embrittlers of nickel and nickel alloys, recent AES results suggest that it segregates to nickel grain boundaries.[4] The model itself will be improved to include the possibility of precipitation at the boundary and also the effect of alloying elements as Cr, Fe, Ti, Al and Mo on impurity element segregation.

The irradiation-induced segregation of an undersized solute, sulfur and an oversized solute, bismuth, will be modeled as a function of increasing dose. A comparison will be made between these two segregation processes and the possible effects of the predicted segregation on mechanical properties discussed.

I. PROGRAM

Title: Fundamental Studies of Radiation Damage Analysis
Principal Investigator: G.R. Odette
Affiliation: University of California, Santa Barbara

11. OBJECTIVE

The object of this work is to develop physical models describing the influence of metallurgical and irradiation variables on the evolution of damage microstructure and the alteration of mechanical properties. These models will be used to correlate available data, to plan and analyse new experiments and, ultimately, to extrapolate to fusion reactor conditions. The effort also involves developing techniques to extract useful mechanical property information from very small test volumes.

111. RELEVANT DAFS PROGRAM PLAN TASK/SUBTASK

SUBTASK II.C.1.2 Effect of Material Parameters on Microstructure-Modeling and Analysis
SUBTASK II.C.2.4 Effect of Helium on Microstructure-Modeling and Analysis
SUBTASK II.C.5.3 Effects of Cycling on Microstructure-Modeling and Analysis
SUBTASK II.C.6.2 Effects of Damage Rate and Cascade Structure on Microstructure-Modeling and Analysis
SUBTASK LI.C.14.1 Modeling of Flow and Fracture Under Irradiation-Model Development
SUBTASK II.C.16.1 Composite Correlation Models and Experiments-correlation Model Development

IV. SUMMARY

A. Microstructural Evolution

An approach to extrapolating data which will be derived from the array of available irradiation environments is described. The composite correlation model analysis technique is partially illustrated for austenitic stainless steels. A comprehensive description of the

data base for AISI 316 Stainless Steel which has appeared in the literature is presented and used to develop a conceptual model of microstructural evolution in these materials. Quantitative computer models are used to illustrate how extrapolation to fusion conditions can be accomplished, and to indicate some possible alloy development considerations. However, the quantitative results cannot be viewed as reliable at this time because a thorough determination of critical mechanisms and definition of parameters has not been completed, and additional experimental data is needed.

B. Mechanical P'roperties

Recently micromechanical models and microstructural information have been successfully applied to predict yield stress changes in irradiated stainless steels. The technique is extended to tensile ductility, and some implications of the results to deformation-fracture mechanisms drawn. Finally, a micromechanical model was used to estimate changes in fracture toughness; while there is insufficient data to allow definitive conclusions, the calculations indicate a substantial reduction in toughness in stainless steels due to irradiation.

C. Flow and Fracture Maps

An initial effort at developing flow and fracture maps for Path A alloys using models and data for unirradiated solution annealed stainless steels is reported. While these tentative maps are useful guides to delineating regimes of deformation and fracture, they do not as yet indicate all critical processes, such as phase instabilities.

D. Development of Instrumented Hardness Tests

Initial efforts at extracting true stress-strain information from instrumented indentation hardness tests are described. Experiments on several materials demonstrate fair agreement between tensile data and the hardness measurements. However, further development is needed to accomplish single penetration microhardness measurements.

V. ACCOMPLISHMENTS AND STATUS

A. Microstructural Evolution Under Irradiation - C.R. Odette

(University of California, Santa Barbara)

A1. Introduction

The evolution of microstructure under irradiation is an extremely complex phenomenon. In order to predict microstructural response in fusion environments using data from an array of test environments, which are "imperfect" simulations, a systematic marriage of theory and experiment is needed [1-43].

In order to accomplish such a marriage a five step approach is proposed. First, a thorough description of experimental observations is required to guide and structure the analysis. Second, a catalog of possible mechanisms and parameter ranges is needed. Third, the mechanisms must be integrated into quantitative models, sufficiently comprehensive to confront the particular set of data to he analyzed, detailed narrower models for controlled mechanism experiments, and more comprehensive models for the general data base. Fourth, an effective strategy for comparing model predictions to experimental results must he developed and applied. Fifth, it is necessary to conduct an iterative cycle of: a) applying the models to design new experiments; and b) using the new experimental data to refine the models.

The process which emerges from these steps is termed composite correlation model analysis (CCMA). The models are semi-empirical and partly phenomenological. While not completely rigorous, such analysis should lead to: a) better and more efficient experimental planning; b) a systematic process for assessing the physical processes governing microstructural evolution (ME); c) and a physically based procedure for extrapolating from sparse and imperfect test matrices to fusion reactor conditions, including estimates of uncertainties implicit in such extrapolations.

This report reviews briefly the status of an effort to develop CCMA as a damage analysis tool. Some preliminary results based on the existing data base and modeling studies reported previously are used as a basis for extrapolating to conditions more closely resembling fusion reactor environments, and to note some possible implications to alloy development efforts. Finally, modeling uncertainties are discussed, and research needed to mitigate them is outlined.

A2. Empirical Phenomenology of Microstructural Evolution

This discussion will be primarily focussed on the data base which has appeared in the literature for solution strengthened stainless steel (SS) alloys, with particular emphasis on AISI 316. The data is predominantly from fast reactor irradiations, but includes some limited results from mixed spectrum reactor and charged particle experiments [13-37]. It should also be noted that this data base represents an enormous investment in irradiation tests and post-irradiation examinations; collectively it represents an extremely rich source of information.

Microstructural evolution involves both microstructural (MS) features including cavities, line dislocations and loops, and microchemical (MC) features such as solute distributions, and precipitates and phase structures. The path of ME is governed by the particular combination of: 1) irradiation variables, including temperature (T), stress (σ), flux (Φ), fluence (Φt), spectrum, the chemical environment and the time-history of these variables; and 2) the material variables, including initial microstructure (MS_o) and microchemistry (MC_o) as influenced by thermo-mechanical processing history.

Figure A-1 schematically illustrates significant relationships between ME and these variables. The data is for fast reactor irradiations of 316 SS, unless otherwise noted. The plots represent the observed behavior only in terms of average trends. Indeed, there may be a number of details not fully represented. The data scatter ranges from about a factor of two to about an order of magnitude around the trend lines.

Figure A-la illustrates that the number density of extended MS defects is a function of temperature, strongly in the case of loops and voids, and only weakly for total dislocation density [13-16, 18]. The rough correspondence between loop and cavity densities is notable. Similar relationships appear to exist between densities of cavities and some precipitate structures [18].

Figure A-lb illustrates the tendency for the MS to evolve to quasi-steady state conditions [16,18]. Figure A-lc to e shows that cavity and loop densities tend to increase with c) stress [16]; d) damage rate [34]; and e) helium concentration [26-33]. Figure A-lc also shows an increase of swelling with stress [16]; A-ld an increase in peak swelling temperature with damage rate [34]; and Figure A-le that gross cavity swelling may either increase or decrease or remain approximately constant with increasing helium [26-33]. Increasing helium has also been observed to alter precipitate densities [28].

Figures A-lf to A-lh show that the temperature dependence of post-incubation void swelling rates may display double peaks, and vary within the same nominal alloy system (A-lf), between alloy systems (A-lg), and between cold-worked and solution-annealed conditions (A-lh) [17-19]. However, the peak swelling rates are roughly similar ($\sim$.5%/dpa), within the range of SS alloy classes considered. Figure A-li shows the effect of major and minor alloy modifications on swelling, which is increased or decreased depending on both solute type and concentration [20,22]. It has been suggested that the dominant effect of minor alloy additions in reducing swelling is on incubation time, and that major alloy constituent content influences both incubation time and post incubation swelling rates [22]. Figure A-lj shows incubation times for various alloys and conditions as a function of T; pure materials and alloys tend to have lower incubation times, with a spread in values of $\sim$ 10. Figure A-lk and A-ll are microstructural "maps" for 316 SS indicating the regimes of the formation of carbides and carbosilicates [13] and cavity structure (A-lk), and γ,' or Ni_3Si, (A-11) which is neither formed by thermal aging nor stable against annealing in these alloys

KEY - N - NUMBER DENSITIES: ϱ_d - TOTAL DISLOCATION DENSITY: S - SWELLING: $\dot{S}$ - POSTINCUBATION SWELLING RATE: 1E, SE, AND ME - ONE, SEVERAL AND MANY EXPERIMENTS: SA, CW AND CWA - SOLUTION ANNEALED, 20% COLD-WORKED AND COLD-WORKED AND AGED 316 STAINLESS STEEL; MM - MANY MATERIALS (316 SOLUTION ANNEALED UNLESS OTHERWISE NOTED): FR, MR, CP AND CP_2 - FAST REACTOR, MIXED SPECTRUM REACTOR, CHARGED PARTICLE AND DUAL ION IRRADIATIONS (FR UNLESS OTHERWISE NOTED): ϕt - EXPOSURE IN DPA UNIT: ϕ - DPA RATE: OTHER SYMBOLS SELF EXPLANATORY.

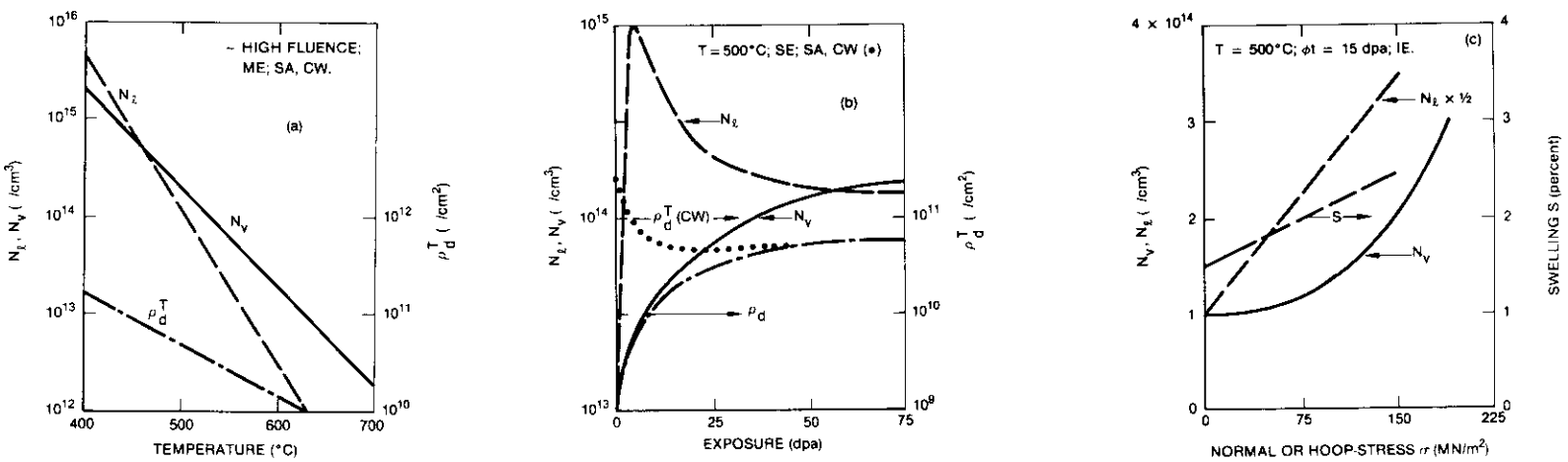

Figure A-1 - Compilation of irradiated microstructure data for fast reactor irradiated stainless steel, unless otherwise noted. See Key for explanation of symbols and text for a discussion. The figure is continued on the next two pages.

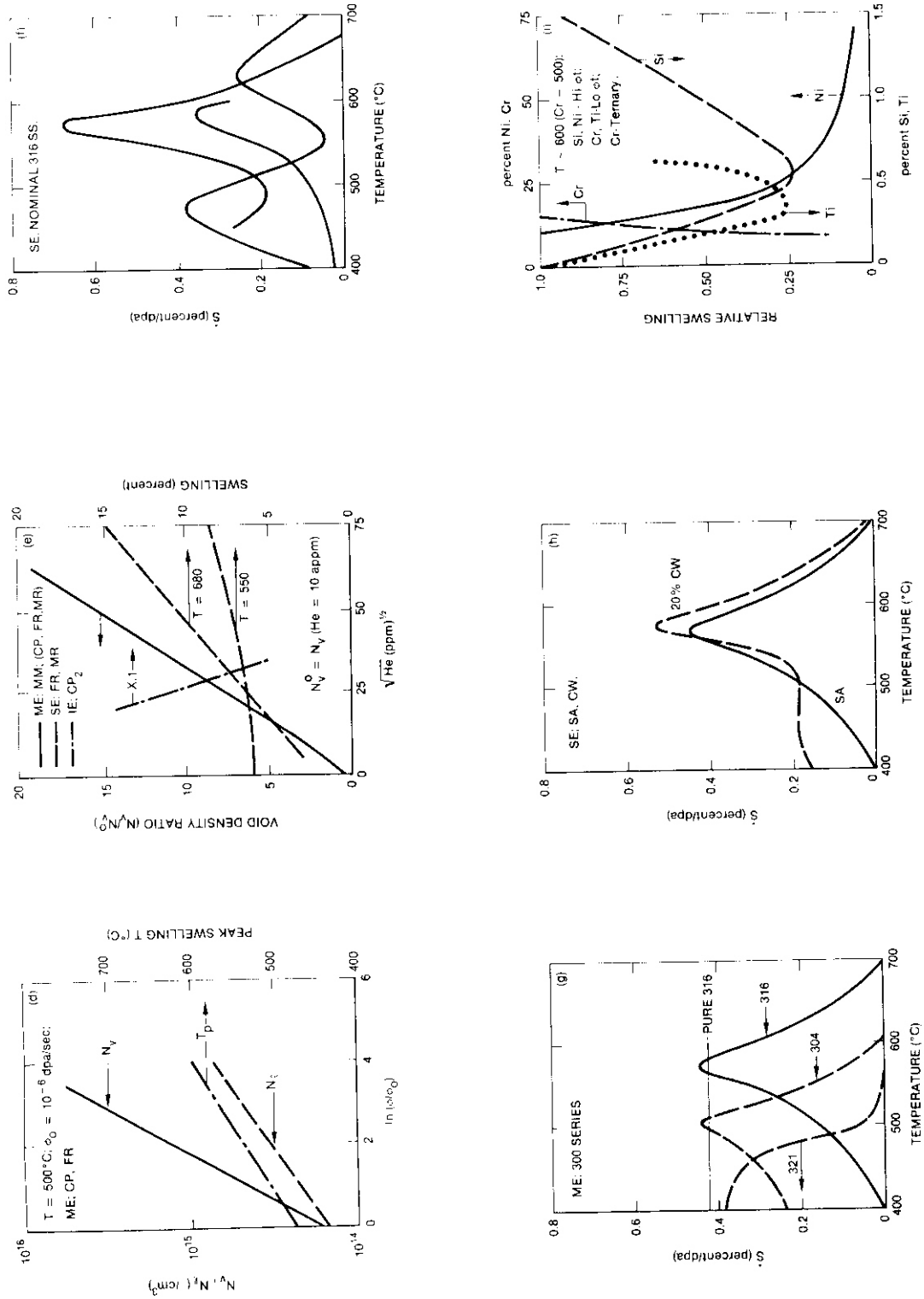

Figure 1 cont.

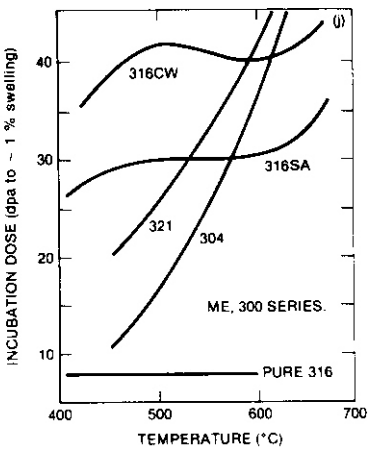

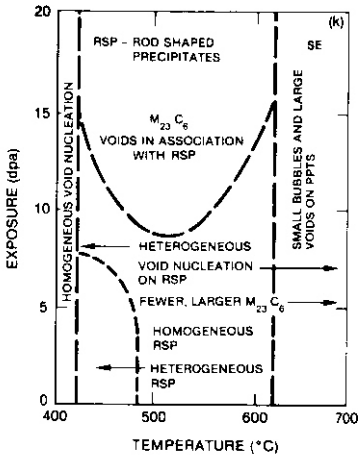

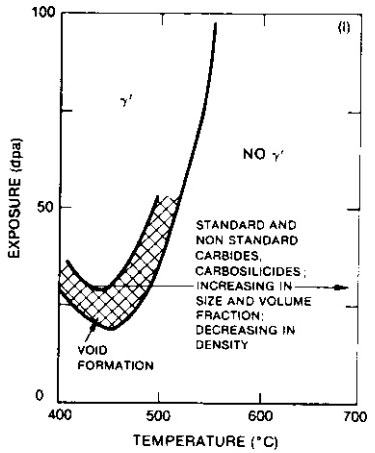

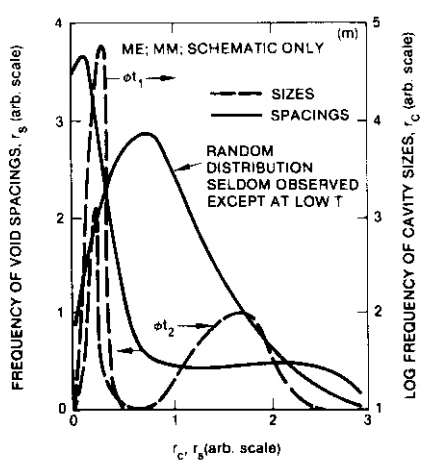

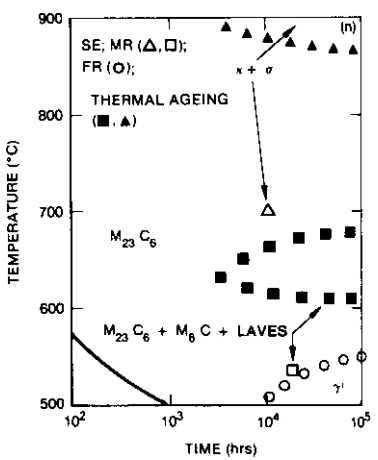

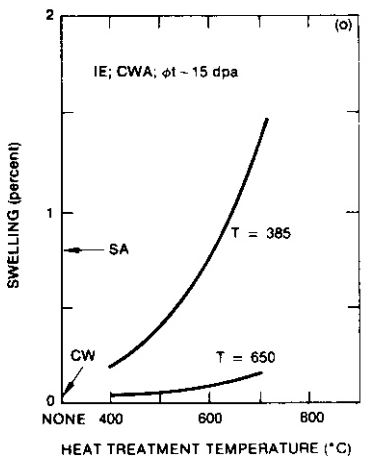

Figure 1 cont.

[18,22,23]. Some spatial associations of the microstructures are also shown. It is notable that over broad temperature ranges, voids form predominantly in association with carbide precipitates [13]. Similar spatial correlations are found for the formation of both γ' and some carbides and dislocation structures [22]. Further, the dose at which γ' forms strongly correlates with the nucleation of voids and the approach to steady state swelling in the *450–525*" C temperature range [23].

Indications of void-dislocation structure associates have also been indirectly observed as strings of voids and/or void dislocations network structures. Some spatial correlations are also indicated in Figure A-lm, where the cavity-cavity separation distances are schematically shown to exhibit distinctly non-random distributions [35] (similar plots of combinations of loop, dislocation, precipitate and cavity spacing would be of interest but such data was not available). An extreme example of non-random distributions is the formation, in some cases, of ordered or partially ordered lattices of MS and MC features such as voids, loops and precipitates [36]. Figure A-lm also shows plots of cavity size distribution at two exposure levels; a population of small cavities coexisting with an evolving void structure is indicated in some data [18,26]. Analysis of these results variously suggest that these small sink structures may be helium bubbles, vacancy loops, small precipitates or some combination of these.

Figure A-ln illustrates the shift in transformation time-temperature boundaries in metals under irradiation. New irradiation induced phases also appear such as y', *G* phase and rod shaped precipitates; phases which would form under thermal aging may not occur under irradiation (i.e. M_6C and Laves in fast reactor irradiations) [28]. Not only are these boundaries shifted by irradiation, but the nominally standard phases may have non-standard compositions and/or morphologies [22]. It is particularly notable that higher helium levels appears to alter the MC evolution paths [28]. Conversely, the precipitate structure of Ti modified 316 has been shown to have a significant and bene-

ficial effect on the influence of helium on both swelling and ductility. It is believed this is related to the Ti carbide precipitate misfit parameters [28]. The path of MC and, hence, coupled MS evolution is also strongly influenced by MS_θ and MC_θ. Figure A-lo shows the effect of thermomechanical treatment on void swelling at two irradiation temperatures, clearly illustrating this point [22,24].

Of course numerous other microstructural response features could and should be shown. A few important examples include: segregation of oversize solutes away from and undersize solutes towards surfaces [12]; irradiation induced ferritic phase transitions in *304 SS* [37]; the effect of irradiation on precipitate size distribution (a crucial feature of nickel based precipitation strengthened alloys) [10]; and the very high density of ordered voids arrays often observed in refractory alloys (perhaps indicative of a homogeneous nucleation and void sink dominated microstructural evolution) [36].

However, even this partial phenomenology demonstrates the clear necessity to go beyond simple "one mechanism, single microstructural feature modeling." Further, viewed comprehensively this data compilation provides a basis for developing a conceptual model of microstructural evolution in stainless steels needed as a basis for quantitative model development.

A3. Conceptual Model For Microstructural Evolution

The most profound conclusion that can be drawn from examining the data illustrated in Section A2, is the strongly correlated nature of the evolution of the various microstructural features. This suggests a dominant underlying mechanism. Indeed, the mechanism is obvious--the coupled segregation of point defects and chemical constituents. Hence, the basic problem is obtaining microscopic material balances. Therefore, a proper combination of accounting procedures, such as rate theory, and the comprehensive data base should, in principle, provide a powerful tool for predicting many of the features of ME.

A non-unique but, nevertheless, physically consistent conceptual description of ME based on the empirical evidence and aided by

the modeling results described in Section 4, goes as follows.

Vacancies (V) and interstitials (I) and, perhaps, small defect clusters are produced along with transmutants (helium, hydrogen and solids) by the primary neutron irradiation. The clusters have finite lifetimes and will eventually reach a quasi-steady state concentration by emitting and/or absorbing vacancies and interstitials.

The lattice diffusion of the various mobile species is highly interactive and can be described in terms of chemical potential gradients and partial diffusion coefficients (including correlation factors). The transport equations have cross terms which are dependent on point defect, solute (or transmutant) and trap concentrations [7-9]. In the rate theory formulation (involving time and spatial averages over population distributions of the various source-sink terms) coupled partial differential equations are used to model the recombination of vacancies and interstitials and the net accumulation of the various diffusing species at sinks. The partitioning is a function of the diffusion coefficients, defect generation rates and effective sink strengths, including bias factors and local chemistry, etc.[4-6]. Again, quasi-steady-state, or a condition of slowly changing fluxes, is quickly reached in most circumstances involving constant irradiation.

Initially the V and I go to preexisting dislocation sinks including vacancy loops, or are recombined primarily at solute trapping sites. Some of the I, however, coalesce to form Frank loops, again primarily at trapping sites. Helium (He) also easily nucleates bubbles either homogeneously in the lattice, or at trapping sites such as preexisting precipitates or dislocations.

Loop populations increase rapidly and undergo bias driven growth to a maximum size where they unfault by intersecting other dislocations; loop nucleation is continuous throughout the irradiation [5]. Simultaneously, new He bubbles are nucleating and previously Eormed bubbles grow with the addition of He. Buildup of sinks for He eventually slows the bubble nucleation process. Both the loops and bubbles are sites for solute segregation; this can alter their bias

factors and effective defect sink-source strengths. For example, coating of bubbles may reduce their surface induced bias for I, alter the rate controlling processes of point defect absorption from diffusion to surface kinetics, and influence V emission rates [5].

Continued segregation to sinks can also lead to second phase precipitation. Segregation of Si by tightly bound Si-I complexes explains the association of γ' with interstitial loops [22]. Segregation and precipitation at bubbles many offer a partial explanation of the association between voids and some carbide precipitates.

The density of cavities and some other microstructural features is largely determined by the nucleation of He bubbles and loops. Bubble densities and spatial distributions are governed primarily by He mobility, trapping characteristics, generation rate; and, perhaps, resolutioning by cascades and collisional coalescence of small mobile bubbles [38]. Loop nucleation and growth is primarily governed by interstitial trapping mechanisms. Cavity and loop density dependence on temperature and He generation rate and, to a lesser extent, dpa rate and stress are consistent with this model. Non-random spatial distributions of cavities such as strings and void-precipitate associations can be partly rationalized on the basis of He trapping and bubble nucleation at dislocations and precipitate interfaces.

The helium bubbles are distributed in size and are the precursors for the formation of voids. The transition of bubbles to voids is governed by temperature, stress, damage rate, bubble size (helium content), bubble chemistry (surface energy and sink/source characteristics), the number of lattice trap or recombination sites, overall sink structure, and the microchemically dependent partial diffusion coefficients. Fast diffusing species (if they migrate by the vacancy mechanism) would alter cluster vacancy emission/absorbtion kinetics. Solute trapping (or equivalently excluded volume lattice diffusion mechanisms) would increase recombination. It is important to realize not only that it is possible for these diffusional effects to occur simultaneously, but also that they derive from the same basic mechanisms:

variable solute–defect binding–exchange interactions. Understanding and quantifying the physics of these processes requires accurate determination of the exchange terms in the partial diffusion coefficients and correlation factors [7-9].

The local sink chemistry may be critically important. Irradiation induced alterations in sink chemistry are mechanistically the consequence of' segregation due to net point defect fluxes. If the only transport mechanism is by preferred V exchange, or strong V drag, concentrations in the vicinity of a sink will depend on the net V accumulation (assuming no sink–solute binding or precipitation). Hence, constituents with lower diffusivities, such as nickel in stainless steel, would tend to concentrate at all of the sinks and would correspondingly be depleted from the lattice. The precise effect of local chemistry on sink characteristics involves several factors which need considerable study to quantify. Undersized SA which form strongly bound I complexes will be transported to sinks by I fluxes, but away only by V mechanisms. If the effective transport efficiency of I is much larger than for V, appreciable SA concentrations at sinks must develop, [8]. This is indicated by Si segregation at dislocations, and loops and cavities [21,22]. Transport efficiencies depend on constituent concentrations, binding energies and the various exchange frequencies. Back fluxes of solutes from sinks limit segregation; hence, precipitation may be needed to permanently remove species from the lattice. Thus, while some sinks are necessary for segregation to take place, a high sink density may prevent or slow precipitation, if local solubility limits are not exceeded. There may be considerable constituent cycling between sinks. For example, Si initially segregated to cavities may end up in precipitates at some later stage of irradiation.

The influence of thermomechanical treatment on MC evolution also qualitatively derives in part from these considerations. Irradiation induced sinks are sites for segregation and are sensitive to lattice diffusional processes. The net point defect and solute fluxes depend on the solute activity; hence, on prior heat treatment in meta-

stable alloys such as *ss*. Similarly, the effect of He, which influences sink structures, might be explained.

Bubbles evolve towards a transition to void growth due to accumulation of helium and microchemical evolution. Segregation processes probably tend to enhance bubbles as void formation sites, and remove solute from the lattice. This lowers trapping-induced recombination, and promotes void growth. After this incubation period, voids form on some, but not necessarily all, bubbles. With the buildup of sinks and exhaustion of the MC propensity to further promote bubble-void conversions, the void nucleation slows and finally ceases. There may be, therefore, a coexisting cavity sink structure of voids and small bubbles which act as neutral sinks. Temperature change experiments and/or charged particle irradiation of neutron preirradiated material resulting in new populations of voids would tend to support the hypothesis outlined above.

Microchemical evolution is dominated by point defect induced segregation. Segregation also tends to slow with time due to back fluxes, precipitation, lattice exhaustion; and, perhaps, with the equilibrating of sink cycling mechanisms. However, segregation effects do not explain all the phase instabilities observed. Numerous alternative mechanisms have been proposed [lo-111, ranging from cascade induced coherent precipitate nucleation [15] (this may be the consequence of segregation on the cascade scale) to complex local extended defect sink-precipitate interactions [39] (as suggested to explain the reprecipitation of γ' in Ni-Si alloys). In particular, thermally driven aging processes occur simultaneously and may be either enhanced or retarded by irradiation. For example, depletion of lattice concentrations may cause otherwise stable precipitates to dissolve. Proper modeling of coupling between thermal and irradiation ME is very important. The evolution of the microchemistry of the lattice would suggest a fluence dependence of the temperature sensitivity of swelling rate, which has been observed [18].

Dislocation structure simultaneously evolves towards a quasi

steady-state. This is due to equilibration of nucleation and annihilation rates of Frank loops; annihilation is due to loop growth to the point of intersection with other dislocations, leading to unfaulting. The unfaulted loops are a source of line dislocations. Line dislocations are, in turn, annihilated by reactions with dislocations of opposite sign, due to irradiation induced climb. At quasi-steady state, the unfaulting source of line dislocations equilibrates with the climb induced annihilation (i.e., loop nucleation ≡ loop unfaulting ≡ dislocation line source ≡ dislocation line annihilation due to climb).

Further evolution of the microstructure is slow, and dominated by steady state swelling largely governed by sink structure, and sink and lattice chemistry. This model predicts a strong tendency towards a roughly equivalent steady state swelling which has been reported in 300 series alloys.

The effect of stress on microstructural evolution can be modeled primarily in terms of its influence on source-sink efficiencies including bias terms [6].

The phenomenology outlined above involves a complex codiffusion and coprecipitation of gas atoms, point defects and chemical constituents; the major driving fource for the ME process is net point defect fluxes due to variable sink bias factors and solute-point defect-flux couplings.

Further insight into how such coupled MS-MC evolution can be modeled by applying basic conservation principles is illustrated with a simple example. For a particular void swelling (S), there has been a net accumulation of J_v^n vacancies to voids, $J_v^n \simeq S/z$, where z is the effective I-dislocation bias factor; similarly J_I interstitials have gone to voids, $J_I \simeq S(1-z)/z$. Taking S = .1 and $z \sim .1$ $J_V \sim 1$ v/atom(a) and $J_I \sim .9$ I/a. Vacancy emission totals can be used to calculate total vacancy fluxes in and out of sinks. Clearly, if V and I can transport SA by preferred binding or exchange mechanisms, such large mass flows can give rise to considerable segregation.

Segregation can be phenomenologically represented in terms of

transport efficiencies/defect $\varepsilon_{v,i}$; where $\varepsilon_{v,i} = J_S^{v,i}/J_{v,i} = f(T,C_S,K_S)$ and $J_S^{v,i}$ is the defect-induced solute accumulation, C_S the solute concentration and K_S a sink term. The ε's can be derived for both dilute and concentrated limits and approximately related to measurable quantities [7-9]. Hence, segregation at an evolving microstructure of sinks can be modeled as a time averaged sum over all transport mechanisms, flow directions, sinks and solute species. Further, the requirement of an overall material balance in the alloy system can be imposed. This approach is easily adaptable to microstructural evolution models; results of calculations of combined microstructural-microchemical evolution models will be presented in future publications.

A4. Quantitative Models and a Modeling Strategy

The preceeding discussion provides a consistent picture of most of the highly correlated ME behavior represented in Figure A-1. However, computer models must be used to translate this qualitative phenomenology to a quantitatively predictive tool.

Numerous mechanisms have been proposed to explain various aspects of microstructural evolution. Often the postulated mechanisms have been developed only qualitatively and in isolation from competing mechanisms, and, only for one microstructural feature--e.g., void growth. In addition, numerous matallurgical, defect and defect production parameters are needed to quantify these mechanisms and precise values of these parameters are not always available. A summary of some of the mechanisms which have been proposed is shown in Table A-1.

A proper goal of quantitative modeling is to identify those combinations of mechanisms and parameters which are consistent with experiment. This means identifying physical regions of mechanism-parameter space (MPS) by comparing the predicted to experimental microstructural responses based on available data. Since numerous combinations of mechanisms ard parameters may fit particular sets of data, and the data is itself highly scattered, an efficient *MPS* mapping strategy must be developed.

Table A-1
SOME MECHANISMS INVOLVED IN MICROSTRUCTURAL EVOLUTION

Mechanism (parameters, submechanisms)

DEFECT PRODUCTION
- Cascade Clusters and Loops (efficiency)
- Free Defects (fraction/dpa)
- Transmutants

MIGRATION AND RECOMBINATION
- Correlated Diffusion (partial diffusion coefficients including exchange frequencies and correlation factors; activation energy for $He_S + I \rightarrow He_I$)
- Trapping (binding energies, solute clustering, saturability)
- Recombination (recombination volume; sink effects)
- Stress Effects and Free Energy Gradients

C. SINK STRENGTHS
- Geometric Parameter
- Efficiency (transfer velocity; shell effects-diffusivity, changes and image interaction effects; shape effect; bias factors; stress effects, pinning effects)
- Multiple Sink Corrections (all sink strengths and distributions)

D. NUCLEATION MECHANISMS
- Homogeneous Nucleation (defect parameters; surface, dislocation and stacking fault energies; segregation; and gas pressure)
- Heterogenerous Nucleation (all above; nucleation sites-cascades, ppt., bubbles, dislocations)
- Bubble Nucleation (helium diffusivity; trapping; resolutioning; small bubble mobility and driving forces)
- Critical Bubbles (He compressibility; surface energy; bubble chemistry; defect fluxes)
- Solute Segregation (see phase instabilities below)
- Precipitate Dissolution (cascade effects)
- Coprecipitation of He, V, I and SA extended defect complexes

E. GROWTH MECHANISMS

Sinks (sink ratios; effective bias factors; sink annihilation fractions)
Emission Kinetics (sink chemistry, stress and gas pressure; dislocation interactions and cavity dislocation networks; dislocation evolution, MC evolution)

F. PHASE INSTABILITIES/SEGREGATION

Enhanced Diffusion (vacancy concentrations)
Thermal Instabilities/Segregation
Disorder and Recoil Dissolution (sputtering, disorder parameters)
Chemical Vacancies (misfit and defect parameters)
Diffusional Instabilities and Sinkless Segregation
Cascade Microsegregation (cascade physics)
Cascade Amorphization
Segregation (partial diffusion coefficients, transport efficiencies, sink structure, solubility limits)
Defect-Precipitate Interactions (dislocation cutting, local sink effects)
Stress Effects

G. ATYPICAL PARAMETERS AND CONDITIONS

Pulsed-Stresses, Temperatures and Fluxes;
Near Surfaces; Time Dependent Contamination;
Foil Stress State; Damage Gradients;
Self Ion Injection

The strategies used in this research include: a) use of models tailored to application--simpler models for mechanism studies and scoping MPS, more comprehensive correlated ME models for the engineering data base and ultimate extrapolations; b) derivation of relatively simple submodels from detailed mechanism studies in forms compatible with inclusion in composite models; c) attempts to use a minimum number of parameters or parameter groups which can be measured in independent experiments or uniquely derived from particular parts of the data base; d) conducting sensitivity studies and statistical model comparisons with the broad data base (as opposed to specific sets of observations) to ascertain various contributions to discrepancies--such as model inadequacy and data scatter; e) attempts to cast both data and model results in terms of parameters which maximize the sensitivity of comparisons and the physical basis for interpretation.

Models developed or under development in this work include: a) the effect of irradiation pulsing on extended defect nucleation and growth; b) bubble nucleation and formation of voids on bubbles which have exceeded the critical size for continuous vacancy driven growth; c) void growth models with direct or parametric treatment of most of the numerous mechanisms which have been postulated to influence swelling and dislocation structure evolution; and d) composite models of the nucleation and growth of various MS and MC features.

Examples of the modeling calculations have been presented previously [38-40]. Generally it is possible to obtain reasonable agreement between the model results and data for a number of materials and experimental conditions using reasonable sets of parameters and mechanisms.

Therefore, it is useful to attempt some tentative extrapolations of the model to fusion reactor conditions. Such an extrapolation is illustrated in Figure A-2 where a model calibrated to fast reactor irradiations of stainless steel is extended to higher helium generation rates G_{He}. An additional adjustable parameter, cavity density N_C, was assumed to vary as $N_C \alpha G_{He}^P$ $1/4 < P < 3/4$. (See references 38 to 40 for a discussion of the effect of helium on cavity density, and Figure 1-Ae.)

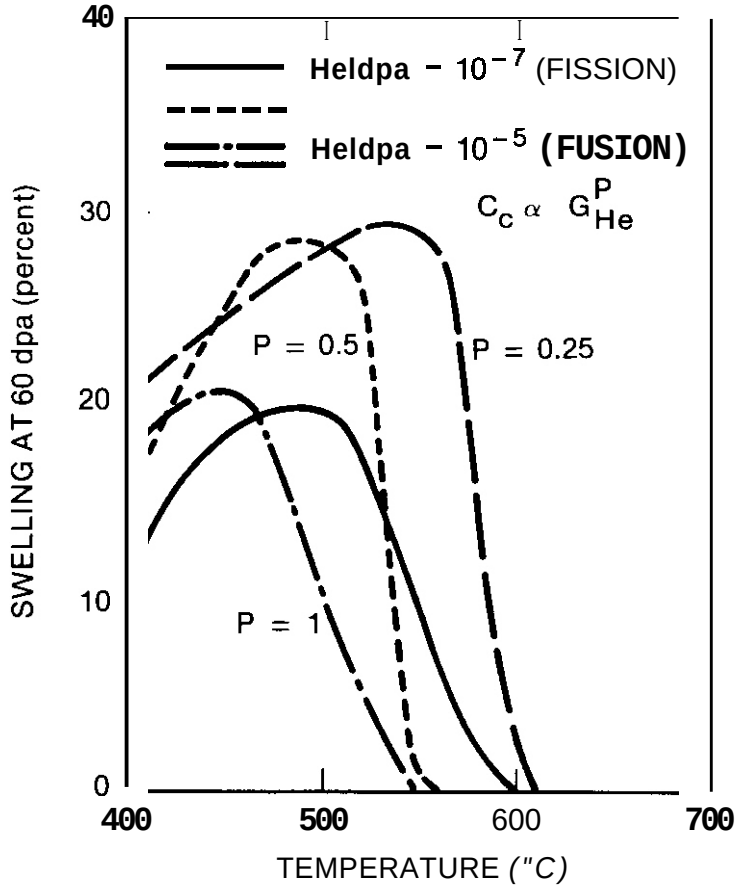

Figure A-2 Model predictions of swelling under fusion reactor conditions

The results indicate that swelling in fusion environments at 60 dpa is slightly increased for a P <1/2 up to T ~ 550, but is less for T ~ 550 for P $\geq$ 1/2. This is the consequence of very high cavity densities (i.e., 7.5 x 10^{15} voids and 7.5 x 10^{16} bubbles for fusion conditions at T = 500 and P = 1/2) and is contrary to some other model predictions which have been reported. Physically it is a consequence of the combination of bubbles acting as sinks for both helium and point defects, void-dislocation sink strenth ratios, and the smaller size of voids at high densities. Indeed, if lower cavity densities are used and other parameters adjusted to maintain reasonable agreement with 304 SS fast reactor data, higher swelling at fusion He/dpa ratios is maintained up to 600° C.

It should be emphasized that none of the model results presented here directly account for MC evolution effects. Further, corrections for other potentially significant differences between fission and fusion environments, viz., pulsing, damage rate, primary recoil spectra and hydrogen generation, have not been made in the extrapolations. In addition, these examples are not meant to suggest that swelling should be the only focus of modeling efforts. Clearly, phase instabilities and helium content and grain boundary distributions are critical factors in high temperature mechanical behavior and are also being studied in this research.

Finally, model prediction-experimentcomparisons are not as simple as the examples reported previously might suggest. First, all of these calculations are model and parameter sensitive. Different sets of mechanisms and parameters which also fit current observations (i.e., regions of MPS) may lead to different extrapolated predictions. Only with further model development, thorough mapping of MPS, and data acquisition will it be possible to place physically justifiable and usefully narrow bounds on predicted responses. Such mappings have not yet been completed. Preliminary results indicate, however, that simultaneously modeling several microstructural features and using the broad data base will be helpful in limiting *MPS* regions, i.e., in reducing the problem of non-uniqueness.

As noted previously, the experimental data is often highly scattered. This variability derives, in part, from experimental uncertainty (i.e., errors in irradiation temperatures and fluences) and, in part, from failure to properly account for all variables such as MC_o. Therefore, *MPS* maps, which are really systematic representations of model sensitivity, can be used to discriminate between the fundamental sources of such variability.

Probably more important than the quantitative results, the modeling studies have supported many of the features of the qualitative model described in Section A-3. Particularly germane to extrapolating to fusion conditions are the following tentative conclusions: a) a strong and time dependent correlation between microstructure and microchemistry, linked primarily through effective point defect mobilities, and sink structure and chemistry; b) influence of the initial nucleation microstructure on subsequent growth stages (therefore, there is a strong sensitivity of ME to bubble nucleation and growth kinetics; hence, helium transport mechanisms) and c) increases in helium generation rate can lead to either increased or decreesad swelling depending on the particular region of model *MPS* and set of damage parameters--viz. dpa rate, He/dpa ratio, temperature, and material parameters. The physical basis for b) and c) have been discussed elsewhere and will not be reviewed further here [38-40].

It may be possible to draw some implications for alloy development efforts from modeling analysis. Clearly a radiation resistant alloy would ideally promote vacancy and interstitial recombination and maintain helium in solution in the lattice. However, as often noted, SA trapping sites tend to be removed eventually from solution by concomitant segregation mechanisms. While high Ni content appears to improve lattice resistance to swelling, higher helium contents and, perhaps, lower ductilities are corresponding trade-offs. Further, while fine helium distributions are desirable for minimizing swelling, non-diffusional transport mechanisms such as dislocation drag of dissolved He during stress transients, may result in higher grain boundary helium contents than would occur if helium were located in larger, less mobile cavities.

The formation of a high density cavity dominated microstructure has previously been suggested as a possible means of promoting irradiation stability [39]. Such cavity structures might be produced by laser or shock hardening or by small ^{3}He gas bubbles generated by the "tritium trick." Figure A-3 illustrates how swelling can be reduced in a cavity dominated microstructure; here swelling at 60 dpa for fusion reactor conditions is plotted against cavity density. The effective bias factor is also varied to reflect possible dislocation pinning and cavity-dislocation network effects. Such a cavity structure, if it remained stable, would trap essentially all the helium and would resist being transported to grain boundaries by dislocations. While cavities would be sites for solute segregation, reasonable lattice solute concentrations might be maintained by back fluxes if local solubility limits are not exceeded because of the high surface areas. One detrimental feature of such an alloy might be a low tensile ductility due to bubble strengthening-flow localization mechanisms. In any event, if such a suggestion were to be pursued seriously, it would be necessary to optimize bubble/cavity densities and sizes considering several potential failure modes.

A5 Summary and Conclusions for Microstructural Evolution

Thisreport has attempted to outline the CCMA approach to utilizing the available data base to extrapolate to conditions not experimentally accessible. The strongly correlated nature of ME has been emphasized. Further, it has been suggested that comprehensive rate theory models resting on the principal material balances, focussing on segregation processes, and phenomenologically representative of the various interacting mechanisms may be a practical approach to tracking the fates of both point defects and chemical constituents. Whatever models are ultimately developed, it will be necessary to limit the number of viable mechanisms and parameters; a systematic and efficient mapping strategy based on comparison of composite model predictions with the broad data base, and the results of careful mechanistic studies will be required to accomplish this goal. Finally, ultimate model validation and calibration must be carried out in a facility such as FMIT.

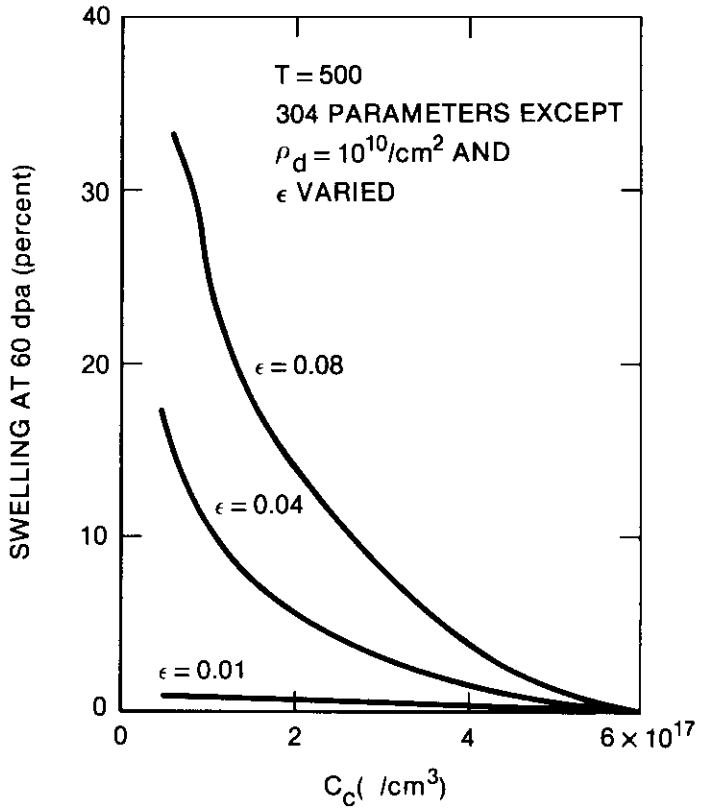

Figure A-3 Model predictions of the effect of high cavity density on swelling for fusion reactor conditions.

B. Mechanical Properties, Mechanical Modeling - G.R. Odette, D. Frey
(University of California, Santa Barbara)

B1 Introduction

In-service mechanical property degradation leading to premature failures of fusion first wall structures is potentially one of the most serious obstacles to commercial fusion power.

Alloy development and fusion design efforts are confronted by at least three major problems when attempting to assess the effect of in-service irradiation, including:

1. There is no completely proper materials test environment in terms of appropriate combinations of neutron spectrum, flux, volume, and time history of temperature, flux (ϕ) and stress, which simulates the fusion environment.

2. The most proper high flux test environments will have small irradiation volumes (<1000 cm^3 for $\phi > 10^{14}$ n/cm^2-sec and < 10 cm^3 for $\phi > 10^{15}$ n/cm^2-sec).

3. There are a large number of potential structural failure modes ranging from creep rupture to catastrophic fracture.

In order to relate the data obtained in test irradiation environments to conditions in fusion reactors, a proper correlation methodology which rests on a firm physical understanding of the radiation effects and on structural failure modes is needed. One important component of such a methodology is developing a better understanding of the relationship between microstructure and properties and simple properties and fracture parameters (other components include high energy neutron and fission reactor data base development, extracting useful mechanical property information from very small test volumes, and establishing the connection between properties/fracture parameters and design criteria). Understanding the relationship between microstructureandproperties would not only be beneficial in optimizing the use of the small test volume in high energy neutron facilties, and in providing a better basis for extrapolating fission reactor data, but also might promote more rapid advances in the development of irradiation

resistant alloys. At least three general classes of analytical tools can be used in such studies, including micromechanical models of flow and fracture; flow, fracture and corresponding microstructure maps; and advanced test/failure analysis methods, including finite element techniques.

Preliminary results of correlating microstructure and yield stress σ_{ys} in irradiated 316 stainless steel have been presented previously [41]. In the work reported here an empirical relationship is used to relate yield and ultimate stress to uniform elongation. Extension of this general approach to other fracture modes is also discussed briefly, with specific application to plane strain fracture toughness.

B2 Correlation of Ductility Parameters

Obviously, knowledge of yield stress alone is not sufficient to design engineering structures. Therefore, an attempt was made to correlate changes in an important ductility parameter, uniform elongation, against changes in the yield and ultimate strengths σ_u. Such correlations are of interest for several reasons, including 1) success or failure of correlations may provide indications of fracture mechanisms; 2) it may be possible to derive only strength data, for example, in an indentation hardness or microtensile test measurement used in small volume high energy neutron experiments (actually, it has been suggested that ductility can be estimated in hardness tests; however, the ductility-strength correlations would provide an independent check on the validity of this assertion).

We have found that uniform elongation ε_u of irradiated and unirradiated stainless steels can be roughly correlated by a simple linear expression

$$\varepsilon_u = C_1 \left(1 - \frac{\sigma_{ys}}{\sigma_u}\right) \qquad (B.1)$$

where $C_1 = .5$ is a function of the macroscopic work hardening coefficient. Figures B-1a - c compare predicted uniform elongations as a function of exposure for T = 400 to 600° C. using Equation (B.1), the yield stress model

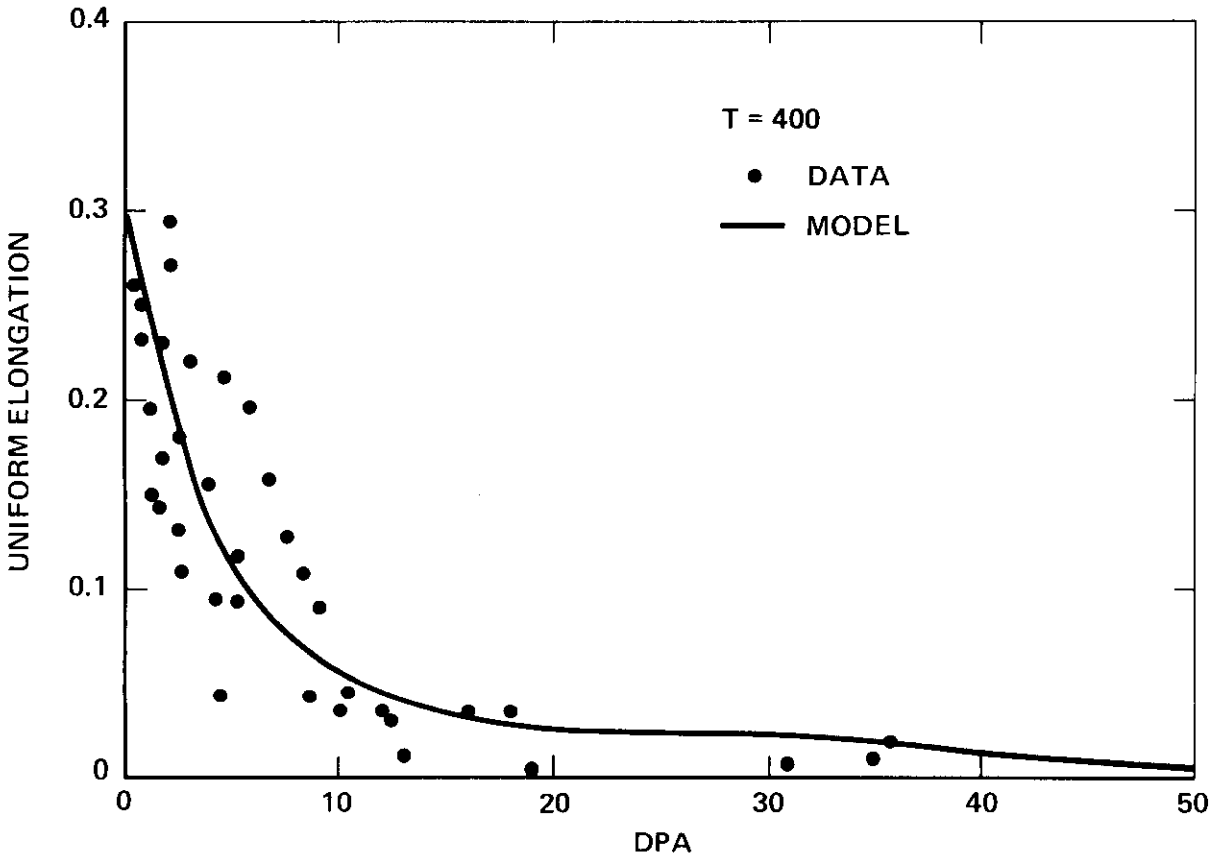

Figure B-1a. Comparison of model predictions and data for uniform elongation of irradiated 316 stainless steel, T = 400°C.

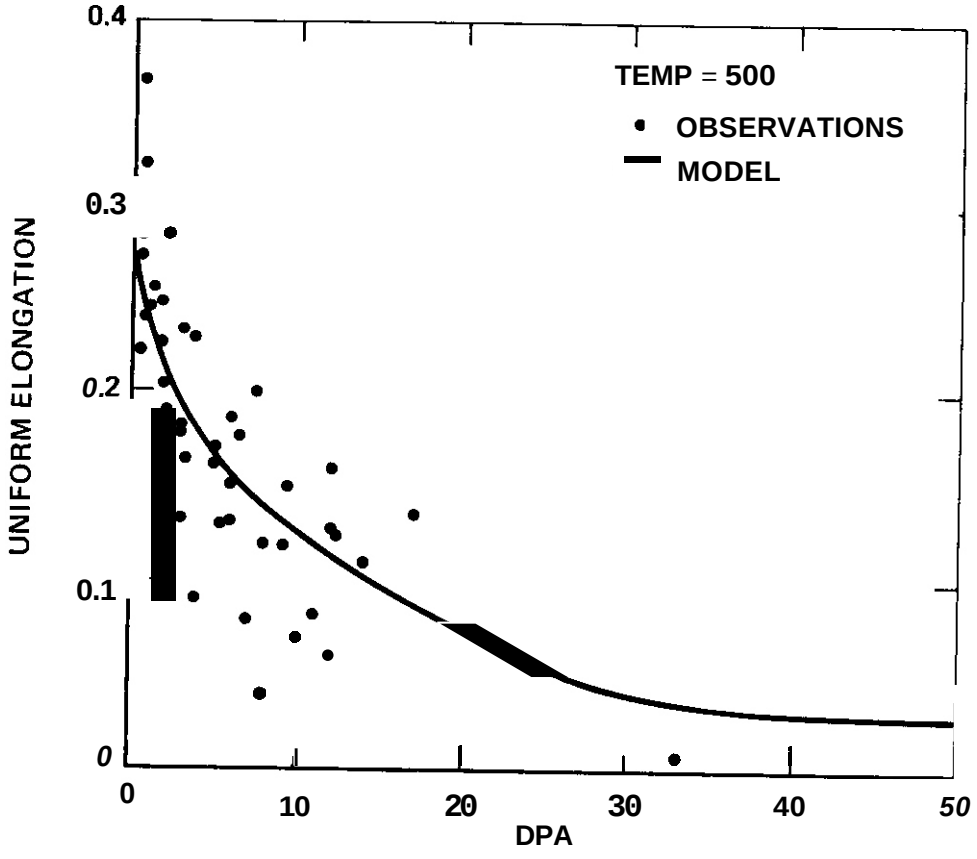

Figure B-lb. Comparison of model predictions and data for uniform elongation of irradiated *316* stainless steel, T = 500.

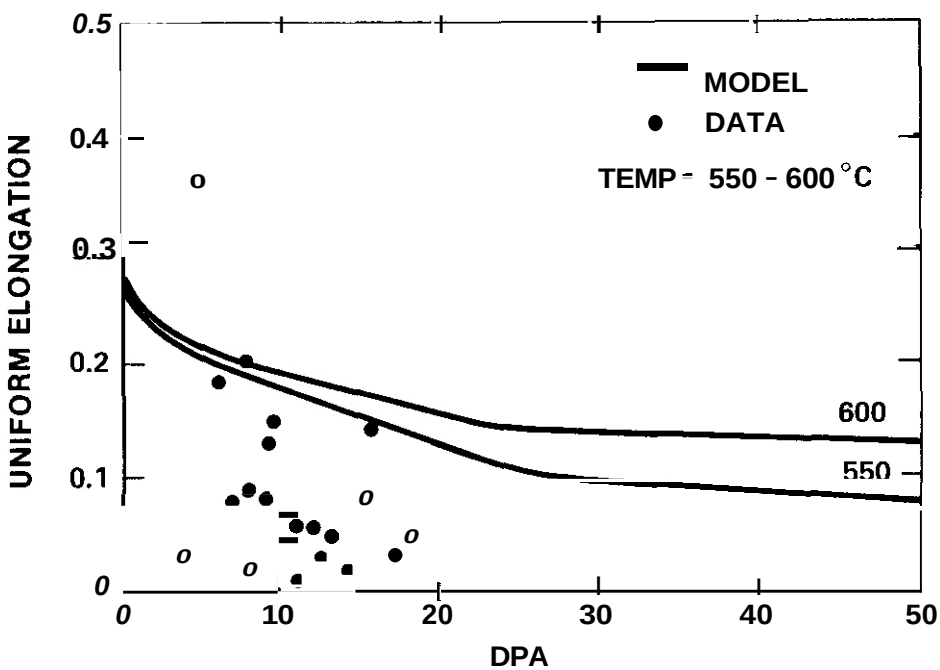

Figure R-lc. Comparison of model predictions and data for uniform elongation of irradiated 316 stainless steel, T = 550-600

described previously [41] and an empirical model of $a_u = f(T,dpa)$ derived from the data base [44]. Clearly, the model and experimental results are in agreement only at low temperatures and moderate exposures and at higher temperatures at low exposures. Figure B-2 crudely maps the regions where the model is applicable as a function of temperature and exposure; in this case, however, actual σ_{ys} and σ_u data, rather than model calculations, were used to compute E_u in Equation (B.1). Closer examination of the data reveals that there is a systematic deviation from Equation (B.1) which can be approximately expressed in terms of an implicit variation of $C_1 = f(\varepsilon_u,T)$. For example, using least Squares fits to the data C_1 is .36 for $T > 600°$ C. and $E_u > 0$, but is only .2 for the range $0 \leq E_u \leq .05$; similarly, for $T < 600$" C_1 decreases from .52 for $\varepsilon_u > 0$ to .38 for $0 \leq E_U \leq .05$.

At high temperatures and moderate to high fluences the deviations may be due to an effect of grain boundary helium, even in relatively high rate tensile tests. Indeed, this is consistent with interpretations given previously [44], which indicate that at increasing temperatures $T \gtrsim 600°C$. a transition between transgranular flow controlled, and intergranular diffusion or creep controlled fracture occurs; in this regime, a combination of matrix hardening and helium grain boundary embrittlement govern fracture strains. While this interpretation is probably oversimplified, it suggests that the high levels of helium in fusion environments may reduce tensile ductility even more.

The helium mechanism is not, however, a likely explanation of the behavior at lower temperatures and higher fluences, where intragranular ductile fracture is observed. It is of interest, therefore, to consider the microstructure in the various regimes giving rise to the "hardness state" of the alloys. Previously [41], we observed that the major component of the hardening structure is dislocations which develop early in irradiation. If, as suggested in the yield stress calculations, the irradiation induced dislocation structure behaves in a manner roughly equivalent to a similar cold-worked structure -i.e., has similar structure parameters -subsequent deformation should proceed along the stress-strain curve more-or-less normally. At high fluences, however, cavity structures develop and contribute a small but significant fraction to the strength. Hence, subsequent

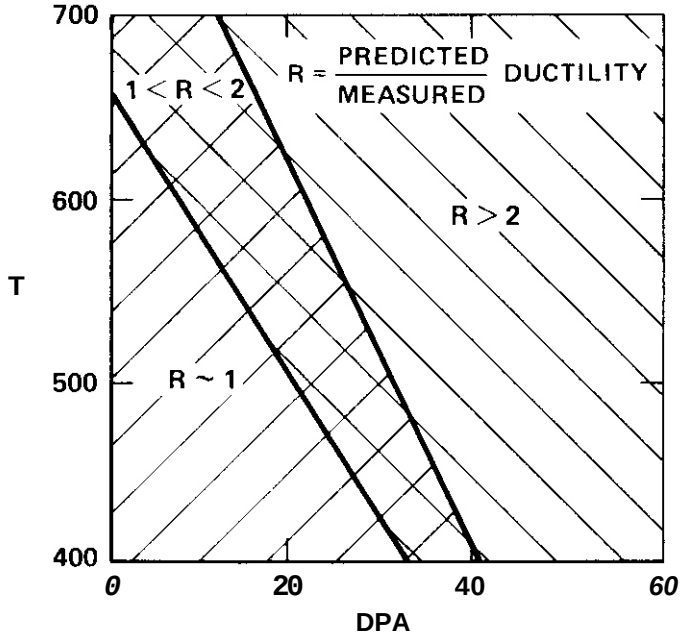

Figure B-2. 316 stainless steel ductility map showing ratio of model prediction/experimental ductility.

deformations may no longer follow the "normal" dislocation structure dominated path. In particular, severe flow localization, and in the limiting extreme, channel fracture occur under these conditions. Channeling has traditionally been viewed as a consequence of shear induced destruction of dislocation obstacles, such as cavities, and/or reduction in cross slip. Further support to this hypothesis is lent by the fact that 316 has somewhat higher ductility in the cold-worked relative to the solution annealed condition at fluences of 30-40 dpa, since significant void swelling is lower in the cold-worked material [46]. It has been observed that deformation and ductility of cold-worked 316 can be modeled by an unirradiated equation-of-state form up to fluences of 40dpa by making small adjustments of the hardness parameter [40]. This may need to be modified at higher fluences where cavity structures become important.

We will not pursue these speculations further except to note that while the equation-of-state approach is both practically and fundamentally appealing, its use will be greatly enhanced if it can be mechanistically interpreted in terms of specific microstructural features.

B3 Fracture Toughness

Clearly, extension of such procedures to other potential fracture properties would be desirable. However, this is not straight-forward since the micromechanical mechanism are generally significantly more complex and/or there is no appropriate data base for analysis. Further, these properties are generally much more sensitive to test details and conditions. Therefore, we will discuss only briefly some aspects of applying micromechanical models to fracture toughness. We believe, however, that improved creep rupture, crack growth, fatigue and creep-failure correlations can also be developed, and this will be pursued in future reserach.

It is not clear that plane strain fracture toughness K_{Ic} is an appropriate measure of static crack propagation resistance for thin first wall structures (indeed, geometries are likely to be in the plane or, perhaps, even antiplane stress state modes [48]). However, K_{Ic} should at least provide lower bound effective toughness limits.

A number of micromechanical treatments have been developed to model the effect of tensile properties and microstructure on K_{lc}. In the simplest form [49]

$$K_{lc} = \left[\frac{4E}{\pi(1-\nu^2)}\right]^{1/2} (L\,\sigma_y\varepsilon_f)^{1/2} \qquad \text{(B-2)}$$

where surface energy terms have been neglected and perfect elastic-plastic behavior assumed. Here E is the Youngs Modulus, ν Poissons ratio, E_f a fracture strain parameter and L a measure of the effective plastic zone size. Local fracture may be primarily governed by the spacing of ductile fracture cavity nucleation sites or, alternately, propensity towards intensive shear deformation. The choice of a proper ductility parameter (critical strain) is not obvious since it is known to depend on both stress state and work hardening behavior. For convenience, it can be taken as the uniform elongation divided by three to crudely account for stress state. In materials where fracture is dominated by shear instabilities or flow localization, which is likely in the case of irradiated stainless steel, it has been found that $L \alpha n^2$ where n is the work hardening exponent ($\sigma = ke^n$); hence Equation (B.2) becomes [50]

$$K_{lc} \simeq C_1 n \sqrt{E\,\sigma_y\,\varepsilon_u/3} \qquad \text{(B-3)}$$

and since $n \simeq E_u$ and taking $C1 \sim 1$

$$K_{lc} \sim \varepsilon_u^{3/2} \sqrt{\sigma_Y E/3} \qquad \text{(B-4)}$$

Numerous other approaches, including highly sophisticated computer based analyses can be used to attack this problem; however, the current lack of irradiated stainless steel toughness data suggests that such treatments are not warrented at this time. Figure B-3 shows Klc calculated from Equation (4) using values based on the yield stress model [41] and the empirical ductility correlation procedure of Section B2. Clearly, the

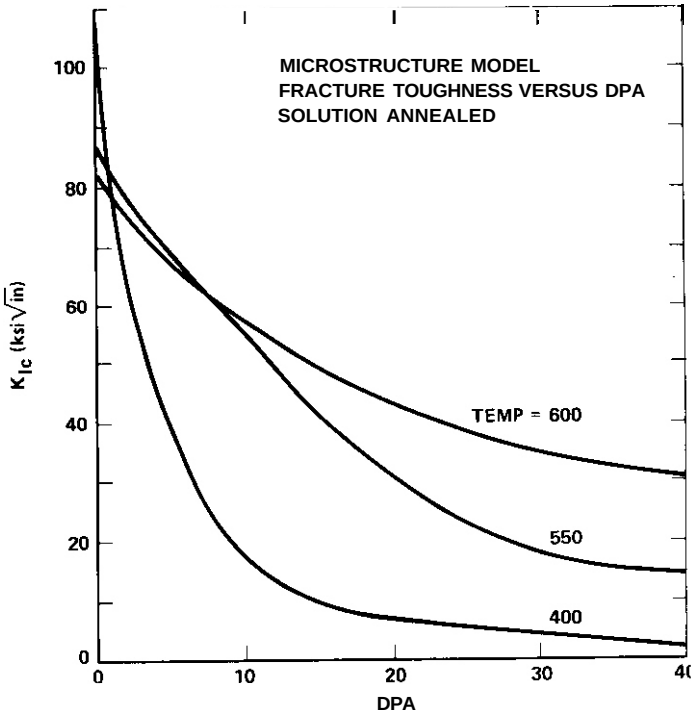

Figure B–3. Model based prediction of fracture toughness in irradiated stainless steel

model predicts a substantial reduction in toughness of irradiated stainless steels. There is little data to compare with these calculations. The absolute values of the toughness tend to be low by a factor of 1 to 2 compared to some values which have been reported for stainless steel [51 - 541. Limited data on irradiated (and some shock hardened stainless steel alloys at an approximately equivalent yield strength) in the range of 1 - 10 dpa (equivalent) and temperatures of 250 - 650°C have indicated reductions in toughness of 30 to 50%. This is consistent with the trends indicated in Figure B-3. In one case involving both metallurgical differences (weld versus plate) and irradiation, a very large reduction in toughness ($\sim$5) was found [54]. The calculations presented here indicate that there may be a significant reduction in toughness in fusion environments. However, data from specifically designed experiments will be needed to determine the actual extent and nature of this problem.

B4. Summary and Conclusion

Some initial steps have been taken to develop physically based correlation methods for extrapolating mechanical property data to fusion environments. The yield stress changes in fast reactor irradiations can be correlated with observed changes in microstructure using simple hardening models. Analysis of tensile ductility data suggests that irradiation may change the deformation-to-fracture path; at higher temperatures this may be associated with grain boundary helium-matrix hardening effects and at lower temperatures with matrix hardening due to shearable cavity structures. A simple micromechanical model was used to extrapolate these calculations to changes in plane strain fracture toughness; while there is not sufficient data to confirm these calculations, the low fluence trends appear to be consistent with limited experimental observations. We conclude, therefore, that microstructural-micromechanical modeling studies will be useful, at least when applied to relatively simple properties.

C. The Flow and Fracture Maps for Unirradiated Solution Annealed 316 Stainless Steel -- S.S. Vagarali and G.R. Odette (University of California, Santa Barbara.)

c1. Introduction

Deformation and fracture in polycrystalline materials occur by several different mechanisms. Therefore, it is convenient to present these mechanisms in the form of maps in which regions for which a particular mechanism is dominant are delineated as a function of critical deformation and fracture parameters. Ashby [55,56] has described in detail the means of constructing such maps. The rapid acceptance of this procedure is evident by the development of deformation/fracture maps for a number of materials. The objective of the present work is to construct detailed flow and fracture maps for unirradiated solution annealed 316 stainless steel; future work will extend the maps to other thermomechanical treatments and irradiated conditions. Some limited results for stainless steel have been presented previously; [57] this work extends and further refines these early efforts.

c2. Flow Map

The deformation mechanisms considered in the construction of flow maps include: a) dislocation glide; b) dislocation creep; c) diffusion creep. The low temperature ($T < .3T_m$) deformation of 316 stainless steel occurs by dislocation glide which is limited by obstacles such as solute atoms, precipitates and other dislocations. Frost and Ashby [57] have analysed this process for 316 stainless steel and the rate equation for dislocation glide is given by

$$\dot{\varepsilon}_1 = 10^6 \exp\left(-\frac{\Delta F}{kT}\right)\left(1-\frac{\sigma}{\sigma_o}\right) \qquad (C.1)$$

where ΔF = strength of the obstacles ($\sim 0.5\ Gb^3$)

σ_o = flow stress at 0°K.

This equation gives a value of 6.3×10^{-3} for normalized athermal flow stress (i.e. σ athermal/G).

Dislocation creep in annealed 316 stainless steel has been investigated by several workers. [58-62] There is considerable scatter in the creep data due to variations in prior heat treatment and alloy chemistry, and hence precise determination of activation energy for creep and creep exponent is not possible. The available creep data in the temperature range from 800 to 1173K is plotted in Figure C-1 in the form of temperature compensated strain rate versus normalized stress. The creep exponent increases from $\sim$ 6.0 at $\sigma/G<2x10^{-3}$ to $\sim$ 12.0 for $\sigma/G>2x10^{-3}$. The apparent activation energy for creep is $\sim$ 450 KJ mol^{-1}. The rate equation for dislocation creep in annealed 316 S.S. is given by

$$\dot{\varepsilon}_2 = 10^{33}(\sigma/G)^6 \exp(-\frac{450000}{RT}) + 2x10^{48}\left(\frac{\sigma}{G}\right)^{12}\exp(-\frac{450000}{RT}) \quad s^{-1} \quad (C.2)$$

The symbols are defined in Table C-1.

Grain boundary sliding is an important mode of deformation during high temperature creep. (Grain boundary sliding is helieved to he controlled by local grain deformation at regions of stress concentration -- e.g. triple points). *Gates* and *Horton [63-64]* have investigated sliding in 316 S.S. in the temperature range from 973 to 1073K and for $\sigma/G<10^{-3}$. Figure C-2 shows a plot of log $\dot{\varepsilon}_{gbs}(\sigma/G)^{-3.8}(\frac{b}{d})^{-1}$ versus the reciprocal of temperature of their data, which yields the following rate equation for ***sliding***

$$\dot{\varepsilon}_3 = 5.6x10^{26}(\sigma/G)^{3.8}(b/d)\exp(\frac{350,000}{RT}) \quad s^{-1} \quad (C.3)$$

It is to he noted that creep exponent and activation energy for sliding are lower than that for dislocation creep. No sliding data is available in the high stress region (i.e. $\sigma/G>2x10^{-3}$).

The rate equations for Nabarro-Herring and Coble creep are given by

$$\dot{\varepsilon}_4 = \frac{14\sigma\Omega D_V}{KTd^2} \quad s^{-1} \quad (C.4)$$

$$\dot{\varepsilon}_5 = \frac{14\pi\delta D_B\sigma\Omega}{KTd^3} \quad s^{-1} \quad (C.5)$$

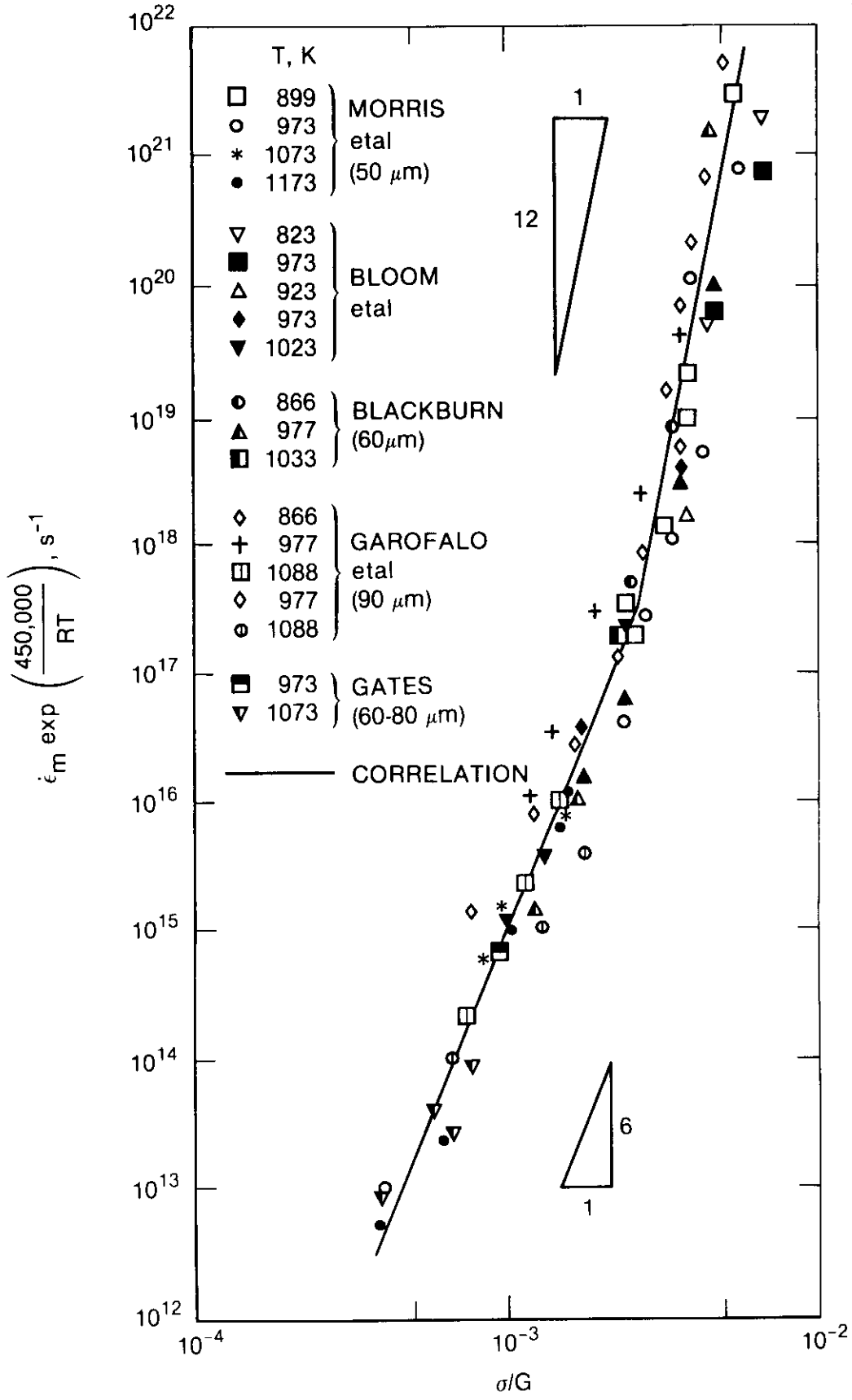

FIGURE C-1. Temperature Compensated Strain Rate Versus Normalized Stress for Unirradiated 316 Stainless Steel.

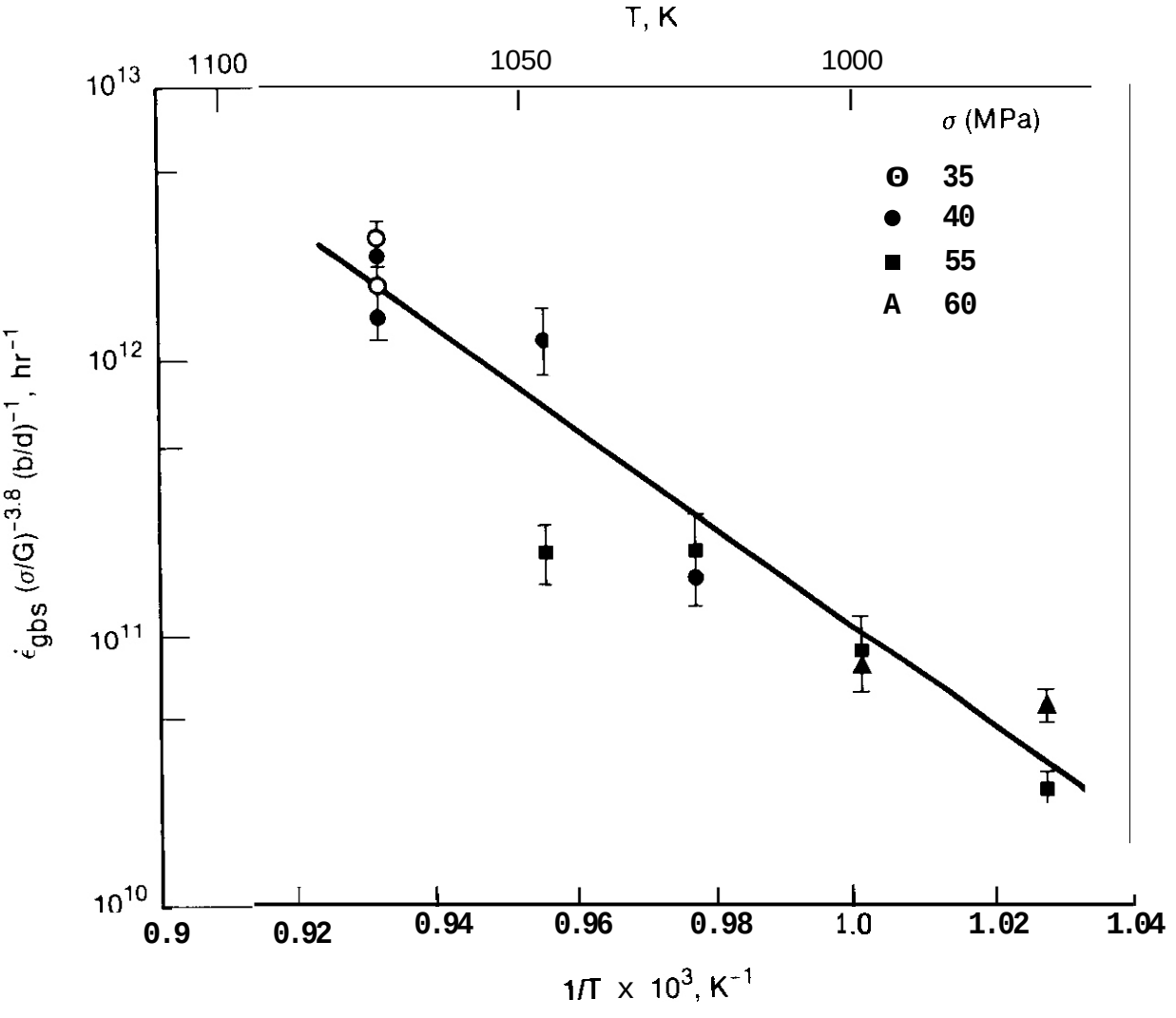

FIGURE C-2. Grain Boundary Sliding Parameter Versus Reciprocal Temperature for 316 Stainless Steel.

A deformation mechanism map for a grain size of 50 μm is constructed using the method suggested by Ashby [55] and is shown in Figure C-3. The parameters used in constructing the map are given in Table C-1. Constant strain-rate contours have been drawn. The relative importance of grain boundary sliding during creep is shown

Table C-1

Parameters Used to Construct Flow and Fracture Maps

Parameter	Symbol	Value
Atomic Volume	Ω	1.21×10^{-29} m^3
Burgers vector	b	2.58×10^{-10} m
Melting Temperature	T_m	1810°K
Shear Modulus at 300°K		8.1×10^{10} Pa
Temperature dependence of shear modulus		4.7×10^{-4} Pa K^{-1}
Lattice Diffusivity	D_v	$4.4 \times 10^{-5} \exp(\frac{280000}{8.32})$ m^2 sec^{-1}
Grain boundary diffusivity	δD_B	$3.6 \times 10^{-14} \exp(-\frac{193000}{RT})$ m^3 sec^{-1}
Nucleation strain	ε_n	0.1
Volume fraction of second phase particles	f_v	0.05
# of particles per unit area of grain boundary	N_B	10^{10} m^{-2}
Effective surface energy of fracture	γ	10 J m^{-2}

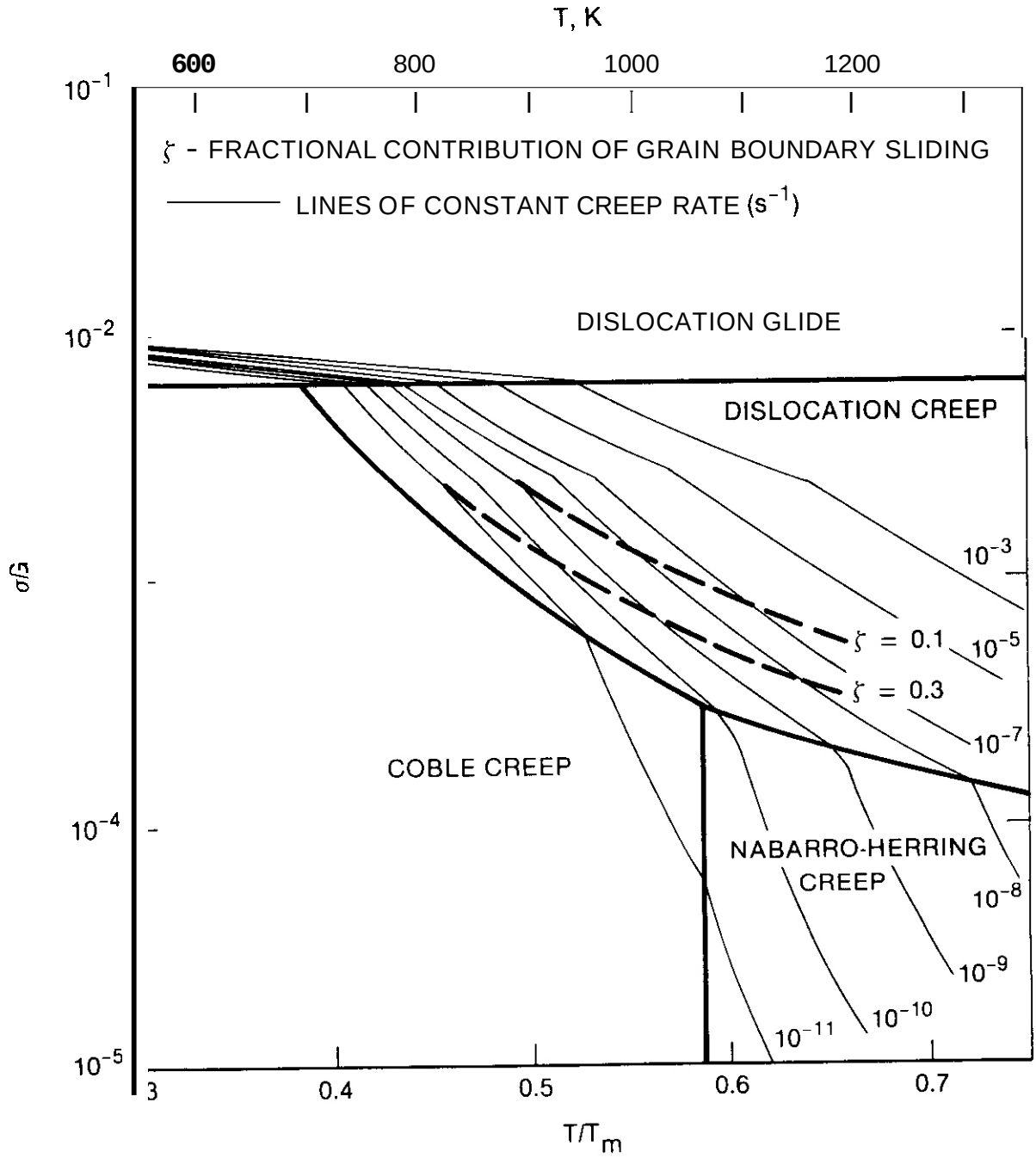

FIGURE C-3. **Deformation Map for Unirradiated** Solution Annealed **316 Stainless** Steel.

in the map by drawing contours for constant strain contribution due to sliding ($\xi = \varepsilon_{gbs}/\varepsilon$). It is evident that ξ decreases with increase in stress and temperature. Another notable feature in the map is that diffusion creep becomes an important mode of deformation at relatively higher stresses as compared to pure metals. This is due to slow dislocation creep rates in the alloy.

c3. Fracture Maps

Elevated temperature fracture behavior of polycrystalline materials may be divided into two categories: a) transgranular creep fracture: b) intergranular fracture.

Both types of fracture involve nucleation and growth of voids. The time to fracture is essentially determined by the time required for voids to grow and coalesce.

In the transgranular creep fracture mode, voids nucleate at second phase particles and grow by the local creep of the matrix. Ashby [56] has analysed the fracture process and time to fracture, t_f, is given by

$$t_{f_1} = \left\{\varepsilon_n + \frac{1}{1.8}\frac{n}{n-1}\ln\left(\sqrt{\frac{0.7}{f_v}} - 1\right)\right\}(\dot{\varepsilon}_2)^{-1} \qquad (C.6)$$

where ε_n is the nucleation strain and f_v = volume fraction of second phase particles. Usually ε_n is assumed to be a constant.

For intergranular fracture voids nucleate at and grow in the plane of the grain boundaries. Failure occurs suddenly without neck formation. There are two distinct intergranular fracture mechanisms, including: a) triple point cracking; b) cavitation fracture.

Triple point cracking is important at low temperatures and high stresses. Crain boundary sliding in polycrvstals leads to stress concentrations at the grain boundary triple junctions which may often be relieved by nucleation of a crack; and following nucleation, the cracking then grows by the wedging action of the sliding process. Williams [65] has analysed this process and the time to fracture is given by

where γ is the efffective surface energy of fracture and d is the grain size.

Cavitation fracture occurs under conditions of very low stresses and high temperatures; growth of cavities occurs by vacancy diffusion along the grain boundaries. Ashby [5b] has analysed this type of fracture and time-to-fracture is given by

$$t_{f_3} = \frac{0.006kT}{\delta D_B N_B^{3/2} \Omega} \qquad (C.8)$$

where N_B is the number of particles/unit area of the grain boundary.

The fracture mechanism map €or annealed 316 S.S. is constructed assuming that the various fracture mechanisms discussed above operate independently of each other, so that failure occurs by the process predicting lowest value of t_f. The fracture map is shown in Figure *C-4* and the parameters used in the construction of the map are given in Table C-1. Contours for constant time-to-fracture have been drawn along with logarithmic values of experimentally obtained times-to-fracture [60,61,65,66]. Good agreement is obtained between experimental and predicted values, particularly for $\sigma/G<2x10^{-3}$. At higher stresses near the ductile fracture regime, the model over-estimates t_f. A likely explanation for this deviation is that Equation (B.3) underestimates the strain contribution due to sliding at higher stresses (i.e., $\sigma/G>2x10^{-3}$). Important features indicated by the map include:

1) Transgranular fracture occurs at high stresses and high temperatures and generally has a small time to fracture ($t_f<10^4$ sec);

2) Triple point cracking occupies a major portion of map which is of interest in laboratory investigation of creep rupture;

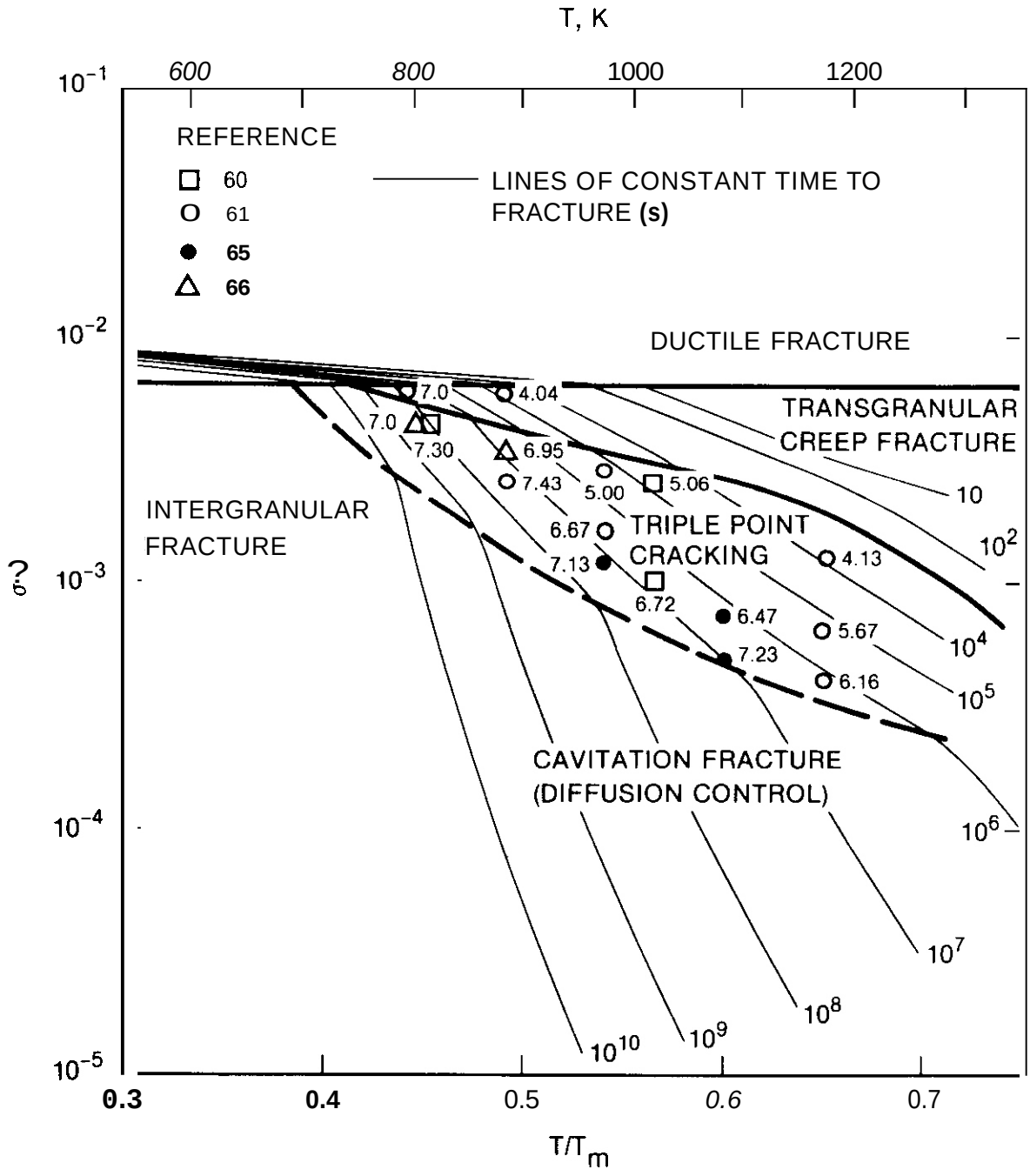

FIGURE C-4. **Fracture** Map *for* **Unirradiated Solution Annealed 316 Stainless Steel.**

3) Cavitation fracture is important at very low stresses and involves very large times-to-fracture.

c4. Summary

The initial mappings were based on a combination of simple models (i.e. Williams wedge crack mechanism) and empirical data (i.e. grain boundary sliding rates); they provide considerable insight about critical processes governing flow and fracture in unirradiated solution annealed 316 stainless steel. However, many details of important mechanisms and processes have not yet been indicated in these maps. For example, a number of recent papers [65,67-69] have addressed the role of thermal phase instabilities in deformation and fracture processes in stainless steels. We are reviewing this work and attempting to develop a more detailed model for the influence of microchemical evolution on flow and fracture. Clearly, this will be critical to developing understanding when extending the maps to other compositions, thermomechanical treatments and irradiated conditions, when microchemical evolution processes may be significantly different.

D. Development of Instrumented Hardness Test Techniques -- G. Lucas, P. Au, W. Sheckhard and G.R. Odette (University of California, Santa Barbara.)

D1. Introduction

The extremely limited irradiation volumes of several fusion test facilities (i.e. RTNS-II and FMIT) necessitate developing methods to extract mechanical property information from small sample volumes. Therefore, as part of the RTNS-II program, techniques are under development to determine flow and ductility data from TEM-disc size specimens. One approach has been to use indentation hardness tests which are instrumented such that penetrations at a single location can be used to derive true stress-strain flow curve data. Ultimately the tests will be extended to the microhardness regime, in which case approximately three to five tests per TEM disc (with a redundancy factor of 5) can be performed. Since many TEM discs (currently more than 50; ultimately,

more than 200) can be simultaneously irradiated even in the limited volume of RTNS-II, significant amounts of data can be generated if these efforts are successful.

This report describes results of the initial phase of the development effort; stress-strain data derived from macro-indentation hardness tests, using two techniques to measure indentation parameters, are compared to tensile data for 6061 T6 Al, *304* stainless steel, yellow brass and mild steel. Although the data reported here were generally obtained from multiple indentations, extension of the technique to a single indention appears straightforward. Some modification of the experimental procedures, however, will be required.

D2. Basis of the Technique

Indentation hardness tests in this program have been performed solely with ball indenters. Previous analyses [70] have shown that there are two limiting regimes of deformation associated with such spherical indentation hardness measurements. In the first regime the penetration is made under small loads and is fully elastic. The end of this regime is characterized by the initiation of a small region of plastic flow directly below the indenter ball. The second limiting regime is characterized by penetrations formed under large loads and the formation of a fully developed plastic zone surrounding the penetration and intersecting the surface of the specimen. In the intermediate, or "transition", regime between these two limiting regimes, the plastic zone grows in size with increasing applied load from the small initiated region to the fully developed type of zone.

A number of experimental and analytical investigations have demonstrated a relationship between characteristics of the indentation process and true uniaxial flow properties of the material. These are reviewed below.

The characteristics of the indentation process which are of interest are a) the chordal diameter of the indent, d, and b) the mean pressure, P_m, between the indent and the indenter under load. The chordal diameter, d, can be measured directly by optical or profilometer

techniques. However, as will be demonstrated, it is more convenient for instrumented test purposes to determine d from a measurement of the plastic indentation depth h_p. The relationship between d and h_p is given by

$$d = \left[K \left(\frac{\frac{D}{2}(h_p^2 + (d/2)^2)}{h_p^2 + (d/2)^2 + h_p D} \right) \right]^{1/3} \qquad \text{(D-1)}$$

where $K = 5.47\ F\ (E_1^{-1} + E_2^{-1})$

F = applied load

E_1 = elastic modulus of indenter

E_2 = elastic modulus of specimen

D = indenter diameter

The mean pressure, P_m, is simply given by

$$P_m = F/\pi d^2 \qquad \text{(D-2)}$$

These characteristics can he related to the uniaxial flow properties as follows. Defining σ_ε as the true uniaxial flow stress at a plastic strain ε, it has been shown that (70)

$$\varepsilon \simeq .20\ d/D \qquad \text{(D-3)}$$

and

$$\frac{\sigma_m}{\sigma_\varepsilon} = \emptyset \qquad \text{(D-4)}$$

where the value of $\emptyset$ depends on which regime of deformation exists at the termination of the indentation process. It has been shown analytically that at the onset of plastic flow (end of the first deformation regime) $\emptyset = 1.1$, and that for the deformation regime characterized by a fully-developed plastic zone $\emptyset \simeq 2.8$. In the transition regime, it has been empirically determined that (70)

$$\emptyset \simeq 1.1 + .53 \ln \left(.47 \frac{d}{D} \frac{E_2}{\sigma_\varepsilon}\right) \qquad \text{(D-5)}$$

These relationships, (D-1) - (D-5), can thus be combined with an instrumented hardness test to predict uniaxial flow properties as follows. By monitoring simultaneously F and h_P during a single indentation, (P_m,d) data pairs can be determined from equations (D-1) - (D-2). These can be converted to true stress-strain data ((σ_ε,ε) data pairs) through equations (D-3) - (D-5). These (σ_E, E) data pairs then provide a means of estimating the $\sigma_E(E)$ relation over the entire E regime of interest.

D-2. Experimental Procedure

The problem is to then measure h_p at various loads so that a true stress-strain curve can he constructed. By connecting the indenter to a calibrated load cell on a standard compression testing machine, the loads during indentation can be monitored in a straightforward manner. The indentation depth h_p can be measured with a precision profilometer after indentation to a prescribed load. Alternately, by measuring the indenter movement through a cycle of applying and removing the load the plastic indentation depth can be measured as illustrated in Figure D-1. In principle, the indentation-load cycles can be repeated at increasing peak loads to establish a series of (σ_ε,ε) data pairs for a single indentation location. In practice, it has been somewhat difficult to establish precise values of small increments of h_p, (and thus E_p) primarily due to current instrumentation limits. Therefore, the present results are limited to $E_p \gtrsim .005$, and make use of multiple indentation. Procedures used to date are described below.

Rockwell type indenters of diameters 1/16, 1/8 and 1/2 inch, were used as the penetrators. These were attached singly to the load cell in the cross head of an Instron Model 1122 Mechanical Testing Machine. Specimens were mounted on a fixed platen stage below the cross head. The movable crosshead was driven at constant speed, which in turn drove the indenter into the specimen. Loads were monitored closely, and were limited in magnitude such that no visible damage appeared on the reverse side of the specimen. Several indentations under different

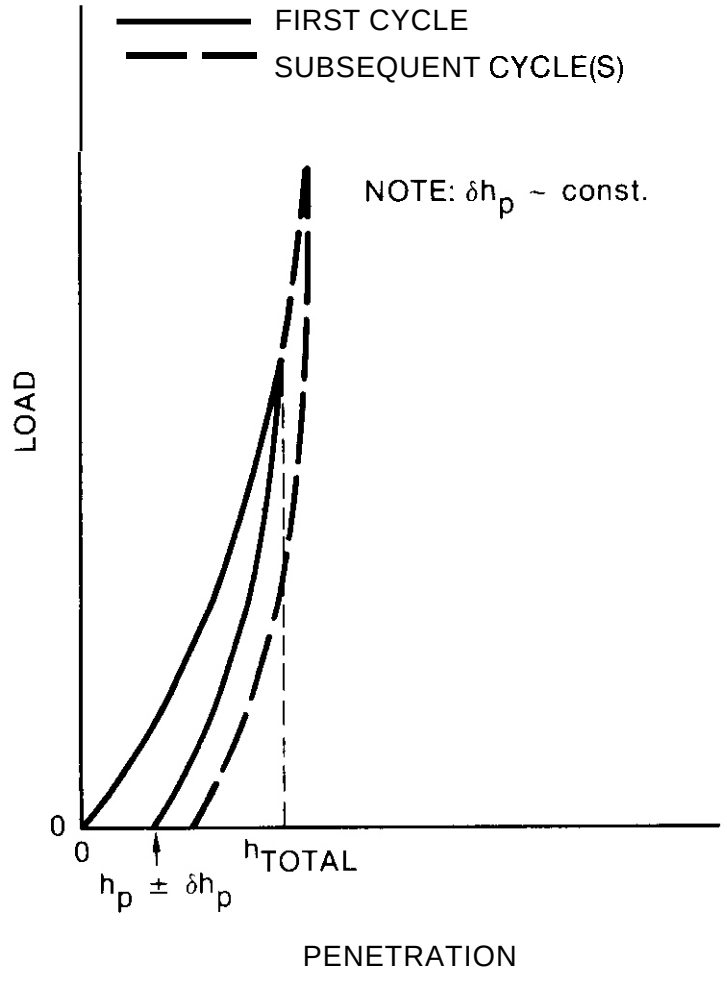

FIGURE D-1. Illustration of Load Versus Penetration Depth Curve.

loads were performed on each specimen at different positions.

Initially, the geometry of each indentation was determined on a Bendix RCC-4 profilometer. Both h_p and d were determined directly, and the validity of equation (D-1) was checked. A typical profilometer trace is shown in Figure D-2.

Although the profilometer gives the precise depth of penetration, it does not serve the primary objective of our experiment; namely, to obtain the stress-strain characteristics of materials from a single indentation. Kemoval of the specimen for profilometer studies disallows repeated indentation in the same spot. However, in situ measurement of h, would permit such repeated indentation. Consequently, a linear variable differential transformer (LVDT) was installed in the hardness apparatus to directly measure the plastic indentation depth in the manner schematically illustrated in Figure D-1. Figures D-3 - D-6 show the initial results of these experiments for 6061-T6 AI, yellow brass mild steel and 304 stainless steel. True stress-strain data derived from the hardness tests via Equation (D.l) to(D.5) are compared to stress-strain curves obtained from tensile tests on the same material. Hardness data includes values derived from measurements of h_p both by post-test profilometer and in situ LVDT techniques.

The agreement in the true strain range from $\sim .005$ to .05 is quite good. The LVDT data is currently restricted to strains of $> .01$ and displays somewhat more scatter than the profilometer measurements. This is believed to be due to the same instrumentation limits which inhibit performing repeated indentations on the same spot. Techniqu!; to overcome these limitations have been identified and are currently being implemented. Finally, it is notable that the disagreement is largest for the steels; particularly, in the higher strain ranges and for stainless steel. It is believed that this may be due, in part, to a stress induced martensitic phase transformation (as reflected by the change in slope of the true stress strain curve) which may be somewhat sensitive to stress state.

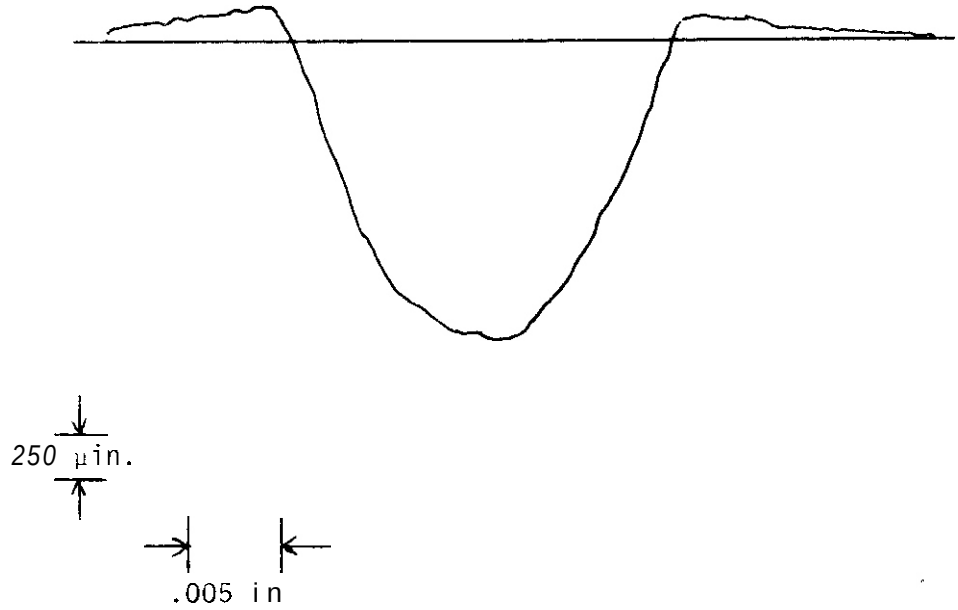

FIGURE 0-2. Typical Indentation Profilometer Trace.

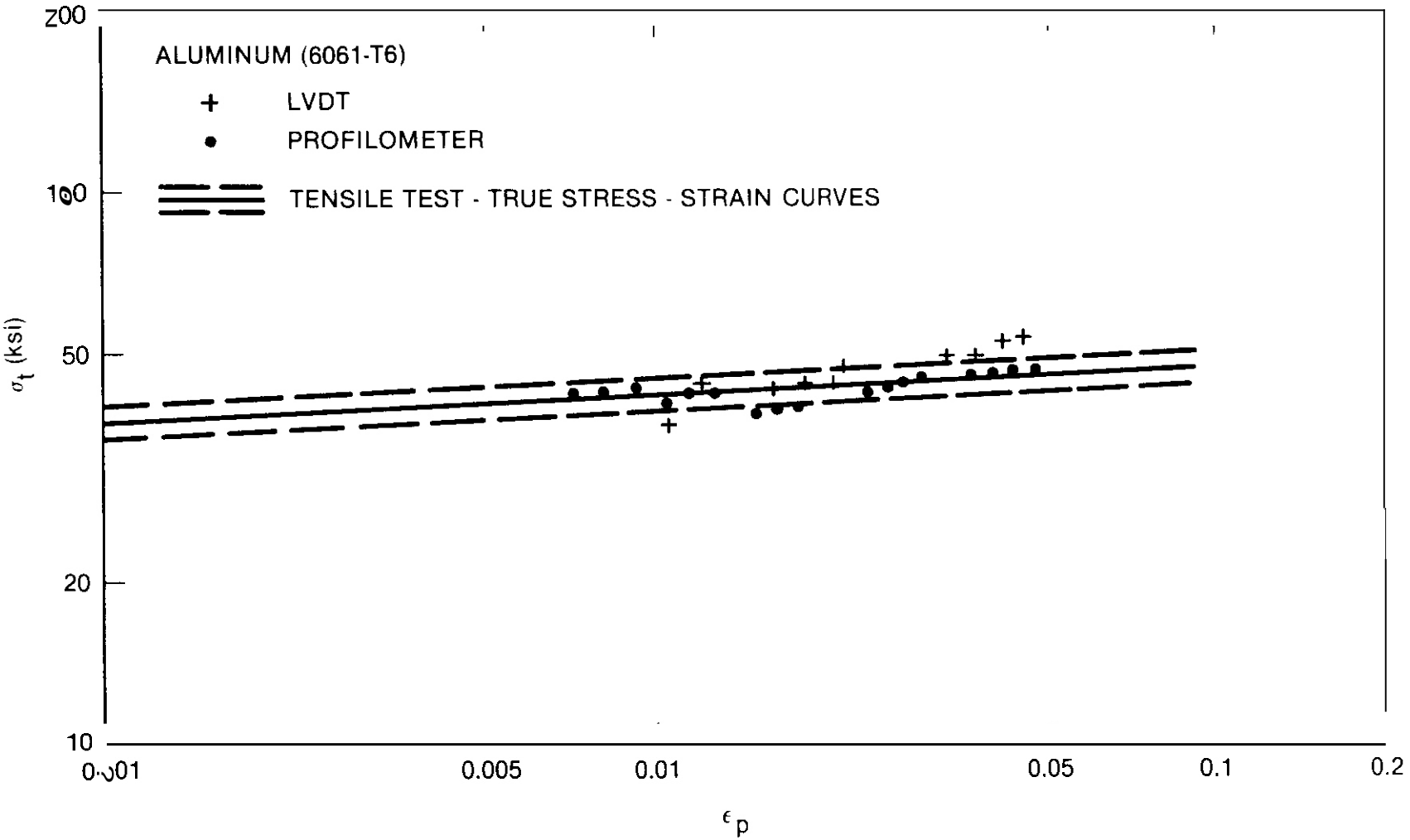

FIGURE D-3. Comparison of Tensile Test True Stress-Strain Data and Data From Indentation Measurements for 6061-T6 Aluminum.

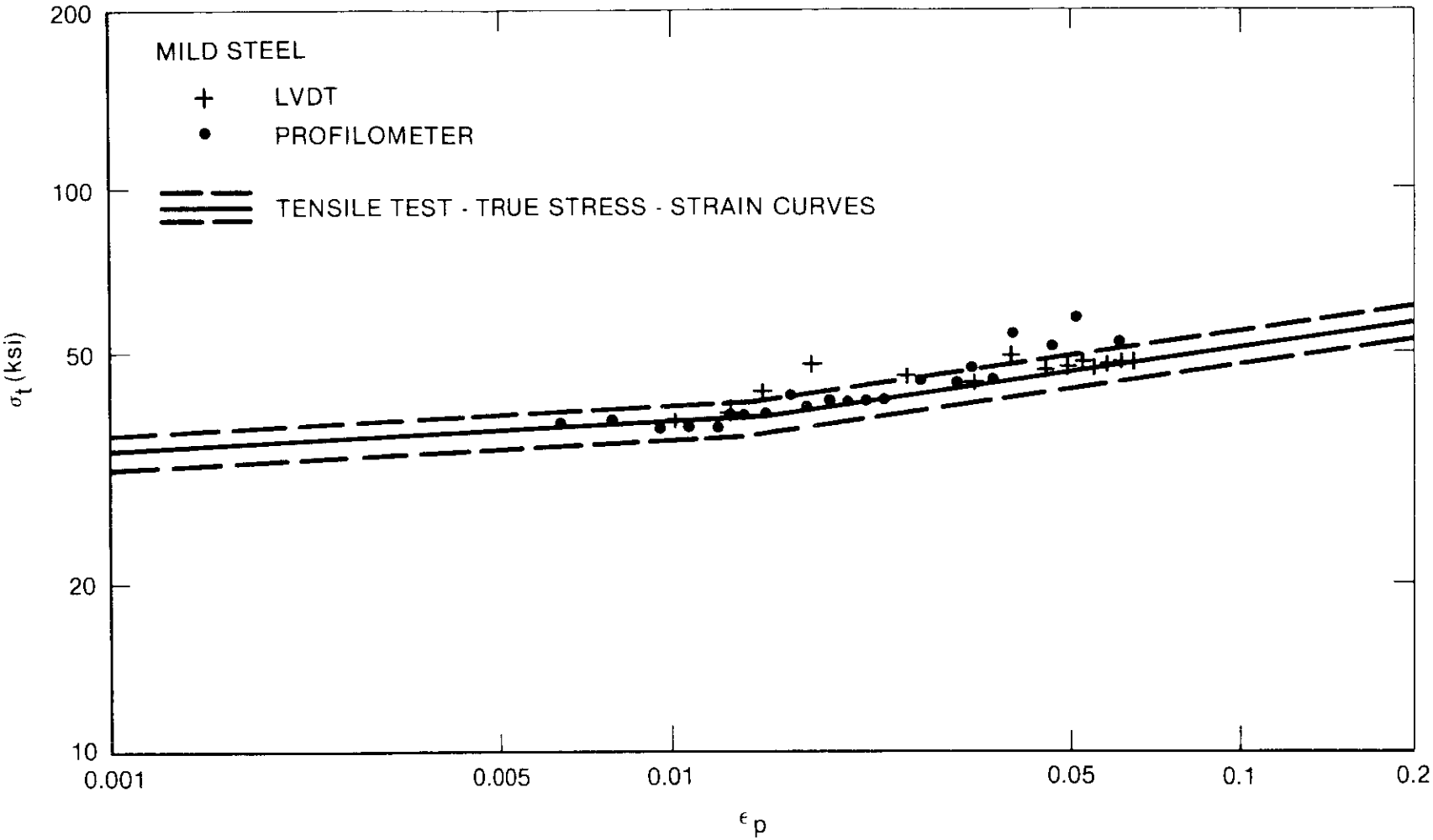

FIGURE D-4. Comparison of Tensile Test True Stress-Strain Data and Data From Identation Measurements for Mild Steel.

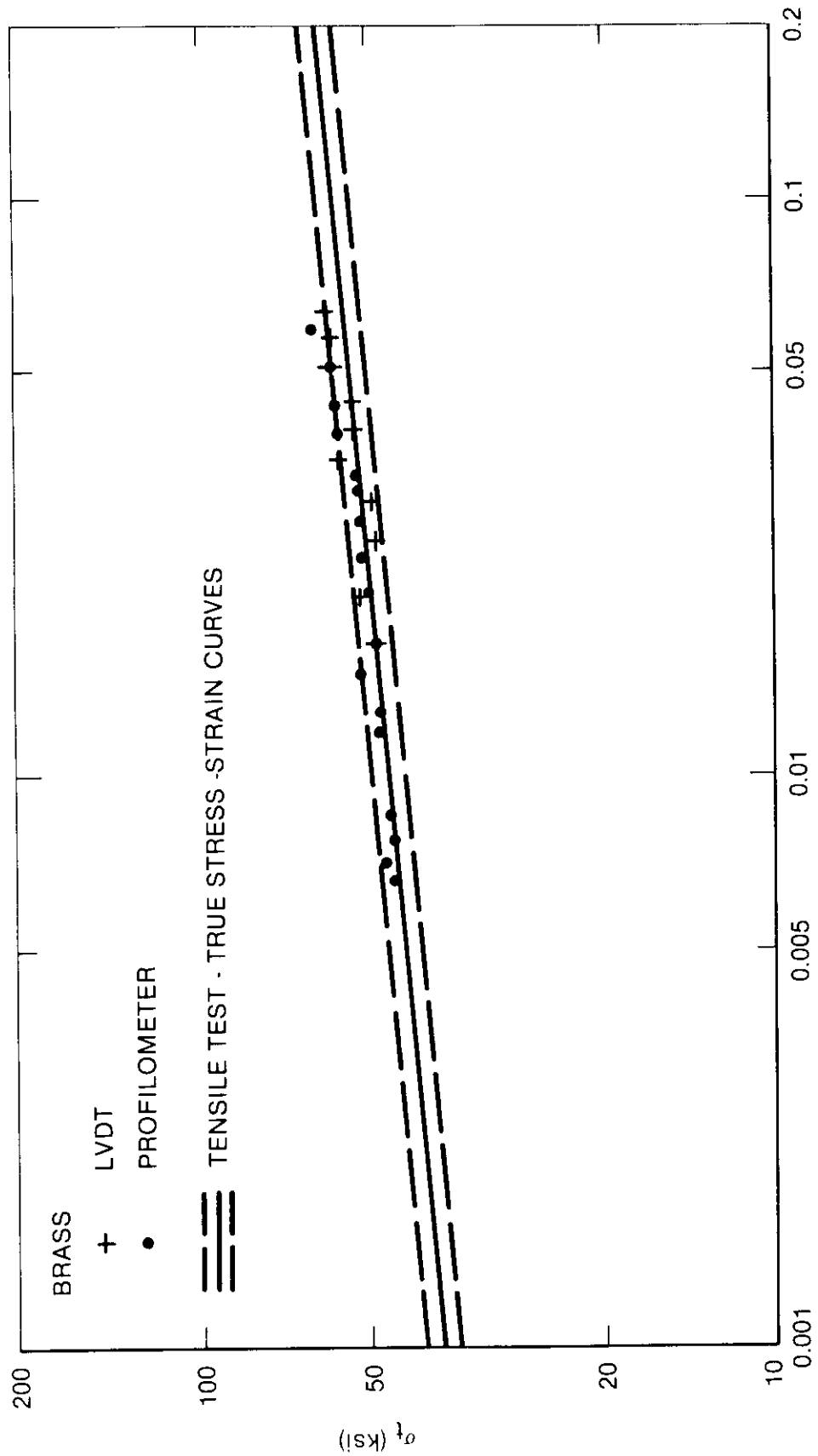

FIGURE D-5. Comparison of Tensile Test True Stress-Strain Data and Data From Indentation Measurements for Yellow Brass.

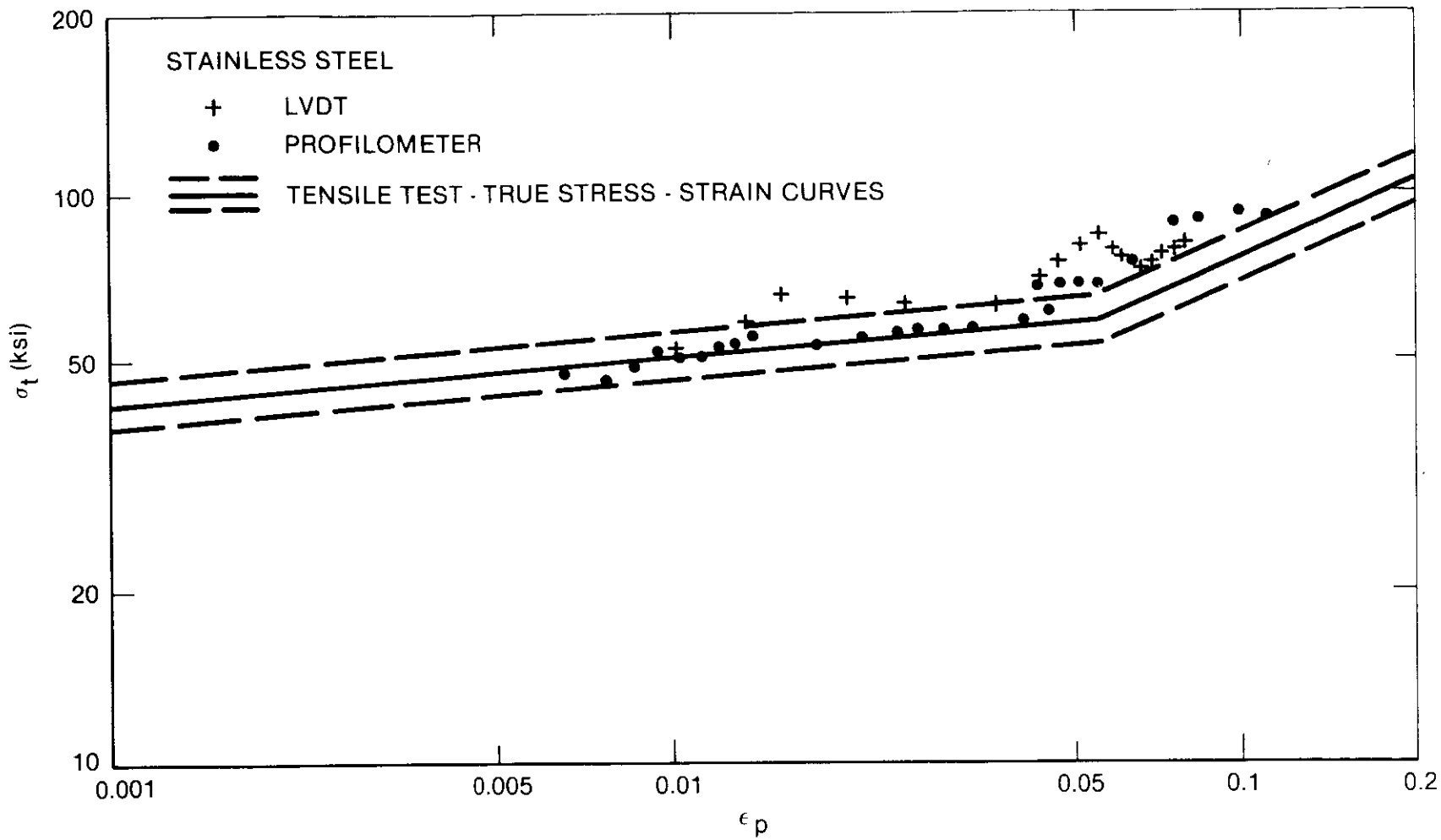

FIGURE D-6. Comparison of Tensile Test True Stress-Strain Data and Data From Indentation Measurements For 304 Stainless Steel.

4. Summary and Conclusions

Some initial indentation measurements of stress-strain curves have been presented. The results are encouraging, but it is clear that further development of both instrumentation and data analysis techniques will be required to extend both the limits and precision of the procedure.

VII. REFERENCES

1. The Fusion Reactor Materials Program - II Damage Analysis and Fundamental Studies, DOE/ET 0032/2 (1978).

2. There have been a number of significant conferences with published proceedings concerned with microstructural evolution including: a) Proc. Int. Conf. Rad. Induc. Voids in Met., CONF-710601 (1971); b) Proc. Conf. Voids Formed by Irrad. of React. Mat., S.F. Pugh and M.N. Loretto, Eds., BNES (1971); c) Physical Met. of React. Fuel El., J.E. Harries and E.C. Sykes, Eds., TMS (1973); d) Defects and Defect Clusters in BCC Metals and Their Alloys, R.J. Arsenault Ed. Nucl. Met 18 (1973); e) Consult Symp. Physics of Irrad. Induc. Voids, R.S. Nelson, Ed., UKAEA AERE-R7934 (1974); f) Proc. Int. Con. Rad. Eff. and Trit. Techn. for Fusion React. CONF-750989 J.S. Watson and F.W. Wiffen, Eds.; g) Proc. Int. Conf. on Fund. Aspects of Rad. Dam. in Met. CONF-751006, M.T. Robinson and F.W. Young, Eds., (1975); h) Proc. Work. Corr. of Neutron Charge Part. Dam. CONF-760673, (1976); i) Proc. Int. Conf. Rad. Eff. in Breed. React. Struct. Met., M. Bleiberg and J.W. Bennet, Eds., AIME TMS (1977); j) Proc. Int. Conf. Prop. of Atom. Def. in Metals, J. Nucl. Mat. 69,70 (1978); k) Workshop on Solute Segregation and Phase Stability During Irradiation ORNL, Stiegler, Ed., Nov. 1-3, 1978 (to be published Jour. Nucl. Mat)

3. The historical roots of void nucleation and growth can be traced to papers by: S.D. Harkness and C.Y. Li, Met. Trans. 2 1457 (1971); H. Wiedersich, Rad. Effect 12, 111 (1972), J.L. Katz and H. Wiedersich, J. Chem. Phys. 55, 1414 (1971); K. Russell, Acta Met 19, 753 (1971); and A.D. Brailsford and R. Bullough, J. Nucl. Mat 44, 121 (1972).

4. A.D. Brailsford and R. Bullough, J. Nucl. Mater. 69 & 70, 434 (1978).

5. L.K. Mansur, Nucl. Techn. 40, 5 (1978).

6. W.G. Wolfer, L.K. Mansur and J.A. Sprague, Reference 2i, p. 841 .

7. Papers on solute segregation of historical interest include a) T.R. Anthony, Ibid, Reference 2a, p. 630 and b) P.R. Okamoto and H. Wiedersich, J. Nucl. Mat. 53, 336 (1974).

8. R.A. Johnson and M.Q. Lam, J. Nucl. Mat. 69 & 70, 424, (1978).

9. H. Wiedersich and P.R. Okamoto, Reference 2k.

10. J.A. Hudson, J. Br. Nucl. Ener. Soc. 14, 127 (1975).

11. K.C. Russell, Reference 2i, p. 821.

12. N.Q. Lam and H. Wiedersich, J. Nuc. Mat. 74, 101 (1978).

13. H.R. Brager and J.L. Straalsund, J. Nucl. Mat. 46, 134 (1973).

14. B.J. Eyre, Ibid, Reference 2g, p. 729.

15. P.J. Barton, B.L. Byre and D.A. Stow, J. Nucl. Mat. 67, 181 (1977).

16. H.R. Brager, F.A. Garner, E.R. Gilbert, J.E. Flinn and W.G. Wolfer, Ibid., Reference 2i, p. 727.

17. W.K. Appleby, E.E. Bloom, J.E. Flinn and F.A. Garner, p. 509.

18. J.I. Bramman, C. Brown, J.S. Wakin, C. Cawthorne, E.J. Fulton, P.J. Barton and J.A. Link, Ibid., p. 479.

19. J.S. Watkin, J.H. Gittus and J. Standring, Ibid, p. 487.

20. J.F. Bates and W.G. Johnston, Ibid., p. 825.

21. D.I. Potter, L.E. Rehn, D.R. Okamoto and H. Wiedersich, Ibid. p. 377.

22. H.R. Brager and F.A. Garner, "Dependence of Void Formation on Phase Stability in Neutron Irradiated Stainless Steel," 9th International Symposium on Effect of Radiation on Structural Materials, Richland, WA, July 1978 (to be publishe

23. H.R. Brager and F.A. Garner, J. Nucl. Mat. 73, 9 (1978).

24. H.R. Brager, J. Nucl. Mat. 57, 103 (1975).

25. N. Asamm, L. Le Naour and J. Delaplace, J. Nucl. Mat. 49, 197 (1974).

26. P.J. Maziasz, F.W. Wiffen and E.E. Bloom, Reference 2f, 1, p. 259.

27. D.T. Mazey and R.S. Nelson, Ibid., p. 26, 240.

28. P.J. Maziasz and E.E. Bloom and M.L. Grossbeck, Alloy Develop. for Irrad. Perf. Q.P.R. DOE/ET-058/1, 40-85 (1978).

29. E.E. Bloom and J.O. Stiegler, J. Nucl. Mat. 36, 331 (1970).

30. D.W. Keefer and D.G. Pard, J. Nucl. Mat. 45, 55 (1973).

31. S.D. Harkness, B.J. Kestel and S.G. McDonald, J. Nucl. Mat., 46, 159 (1973).

32. R.S. Nelson and J.A. Hudson, J. Nucl. Mat. 58, 11 (1975).

33. S.C. Agarwaal and G. Ayrault, Dam. Anal. and Fund. Stud. QPR Jan-March 1978 DOE/ET-0065 1,136 (1978).

34. N. Packen, K. Farrell and J.O. Stiegler, Correlation of Neutron and Charged Particle Damage: Part I, J. Nucl. Mat. (in press).

35. E.E. Bloom, K. Farrell, M.H. Yoo and J.O. Stiegler, Reference 2e, P. 330.

36. A.M. Stoneham, Reference 2g, P. 2, 1221 (1976).

37. D.L. Porter and G.L. McVay, Reference 2k.

38. G.R. Odette and M.W. Frei, Proc. 1st Topic. Meet. on Tech. of Control. Nucl. Fus., CONF-740402 2, 485 (1974).

39. G.R. Odette, Notes on a presentation at Nuclear Engineering Seminar at the University of Wisconsin. Dept. of Nucl. Eng., UC Santa Barbara (1976).

40. G.R. Odette and S.C. Langley, Reference 2f, p. 395.

41. G.R. Odette D. Frey, P. Lombrozo, L. Parme, S. Schwartz and R. Stoller, Microstructural Evolution, Dam. Analy, and Fund. Stud., Q.P.R., July-Sept. 1978, p. 97 DOE/ET-0065/3 (1979).

42, C.R. Odette and R. Myers, CTR QPR, April-June 1975, HEDL TME 15-90 p. 2 (1975).

43. R.W. Powell and G.R. Odette, "Effect of Pulsed HVEM Irradiation of Microstructure Evolution in a Simple Fe-Ni-Ci Alloy." Dam. Anal. and Fund Studies QPR DOE/ET-0065/4, 155, (1979).

44. J.J. Holmes, A.J. Lovell and R.L. Fish, Effects of Irradiation on Substructure and Mechanical Properties of Metals and Alloys, ASTM-STP 529 (1974) 383.

45. E.E. Bloom, Radiation Damage in Metals, ASM, (1975) 295.

46. R.L. Fish and J.D. Watrous, Irradiation Effects on the Microstructure and Properties of Materials, ASTM-STP-611 (1976) 91.

47. R.W. Fish, N.S. Cannon and G.L. Wire, "Tensile Property Correlations for Highly Irradiated 20% C.W. 316 Stainless Steel," in the Proceedings of the 9th Symp. on Effects of Irrad. on Structural Alloys, Richland, WA (July 1978).

48. J.F. Knott, Fundamentals of Fracture Mechanics, John Wiley and Sons, (1973) 116.

49. J.P. Hirth and F.H. Froes, Met. Trans. 8A (1977) 1165.

50. G.T. Hahn and A.R. Rosenfeld, Met. Trans. 6, (1971) 653.

51. F.J. Loss and R.A. Gray, "J-Integral Characterization of Irradiated Stainless Steels," NRL Report 7569 (1973).

52. J.W. Sheckherd, M. Kangilaski and A. Braun, Instrumented impact Testing, ASTM-STP-563 (1974) 118.

53. J.R. Hawthorne and H.E. Watson, Reference 1, p. 327.

54. J. Dufrense, B. Henry and H. Larsson, Fracture Toughness of Irradiated AISI 304 and 316 Stainless Steels, Reference 47.

55. M.F. Ashby, Acta Met., 20, 887 (1972).

56. Ashby, M.F., CUED/c/MATS/TR 34, Cambridge University Engineering Department, Cambridge, England (1978).

57. H.J. Frost and M.F. Ashby: Fundamental Aspects of Structural Alloy Design. R.I. Jaffee and B.A. Wilcox eds., pp. 27-38, Plenum Press, New York, 1977.

58. Garofalo, F., C. Richmond, W.E. Domis, and F. von Germininger, Joint International Conference on Creep, Institute of Mechanical Engineers, London, England (1963).

59. L.D. Blackburn, Generation of Isochronous Stress-Strain Curves, A.O. Schaefer, ed., pp. 15-48, American Society for Mechanical

Engineers, New York, 1972.

60. E.E. Bloom and J.O. Stiegler, ASTM STP 529, p. 360, 1973.

61. D.G. Morris and D.R. Harries, Metal Science, 12, p. 525 (1978).

62. R.S. Gates and C.A.P. Horton, Mater. Sci. Eng., 27, p. 105 (1977).

63. R.S. Gates, Mater. Sci. Eng., 27, p. 127 (1977).

64. J.A. Williams, Acta. Met., 15, p. 1559 (1967).

65. F. Garofalo; R.W. Whitmore, W.F. Domis and F. Von Gemmingen, Trans. AIME, 221, p. 310 (1961).

66. A.J. Lovell, Nuclear Technology, 26, p. 297 (1975).

67. D.G. Morris and D.R. Harries, Met. Sci. 12, 542 (1978).

68. J.O. Nitsson, P.R. Howell and G.L. Dunlop Acta Met. 27, 179 (1979).

69. D. Tabor, Hardness of Metals, Clasender Press (1951).

70. H.A. Francis, "Phenomenological Analysis of Plastic Spherical Indentation," Trans. ASME, 98. 272 (1976).

VIII. FUTURE WORK

Continued efforts will be directed at improving all of the microstructure models discussed previously; particular emphasis will be placed on facilitating physical interpretation of the results and comparisons of the model predictions with experimental observations--viz. efficiently defining physically valid regions of MPS. The simpler models will still be used for scoping studies of MPS, and for designing and interpreting new experiments. Continued effort to implement more fully the components of the composite model in a computationally tractable manner will also be a high priority goal, with special efforts directed at including microchemical effects.

Micromechanical models will be applied to relate basic properties and microstructure to failure-related properties such as fracture toughness, fatigue strength and crack growth resistance. Emphasis will

he on integrating strengthening, work hardening and flow localization mechanisms. In addition, models of grain boundary failure in the creep regime including the influence of helium, matrix hardening, stress relaxation and the like are being assembled. These models and the available data base will he used to develop microstructure - flow and failure maps for the entire range of temperature and stresses of interest. An assessment of the influence of extrinsic parameters such as stress state and stress concentrations related to macroscopic defects (i.e. cracks) will also be extended. Finally the modeling and analytical effort will consider what constitutes appropriate failure criteria and test procedures for fusion first wall structures.

An experimental program currently centered around utilization of the RTNS-II facility has been recently initiated in collaboration with HEDL and LLL. This effort is not only aimed at designing, conducting and interpreting RTNS-II experiments, but also developing new test techniques for the fusion program. In particular, an effort is under way to develop quantitatively useful microminiaturized mechanical tests, with initial emphasis on instrumented hardness.

XI. PUBLICATIONS

1) G.R. Odette, "Modeling Microstructural Evolution Under Irradiation." Accepted for publication in the Journal of Nuclear Materials.

2) G.R. Odette and D. Frey, Development of Mechanical Property Correlation Methodology for Fusion Environments, Ibid.

I. PROGRAM

Title: Effects *of* Irradiation on Fusion Reactor Materials
Principal Investigator: F. V. Nolfi, Jr.
Affiliation: Argonne National Laboratory

II. OBJECTIVE

The objective of this work is to determine the microstructural evolution, during irradiation, *of* first-wall materials with special emphasis on the effects of helium production, displacement damage and rates, and temperature.

III. RELEVANT DAFS PROGRAM PLAN TASK/SUBTASK

SUBTASK II.C.2.1 Mobility, Distribution, and Bubble Nucleation

IV. SUMMARY

The morphology of ß-phase platelets which form during irradiation of Ti-6 wt. % AI-4 wt. % V has been examined by TEM. The crystallographic orientation of the precipitates obeys the Burgers orientation relation, for which there are six equivalent orientations. Precipitates of one variant were isolated and found to lie nearly parallel to one-another; the habit plane was near $(7\bar{2}50)$.

In order to improve quantitative control of ^{3}He injection in the ANL Dual-Ion Irradiation Facility, experiments have been performed to characterize the degraded ^{3}He beam at the normal sample position in the target chamber. Experiments were performed as a function of Ni-degrader foil thickness and incident ion-energy. Plots of energy centroids are presented.

Samples of V-15Cr-5Ti, Type 316 stainless steel, Fe-20Ni-15Cr, and CE-3177 (9 Cr Ferritic Steel obtained from Combustion Engineering) have been dual-ion irradiated, and also pre-injected and single-ion irradiated. Temperature, dose and helium injection rate investigations will be performed on the V-15Cr-5Ti. The 316 stainless steel and Fe-20Ni-15Cr irradiations were for studies of helium injection rate and dose in the high dose range (up to 100 dpa). In CE-3177, the dose dependence will be studied.

V. ACCOMPLISHMENTS AND STATUS

Microstructure of Irradiated Fusion Reactor First-wall Materials — G. Ayrault (ANL)

A. Precipitate Morphology in Irradiated Ti-64

We previously reported [1,2] that heavy-ion (2.6 MeV V^+) irradiation of Ti-64 caused profuse precipitation of β-phase (BCC) platelets in the u-phase (HCP) matrix, and that the crystallographic orientation of the precipitate obeyed the Burgers relation:

$$(0001)_\alpha \;||\; (011)_\beta \qquad (1)$$

$$\langle 1\bar{2}10\rangle_\alpha \;||\; \langle 11\bar{1}\rangle_\beta \qquad (2)$$

Six different orientations are allowed by (2), and each can be inidividually identified in TEM by the orientation of its diffraction pattern relative to that of the parent crystal. Since a TEM image is a 2-dimensional projection, it is necessary to know the precipitate habit plane before reliable quantitative information (e.g. size distribution or volume fraction) can be extracted from the micrographs; determination of the habit plane of the β-platelets is reported here.

Figure 1 shows a sample irradiated to 6 dpa, at 635°C and 5 x 10^{-3} dpa·s^{-1}, tilted about the [0001] direction until the image width of a

predetermined set of precipitates went through a minimum. The foil, with a normal near $(11\bar{2}0)$, was first tilted 5^o away from $(11\bar{2}0)$ where $(01\bar{1})$ β-planes in only one of the six precipitate orientations were diffracting; a dark field micrograph, Fig. 1a, identified that set of precipitates. After a total tilt of 44^o from $(11\bar{2}0)$ about [0001], a minimum image width was observed, Fig. 1d, and almost all the precipitates were found to lie within $\pm 5^o$ of the [0001] direction (one of only two observed violations of this is marked D in Fig. 1d). Thus the habit plane is near $(7\bar{2}\bar{5}0)\alpha$ and, through the Burgers relation, near $(8\,7\,\bar{7})\beta$. The orientation relation is shown schematically in Fig. 2 for two of the six variants allowed by the Burgers relation together with the habit plane (which is normal to the plane of the paper) for each of these variants. Fig. 2b is seen to be a mirror image of Fig. 2a through the $(11\bar{2}0)$ plane.

B. Energy Analysis of Degraded ^{3}He Beams

In the ANL Dual-Ion Irradiation Facility[3], a monoenergetic helium beam is energy degraded to reduce the range and to spread the He distribution throughout the heavy-ion damaged region. For the large energy reductions of ~75% (i.e. from ~0.900 MeV to ~0.225 MeV) which are used, early attempts at theoretical characterization of the degraded beam proved unreliable. To remove this quantitative uncertainty, experiments were performed to measure the degraded energy spectrum and the effective transmission coefficient (or conversely, the reduction in ion current density due to scattering through angles large enough to prevent the helium from reaching irradiated samples, viz., ~5^o in our dual-ion irradiations).

1. Experimental Procedure

As shown in Fig. 3, the Ni degrader foil was placed at aperture d_1, (0.04 cm^2), and a carbon thin-film (~5$\mu g \cdot cm^{-2}$) at aperture d_2(0.08 cm^2), d_1 and d_2 are at the normal degrader foil and sample

positions, respectively, and separated by 5.4 cm. The intensity versus energy spectrum at d_2 was computed from a related spectrum recorded at d_3 using standard formulas for Rutherford scattering. Direct-beam spectra were recorded with the degrader removed for calibration of energy and intensity (thus eliminating the carbon film thickness from intensity calculations). It should be noted here that the seemingly unnecessary intermediate step of Rutherford scattering was introduced primarily to reduce the beam intensity from the high value needed for automatic accelerator and beam transport control, to the low value required for measurement.

2. Energy Centroid

Beam-energylfoil-thickness combinations were chosen to span the degraded energy range used in our dual-ion irradiations. Degraded energy centroids, obtained from Gaussian fits to intensity versus energy spectra, are presented in Fig. 4 for two highly uniform electroformed Ni foils obtained from Chromium Corporation of America. The angle α, Fig. 3a, of each foil with respect to the beam was varied to provide a range of effective foil thicknesses. From these plots, the correct beam energy for a given implant depth and degrader foil thickness can be chosen directly.

Values of the transmission coefficient and standard deviation of the degraded energy have not yet been obtained. Background in the intensity versus energy spectra, apparently due to slit scattering at the carbon foil, requires a more sophisticated analysis of the data to extract this information. This analysis is in progress.

C. Dual-Ion Irradiation of V-15Cr-5Ti

A scoping refractory alloy for MFR applications is V-15Cr-5Ti, which exhibits good radiation response, creep strength, and is more fabricable than binary V-Cr alloys. Comparison of irradiation response

in V-Cr and V-Cr-Ti alloys will enable determination of the effects of Cr versus Ti so that alloy modifications for optimum performance can be made. As a continuation of effort toward this end, samples of V-15Cr-5Ti have been irradiated under essentially similar conditions to those in a previous ANL study of V-15Cr.[4,5]

A dose dependence study and a temperature dependence study were carried out on specimens annealed at 1200°C in UHV for 2 hours. In the dose dependence study, samples were dual-ion irradiated with 2.6 MeV V^{+} and 0.83 MeV degraded $^{3}He^{+}$ at 650°C to doses of 5-60 dpa at 3:1 He:dpa, and to doses of 5-30 dpa at 10:1 and 50:1 He:dpa. For comparative purposes, additional samples were preinjected at room temperature with 10 appm ^{3}He, and were single-ion irradiated with 2.6 MeV V^{+} at the same temperature and doses as above. In the temperature dependence study, the helium injection rate and dose were held constant at, respectively, 25 dpa and 10:1 appm He:dpa, and the irradiation temperatures were 450, 500, 550, and 600°C. As in the dose dependence study, preinjected samples were single-ion irradiated under identical temperature and dose conditions.

D. High Dose Irradiation of Type 316 SS and Fe-20Ni-15Cr

In previous irradiations of Type 316 SS and Fe-20Ni-15Cr in the ANL Dual-Ion Irradiation Facility, the maximum dose was 25 dpa, a limit set by a practical irradiation time of 2.3 hours at 3×10^{-3} dpa·s^{-1}. In order to identify any changes in swelling rate or irradiation microstructure peculiar to high doses, the dose range has been extended to 100 dpa for a limited set of samples. The Type 316 stainless steel (MFE Ht.-15893) was initially 50% cold worked, then annealed at 1050°C for 1 hour and aged 10 hours at 800°C. The Fe-20Ni-15Cr alloy (supplied by W. G. Johnston) was solution annealed and quenched in helium. Both alloys were dual-ion irradiated *to* doses of 40-100 dpa with 3.0 MeV Ni^{+} and 3.83 MeV degraded $^{3}He^{+}$ at 700°C and 4×10^{-3} dpa·s^{-1}, and He:dpa ratios of 15:1 and 50:1 appm:dpa. For comparative purposes, a second set

of samples was pre-injected with 15 appm ^{3}He and irradiated with Ni^{+} ions alone to the same doses at the same dose-rate and temperature.

E. Dual-Ion Irradiation of CE-3177

The low swelling of ferritic stainless steels compared to austenitics makes them potentially attractive for MFR applications, but little is presently known about the effect of simultaneous helium production on irradiation microstructure in these alloys. In a "first effort" at isolating the influence of helium, samples of CC-3177 have been single and dual-ion irradiated. Single-ion samples were room-temperature preinjected with 15 appm ^{3}He and irradiated with 3.0 MeV Ni^{+}. Dual-ion samples were irradiated with 3.0 MeV Ni^{+} and 0.83 MeV degraded Ni^{+} at a helium injection rate of 15:1 appm He:dpa. For both sets of samples, the doses were 5,10 and 25 dpa and tne irradiation temperature 500°C, which is expected to be near peak swelling temperature for the dose rate used, 4×10^{-3} dpa·s^{-1}. TEM examination of these samples is in progress.

VI. REFERENCES

1. F. V. Nolfi, Jr., DAFS Progress Report, July-Septeinber 1978, DOE/ET-0065/3.

2. S. C. Agarwal, G. Ayrault, D. I. Potter, A. Taylor and F. V. Nolfi, Jr., First Topical Meeting on Fusion Reactor Materials, Miami, FL, January 29-31, 1979, to be published in J. Nucl. Mat.

3. A. Taylor, D. G. Ryding, J. Wallace, B. Okray Hall and D. I. Potter, Proc. Intl. Conf. on "Radiation Effects and Tritium Technology for Fusion Reactors," Vol. I, p. 158, 1975.

4. F. V. Nolfi, Jr., DAFS Progress Report, January-March 1979, p. 135, DOE/ET-0065/5.

5. F. V. Nolfi, Jr., A. Taylor and K. S. Grabowski, IEEE Transactions on Nuclear Science, Vol. NS-26, #1, p. 1257 (1979).

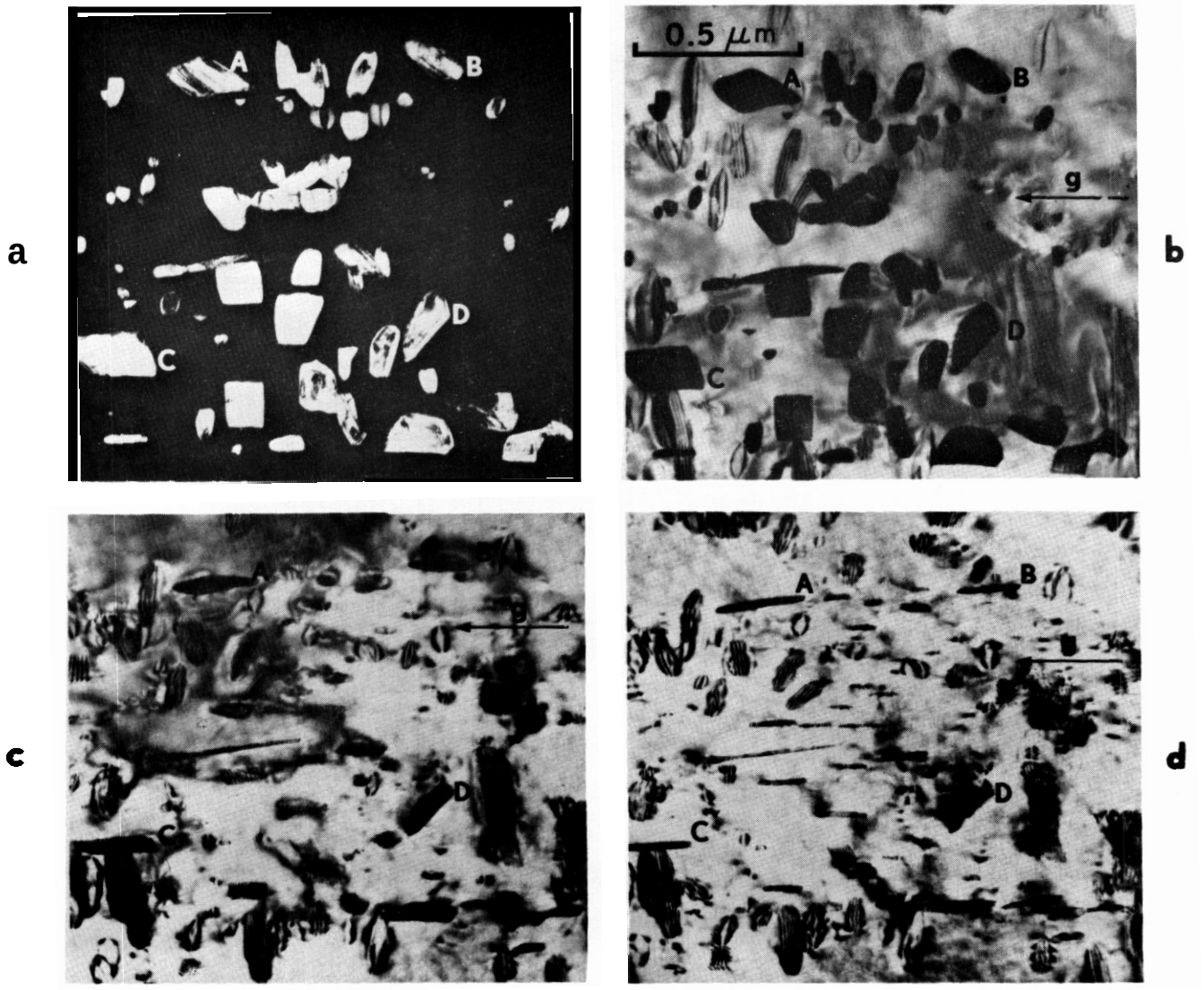

Figure 1. Precipitates in Ti64 irradiated with V^+ ions to 6 dpa at 630°C. a) Tilted 5° from $(11\bar{2}0)$ about [0001]; dark field from an $(01\bar{1})$ precipitate reflection. b) Tilted 5° from $(11\bar{2}0)$ about [0001], bright field, g = (0002). c) Tilted 33° from $(11\bar{2}0)$ about [0001], g = (0002). d) Tilted 44° from $(11\bar{2}0)$ about [0001], g = (0002).

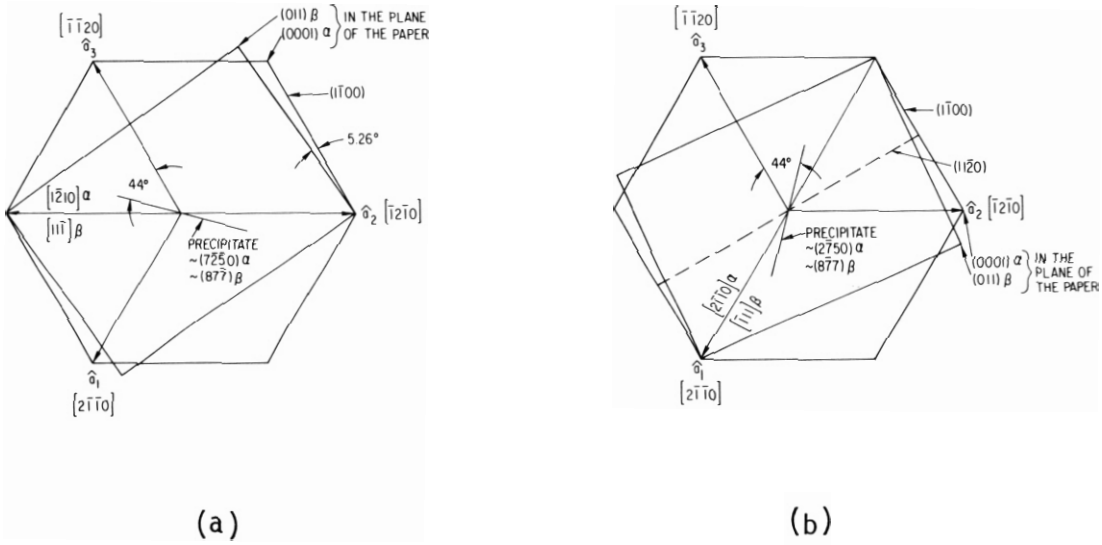

Figure 2. Crystallographic orientation and habit plane of B-phase (BCC) platelets in a-phase (HCP) Ti64. a) and b) show two of six orientations allowed by the Burgers orientation relation, and have mirror symmetry through the $(11\bar{2}0)$ plane.

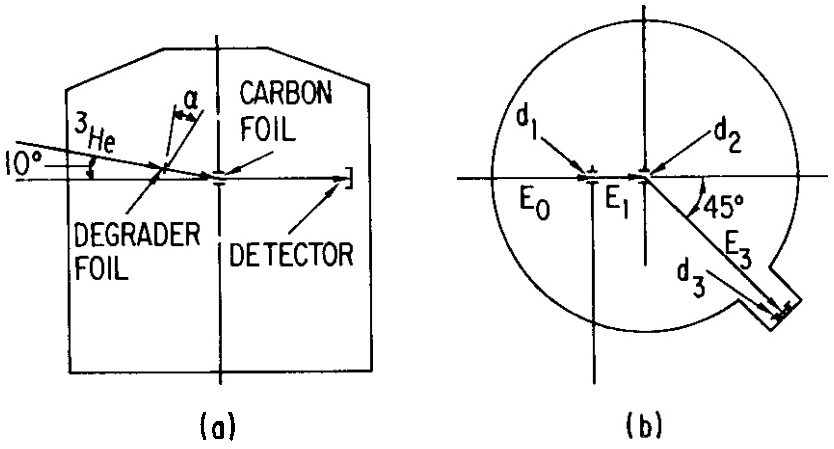

Figure 3. Configuration for energy analysis of degraded $^3He^+$ beam; degrader foil at aperture d_2, carbon thin-film at aperture d_1, detector at aperture d_3. a) side view b) top view.

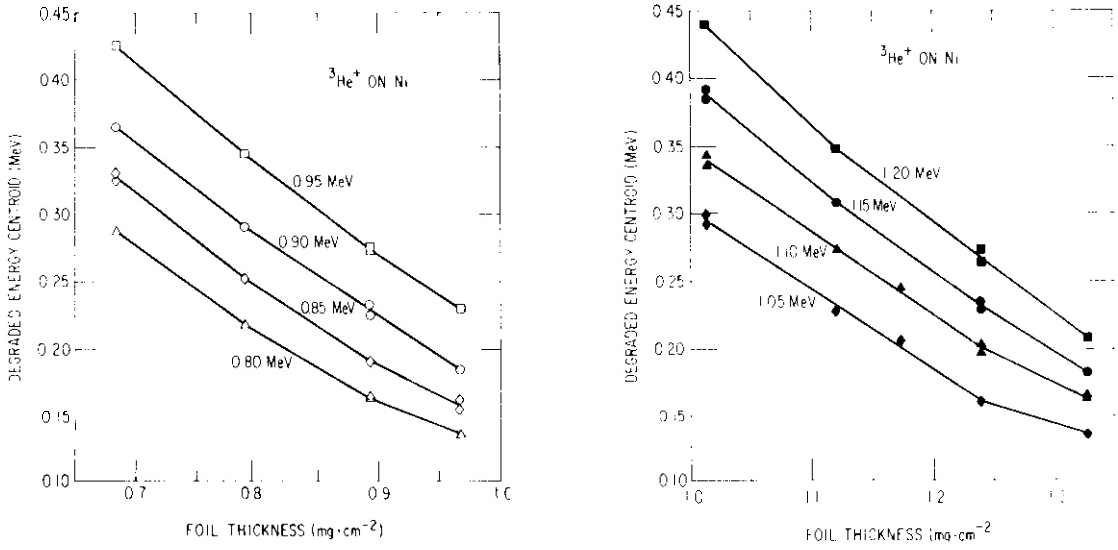

Figure 4. Centroid of the intensity versus degraded energy spectrum for $^3He^+$ on Ni foils a) 0.684 mg . cm^{-2} foil, $\alpha = 0^o$ to 45^o b) 1.016 mg · cm^{-2} foil, $a = 0^o$ to 40^o.

I. PROGRAM

Title: Radiation Effects to Reactor Materials
Principal Investigator: G. L. Kulcinski and P. Wilkes
Affiliation: University of Wisconsin

II. OBJECTIVE

To develop a fundamental understanding of the formation of voids, loops and precipitates in heavy ion and electron irradiated metals and alloys.

III. RELEVANT OAFS PROGRAM TASK/SUBTASK

II.C.6 Effects of Damage Rate and Cascade Structure on Microstructure

IV. SUMMARY

This paper reports on an investigation into swelling and phase instability in the binary Mo-Zr system under 14 MeV Cu ion irradiation as compared with similar irradiation of pure Mo. The 9.1 at.% Zr alloy used contains particles of $\gamma(Mo_2Zr)$ in a saturated Mo-rich matrix. The oversized Zr atoms slow down or eliminate void nucleation in the temperature range 700-900°C, where voids form rapidly in pure Mo. In the alloy at 700°C, voids are suppressed up to 7 dpa, at 800°C they form only after an incubation dose of 6 dpa and even at 900°C, nucleation continues at 6 dpa. However, the growth of voids once nucleated is more rapid than in Mo. Dislocation loops nucleate and grow continuously in the alloy and only at 900°C and 6 dpa does a dislocation network form and inhibit further nucleation. Although the alloy was aged to equilibrium before irradiation, many small additional precipitates of Mo_2Zr formed at the grain boundaries, especially during irradiation at 900°C. These effects are understandable in terms of vacancy-solute binding for the oversized Zr atoms and this

explanation is detailed.

V. ACCOMPLISHMENTS AND STATUS

A. Void Swelling and Phase Instability in Heavy Ion Irradiated Mo-Zr Alloy - K-Y. Liou, P. Wilkes, G. L. Kulcinski, and J. H. Billen (U. Wisc.)

1. Introduction

Radiation damage in molybdenum and its commercial alloy, TZM, has been widely studied[1-4] because of the interest in these materials for use in fusion reactors. Void swelling in TZM produced by heavy-ion or neutron irradiation is lower than that in pure molybdenum. This study was aimed at elucidating the effect of zirconium, one of the major solutes in TZM. A Mo-9.1 at.% Zr alloy was chosen and the damage microstructure produced by 14 MeV copper ion irradiation was studied. The effect of the oversized Zr solute on the nucleation and growth of voids was studied around the threshold temperature for void formation (700 ~ 900°C). The preirradiation annealing and heavy-ion bombardment were carried out in the two-phase [$\gamma(Mo_2Zr)$ and molybdenum solid solution] region but close to the phase boundary so that any effects of irradiation on phase stability could be investigated in the same experiment.

2. Experimental Procedure

A Mo-9.1 at.% alloy was prepared by arc melting MARZ grade materials and homogenized at 1650°C for 30h under high (1.3×10^{-6} Pa) vacuum. The samples were then outgassed thoroughly at 1050°C after cutting and electropolishing. Finally, the alloy was equilibrated at the chosen irradiation temperature for ~40 hours under vacuum. The latter two annealing stages lay in the two-phase [Mo-rich solid solution + $\gamma(Mo_2Zr)$] region of the phase diagram.

Typical pre-irradiation microstructures contained

y-precipitates ($\sim$1 μm diameter), uniformly distributed in a homogeneous matrix of Mo-rich solid solution. The number density of γ-precipitates is small enough that a large region of matrix (Mo-7.5 at.% Zr between 700°C and 900°C) was available to observe damage structure produced by irradiation. The γ-phase (Mo_2Zr) particles were not transparent to the electron beam, since they were not polished by the polishing solution. The phase diagram[4] indicates that the matrix contained 7.5 at.% Zr. This composition was verified using X-ray microanalysis with reasonable quantitative agreement.

The specimens were irradiated with 14 MeV copper ions with a damage rate at 1 μm from the irradiated surface, where the damage structure was analyzed, in the range 5-8 x 10^{-4} dpa/sec.

3. Results

Void Formation. Void swelling data in the alloy are shown in Figures 1 and 2. No voids were observed in samples irradiated at 700°C up to 7 dpa. At 800°C, voids were observed only at 7 dpa and above, while void swelling was reduced compared to Mo. Zr additions also reduced swelling at low doses ($\lesssim$4 dpa) at 850°C and 900°C, but high void growth rates were observed, resulting in larger swelling than pure Mo at higher doses. In pure Mo,[6] voids were observed at all temperatures from 700°C to 1000°C, and the incubation dose for void nucleation, if it existed, was very small. In the alloy, however, void nucleation became difficult, while the void growth rates became relatively high. The incubation doses necessary to observe voids were estimated to be 1.5 dpa at 900°C, 3 dpa at 850°C, and 6 dpa at 800°C. Void formation in the alloy was suppressed altogether at 700°C.

Dislocation Structure. The addition of Zr to Mo was found to promote dislocation loop formation. A high density of dislocation loops of ($\sim$1 x 10^{16} cm^{-3}) was formed in the alloy in the early stages of irradiation. At 700°C and 800°C, small loop growth rates were observed, except for a few

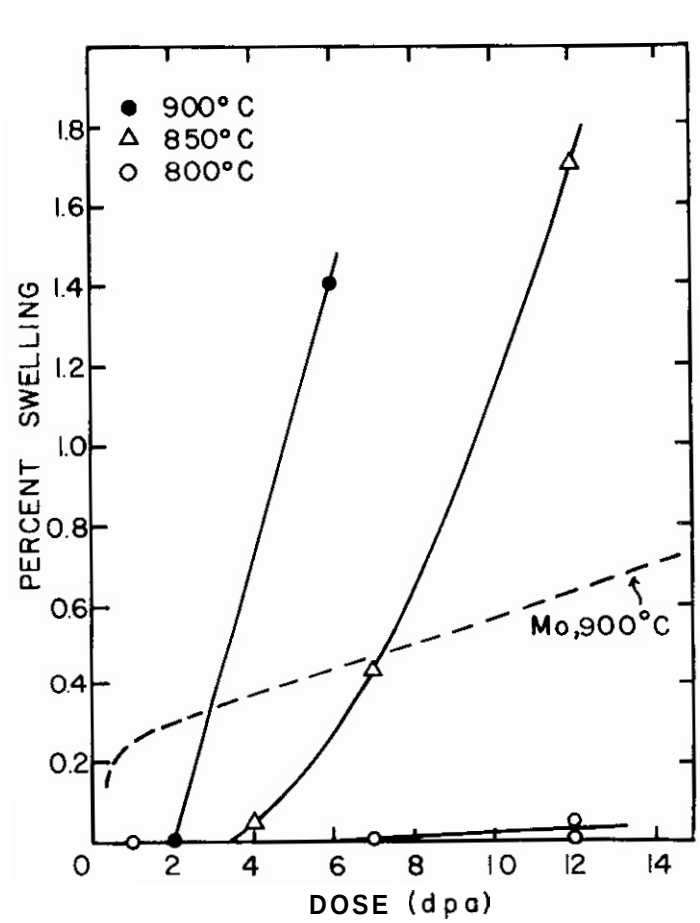

FIGURE 1. Irradiation Swelling of the Mo-7.5% Zr Matrix at 800, 850 and 900°C. The swelling of pure molybdenum at 900°C (6) is included for comparison (dashed line).

loops which intersected to form network dislocations at higher doses. Because new loops still nucleated as dose increased, the loop density remained approximately constant ($1\sim2 \times 10^{16}$ cm^{-3}) at 700°C and 800°C, and the variations in the average loop size were within experimental error ($\overline{d_L}$ = 55 Å at 700°C; $\overline{d_L} \simeq 90$ Å at 800°C). At 850°C and 900°C, however, large loop growth rates were observed. At 900°C and 2 dpa, the average loop diamter, $\overline{d_L}$, was 112 Å, and the number density, N_L, was 8×10^{15} cm^{-3};

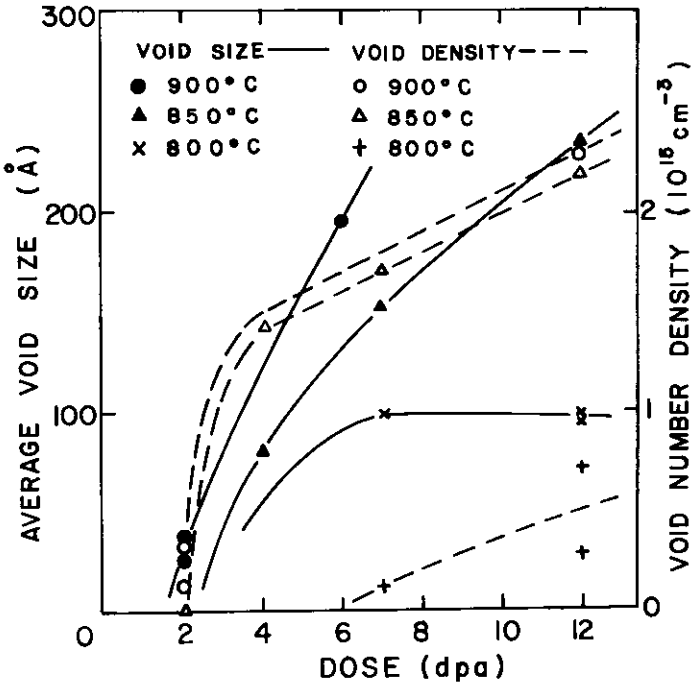

FIGURE 2. Void Density and Average Diameter Versus Dose for the 7.5% Zr Matrix.

almost all of these loops grew into a dislocation network (ρ_d = 2 x 10^{10} cm^{-2}) at 6 dpa. Electron micrographs of typical microstructures observed at 850°C are shown in Figure 3. Analysis of the loop nature was difficult because of the high loop densities and the small sizes. However, some larger loops (200 - 300 Å) were analyzed; they were of the interstitial type with $\vec{b}$ = 1/2 <110> which implies that the loops were faulted.

Radiation Induced Precipitation at the Grain Boundary. After irradiation, new precipitate particles were observed at grain boundaries (Figure 4). They were identified to be γ-phase (Mo_2Zr) by electron diffraction. The bright field and dark field micrographs in Figure 4 also show a shifted void denuded zone in the 900°C, 6 dpa sample due to the migration of the grain boundary during irradiation. The formation of γ-particles following migration of the grain boundary can be seen especially in the dark field micrograph. This irradiation induced γ-precipitation was not observed at low angle grain boundaries. At high angle boundaries, the

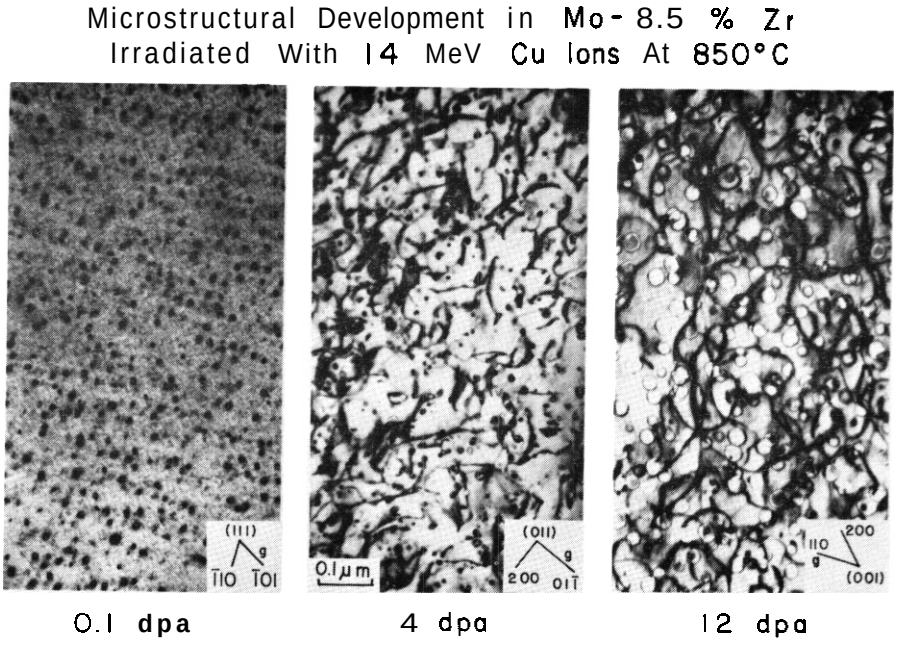

FIGURE 3. Microstructural Development of the Matrix During Irradiation at 850°C. a) 0.1 dpa, b) 4 dpa, c) 12 dpa.

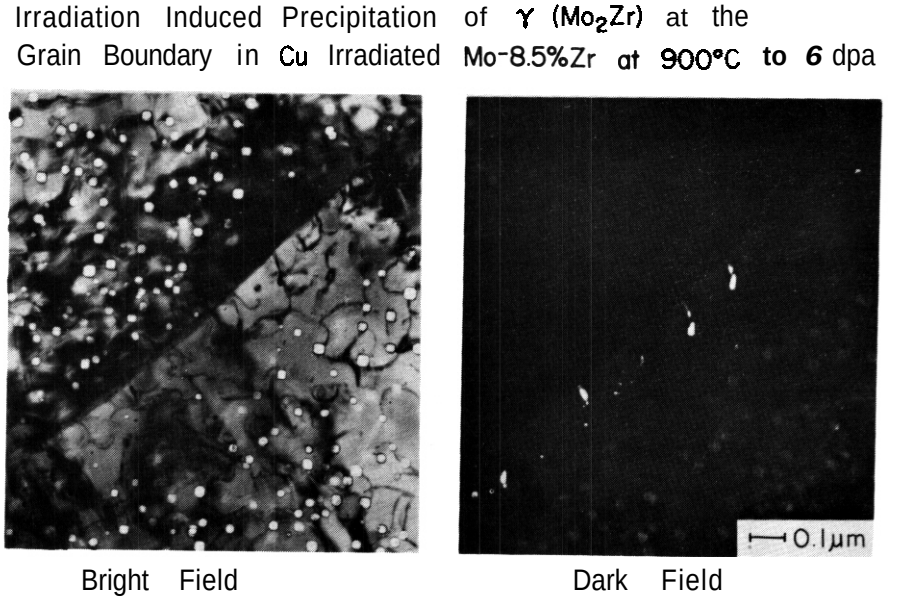

FIGURE 4 Grain Boundary Precipitation of γ (Mo_2Zr), a) Bright Field, and b) Dark Field, Using a Precipitate Reflection. Note that the Boundary Has Moved During Irradiation, Causing Elongation of the Precipitates.

amount of precipitate increased with temperature and dose. No change in the pre-existing y-precipitates was observed.

4. Discussion

The effective atomic volume of Zr[5] is 26 percent larger than Mo in the Mo-rich solid solution. Binding between the vacancies and Zr atoms is expected from strain field considerations. It is therefore tempting to ascribe the incubation period for voids to increased interstitial-vacancy recombination. However, the increased total swelling at high dose for the alloy over pure Mo at 850°C and 900°C indicates that this is not the case.

It is more likely that the Zr is gettering a necessary impurity for easy void formation (probably oxygen), so delaying void nucleation. The enhanced void growth rate compared to pure Mo is probably due to the higher dislocation density, which provides a larger biased sink strength for the point defects.

The enhanced loop nucleation when Zr is added to the BCC Mo solution is probably due to a reduction in the stacking fault energy, since faulted loops were observed. Loop nucleation becomes easier when the stacking fault energy is reduced but loop glide becomes difficult.[7] This explains the absence of loop "rafting" which is observed in pure Mo.[7]

The formation of y-phase particles on the grain boundaries, which are sinks for point defects, may be explained by radiation-induced solute segregation if a large binding energy between the vacancy and the oversized Zr atom is assumed.[8]

Since the alloy was previously equilibrated in the two-phase region, these new precipitate particles imply Zr enrichment of the grain boundary during irradiation. This could be produced by a coupling of either the vacancy or the interstitial flux with a solute flux. The size

of Zr suggests that a vacancy coupling is more likely.

5. Conclusions

The addition of 7.5 at.% Zr to Mo (the saturated solid solution) causes the following changes in radiation damage microstructure.

1) An incubation period was required for void nucleation (1.5 dpa at 900°C, 6 dpa at 800°C). This may be due to Zr gettering a gas impurity which stabilizes voids. Total swelling is increased at higher temperatures and doses in the alloy due to the higher dislocation loop density.

2) Dislocation loop formation was promoted early in the irradiation. Analysis of the larger loops shows that they are faulted ($\underset{\sim}{b}$ = 1/2 <110>), so that Zr clearly reduces the stacking fault energy and hence eases loop nucleation. Unlike pure Mo, the loops being faulted are *not* able to glide.

3) Solute-defect flux coupling effects were observed in the form of incoherent precipitation of $\gamma(Mo_2Zr)$ at the grain boundaries.

VI. REFERENCES

1. J. Bentley, B. L. Eyre, and M. H. Loretto, Proceedings of Int. Conference on Radiation Effects and Tritium Technology for Fusion Reactors, Gatlinburg, Tennessee, October 1975, P. 1-297, CONF-750989, (1976).

2. A. G. Pard and K. R. Garr, Proceedings of Int. Conf. on Radiation Effects and Tritium Technology for Fusion Reactors, Gat1inburg, Tennessee, October 1975, P. 1-312, CONF-750989, (1976).

3. J. E. Stubbins, "Heavy Ion-Induced Radiation Damage and Void Formation in Molybdenum and Its Alloys," Ph.D. Thesis, University of Cincinnati, (1975).

4. J. Bentley and F. W. Wiffen, 2nd Topical Meeting on Tech. of Controlled Thermonuclear Fusion, Richland, Washington, 209 (1976).

5. E. Rudy, Compendium of Phase Diagram Data, Part V, Air Force Materials Lab Report, AFML-TR-65-2, (1969).

6. H. V. Smith, Jr., K-Y Liou, G. L. Kulcinski, and P. Wilkes, University of Wisconsin Report, UWFDM-177, October (1976).

7. B. L. Eyre and D. M. Maher, Phil. Mag. 24, 767 (1971).

8. P. R. Okamoto and W. Wiedersich, J. Nucl. Mat. 53, 336 (1974).

VII. FUTURE WORK

No future work is planned at this time.

VIII. PUBLICATIONS

This information will be published in the Proceeding of the First Topical Meeting on Fusion Reactor Materials, January 29-31, 1979, Miami Beach, Florida.

I. PROGRAM

Title: Simulating the CTR Environment in the HVEM

Principal Investigators: W. A. Jesser, R. A. Johnson

Affiliation: University of Virginia

II. OBJECTIVE

The objective of this work is to investigate the mechanism of helium bubble enlargement during plastic deformation of helium implanted 316 stainless steel.

III. RELEVANT OAFS PROGRAM TASK/SUBTASK

Subtask II.C.8.1 Helium Injection Experiments

II.C.2.1 Helium Mobility, Distribution and Bubble Nucleation

IV. SUMMARY

HVEM tensile samples of 316 stainless steel were irradiated by 80 keV helium ions to produce a population of bubbles of various sizes and number density. The samples were tensile tested at elevated temperature, 600° C, over a range of strain rates. The bubble enlargement behavior was viewed in terms of a dislocation mechanism which is athermal. It was shown that plastic deformation was necessary for the bubble enlargement to occur during crack propagation. Brittle cracks propagate without an associated bubble enlargement and without accompanying plastic deformation. Ductile crack propagation occurs with commensurate plastic deformation and bubble enlargement. These results are related to other work on dislocation

dragging of small bubbles and to other work on vacancy production per unit strain. Both mechanisms may be responsible for bubble enlargement during plastic deformation, however data tend to favor the vacancy production mechanism or a plastic deformation mechanism of microcrack formation under the action of multiple slip systems.

V. ACCOMPLISHMENTS AND STATUS

In-Situ HVEM Tensile Tests of Helium Irradiated 316 Stainless Steel

J. I. Bennetch, J. A. Horton and W. A. Jesser (U. Virginia)

1. Introduction

Helium embrittlement is regarded as the ductility loss accompanying the presence of helium in a material. The fracture mode associated with this embrittlement is typically brittle, intergranular fracture. The current belief as to the role of helium in this process is that it promotes a relative strengthening within grains and a weakening of the grain boundaries.[1-3] Matsumoto et al.[3] tensile tested helium implanted 316 stainless steel at 700° C and found that when the strain rate is increased from 10^{-4} sec^{-1} to 10^{-1} sec^{-1}, the fracture mode changes form intergranular to transgranular. They concluded that helium bubbles move to the grain boundaries during the tensile test, presumably assisted by dislocation dragging.[4] In the previous report, the present authors investigated the fracture behavior of 316 stainless steel helium irradiated to very high doses (2-3 x 10^{18} cm^{-2}). At 600° C the failure occurred by a mixture of intergranular and transgranular fracture while at ambient

temperature the fracture was transgranular only.[5] Clearly a low strain rate and elevated temperature aid in allowing the plastic deformation assisted mechanisms of helium embrittlement to operate. In this report, the continuing study of helium embrittlement is expanded by considering tests at lower strain rates than those employed earlier.

2. Experimental Details

All tensile samples, annealed 316 stainless steel, were irradiated in-situ with a flux of 2×10^{15} $cm^{-2}sec^{-1}$ of 80 keV He^+ ions at a temperature of about 600° C to a fluence of about 3×10^{18} cm^{-2} to provide a high density of large helium bubbles (≃140 nm diameter, 7×10^{13} cm^{-3}). During irradiation, continuous observations of the specimen were performed via a TV recording system. Tensile testing was at 600° C during irradiation. Localized strain rates were obtained from measurements of length changes shown on the dynamic recording. Values of $9 \times 10^{-4}sec^{-1}$ were obtained. This localized strain rate is less than that corresponding to the $10^{-4}sec^{-1}$ macroscopic strain rate employed earlier.[5]

3. Results and Discussion

It has been observed that crack propagation through bubble and/or void containing stainless steel can enlarge the cavities. This result is of interest as it suggests a possible mechanism for helium bubble enlargement in helium embrittled materials. In the present report the experimental evidence is viewed with the aim of determining the bubble enlargement mechanism. There are at least three possibilities, any one of which

could be dominant over the others depending upon the prevailing stress and deformation conditions as well as specimen temperature. The three mechanisms considered here are: 1) the dragging of small bubbles by moving dislocations with the result that the small mobile bubbles coalesce with other bubbles to produce an enlarged bubble[4], 2) the motion of dislocations through the dragging of jogs and collection of vacancies to the dislocation line can provide vacancies for absorption by the bubble when the dislocation reaches the bubble, 3) the triaxial stress distribution near the crack tip can cause microcrack formation through the cooperative action of many dislocations moving on several active slip systems. All of the above mechanisms invoke dislocation motion and hence are not easily separated from each other. There are some distinguishing tendencies which may be associated with the mechanisms. In the case of bubble dragging by dislocations, one might expect that thermal activation would enhance the process and promote bubble enlargement at elevated temperatures.[6] The temperature dependence of mechanism 3, microcrack formation, would be negligible and that of the dislocation generated vacancy absorption would be expected to be only mildly temperature dependent when the action of the dislocations in moving the vacancies to the bubble is dominant.

In the case of helium irradiated samples, bubble enlargement was found to occur at 600° C as well as at ambient tmperature and hence the bubble enlargement mechanism is essentially athermal in nature. Ruedl and Schiller[7] observe that in helium implanted aluminum tensile tested at room temperature bubble alignment and enlargement occurs in a manner which

excludes bubble dragging by dislocations and favors absorption of vacancies generated by plastic deformation. In their experiments the bubbles were small, 1-5 nm in diameter, and increased in volume by a factor of 8 near the crack flanks leading to a vacancy production, C_v, per unit strain, ε, of $C_v/\varepsilon \simeq 10^{-3}$. These experiments are consistent with the essentially athermal nature of the bubble enlargement mechanism. A similar enlargement factor was observed in the present study of neutron irradiated 304 stainless steel tensile tested at 600° C. The initial cavity size and density was 30 nm and 1×10^{14} cm^{-3} which corresponds to 0.15 % swelling. After the crack propagated through the grain, the bubble size increased to 60 nm through a region extending 200 nm from the crack flanks which corresponds to a cavity volume fraction of 1.1 %. The plastic strain associated with this ductile crack propagation is of the order of magnitude of unity which corresponds to a vacancy production per unit strain of $C_v/\varepsilon \simeq 10^{-2}$. That this number is higher than that for aluminum tested at room temperature, may be a result of the higher test temperature for the stainless steel. It may be significant that the shape of the cavities before and after enlargement was unaltered by the enlargement mechanism. From the above experimental observations it seems that bubble absorption of vacancies generated during plastic deformation is a possible mechanism which may play a role in helium embrittlement.

There is an additional experimental observation on helium irradiated 316 stainless steel which does not fit the above suggestion that dislocation generated vacancies may be responsible for bubble enlargement at the crack flanks. In this case a high dose (3×10^{18} cm^{-2}) helium irradiation

at 80 keV produced a bubble size and density of ≈100 nm at 3×10^{13} cm^{-3}. During a 600° C tensile test, a crack produced several hundred percent strain and a bubble volume enlargement by a factor 8. However, the crack caused a distortion of the bubble shape and hence the bubble enlargement is likely a result of the third mechanism which relies on multiple active slip systems and cooperative dislocation motion. If the vacancy absorption mechanism is assumed applicable to this case, the vacancy production per unit strain is almost an order of magnitude higher than that for the case of neutron produced cavities discussed above, namely $C_v/\varepsilon \simeq 8 \times 10^{-2}$. While it is interesting that the bubble enlargement factor is 8 in all three cases mentioned above, no significance has been attributed to this number which applies to the case of small bubbles as well as that of large bubbles.

A result related to the above set of postulated mechanisms is that obtained from video recordings of in-situ helium irradiation of a 316 stainless steel sample which showed separation between a circular surface region and the underlying material. This effectively corresponds to a crack propagation parallel to the film plane and normal to the viewing direction. The event took place at 600° C during helium irradiation and showed that bubble enlargement by a factor of 1.6 occurred within less than 0.1 sec.[8] A calculation of the vacancy production per unit strain for this case yields $C_v/\varepsilon \simeq 9 \times 10^{-2}$ which is a number similar to that for the case of crack propagation under a tensile stress. The bubble density decreased during the separation event only by 20% which shows that coalescence is not a significant factor. The distance of interaction of the

crack flank in this surface separation is roughly 100 nm which would require vacancy diffusivities greater than 10^{-10} cm^2 sec^{-1} in order to account for the above process via a thermal diffusion mechanism. Such diffusion would be assisted by the concurrent irradiation which took place at a flux of $2 \times 10^{15} cm^{-2} sec^{-1}$. Even so, it is unlikely that thermal diffusion is responsible for the bubble enlargement at 600° C in this case because the bubblesnearby, within a distance of 500 nm of the enlarging bubbles, remained substantially unaltered during the same time that the neighboring bubbles enlarged abruptly in diameter by a factor of 1.6. Of course, bubble enlargement occurs slowly during irradiation and also may occur slowly during long term annealing in the absence of applied stress, however these processes are sufficiently slow compared to the above discussed rate of bubble enlargement that they can be ignored as a significantly contributing factor. Further, abrupt bubble enlargement with crack propagation has been observed in neutron irradiated samples and helium irradiated samples tensile tested in the absence of irradiation and hence the effect does not rely on the presence of irradiation during plastic deformation.

Bubble enlargement associated with plastic deformation occurs at ambient temperature as well as at elevated temperature and hence cannot be directly responsible for the intergranular fracture associated with helium embrittlement which occurs only at elevated temperatures. In the present set of experiments conducted at low strain rate, it has been observed that a crack may propagate at 600° C through a grain containing helium bubbles of a size and density (≃140 nm, 7×10^{13} cm^{-3}) and not

enlarge the bubbles adjacent to the crack flanks. This observation was made during irradiation at a helium flux of 2×10^{15} $cm^{-2}sec^{-1}$. In this case brittle crack propagation without noticeable plastic deformation occurred. This result emphasizes the necessity for plastic deformation in the bubble enlargement process associated with crack propagation. The brittle crack and bubble population around the crack are shown in the micrograph of figure 1. The crack direction does not correspond to a low index direction and hence the crack plane is not a low index plane.

From the above experimental evidence and evaluation it is clear that the rapid bubble enlargement mechanism is directly related to the presence of plastic deformation in the form of dislocation motion. Calculations show that bubble absorption of vacancies produced during plastic deformation is a reasonable mechanism when bubble size is small ($\simeq$50 nm) but that it is less likely to account for the bubble enlargement mechanism in the case of large bubbles (>100 nm).

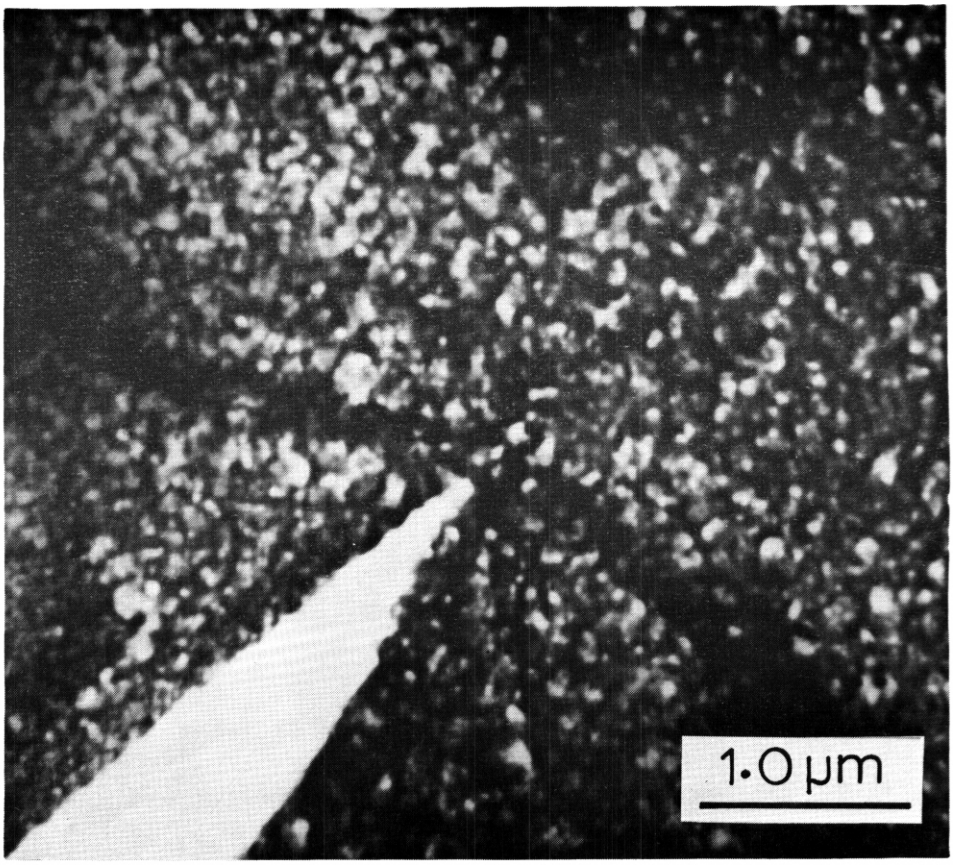

Figure 1 HVEM micrograph of 316 stainless steel irradiated at 600° C by 80 keV helium of flux 2 x 10^{15} $cm^{-2}sec^{-1}$ to a fluence of 3 x 10^{18} cm^{-2}. Average bubble diameter and density are 140 nm and 7 x 10^{13} cm^{-3} corresponding to 9.5 % swelling. Note the brittle crack which propagated without significant plastic deformation or bubble enlargement along the crack flanks.

VI. REFERENCES

1. R. S. Barnes, Nature, 206(1965)1307

2. A, A. Saques, H. Schroeder, W. Kesternich and H. Ullmaier, J. of Nucl. Mat., 78(1978)289.

3. K. Matsumoto, T. Kataoka, M. Terasawa, M. Shimada, S. Nakahigashi, H. Sakairi and E. Yagi, J. of Nucl. Mat., 67(1977)97.

4. W. Beere, Scripta Met., 9 (1975) 999.

5. J. A. Horton, J. I. Bennetch and W. A. Jesser, DAFS Quarterly Progress Report, October-December 1978, DOE/ET-0065/4 (1979).

6. H. Trinkaus and H. Ullmaier, to be published J. Nucl. Mat.

7. E. Ruedl and P. Schiller, to be published J. Nucl. Mat.

8. J. I. Bennetch, M. L. Sattler, L. L. Schiestle Horton, J. A. Horton and W. A. Jesser, to be published J. Nucl. Mat.

VII. FUTURE WORK

Similar experiments for low bubble diameters and low strain rates are planned as well as further tensile tests of neutron irradiated samples at low swelling and low test temperature.

DISTRIBUTION FOR DAFS QUARTERLY REPORTS

uc-20 (122)
UC-20c (80)
APPROVED SPECIAL DISTRIBUTION (82)

Argonne National Laboratory (3)
700 South Cass Ave.
Argonne, Illinois 60439

L. R. Greenwood
A. Taylor
H. Wiedersich

Brookhaven National Laboratory (1)
Associated Universities
Upton, New York 11973

Chairman, Department of Nuclear Energy

Columbia University (1)
Plasma Physics Laboratory
New York, New York 10027

R. A. Gross

Department of Energy (7)
Mail Stop B-107
Washington, D.C. 20545

Assistant Director for Materials Technology, RRT
N. A. Davies
J. F. Decker
P. B. Hemmia
K. G. Moses-
R. E. Price
F. T. Scott

Department of Energy (3)
Richland Operations
Richland, WA 99352

W. A. Burns
G. M. Chenevert
L. A. Pasquini

General Atomic Company (3)
P. O. Box 81608
San Diego, California 92138

C. Baker
G. R. Hopkins
L. Royner

Hanford Engineering Development Laboratory (28)

W. L. Bunch/L. L. Carter	W/B-47
T. T. Claudson	W/C-16
D. G. Doran (10)	W/A-57
F. A. Garner	W/A-57
D. S. Gelles	W/A-57
R. E. Gold	W/C-39
H. L. Heinisch	W/A-57
F. M. Mann	W/FED-429
W. N. McElroy	W/C-39
G. H. Moulthrop	W/C-115
R. E. Nygren	W/A-58
E. K. Opperman	W/A-58
N. F. Panayotou	W/A-53
R. E. Peterson	W/E-18
E. W. Pottmeyer	W/E-14
R. W. Powell	W/A-57
R. E. Schenter	W/FED-420
J. O. Schiffgens	W/A-57
R. L. Simons	W/A-57

Lawrence Livermore Laboratory (2)
University of California
P. O. Box 808
Livermore, California 94550

M. W. Guinan
C. M. Logan

Los Alamos Scientific Laboratory (3)
University of California
P. O. Box-1663
Los Alamos, New Mexico 87544

D. J. Dudziak
C. R. Emigh
W. Green

Massachusetts Institute of Technology (1)
Cambridge, Massachusetts 02139

L. Lidsky, Department of Nuclear Engineering

McDonnell-Douglas Astronautics (1)
P. O. Box 516
St. Louis, Missouri 63166

D. Kummer

Mound Laboratory (1)
P. O. Box 32
Miamisburg, Ohio 45342

Manager, Technology Applications and Development

National Bureau of Standards (1)
Gaithersburg, MD 20760

C. D. Bowman

Naval Research Laboratory (2)
Metallurgy Division, Code 6390
Washington, D.C. 20375

I. Manning
J. A. Sprague

North Carolina State University (1)
Department of Nuclear Engineering
Raleigh, North Carolina 26707

J. R. Beeler, Jr.

Oak Ridge National Laboratory (8)
P. O. Box Y
Oak Ridge, Tennessee 37830

Director, Thermonuclear Division, Bldg. 9201-2
R. J. Colchin, Bldg. 9201-2
W. R. Martin, Bldg. 4500 S
F. G. Perey
M. Roberts, Bldg. 9204-1
J. O. Steigler
C. Weisbin
F. W. Wiffen

Pacific Northwest Laboratory (4)
P. O. Box 999
Richland, Washington 99352

J. L. Brimhall
T. Chikalla
A. B. Johnson
L. C. Schmid

Plasma Physics Laboratory (3)
Princeton University
Forrestal Campus
Box 451
Princeton, New Jersey 08540

C. Osgood
W. Price
K. Wakefield

Rockwell International (1)
Energy Systems Grouo
8900 DeSoto Ave.
Canoga Park, California 91304

D. Kramer

Sandia Laboratories (2)
Albuquerque, New Mexico 87115

F. L. Vook (2)

Sandia Laboratories (1)
Livermore, California 94550

W. D. Wilson

University of Michigan (1)
Nuclear Engineering Department
College of Engineering
Ann Arbor, Michigan 48105

T. Kammash

DISTRIBUTION (cont'd)

University of Virginia (1)
Charlottesville, VA 22901

W. A. Jesser

University of Wisconsin (1)
1500 W. Johnson Drive
Madison, WI 53706

P. Wilkes

Westinghouse Electric Corporation (2)
Research and Development Center
Beulah Road
Pittsburgh, Pennsylvania 15234

H. R. Holland
J. A. Spitznagel

☆U.S. Government Printing Office: 1979 698-602-15